ISBN 978-82-326-1898-9 (printed ver.)
ISBN 978-82-326-1899-6 (electronic ver.)
ISSN 1503-8181

NTNU
Norwegian University of
Science and Technology

Bjørn Kolbrek

Doctoral thesis

Doctoral theses at NTNU, 2016:280

NTNU
Norges teknisk-naturvitenskapelige universitet
Thesis for the Degree of
Philosophiae Doctor
Faculty of Information Technology, Mathematics
and Electrical Engineering
Department of Electronics and
Telecommunications

NTNU

Doctoral theses at NTNU, 2016:280

Bjørn Kolbrek

Extensions to the Mode Matching Method for Horn Loudspeaker Simulation

NTNU
Norwegian University of
Science and Technology

Bjørn Kolbrek

Extensions to the Mode Matching Method for Horn Loudspeaker Simulation

Thesis for the Degree of Philosophiae Doctor

Trondheim, October 2016

Norwegian University of Science and Technology
Faculty of Information Technology, Mathematics
and Electrical Engineering
Department of Electronics and Telecommunications

NTNU
Norwegian University of
Science and Technology

NTNU
Norwegian University of Science and Technology

Thesis for the Degree of Philosophiae Doctor

Faculty of Information Technology, Mathematics and Electrical Engineering
Department of Electronics and Telecommunications

ISBN 978-82-326-1898-9 (printed ver.)
ISBN 978-82-326-1899-6 (electronic ver.)
ISSN 1503-8181

Doctoral theses at NTNU, 2016:280

Printed by NTNU Grafisk senter

ABSTRACT

For loudspeaker horns, the throat acoustic impedance and the far field directional characteristics are important measures of performance. Both quantities depend greatly on the shape of the horn, and the acoustical conditions at the mouth of the horn.

The Mode Matching Method (MMM) is a semianalytical method for the simulation of sound propagation in ducts, and is the method used as the fundamental building block in this work. In previous work using this method, the horn has usually been assumed to be mounted in an infinite baffle, a condition that is not realistic for most real-world applications. Most horns are usually mounted in finite baffles or cabinets, or placed close to reflecting surfaces or in rooms. This work has therefore focused on extending the MMM to new cases closer to real-world applications.

For horns without baffle, or with finite baffles or flanges, two methods have been explored; one for axisymmetric horns based on the solution for a semi-infinite unflanged duct, and one for general geometries based on edge diffraction. For horns near infinite reflecting surfaces, a method has been derived to compute the modal mutual radiation impedance. For the final radiation condition, a horn mounted in the wall of a room, two methods have been explored, where in both cases analytical expressions for radiation impedance and radiated pressure are found for shoebox shaped rooms. Experimental verification of some of the cases mentioned above is provided.

The MMM is restricted to certain cross-sectional geometries; round and rectangular geometries are treated in this work. In many practical cases a rectangular horn is connected to a circular loudspeaker, and in order to simulate this and similar configuration, a method has been developed to interface the MMM with the Boundary Element Method.

By modifying the MMM, it has also been possible to simulate radiation from concave structures like loudspeaker diaphragms. Using this approach it is also possible to simulate concave reflectors, as long as the source is not outside of the cavity.

A final application of the MMM in this work, is the use of the method to compute the transfer function and resonance frequencies of non-shoebox shaped rooms. While the shape of the room is still somewhat restricted compared to Finite Element Method simulations, a wide range of rooms can be simulated.

PUBLICATIONS

List of published journal and conference papers:

Kirkup, S. M., Thompson, A., Kolbrek, B., and Yazdani, J., “Simulation of the acoustic field of a horn loudspeaker by the Boundary Element-Rayleigh Integral Method,” *Journal of Computational Acoustics*, vol. 21, no. 1, pp. 1–17, 2013 (Cited on pages 37, 56, 209, 217, and 235.)

Ortiz, S., Kolbrek, B., Cobo, P., González, L. M., and Colina, C. d. l., “Point source loudspeaker design: Advances on the inverse horn approach,” *J. Audio Eng. Soc*, vol. 62, no. 5, pp. 345–354, 2014.

Kolbrek, B., “Using mode matching methods in horn loudspeaker simulation,” in *Proceedings of Forum Acusticum 2014*, 2014

Kolbrek, B., “Development of horn loudspeakers before 1940,” in *Proceedings of Forum Acusticum 2014*, 2014 (Cited on page 28.)

Kolbrek, B. and Svensson, U. P., “Using mode matching methods and edge diffraction in horn loudspeaker simulation,” *Acta Acustica united with Acustica*, vol. 101, no. 4, pp. 760–774, Jul/Aug 2015 (Cited on pages 9, 10, 71, 106, 131, and 191.)

Evensen, K. B. and Kolbrek, B., “Mode matching method for concentric horns,” *62nd Polish Open Seminar on Acoustics*, 2015 (Cited on page 71.)

Kolbrek, B., “Modal impedances and the boundary element method: An application to horns and ducts,” *139th Convention of the Audio Engineering Society*, Oct 2015, preprint no. 9369 (Cited on pages 10 and 215.)

Kolbrek, B., “Horns near reflecting boundaries,” *139th Convention of the Audio Engineering Society*, Oct/Nov 2015, preprint no. 9412 (Cited on pages 10, 161, 191, and 207.)

Kolbrek, B. and Svensson, U. P., “Modeling non-shoebox shaped rooms with the mode matching method,” *140th Convention of the Audio Engineering Society*, Jun 2016, preprint no. 9506 (Cited on pages 11 and 249.)

Kolbrek, B., Evensen, K. B., and Svensson, U. P., “Simulating axisymmetric concave radiators using mode matching methods,” *J. Audio Eng. Soc.*, vol. 64, no. 5, pp. 311–319, May 2016 (Cited on pages 11 and 227.)

Sjösten, P., Svensson, U. P., Evensen, K. B., and Kolbrek, B., "The effect of Helmholtz resonators on the acoustic room response," *Baltic-Nordic Acoustic Meeting*, Jun 2016 (Cited on pages 10 and 177.)

PREFACE

This thesis is submitted to the Norwegian University of Science and Technology (NTNU) in partial fulfillment of the requirements for the degree of Philosophiae Doctor (Ph.D.). The work was carried out at the Acoustics Research Center at the Department of Electronics and Telecommunications, with under the supervison of Professors Peter Svensson (main supervisor) and Ulf Kristiansen (co-supervisor).

This thesis is the result of many years spent on horn loudspeaker research, from when I first became interested in the subject around 1999, until 2016. My interest in horn speakers started with a comment in a catalog for the Norwegian company Demostenes, a company selling vacuum tubes, that stated that "once you hear a horn loudspeaker, you will never be the same again". This intrigued me, and started me on a fascinating trip of discoveries of reading, building and listening. Around 2003-2004 I met Thomas Dunker, another horn speaker enthusiast, and we quickly joined our efforts. For several years we worked as "hobby researchers", digging up large amounts of horn loudspeaker knowledge, much of which, it turned out, was from the period 1920–1940.

As we were going deeper into the matter, a few of my friends suggested that I should try to obtain an M.Sc. degree in acoustics, based on the knowledge I had accumulated. So in 2009 I enrolled part-time in the 2-year M.Sc. program at NTNU, and in 2010 I quit my job as R&D Engineer at Scana Mar-El. After a while, I started considering getting a Ph.D. while I was at it, since that could be my only chance to work full time with horn loudspeakers, and I was accepted for the Integrated Ph.D. program in 2011.

My motivation for quitting a secure job to go full in for what was once purely a hobby is not easy to explain. It is probably a combination of a passion for research and innovation and the desire for more knowledge, combined with a desire to do things thoroughly. Another motivation is the ongoing joint project I have with Thomas Dunker, of collecting and completing the existing knowledge about horn loudspeakers, and presenting it in book form. The work done in this thesis is a step towards that goal. I hope you like it.

> *All the horns of the wicked also will I cut off;*
> *but the horns of the righteous shall be exalted.*
>
> Psalm 75:10

ACKNOWLEDGMENTS

First of all I want to thank my supervisor, Prof. Peter Svensson for guiding me through this Ph.D., for all the help along the way, for all the helpful suggestions, and for the many interesting discussions we have had. Thanks to Dr. Jonathan Kemp, for help in understanding the mode matching method. To Prof. Anna Snakowska, who received me at AGH in Krakow, for the cooperation and discussions on unflanged ducts. To Dr. Jerzy Jurkiewicz at AGH, for invaluable help in computing the complex functions associated with unflanged ducts. To Tim Mellow and Leo Kärkkäinen for exiting collaboration and discussions that sadly didn't make it into this thesis.

To Thomas Dunker for cooperation on horn loudspeaker research since 2004, for many interesting discussions over the years, and for keeping up my motivation in this big project. To David J. McBean for many interesting discussions on horn theory and horn simulation, for help with horn simulation problems, and for proof reading.

To the NTNU acoustics group, and especially to Tim Cato Netland for discussions, challenges and practical help. To Tore Landsem and Tore Berg at the workshop at IET, NTNU, for building the horn and associated equipment used in the experiments.

Finally, thanks to my parents and my friends (you know who you are) for believing in me through this project. And last but not least, thanks to God.

CONTENTS

ACRONYMS

BTL	Bell Telephone Laboratories
RCA	Radio Corporation of America
BEM	Boundary Element Method
FMBEM	Fast Multipole BEM
FEM	Finite Element Method
BERIM	Boundary Element Rayleigh Integral Method
MMM	Mode Matching Method
FDM	Finite Difference Method
FDTD	Finite Difference Time Domain
TLM	Transmission Line Method
SSM	Source Superposition Method
MFS	Method of Fundamental Solutions
EDM	Edge Diffraction Method
IB	infinite baffle
MMBEM	Mode Matching Boundary Element Method

Part I

INTRODUCTION AND BACKGROUND

This part is an introduction to this thesis, and is divided into three chapters: a general introduction describing the background and motivation for this work, a historical background that serves as an introduction to horns used for sound reproduction, and an overview of horn simulation methods.

1

INTRODUCTION

The introduction of this thesis is split into three chapters. This chapter is mainly a short description of the background and motivation for this work, and an overview of the rest of thesis. The following two chapters will give a historical background and an overview of horn simulation methods.

1.1 BACKGROUND

Horns and horn loudspeakers are in use in a variety of fields. Horns as used in music instruments are of course of great interest, and much work has been done on this topic. Horn loudspeakers are mainly used in three fields: sound reinforcement at concert venues and the like, public address and paging, and for cinema sound systems. A fourth field is the use in high fidelity home audio systems, but this field is a rather small part of the total volume of horn loudspeakers in use.

Originally, horns were used in gramophones and loudspeakers to increase the power output of the source by impedance matching. High efficiency loudspeakers were required due to amplifier power being very expensive. Extensive use of horns in early cinema and public address systems also highlighted the problem of directivity: the exponential horns, almost universally used in the early days because of their impedance matching properties, had directional characteristics that varied with frequency. Clusters of horns were necessary to cover the entire audience with a reasonably uniform frequency response.

Horn loudspeakers for home entertainment use were common in the early 1920s, but fell out of favor when the direct radiating cone loudspeaker was introduced. Even if horn speakers are in use for home entertainment by quite a few enthusiasts (the author included), the percentage of the total home audio market is small.

As amplifier power became cheaper, the purpose of horns became more and more directed towards directivity control. Still, for many years horn designers also put effort into designing horns that provided uniform acoustic loading over the horn's working range. Multicellular horns used exponential cells [1], radial horns sought to keep the wave front area expansion exponential, and Keele's Constant Directivity design from the 1970s used an exponential throat section for loading, followed by a radial conical section for directivity control [2]. It was probably the Manta-Ray horns developed by Altec Lansing [3] that first disregarded horn loading in favor of directivity control.

In horn design today, directivity is of prime importance, and any numerical tool used for horn simulation should aim to accurately predict the directivity performance of the horn.

This thesis is concerned with the development of numerical methods for horn loudspeaker simulation, but the methods are not restricted to this area of application: the methods are applicable in the rather broad field concerning sound propagation in, and radiation from, ducts.

1.2 AREAS OF APPLICATION

The three main areas of application for horn (or duct) simulation methods are horn loudspeakers, musical wind instruments, and duct systems such as ventilation systems and acoustic filters. In addition, simulations of the ear canal and vocal tract may employ similar methods, sometimes with non-rigid walls (See for instance Hudde [4]). The main three areas of application do, of course, have some similarities and some differences, and these will be highlighted in the following sections. But basically, the similarities are in how the sound field in the horn or duct is calculated, the differences lie in the emphasis put on the different quantities that are calculated. Importance of input impedance, directivity and flow differs widely between the methods.

1.2.1 *Horn Loudspeakers*

Simulation of horn loudspeakers is the main motivation behind the work described in this thesis. Horn loudspeakers differ from the two other main areas of application for duct simulation methods in at least three ways. Firstly, the frequency range (in terms of wave length vs. size, kL) usually extends far beyond that of ventilation systems, and often into a higher kL range than for many musical instruments. Secondly, the computation of directivity is extremely important, as one of the main reasons for using horns in modern sound reinforcement systems is directivity control [3, 5]. Thirdly, since horns in sound reinforcement systems are often operated at very high levels, nonlinear distortion can be considerable, and this has implications for the perceived sound quality [6, 7].

As the acoustic load of the horn also affects the smoothness of the frequency response. This parameter that is still important despite the availability of equalization [8], so it should not be forgotten. Knowing the acoustic load presented by the horn is also required in order to couple the horn with a loudspeaker driver model.

1.2.2 *Musical Instruments*

In musical wind instruments, horn simulation has two primary purposes: the *forward problem*; to accurately predict the resonance characteristics of instruments of a given bore profile, and the *inverse problem*; to reconstruct the bore profile of instruments from measurements, to aid in repair, modifications or analysis. Resonance frequencies should ideally be predicted with the accuracy of a few cents of a semitone, and therefore the methods developed for this purpose aim to give good accuracy in this respect. As peaks of the input impedance curve are usually what is used for detecting resonance frequencies, the input impedance is what has received most attention in wind instrument modeling research.

The forward problem may relate to the design of new instruments, or to the synthesis of instrument sounds. For the last application, computational efficiency is usually very important, as the synthesis may have to be performed in realtime.

In the inverse problem, the task is often to reconstruct the bore profile based on measurement of the input impedance[9, 10, 11, 12], or to produce a horn with a given set of resonance frequencies [13, 14]. This is usually done by running an optimization algorithm that tries to minimize the difference between the measured (or specified) and the simulated impedance. For this, it is important that the simulation algorithm is fast, and at the same time accurately calculates the resonance frequencies.

Directivity has largely been neglected, but if it is to be included, it is often desirable to include the radiation from finger holes as well as from the bell [15]. Nonlinear effects are usually also neglected. While wind instruments also have flow, this is often neglected in the models, but viscous losses and the effect of temperature gradients along the instrument are often taken into account. The effects of bends may also be included [16, 17, 18, 19, 20, 21, 22].

1.2.3 *Duct Systems and Acoustic Filters*

Simulation of ducts, like HVAC systems, silencers, mufflers and other acoustic filters, and also sound radiation from turbofan engines, often use methods similar to, and often applicable to, horn simulation. The main purpose of the simulation is usually to calculate the transmission loss of the system, often with the purpose of computing the attenuation of noise from the fans. Pioneers in this field were George Walter Stewart, who analyzed acoustic filters as early as 1922 [23, 24, 25, 26, 27], and Warren P. Mason of The Bell Telephone Laboratories, who developed approximate equations for designing several types of such filters based on filter theory [28, 29].

For duct systems, the effects of cavities, step discontinuities, junctions and bends, on the transmission loss are often of great interest. Acoustic impedance as a separate quantity is usually not important, but may be useful during calculations. Directivity is usually of little importance. This is both because the duct cross sectional dimensions in many cases are small compared to the wavelength, but most often because the investigations are only concerned with what happens inside the duct, and not outside the radiating end. An exception is in the case of turbofan machinery, where directivity may have some importance [30, 31]. Often the effect of flow is of some importance too, again especially in turbofan machinery, where the flow velocity is not negligible [32].

1.3 MOTIVATION

To describe the motivation for this work is not a simple task. Motivation ranges from personal interest (which fits better in the preface) to the needs of horn designers, and the need to investigate certain aspects of horn loudspeakers that have not been sufficiently covered in the literature.

Designing a horn with certain properties can in many cases look more like art than science. The reason for this is mainly the complex nature of acoustic wave propagation in horns, which in general is not analytically solvable, except for in a few special cases. And even though analytical solutions can be found for some cases, there are still issues to be solved. For instance, a conical horn in a sphere (a problem which is analytically solvable) will have significant diffraction at the mouth, which gives a less-than-perfect directivity pattern [33]. This problem can be reduced by introducing a flare at the mouth of the horn, but then we no longer have an analytical solution of the problem. In addition, it is usually impractical to mount horns in large spheres; more often they are mounted in rectangular loudspeaker enclosures.

The traditional approach, dating back to Rayleigh [34] and Webster [35], is to reduce the three-dimensional wave equation to a one-dimensional one, which can then be analytically solved for a number of horn contours. However, a one-dimensional equation gives no information about directivity. Since directivity control is the main reason for using horns today, this is not a viable option.

For general horn design, one therefore must resort to numerical methods. There are several methods available, all of them usually require some discretization of the boundary and/or domain. A common factor for these methods is that they require relative large amounts of memory, and often long computation times. While these limitations are slowly reduced as computing power increases, they still impose a challenge, especially when it comes to using them in optimization algorithms, which requires hundreds or thousands of evaluations of the complete horn design.

Therefore, one motivational factor for the work described in this thesis is to develop methods that make faster and more efficient simulation of horn speakers possible. The Mode Matching Method (MMM), first implemented by Alfredson [36] and Roure [37], appeared to be a good candidate, and I familiarized myself with the method during the work on my Master's thesis [38].

The use of the method, as presented in the literature, had clearly been limited to horns mounted in infinite baffles. Since this is rarely the case in practice, another motivational factor was to extend the applicability of this method to other cases, like free standing horns and horns near reflecting boundaries.

Placing horns near corners is an old technique for reducing the size of the horn, by utilizing the image sources created by the walls [39]. But nothing appeared to have been done on investigating how the distance to the walls would effect the performance of the horn beyond the classical Waterhouse curves [40]. Another question was how a horn would perform when radiating into a room. These questions provided another motivational factor.

The Mode Matching Method has some restrictions on geometry. To be truly useful in more general horn speaker modeling, the ability to couple the method with other numerical methods that could be used in the more complex parts of the horn, had to be investigated.

As the work progressed, new questions appeared: extension to new geometries, application of the Mode Matching Method to loudspeaker cones and room acoustics, simulation of folds in horns, and the inclusion of geometrical acoustics for high frequency modeling. Some of the questions have been answered, the rest will be discussed under Future Work in Chapter 13.

Throughout the work, the main motivation has been to extend the toolbox of the horn designer with efficient tools that can easily be applied to a variety of different cases. The practical aspects of the methods have been very important. Elegant methods that are impractical to use are of little value.

1.4 SCOPE

A sketch of a typical horn loudspeaker is shown in Figure 1. A horn driver is connected to the throat of the horn, and the mouth of the horn radiates into the surrounding environment. The acoustical conditions outside the horn influences the radiated pressure and the radiation impedance, Z_{rad}, at the horn mouth. The shape of the horn determines its directivity, and how the radiation impedance is transformed into the throat impedance, Z_{th}, seen by the driver.

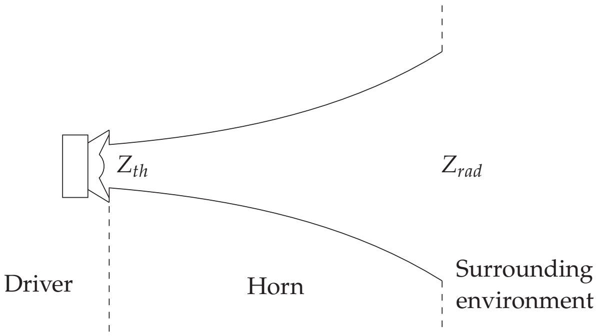

Figure 1: A horn loudspeaker.

The work presented in this thesis focuses mainly on the horn and the surrounding environment. The properties of the driver is to a large degree separated from the properties of the horn [41, 7]. Therefore it makes sense to leave out the driver modeling from this study, but instead make room for exciting the horn with an arbitrary sound field. This way, the effects of the driver can be taken into account at a later stage.

Some work has, however, been done to include the driver: the basic MMM has been extended to cases where the entire structure vibrates, and it is therefore possible to take the geometry of the driver diaphragm shape into account. Structural and electromechanical coupling in the driver is considered beyond the scope of this work, and is not included.

Nonlinear distortion in the horn is a complex task even in simple, one-dimensional horn models [42]. To extend distortion modeling to the MMM is considered beyond the scope of this work. Viscous and thermal losses, often of great interest in music instruments, have also been neglected, since they play a relative minor part in the performance of horn loudspeakers.

Another task that is considered to be outside the scope of this work is the investigation of the subjective perception of horn based sound reproduction. To properly investigate this side of horn loudspeakers would require large, and presumably expensive, subjective tests. Some work has also already been done on this topic [43].

1.5 THIS THESIS

Since there are relatively many chapters in this thesis, it has been divided into four parts, which are described below.

PART I is the introductory part, and is divided into three chapters, the first of which is this one. In addition come the following two chapters:

- CHAPTER 2 gives the historical background and context of horn loudspeakers. The chapter is somewhat more detailed than what one would usually find in a thesis about numerical simulation, but this is due to my great interest in the history of audio technology.
- CHAPTER 3 gives an overview of methods used for simulation of horns and ducts.

PART II is devoted to the Mode Matching Method, which is the main method that is used in this text.

- CHAPTER 4 presents the theoretical foundation for the MMM, and contains all the equations necessary for implementing the discrete version of the method. This chapter is mostly based on the work of others. The coupling matrices for asymmetric rectangular ducts were derived in my Master's thesis [38], and is not part of this work. The coupling matrices for annular ducts were derived by Karen Brastad Evensen in her Master's thesis [44] under my supervision. My contribution in this chapter is the rearrangement of the basic MMM algorithm to reduce memory requirements, first presented in [45].
- CHAPTER 5 covers some general aspects of modal radiation from horns. New in this chapter is the discussion of modal radiation impedance matrix and its relation to the modal reflectance matrix. Here it is shown how the higher order terms in the reflectance matrix directly influences the smoothness of the plane wave radiation impedance. The computation of the radiated pressure is treated, including the far field radiation from horns based directly on the mouth velocity mode amplitudes. The treatment of asymmetric rectangular horns in this respect is new. A rather large part of this chapter is devoted to efficient computation of the radiation impedance for ducts ending in an infinite baffle. Various methods are discussed and compared. This work is new.
- IN CHAPTER 6, two methods are presented for computing the response of an unbaffled horn. The first method is applicable to axisymmetric horns, and is based on the work of Anna Snakowska on unflanged circular ducts (see for instance [46, 47, 48]). Her methods and results have been adopted, as far as possible, to the problem of unflanged circular horns. The contribution of this work is to integrate Snakowska's method with the MMM, and comparing the results with a BEM simulation. This work is not complete. The second method is based on the edge diffraction method of Peter Svensson [49, 50], and is based on

the work presented in [45]. The contribution of this work is to use Svensson's method to compute the contribution of the diffracted field to the modal radiation impedance at the horn mouth and to the radiated pressure. The total impedance and radiated pressure is found as a sum of the two components; the diffraction component and the direct sound.

CHAPTER 7 covers the problem of horns placed near reflecting boundaries, like walls. The material in this chapter is based on the work presented at the 139th AES Convention [51]. The contribution of this work is to develop a new method for computing the multimodal mutual radiation impedance matrix using matrix multiplication, and also showing the effect of horn-to-wall distance on throat impedance. This distance has a rather greater effect on horns than on direct radiators, and this appears to not have been investigated before.

CHAPTER 8 is a continuation of Chapter 7 in that more walls are added; in fact a complete room. The problem of a horn placed inside the room is not solved, but the related problem of a horn mounted in the wall of a room is investigated using two different methods. The contribution of this work is to present analytical expressions for the modal radiation impedance seen by a rectangular distributed radiator in the wall of a room. A part of this work has been published in [52].

CHAPTER 9 gives experimental verification of the mode matching methods for several of the cases presented previously in this part: half-space, full space and fractional space. This chapter is based on measurements in the anechoic chamber at NTNU, and the material has previously been presented in [45] and [51]. The contribution in this chapter is the verification of the accuracy of the MMM for horns not mounted in an infinite baffle, by the addition of diffraction or reflections.

IN PART iii, the MMM is extended in several ways, to make it a more flexible and versatile tool in loudspeaker simulation applications.

CHAPTER 10 couples MMM to a BEM mesh. Methods for using the BEM mesh as a load or boundary condition for MMM, and MMM as a boundary condition for BEM, are given. This work has been presented at the 139th AES Convention [53]. The contribution of this work is to find simple ways of coupling the two methods, and expressing this coupling in a straight-forward matrix formulation.

- IN CHAPTER 11, the MMM is extended to include velocity on the walls of the "horn", as well as on the throat surface. This work has been published in [54]. The contribution of this work is to present a straightforward method of solving the problem of concave radiators, in contrast to the overly complicated methods previously published [55, 56], making the MMM able to simulate the radiation from differently shaped loudspeaker cones. With the inclusion of a source inside the domain, which is possible with this method, reflectors can also be simulated.
- IN CHAPTER 12, the MMM is applied to the simulation of non-shoebox shaped rooms. The contribution of this work is the application of MMM to room acoustics as an alternative to FEM and BEM for finding the resonance frequencies and transfer function of a non-shoebox shaped room. The chapter is based on the work described in [57].

PART IV gives a summary and conclusion of the work presented in this thesis, with suggestions for further work.

THE APPENDICES contain the following chapters:

- APPENDIX A compares the one-dimensional plane wave solution for the throat impedance of a finite exponential horn to the results obtained using MMM, in order to show that there is no "optimum" mouth size for an exponential horn.
- APPENDIX B lists the expressions for the polynomial coefficients for the low frequency modal radiation resistance of a circular duct ending in an infinite baffle.
- APPENDIX C presents a summary of the theory of the unflanged circular duct, including the numerical methods to compute the special functions involved.
- APPENDIX D describes the model horn used in the experiments in Chapter 9.
- APPENDIX E is a summary of the equations derived for the radiation impedance and radiated pressure for a multimodal distributed source placed inside a hard-walled room.

2

HISTORICAL BACKGROUND

Texts on horn loudspeakers usually start with a short historical introduction, often stating that horns have been in use for a very long time, then mentioning Webster and the need for high efficiency in earlier times, before moving on to introducing the background of the problem at hand. This often leaves the reader with the impression (unless he or she has been active in the field for some time) that horn loudspeaker technology has been in a rather primitive state until quite recently. Also common in technical texts is to present the technology in question as a given entity, as if its origin and its originators were not worthy of study.

So while the main focus of this thesis is simulation models for horn loudspeakers, this chapter will give an overview of the development of horn theory and horn loudspeakers, with extra emphasis on the work done during the early sound film era.

2.1 EARLY USE OF HORNS

The horn for sound production has been in use since ancient times, and both empirical and approximate methods for designing them have been available. The horn used for sound amplification[1] might also be ancient, especially if we regard cupping one's hands in front of the mouth when shouting as a form of horn.

However, the first scientific descriptions of using horns for something other than sound production, are found in the 17th century, and I will in the following give a short summary of the accounts found in Miller [58] and Hunt [59].

Athanasius Kircher (1602-1680), a German learned Jesuit, developed the speaking tube, and also claims to have invented the speaking trumpet. In his work *Musurgia Universalis*, a richly illustrated encyclopedic book of 1100 pages, he also gives dimensions for a parabolic speaking trumpet, see Figure 2b, and an exponential ear trumpet. The material was also published in *Phonurgia Nova* in 1673, expanding on the original text. The republication of this material, which seems to have been done in haste, was perhaps to press his claim of discovering the loud-speaking trumpet before Morland (see below).

---

[1] Although a horn does not amplify sound, but rather makes it possible for the source to radiate sound more efficiently, in addition to restricting the solid angle into which the sound radiates.

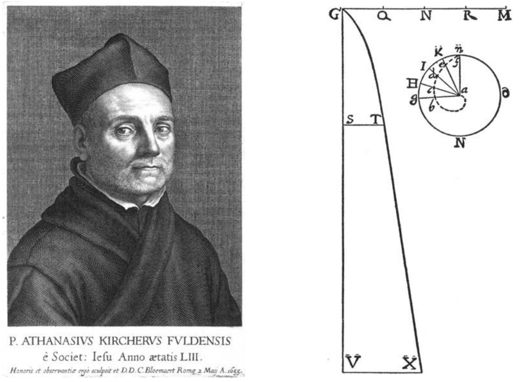

(a) Athanasius Kircher (1602-1680) (Wikimedia Commons).

(b) Kircher's horn, 1650 (from Miller [58]).

Figure 2: Kircher and his horn.

Kircher's claim is based on a conical horn, about 16 feet long and made from iron plates, extending from a 2 inch diameter throat in his office to a 2-foot mouth in an outside wall facing a courtyard. He used is both as a megaphone, and for eavesdropping.

He also discussed the effect of giving various shapes to horns, but his work did little to advance the art. He did, however, present various uses for horns, for instance for broadcasting music from players inside a room to dancers in the courtyard, see Figure 3, giving voice to statues, and for eavesdropping. He also made a "portable" loudspeaking trumpet nearly 10 feet long and 3 feet in diameter that was used to summon 2200 people to a special church service from as far away as four miles.

Another 17th century scientist that claims to have invented the speaking trumpet, is Sir Samuel Morland of London. In 1671 or 1672 he published a 17–page brochure entitled *Tuba Stentoro-Phonica*, where he describes, with illustrations, the design for a

> *"loud speaking trumpet, which may be used in a storm at sea, in calm weather on a dark night, in case of fire, by a town besieged, by the general of an army in giving order, by an overseer of works, and in case a number of thieves and robbers attaque a house that is lonely and far from neighbors."*

He concludes that

> *"the instrument must be enlarged by degrees and not too suddenly,"*

and he refers to experiments he has done with a vessel of quicksilver of the "same figure", that confirmed this. But to find the exact shape, he proposes as a problem for the learned philosophers.

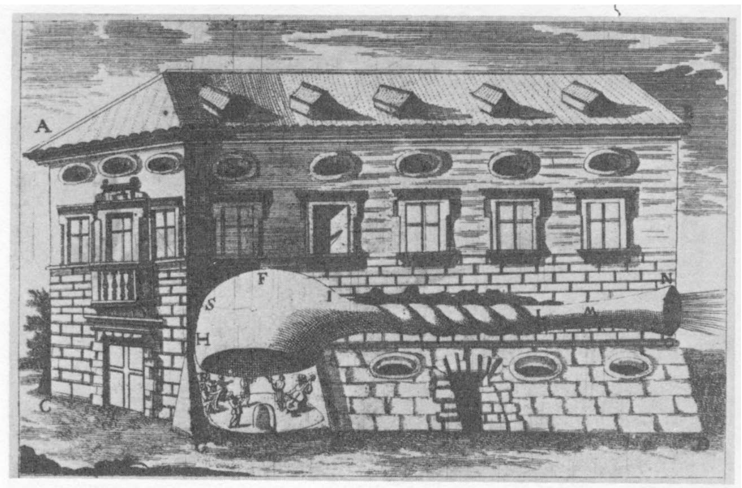

Figure 3: Broadcasting music from musicians in a room (Kircher, 1650, Wikimedia Commons).

Morland's first horn was a 32 inches long glass instrument, 11 inches in diameter, and later he progressed to a 21 feet horn with a 2-foot mouth. He also worked with a "parabolical concave" of pewter. Morland appears to be the first to investigate the directivity of horns, by moving both along the axis of the horn, and along a line perpendicular to the axis.

In 1672, Cassegrain proposed that the speaking trumpet should have a hyperbolic form. Sir John Conyers (1644-1719) suggested that the shape should be a paraboloid. In 1678 he demonstrated a modified horn, and the drawings of the horn clearly show that this is a form of a what is now called a re-entrant folded horn, with side feed.

The form of a hyperbola, not to be confused with hyperbolic-exponential horns.

Richard Helsham (1680-1738) gave the first demonstration of an exponential horn. In analyzing the problem of the optimum shape of the horn, he divided the air into thin slices perpendicular to the axis, and looked at the transmission of motion from one to the next. He concluded that the area of any slice should be the geometrical mean of the two slices next to it, which is still a valid argument for the exponential horn. He explains,

> *"From this reasoning they have been led to consider the best form for such tubes, and have concluded that to be the best, which is generated by the revolution of the logarithmic curve round its axis, as in a tube of this form the elastic bodies will increase in such a manner as most to increase the quantity of motion."*

2.1.1 *Early Mathematical Analysis*

The mathematical analysis of horns begins somewhat later in history, and the early history of the horn equation is given in a paper by Eisner [60], which forms the basis for this section. While Eisner was mainly concerned with the history of the equation itself, this text will look more the history of the treatment of horns in connection with sound reproduction.

Where no references are given in section 2.1.1, these can be found in Eisner.

The horn equation looks like this:

$$\frac{\partial^2 p}{\partial x} + \left[\frac{1}{S}\frac{\partial S}{\partial x}\right]\frac{\partial p}{\partial x} - \frac{1}{c^2}\frac{\partial^2 p}{\partial t^2} = 0, \tag{1}$$

where S equals the cross-sectional area of the horn. Equations on the form of Eq. (1) govern not only wave propagation in horns, but also propagation in strings where the mass varies along its length, and non-uniform transmission lines, for example. One would expect Isaac Newton to have looked into the matter, but he only gave a qualitative remark about the speaking trumpet. John II Bernoulli gave a differential equation for transverse vibrations in a string of linearly varying diameter, but did not solve it. Daniel Bernoulli derived the equation for sound propagation in a tube of varying cross section, and solved it for the conical horn. His work was published in 1764, but was probably performed in the 1740s. In the meantime, Lagrange had published a better derivation (in 1760), and solved the equation for a wedge, a cone, and the general Bessel horn. He also discussed the problem of transverse vibrations in a non-uniform string, as did d'Alembert, D. Bernoulli and Euler in the 1760s and 70s. Euler derived and solved the equations for cylindrical and spherical sound waves, and gave the dynamical equation for sound of finite amplitude, in a fluid of varying density, contained in a tube of varying cross section, including the effect of gravity. He also discussed solutions for the case of infinitesimal amplitude, and gave a detailed treatment of the cone and the hyperboloid ($S \propto x^{-2}$).

After all this work on the horn equation in the 18th century, little happened until the 20th century. There are just a few exceptions: a detailed treatment in 1839 by Duhamel of sound in cones and wedges, without the restriction to small cross section, a treatment by George Green of water waves in tapered channels in 1837, and work by von Helmholtz in 1898 on short, non-cylindrical tubes smoothly joined to cylindrical tubes. Also, a treatment of the conical horn was given by Barton in 1908 [61].

2.1.2 *Birth of Sound Reproduction*

The invention of the telephone and the phonograph marks the beginning of the era of the reproduction, and not merely the production, of sound. Space does not permit a detailed treatment of the history of the telephone in this text. A rather detailed history of electroacoustics up to about 1950 can be found in the excellent book by Frederick V. Hunt [62], where he also covers in detail the telegraph and telephone. Sufficient for the current text is a short summary.

Alexander Graham Bell is usually considered to be the inventor of the telephone, but there were several others tinkering with similar ideas several decades before him. Charles Bourseul, Antonio Meucci and Johan Philipp Reis all had ideas, and some of them were put into (more or less successful) practice, in the 1850s and 60s. Then two inventors with significantly improved, successful telephone devices made it to the patent office on the same day, February 14, 1876. These two inventors were Elisha Gray (1835-1901) and A. G. Bell (1847-1922). Of these two, Bell was awarded the patent for the telephone, a patent which was upheld in several court cases. With the invention of the telephone, the foundation of modern communication technology was laid. Bell's company grew quickly, and today's American Telegraph and Telephone Company, AT&T, has evolved in direct line from the first gentlemen's agreement between Alexander Graham Bell and his investors, through several iterations. The corporate history of the Bell System and AT&T is covered in detail by others, see for instance Fagen [63], and will not be repeated here.

When Thomas A. Edison in 1877 managed to record *and* reproduce sound with his phonograph, the foundation was laid for musical home entertainment for the masses.

Edison's device was purely mechanical, as there were no amplifying devices available that could be used, no electrical pick-ups, and no loudspeakers. The only way to get enough volume was to attach a horn to the needle and diaphragm. As the little work that had been done on horn theory was largely unknown or forgotten by this time, progress was by trial and error. Figure 4 shows a few examples of Victor gramophones from the years 1900–1906. Reproduction was rather poor by today's standard, but that didn't stop the public from buying records.

2.2 AMPLIFICATION AND EARLY LOUDSPEAKERS

During the first decade or two of the 20th century, gramophones and phonographs were sold by the thousands, all employing some form of horn. Horns were also used to create one of the first loudspeakers worthy of the name. Peter L. Jensen and Edwin S. Pridham had been developing a moving coil telephone receiver, Figure 5, but it was too heavy and bulky for the telephone companies [64]. The moving coil principle was not new, it had been suggested as early as 1874 by Ernst Werner Siemens [65], but it is probably Jensen and Pridham that first used the principle in a device actually performing loudspeaker duty.

Actually, a few gramophones also employed direct radiating diaphragms, actuated by a lever from the needle.

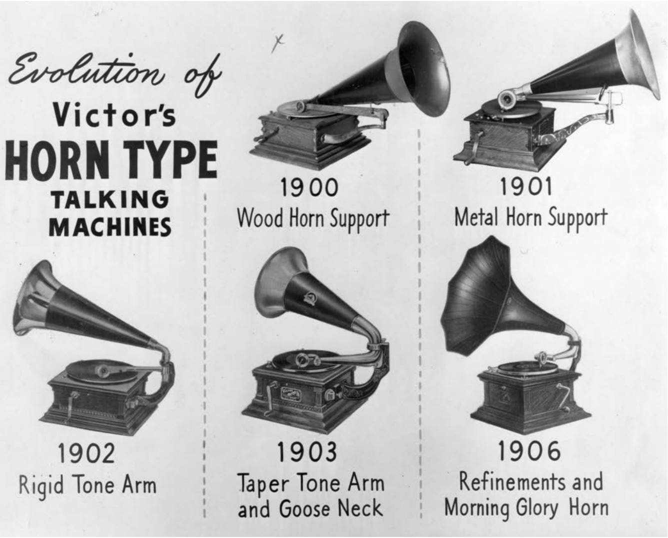

Figure 4: The evolution of Victor gramophones. Note the exponential-like horn from 1906. (Image courtesy of Hagley Museum.)

In 1914 the uncle of Jensen's wife suggested attaching a phonograph horn to their moving coil receiver, and the result was a quite good loudspeaker, which they called *"Magna Vox"* (Latin for "great voice"). The first public demonstration of the Magna Vox loudspeaker was made in the Golden Gate Park on December 10, 1915. Jensen and Pridham formed the Magnavox Company in 1917.

Means for amplification is needed to turn any loudspeaker into a practical device. The large inherent gain of the carbon microphone provided some system gain, but it was noisy and had a limited frequency response. In 1907 Lee DeForest patented the first three-electrode vacuum tube (the "Audion"), and in 1912, he offered AT&T the rights. The device was still crude and too weak to be directly employed in telephone service, but Harold D. Arnold of the Western Electric Engineering Department grasped the underlying physics, and began work to develop the Audion into a practical device. After he had demonstrated the promise of the improved Audion, AT&T bought the patent from deForest. By the end of 1914, vacuum tube amplifiers had been successfully tested in repeater service between New York and San Francisco. Magnavox obtained the right to use the DeForest Audion in 1915, but not the AT&T tube.

In 1919, Magnavox loudspeakers were used to amplify a speech by Woodrow Wilson in San Diego, and were also used in 1920 political conventions, in the campaigns of James Cox and Warren Harding. By this time the AT&T had developed their public address systems to a point where they dominated the market, and the Magnavox company backed out of the public address system business, instead directing

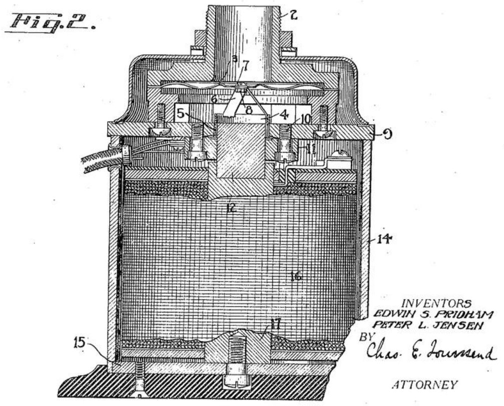

Figure 5: Patent figure of the Pridham/Jensen receiver, from US patent 1,448,279.

its efforts at producing loudspeakers for the radio and phonograph industries.

With vacuum tube amplifiers available, Western Electric, the manufacturing arm of AT&T, soon applied the new amplification technology to problems other than telephone repeaters. One of the first applications were public address systems. I. B. Crandall and others had experimental loudspeakers in use in 1914-1915 [66]. The development proceeded to the stage of large scale arena tests before the work had to be stopped due to World War I [67]. During the war, the W. E. engineers worked on underwater detection and transmission, and one of the results of this was a greatly improved loudspeaker unit, the 196-W armature transducer.

The first major demonstrations of this system were at the 1920 presidential conventions, and at the inauguration of President Harding in March 1921. But it was perhaps Harding's dedication of the Tomb of the Unknown Soldier on November 11, 1921, that was the major boost for this system. Harding's speech was transmitted from the Arlington National Cemetery over telephone lines to loudspeakers in New York and San Francisco. By the end of 1922, the W.E. public address system was a standard.

2.3 THEORY AGAIN

As mentioned, wave propagation in ducts and horns had been treated to a degree in the 18th and 19th century, but the publications were of highly academic nature, and inaccessible to the practical workers in the field. No one seemed to be interested in treating sound propagation in horns until Lord Rayleigh in 1916 [34], and Arthur Gordon Webster in 1919 [35] published their papers. Webster's paper was ac-

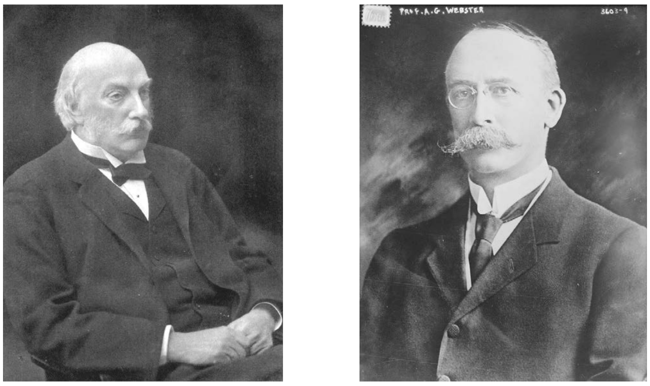

(a) John William Strutt, 3rd Baron Rayleigh (1843-1919).

(b) Arthur Gordon Webster (1863-1923).

Figure 6: Rayleigh and Webster (Wikimedia Commons).

tually read at a meeting of the American Physical Society at Philadelphia in December, 1914, but was held back due to development of experimental apparatus.

When Rayleigh and Webster rediscovered the horn equation, it came as a very timely contribution to the art. Webster's equations provided engineers with the ability to compute the loading performance of finite horns, given the radiation impedance at the mouth. Coupled with the knowledge of how the electrical and mechanical parts of the transducer mechanism were connected, as provided by A. E. Kennelly and G. W. Pierce [68], and the analogy between electrical and mechanical impedances as described by W. S. Franklin [69], performance of the entire electro-mechano-acoustical system could be computed. Still, little appeared in the literature on the subject the first years after the publications. George Walter Stewart used Webster's equations in his studies of the performance of conical horns in 1920 [70], and Webster mentions that Stewart had used his then unpublished theory in the design of horns during the First World War. But perhaps the best known paper dealing with horn theory is the classical paper by Clinton R. Hanna and Joseph Slepian in 1924 [71]. They both worked for the Westinghouse Electrical and Manufacturing Co., and their paper has a good discussion of horn theory, especially exponential horns, mouth size, and flare rate, and how to match the horn to a loudspeaker to obtain the desired response.

In the discussion after the presentation of the paper, Prof. V. Karapetoff gives a very fitting remark about the state of theory and practice in loudspeaker design at the time:

> *This problem of horns is a 'house-on-fire' problem, in the sense that loud speakers are now being manufactured by the thousand,*

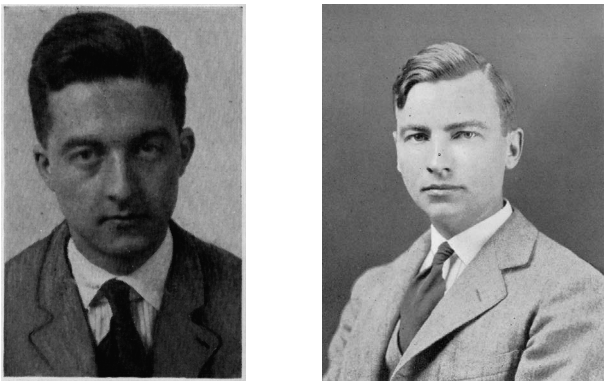

(a) Paul B. Flanders (b) Donald A. Quarles

Figure 7: Flanders and Quarles, who did the mathematical analysis of horns at Western Electric. (Images courtesy of the AT&T Archives and History Center.)

> *and while they are being manufactured and sold, we are trying to find out their fundamental theory.*

It is perhaps less known that similar work on the theory of horns and horn loudspeakers was undertaken by the Western Electric Engineering Department, and patents by Henry C. Harrison in 1923 [72] and Paul B. Flanders in 1924 [73] show a clear understanding of the exponential horn and its mouth termination. The patents are good summaries of basic horn theory, and also show that it was known that the wave fronts in the horn are not plane but curved. A method to design a horn based on curved wave fronts with exponentially increasing area is described. It was Harrison who introduced the exponential horn to Western Electric [74], but the mathematical analysis was done by Flanders and Donald A. Quarles.

The analysis by Flanders and Quarles was published as two internal memoranda in 1924 [75, 76], and it is clear that this material was not intended to be published: these memoranda are filed in an AT&T file case marked "strictly confidential". Part of the theory (for the exponential horn only) was, however, published in the book "Theory of Vibrating Systems and Sound" by Irving B. Crandall [77] in 1926. The analysis is interesting, in that it differs from the analysis of Rayleigh and Webster, and seems to have been derived independently of their work. Flanders' memoranda also computed the response characteristics of a Western Electric horn speaker. These calculations used a lumped parameter model for the transducer and throat chamber, and the one-dimensional analytical solution for the horn. The mouth radiation impedance was that of a piston in an infinite baffle.

The 1920s saw much development in horn loudspeakers, perhaps mostly practical, but some theoretical work was also done. The work of Hanna and Slepian is already mentioned. The same year, in 1924, Alfred N. Goldsmith and John P. Minton, both of Radio Corporation of America (RCA), published a long paper entitled "The Performance and Theory of Loudspeaker Horns" [78], in which they presented extensive measurements on various types of horns; 16 conical horns of various sizes and shapes were built and tested. Most of the horns were rather narrow, and appear to be quite resonant. The measurement results were presented as pressure responses on a linear scale, which makes it hard to judge the actual performance of the horns for someone used to a decibel level scale.

They also gave a detailed mathematical analysis based on Webster's work for conical, exponential and parabolic horns. The analysis did, however, result in some peculiar conclusions. First, their comparison of conical and exponential horns led to the conclusion that conical horns are better than exponential horns at both low *and* high frequencies. The sharp cutoff of the exponential horn does of course mean that an equivalent conical horn will provide more output below the cutoff frequency of the exponential horn. At high frequencies, however, they should converge to the same output[2]. This is, however, not the conclusion of Goldsmith and Minton, and the reason is that they assume the conical horn to have a point source at its vertex. This leads to a pressure that increases proportionally with frequency for a constant volume velocity, and will at some point produce more output than the exponential horn, where a source of finite size was assumed. With a realistic source for the conical horn, the conclusion would have been different.

Their second erroneous conclusion is that pressure and velocity in a parabolic horn are 90° out of phase for all frequencies, and that the horn does not produce any output. This is due to selecting the standing wave solution instead of the traveling wave solution to the horn equation for parabolic horns.

In 1925, Hoersch investigated the existence of "non-radial vibrations", i.e. higher order modes, in conical horns [79]. This is perhaps the first treatment of this phenomenon in horns. Little was, however, done on the subject for years. Hoersch's interest in the more complex behavior of horns came from a desire to better understand the "optimum angle" for receiving conical horns that Stewart had found in his investigations [70, 80, 81]. Conical horns as receivers of sound was in extensive use at the time for recording purposes, but this was soon to change, as will be covered in the next section.

Empirical data on horns of various kinds, including the effect of curving, was provided in 1926 by S. T. Williams, chief engineer at the Victor Talking Machine Company [82].

---

[2] This analysis is based on the horn equation, and real life behavior is somewhat more complex.

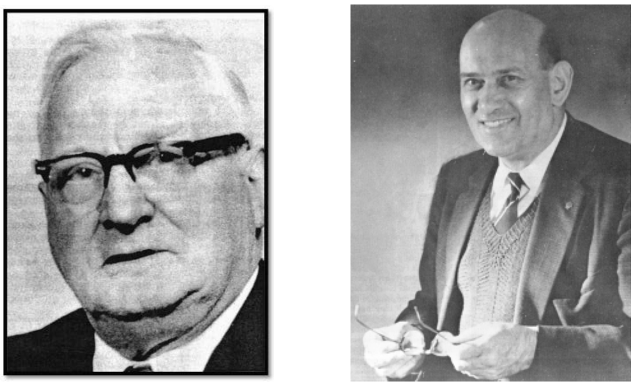

(a) Percy Wilson

(b) Paul G. A. H. Voigt (Image courtesy of the Lowther Voigt Museum).

Figure 8: Wilson and Voigt, two British contributors to the science of horn loudspeakers.

In England, Percy Wilson became interested in gramophones at this time [83, 84], and thanks to his two articles on the needle tracking alignment problem in *The Gramophone*, he became part of the *Expert Committee* of that publication. In 1925-26, he applied his mathematical mind to the problem of sound propagation in horns and extended Rayleigh's analysis to exponential horns, unaware of Webster's work. Wilson also recognized the fact that wave fronts in an exponential horn cannot be plane, as is usually assumed in the theory, and that it is the wave front areas, not the cross section, that should increase exponentially. He therefore proceeded to derive a modified exponential horn, the theory of which is presented in the book *Modern Gramophones and Electrical Reproducers* [85].

Paul Gustavus Adolphus Helmuth Voigt, a British engineer, also made contributions to horn technology at the time. While he was a few months too late to patent the moving coil loudspeaker (that patent went to Rice and Kellogg [86, 87, 88]), he contributed to the art of horn speakers by inventing the tractrix horn [89]. This horn is formed by a revolution of the tractrix curve, and the mouth ends with a tangent that is normal to the axis. Voigt's reason for choosing this kind of horn profile was not based on mathematical reasoning; he admitted himself that he was "rotten at math". It was rather based on intuitive and geometrical reasoning, with a desire to produce a gentle transition from the horn throat to a 90° termination at the mouth.

The existence of a cutoff frequency in exponential horns led some to question the validity of Webster's horn theory. One of these were Stuart Ballantine who in 1927 analyzed horns of the general shape $S \propto x^n$ [90]. These horns are called Bessel horns due to the appearance

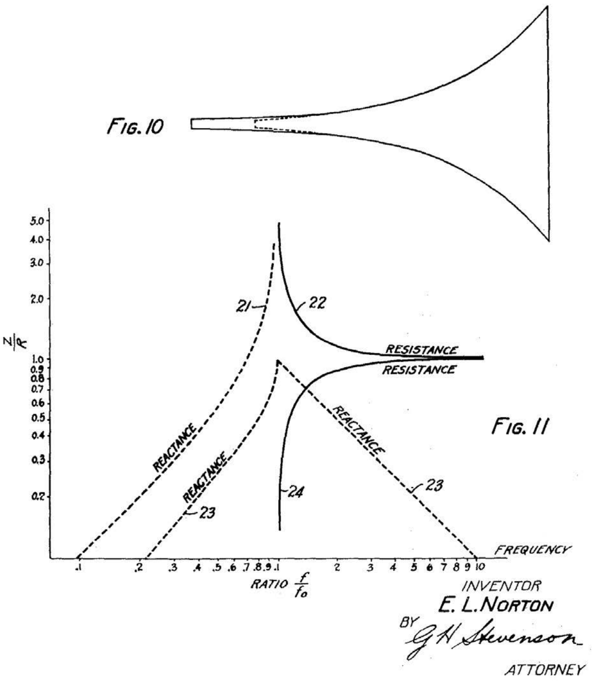

Figure 9: The catenoidal horn, described in Norton's patent 1,792,655.

of Bessel functions in the solution. These horns do not show the cutoff phenomenon of exponential horns. But it was subsequently shown by Hanna [91] that if n goes to infinity, the horn becomes an exponential horn.

Edward L. Norton of the Bell Telephone Laboratories (BTL) made a little recognized contribution to the technology of horn loudspeakers in his 1929 US patent 1,792,655 [92], where he introduced the catenoidal horn. This was later shown to be a member of the hyperbolic-exponential horn family introduced by Salmon [93]. The catenoidal horn is special in that the infinite horn does not have any reactance above cutoff. Norton also did an analysis of annular slit phase plugs, and correctly identified the best placement of the annulus for a single-slit phase plug. Both these contributions have been largely forgotten.

In 1930, G. W. Stewart and and Robert Bruce Lindsay [94] published a much-needed textbook [94] on acoustics with a large chapter on horn theory. With this publication, Crandall's book, and consequently the horn theory of Flanders and Quarles, lost its significance, although it was deeply founded in practical loudspeaker research. Harry F. Olson, one of Stewart's students, used the work of Stewart and Webster, and thanks to his large number of publications, this approach dominated the field for many decades. More details on Olson's contributions to the science will be given in Section 2.5.

Some work on horn loudspeakers was also done in Germany at this time by Heinrich Stenzel at AEG [95], who treated Bessel horns of even order (with a series expansion for the throat resistance and reactance components), and exponential horns. The work at AEG was part of the development of the Klangfilm-Tobis sound film system [96].

It was clear from the beginning (Webster mentions it himself) that the horn theory was only approximate. It is a one-dimensional approximation, which means that it cannot predict the directivity of horns, a serious limitation of the method. In an effort to shed some more light on what actually happens inside a horn, as a first step towards a more complete theory, William M. Hall, in his M.Sc. thesis at MIT, built a small condenser microphone and made measurements of the sound field inside an exponential and a conical horn [97, 98]. His hopes for an improved theory of horns were not fulfilled, though.

That the horn equation method could not predict directivity was well known in the early days of horn technology; at least no one tried to use it as a basis for directivity predictions. There actually is no starting point for building a directivity model from a one-dimensional horn equation. But since directivity early on became an important issue in high quality cinema sound systems, a way to design horns with the desired characteristics had to be found. Empirical data was used in the early days. For instance, Olson of RCA built and tested several conical and exponential horns, where size and shape were systematically varied [99]. Measurements on scale models of horns were also used [100]. Kozi Sato seems to be the first to have investigated the directivity of horns mathematically with a more realistic model than the equivalent piston [101, 102], by using the radiation from a conical horn in a sphere. Wolff and Malter[3] [103] investigated the directivity of lines and arcs of point sources, and applied the method to horns.

Although mostly interested in direct radiating loudspeakers, Norman William McLachlan gave a detailed treatment of horn loudspeakers in his 1934 book [104], including a good discussion on mouth radiation impedance models and mouth size. He also gave an outline of how to calculate distortion in horns, a problem that was starting to receive attention at the time because of the increased power and frequency range of loudspeakers. Distortion was also investigated by Jenkins, Thuras and O'Neil at BTL in 1935 [105], and McLachlan (with Goldstein) published his own completed treatment the same year [106]. He also contributed to the theory of Bessel horns [107], and investigated the transient behavior of horns (with McKay) [108].

An important, but for many years largely forgotten, contribution to the theory of horns, was the study by John Edwin Freehafer of the hy-

---

[3] RCA and RCA Photophone

perbolic horn (presently better know as the oblate spheroidal waveguide), for which there is an analytical solution to the wave equation. In his Ph.D. thesis at MIT (1937) [109] he also shows the existence of higher order modes, and plots equipotential curves for two of the radial modes. His results were presented in a paper a few years later [110].

2.4 TALKING PICTURES, GRAMOPHONES AND AT&T

The commercialization of talking motion pictures, or sound film, resulted in lot of research into high quality sound reproduction. Let us backtrack a little, and look at how this revolution in entertainment came about, and what it meant for the loudspeaker industry.

The idea of combining sound and moving pictures (movies) is almost as old as film itself [111]. Edison's invention of the phonograph in 1877, which provided means for recording and reproducing sound, and his Kinetograph and Kinetoscope for recording and reproducing movies, resulted in two large industries: the record industry and the film industry. It did not take much imagination to come up with the idea to combine the two, which Edison did with his Kinetophone in 1895. But there were two big problems with this system, and with almost all the systems that were unsuccessfully tried in the years to follow: synchronization and volume. Without accurate synchronization, sound film was not more than a novelty that the public quickly lost interest in, and without means for amplification, including good microphones and loudspeakers, only the first few rows could understand the dialogue. Several systems were tried, and failed, convincing the film industry that sound film would never, *could* never, work.

Sound recording was needed at the Western Electric Engineering Department for quite other reasons than the commercial exploitation of music reproduction or sound films. From about 1913, huge efforts were being made to analyze speech and hearing in order to enhance the quality of the telephone networks in the areas where it mattered most, and the ability to record speech for later reproduction and analysis was crucial. While Edison's Phonograph made this possible, the quality of the acousto-mechanical system was not good enough for research purposes, and would have to be re-engineered completely. Another option was of course sound-on-film. After WW I, work began in earnest, and two groups were set down: one, headed by I. B. Crandall, and including E. C. Wente and D. MacKenzie, should look into sound-on-film, while the other, headed by J. P. Maxfield, should work on disc recording.

By mid-1922, Maxfield's group had a workable system for electrical disc recording, using Wente's condenser microphone, Arnold's amplifiers, and a rubber line recorder developed by Harrison and Norton [112]. Maxfield and Harrison also improved the mechanical

Figure 10: The Orthophonic Victrola, showing the internal contruction of the folded horn (Image courtesy of Hagley Museum).

playback system to a high state of perfection using electrical filter theory applied to the mechano-acoustical system. E. B. Craft encouraged them to develop their prototype into a commercially workable system, which took two more years. In 1921, an effort had been made to commercialize an early version of the rubber line recorder, through the short-lived company Phonic Laboratory, but this had not been successful [62]. Three years later, however, things had changed. Radio had become a more dangerous competitor to the record industry, and the Columbia Phonograph Company obtained a license for using the rubber line recorder late 1924 or early 1925. Later, but in time for the 1925 Christmas trade, Victor Talking Machine Company obtained licenses for both the rubber line recorder and the improved mechanical playback system, which were marketed under the trade name Orthophonic Victrola.

In 1922, a set of records for a running commentary for the film *The Audion*, a film explaining the workings of the vacuum tube, were made, and a crude system of synchronization devised, consisting of two revolution counters that the projectionist would keep reading alike by adjusting the speed of the film projector [113, 114]. Further work was done on synchronization, and Craft got clearance from the management to try to sell the system to the film industry. Due to the history of (often expensive) sound film flops over the last 25-30 years, no one was interested, apart from the Warner brothers.

On April 20, 1926, after enough of the initial problems were overcome, Warner and AT&T signed a contract giving the Vitaphone Corp., a new subsidiary of W. E., an exclusive license to produce sound films using the W. E. equipment, and to equip theaters with W. E. reproduction equipment. The idea was that other producers would take out sub-licenses from Vitaphone. W. E.'s management was impatient with the Warners' sub-licensing efforts, however, and January 1, 1927, W. E. formed a new subsidiary to take care of their sound picture and other non-telephone business, Electrical Research Products Inc. (ERPI). ERPI's president, John E. Otterson, pressed Warner Bros. to renegotiate the contract, giving ERPI the rights to theater installations and relations with other producers, and making Warner Bros. a non-exclusive licensee of ERPI.

The industry was still largely uninterested, but the simultaneous development of the Fox Movietone sound-on-film meant that it was time to either "go talkie" or see Warner and Fox run off with the business. In February, 1927, the "Big Five", Paramount Famous–Lasky, Loew's (MGM), First National, Universal and the Producers Distributing Corporation, agreed to study the sound question for one year, and then decide on a single system to avoid the disastrous consequences of incompatible systems. In January 1927, RCA had entered the scene, offering a well-financed alternative in the RCA Photophone system. At this time, ERPI offered a combination system, with both sound-on-disk and sound-on-film. Early in 1928, ERPI was selected, partly because they would take responsibility for equipment manufacture, installations and maintenance. The contract was signed on May 11, 1928. It was now either "sound or sink", and the question was not "how much will it cost", but "how fast can it be done" [115].

Bell Telephone Laboratories, formed in 1925 as a successor of the W. E. Eng. Dept., did the main part of the research on sound recording and reproduction, including the loudspeakers for the Vitaphone sound system, as detailed in [116]. This included of course the horns, but also important contributions like the W. E. 555-W horn compression driver, and later the 596-A horn tweeter. Cooperation with the famous director Leopold Stokowski resulted in the Auditory Perspective experiments in 1933, where the sound of an orchestra was transmitted in three-channel stereo and with full volume- and frequency range, from the ball room of the Academy of Music in Philadelphia, to the auditorium in the Washington Constitution Hall [117]. The experiment resulted in the development of perhaps the best loudspeaker system available at the time [1], see Figure 11, and the multicellular horns and high frequency compression drivers used in this system

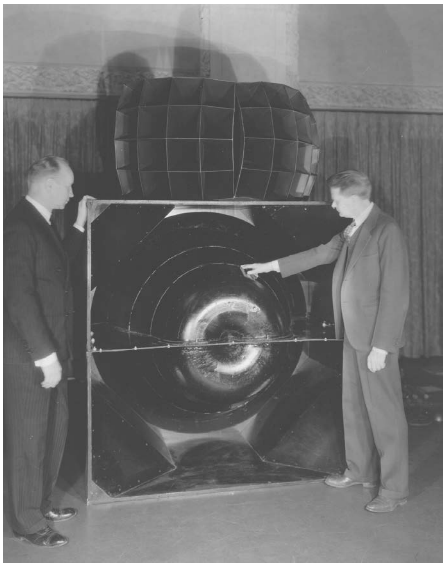

Figure 11: Albert L. Thuras (left) and Edward C. Wente, of BTL, with one of the loudspeakers that were used for the Auditory Perspective demonstrations (Image courtesy of the AT&T Archives and History Center).

was adopted by the industry [118] and remained standard for several decades.

In 1937, the servicing and installation division of ERPI was sold to its employees and became the Altec Service Corporation. W. E. still remained on the recording side of the business for several years.

2.5 RCA PHOTOPHONE AND H. F. OLSON'S CONTRIBUTIONS

The RCA Photophone sound system was originally based on direct radiating full-range cone loudspeakers of the Rice-Kellogg type [88, 119], set in two columns, one on each side of the stage. This system was satisfactory for music and sound effects, but less so for speech, due to the reverberation. Large throat horns using cone drivers were developed by John D. Seabert (then at Westinghouse) in 1929, and these were called *directional baffles* to distinguish them from the long small-throat horns, and to emphasise that the primary function of these devices was directivity control, not acoustical loading [120].

In 1928, Harry F. Olson (1901-1982) joined the RCA Laboratories in New York City, and started working with Irwing Wolff on loudspeakers and microphones. Olson had B.E., M.Sc., Ph.D. and E.E. degrees from the University of Iowa, where he had studied under G. W. Stewart. His first contribution to horn loudspeakers was an analysis and design of new MI-477 directional baffles in 1930 [122, 123]. This

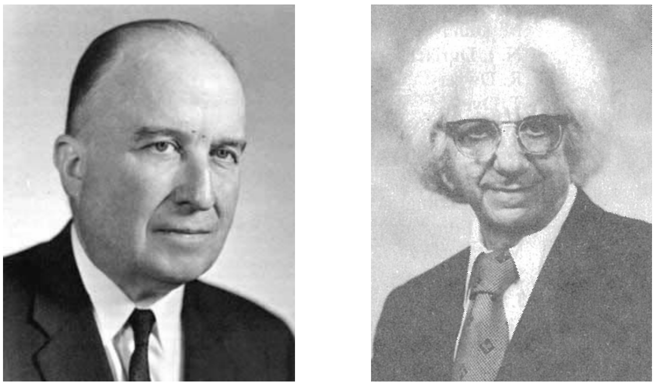

(a) Harry Ferdinand Olson (Image courtesy of the ethw.org).

(b) Frank Massa (Reproduced from [121], with the permission of The Acoustical Society of America).

Figure 12: Olson and Massa, RCA.

is probably the first published work where a complete analysis of a horn loudspeaker has been made, including the driver parameters and the effect of a finite horn, and the resulting efficiency computed. As mentioned in Section 2.3, similar work had been done at W.E. in 1924, but this had not been published.

In 1929, RCA bought the Victor Talking Machine Company, and Frank Massa (1906-1990) joined the team. Together he and Olson made many contributions to the loudspeaker art, including the publication of the book *Applied Acoustics* in 1934 [124]. The horn theory in this book is basically a restatement of the theory in [122], in addition to comparisons of the throat impedance characteristics of infinite horns. Some of the early work of Olson and Massa was on improving the driving units of the Photophone equipment, by for instance introducing corrugations in the cone [125].

As the RCA High Fidelity range of cinema loudspeakers was introduced, a folded low frequency horn was designed to extend the low frequency end of the spectrum [126]. This horn included the interesting feature of a Helmholtz resonator near the throat, tuned to 170 Hz, to provide a sharp acoustic roll-off above the intended 35-125 Hz pass band.

Olson and Massa also worked on compound horns [127, 128], where a single driver is loaded on the rear side by a bass horn, and on the front side by a small high-frequency horn, Figure 13. Compound horns were also designed for cinema use [129], and a series of compound horns were designed and tested for use with high quality radio receivers [130], but the extended frequency range of these horns did not give the desired advantage due to noise and distortion

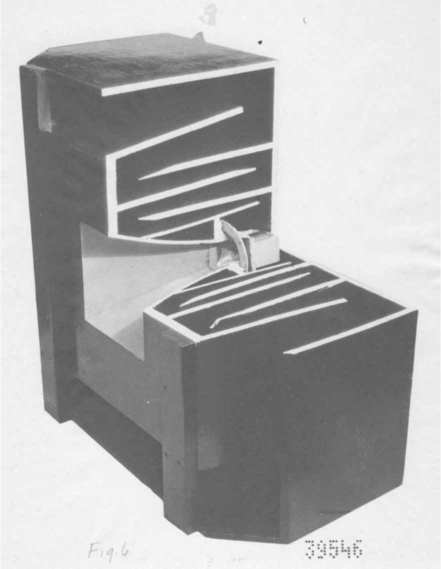

Figure 13: Compound horn by Olson and Massa (Image courtesy of Hagley Museum).

in the radio channel [131]. The work did, however, result in at least one commercial product [132].

It was during this time in the mid-1930s, that Olson did most of his work on horns. Some of it was published in *Applied Acoustics*[4], and some in RCA technical reports [133, 134]. Two papers in *RCA Review* in 1937 summed up much of the work done until then [135, 99].

These papers include both theoretical work and results from practical investigations[5]. Perhaps of special interest are the investigations of the directivity characteristics of various conical and exponential horns, where the size and shape was systematically varied, Figure 14. This was data that was much needed for horn designers, since no good model for horn directivity existed. Multicellular horns were also investigated, and a method to predict the directivity of such horns presented.

For maximum efficiency at low frequencies, a horn loudspeaker should have a large throat. As the mass reactance of the diaphragm increases toward higher frequencies, the throat area must be small in order to maintain the efficiency, but this reduces the low frequency

---

[4] The book, not the journal.

[5] Although some claim that Olson was known "to just draw in the data curves" (see for instance `http://www.diyaudio.com/forums/multi-way/103872-geddes-waveguides-613.html#post3676299`), there is no support for this in his notes or in the lab reports. While the resolution and numerical accuracy is far lower than what we are accustomed to today, there is no doubt that there is a large amount of experimental work behind what he published.

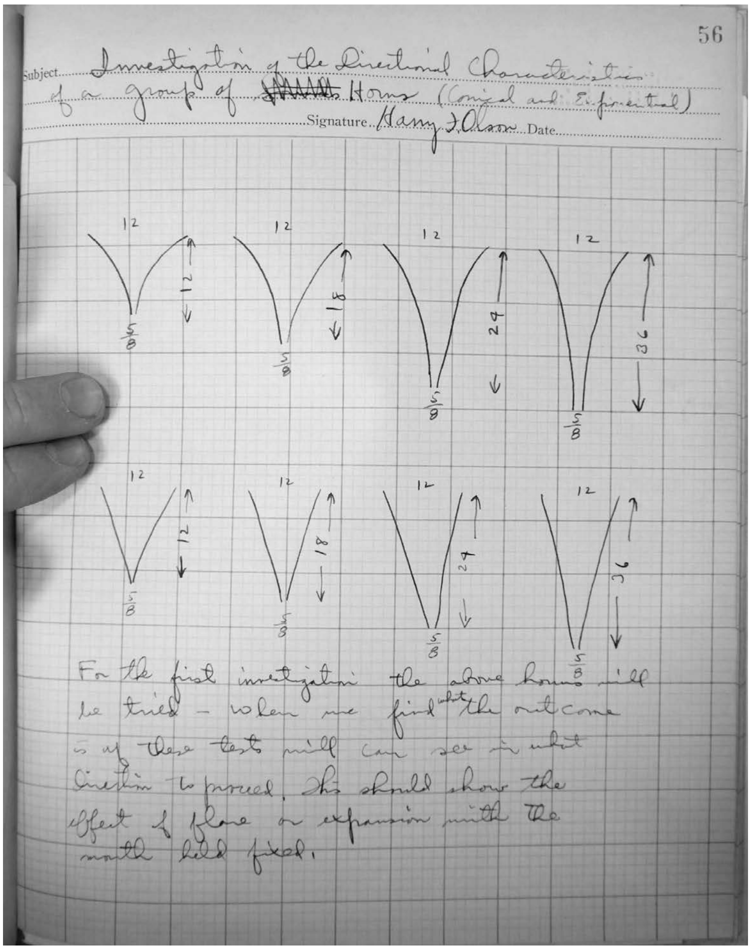

56

Subject Investigation of the Directional Characteristics of a group of Horns (Conical and Exponential)

Signature Harry F. Olson Date

For the first investigation the above horns will be tried – when we find what the outcome is of these tests will can see in what direction to proceed. This should show the effect of flare or expansion with the mouth held fixed.

Figure 14: Page from Olson's note book #2158 [130], showing sketches of the first horns to be tried in the investigation of directional characteristics. The page is undated, but judging from the dates on the previous and following pages, it was written between August 21, 1935 and April 6, 1936.

efficiency. Therefore, the effective throat area should change with frequency. In addition, distortion in the horn increases with the ratio of operating frequency to cut-off frequency, and with the power per area at the throat, so a small throat horn horn with a low cutoff will have high distortion. The initial flare should therefore be rapid. The idea of combining several exponential segments to achieve this, appears to have occurred to Olson in late 1936 [130, p. 74], and he did the theoretical work early 1937. Using a series connection of exponential horns of different flares required calculation of the throat impedance below the cutoff frequency of the horn, which seemingly caused some head-scratching, judging from the correspondence between Olson and Stewart [136]. However, the theory was successfully worked out [137, 138], and used in commercial products [139].

In 1940, the successor of *Applied Acoustics*, *Elements of Acoustical Engineering*, was published, with Olson as the only author. After World War II, Olson published two revisions of his book in, 1947 [140] and in 1957 [141].

2.6 OTHER, AND MORE RECENT, DEVELOPMENTS OF HORN THEORY

In 1938, Vincent Salmon wrote his Ph.D. thesis at MIT on a generalized plane wave horn theory, with the purpose of simplifying Freehafer's exact analysis of the hyperbolic horn, and also verifying his predictions by measurements on a model horn [142]. Salmon subsequently developed his generalized theory further [143], and based on this work a new family of horns was found, the hyperbolic-exponential horns [144, 93]. This horn type was trademarked *Hypex horns* by Jensen Mfg. Co., Salmon's employer. Daniel J. Plach and Philip B. Williams, also at Jensen, showed how a horn loudspeaker system could be designed using Hypex horns, including how to resonate the driver suspension compliance with the air mass of the horn to improve low frequency performance [145, 146], a method originally developed by Thuras of BTL and first used in the W. E. 555-W compression driver [147].

Philip M. Morse introduced the concept of one-parameter horns in his 1948 book *Vibration and Sound* [149], and presented a treatment of the transient response of horns.

At this time, late 1940s to mid 1950s, almost everything a loudspeaker designer needed to know was found in Olson's book *Elements of Acoustical Engineering* [140, 141] and in Leo L. Beranek's *Acoustics* [150]. In particular, the method of lumped parameter analysis coupled with the horn equation was used to predict the power response of horn speakers. Basically, the method is based on computing the throat impedance Z_{th} of the horn, which together with a lumped parameter representation of the transducer, makes it possible to com-

(a) John Edwin Freehafer (Image courtesy of the MIT Museum).

(b) Vincent Salmon (Reproduced from [148], with the permission of The Acoustical Society of America).

Figure 15: Freehafer and Salmon, who both worked on the hyperbolic (oblate spheroidal) horn.

pute the volume velocity into the horn throat, U_{th}. Assuming a lossless horn, the radiated power is given as

$$P = |U_{th}|^2 \operatorname{Re}(Z_{th}).$$

As computers, often analog computers, were applied to loudspeaker simulations, approximating the horn as well by lumped parameters had some advantages, and this was done by Locanthi in 1952 [151].

The use of either pure lumped parameter simulation, or a combination of lumped parameter and solutions to the horn equation, completely dominated the field until the 1970s, and is still much used. It still has some value in simulating low frequency systems like bass horns, and can often be used as a starting point for a design [152].

In the field of horn theory, some work was done after 1945 on mathematical transformation and more general solutions of the horn equation. Mawardi discussed generalized solutions of the horn equation, and showed how an investigation of the singularities of the equation could lead to the discovery of new families of horns [153]. Charles T. Molloy (BTL) investigated resonance peaks in Hypex horns, and showed how to calculate the parameters of horns having predetermined peaks [154]. He also computed the directivity index of several types of radiators, including sectoral and multicellular horns, based on “what seemed to be reasonable pressure distributions” [155].

The tractrix horn was analyzed theoretically for the first time by Robert F. Lambert [156, 157] in 1954. Lambert also measured the throat impedance of a tractrix horn to validate the theory, and investigated the directivity of two horns.

Attempts on a more complete horn theory was made. Stevenson presented a solution in the form of an infinite set of differential equations [158]. Holtsmark et at. [159] analyzed exponential horns of small flare, and showed the existence of higher order modes and modal coupling. Maezawa [160] introduced higher order correction terms to the horn equation. These attempts do not seem to have penetrated into the practical design of horns.

What did penetrate into the engineering community, however, was Don B. Keele's analysis of the optimum mouth size for exponential horns [161]. This analysis concluded that there is an optimum mouth size for exponential horns that minimizes the throat impedance ripple, and that ripple increase for larger mouth sizes. This had already been shown by Flanders [73], although not as detailed as in Keele's analysis. It can, however, be shown that this analysis is not correct, as it is based on plane wave propagation in the horn. If a more advanced model is used (See Appendix A on page 271, see also [162] for simulations using a corrected one-dimensional model), the ripple will decrease instead of increase as the mouth size is increased.

Keele also analyzed horn loudspeaker systems using the Thiele-Small parameters [163], as did Richard H. Small [164], in 1977. Marshall W. Leach followed up with a design methodology for horn loudspeakers, also based on Thiele/Small parameters, where front and rear chamber volumes, throat area etc. could be calculated from specifications [152].

While the development of horn theory continued in other fields, such as in the analysis of musical instruments [165, 166], jet engines etc [30], developments in the field of electroacoustics were more in the form of practical implementations or numerical investigations.

The work of Earl R. Geddes on the Oblate Spheroidal Waveguide, earlier analyzed by Freehafer and Salmon as mentioned above, is an interesting exception. Geddes first presented his work in an AES preprint in 1987 [167], which was later made into a JAES paper in 1989 [5]. Geddes abandoned the earlier question of horn theory, "what is the loading characteristics of a specified horn contour?" and instead asked the question "what horn contour is *required* to yield the desired performance?" He sought the answer to this question in finding a one-parameter solution (see [149]) to the wave equation in separable coordinate systems, and adopted the oblate spheroidal (OS) coordinate system as a good candidate, as its coordinate surfaces produce a suitable horn shape.

The claim set forth by Geddes in [167], that sound propagation in the OS coordinate system is in the form of a one-parameter wave, was challenged by Gavin R. Putland [168], leading Geddes to perform a more detailed analysis, including higher order modes [169]. Putland demonstrated that only three coordinate systems admit one-parameter waves [170].

2.7 PRACTICAL DEVELOPMENTS

This chapter has focused on the development of horn theory, and in order to not make it too lengthy, many of the practical engineering developments have been left out. This includes Paul W. Klipsch' introduction of the corner horn [171, 39], the Electro-Voice Constant Directivity horn [2], the Altec Lansing Manta-Ray horns [3] and two-segment exponential horns [172], and a host of other developments.

2.8 HORN LOUDSPEAKER SIMULATION

As mentioned above, a lumped parameter model combined with a one-dimensional model of the horn and empirical directivity data, was the basis for computing the performance of horn loudspeakers for many years. But as more powerful computers became available, more advanced methods were used.

Geddes and Clark [167] also used an approach based on lumped parameters for the transducer and associated cavities, and equations based on the horn equation for describing the horn, but computed the sound field based on the radiation from a spherical cap in a sphere. In [173], Geddes investigated various source velocity distributions based on numerical integration of the Rayleigh integral, and in [174], he looked at aperture diffraction in sources where a more realistic source condition was assumed; the source was no longer assumed to have infinite impedance. The problem still remained to calculate the source velocity distribution. Geddes had in a way circumvented the problem by using the oblate spheroidal waveguide and assuming that the mouth wave front was essentially spherical. Then what remained was more or less to take aperture diffraction into account. A similar circumvention, or simplification, of the design problem is found in the Manta-Ray horns designed by Henricksen and Ureda [3], where the horn was designed based on line-of-sight geometrical considerations, aided by a few empirical observations. Approximate methods for directivity prediction have also been applied in recent years, see for instance Gloukhov [175], who used a method based on the Huygens-Fresnel principle. The interest in directivity control has also resulted in investigations of the actual sound field in the horn mouth, in an effort to better understand directivity anomalies [176, 177, 178].

As more general numerical methods became available, these were also applied to horn loudspeaker simulation. Kagawa et al. [179] and Morita et al. [180] in 1980 computed the throat impedance and directional characteristics of a horn using the Finite Element Method (FEM). In 1981, Kyouno et al. [181] expanded the method to also include the diaphragm. Kristiansen [182] used a method where a finite element description of the near field was coupled to an analytical solution for the far field. Kristiansen and Johansen [183] used the indirect Boundary Element Method (BEM) for simulation of a horn, with more work done by Johansen on horn directivity using BEM [184, 185]. Henwood [186] and Henwood and Geaves [187] applied BEM to the design and optimization of a horn tweeter. Other applications of BEM to horn speaker design include Shindo et al. [188], who used BEM in combination with semi-analytical methods, Hodgson and Underwood [189], who gave an example of comparison of BEM with one-dimensional theory, Bright et al. [190], who studied a folded low frequency horn, Morgans [8] who used BEM and a source superposition model to optimize horns for coverage angle and smoothness of response, and Makarski [7]. A version of BEM that should also be mentioned is the Boundary Element Rayleigh Integral Method (BERIM) developed by Stephen Kirkup, and described in Kirkup et al. [191]. This method combines BEM with the Rayleigh integral, and makes it possible to simulate cavities opening up into an infinite baffle. This removes the need for discretizing the outside of the horn, resulting in a reduced computational load.

FEM continues to be popular for horn simulations, see for instance Holm, 2010 [192], who compared FEM models of horns with measurements, and the method has also been used in optimization of horn shapes, see the work of Wadbro et al. and Udawalpola et al. [193, 194, 195].

As air non-linearity in horns can be considerable at the levels occurring in sound reinforcement and public address situations, proper analysis of this phenomenon is important. Including air non-linearity is not a simple task, however, as the governing equations now are non-linear, and require different solution methods than the linear equations. Most of the analyses of non-linearity in horns have been based on one-dimensional approaches. Thuras et al. [105], Goldstein and McLachlan [106] and Bequin and Morfey [196] analyzed non-linear distortion in exponential horns analytically. Zamorski [197] analyzed non-linearity in Bessel horns. Usually more general horns must be analyzed, and models for predicting the resulting distortion from such horns have usually been one-dimensional. Klippel has had several papers on models for non-linearity in horns [42, 198, 199, 200], and Holland et al. [201] developed a computational model that showed reasonable agreement with measurements. The work by Voishvillo should also be mentioned [202]. Few fully three-dimensional non-linear models have been published, although it has been shown that directivity has a bearing on the relative magnitude of the distortion products [203]. For instance, if directivity is narrower at the frequencies of the harmonics than at the frequency of the fundamental, the relative magnitude of the harmonics, and thereby the distortion, will be greater on-axis than off-axis.

Tsuchiya et al. presented an FEM model for horns that also includes transducer non-linearity [204]. A simplified model was presented by

Makarski [205], who used BEM to compute the pressure along a line extending from the horn throat to the far field point where it was desired to calculate the distortion, and used a post-processing technique to estimate the distortion at this point based on the sound pressure along the line of field points. This technique should be adaptable to other computational methods.

The next chapter will go into simulation methods in more detail.

3

OVERVIEW OF HORN SIMULATION METHODS

This chapter is a combination of a literature review and an overview of methods for simulating horns. Chapter 1 discussed the three main areas of application of the simulation methods, and their similarities, differences and requirements. In this chapter, a review of the various methods are given. Review of previous work is made where relevant. It is of course impossible to give a complete review of all existing literature on the subject, but an attempt is made of making the review rather comprehensive.

It is not felt necessary to give detailed derivations of the various methods in this work. This can be found in the references provided. Derivations or equations given in this chapter rather serve to illustrate the basic ideas of the methods.

3.1 ANALYSIS APPROACHES

Methods for simulating the horn ranges from simple lumped parameter models that are based on a one-dimensional approximation of the horn, to full three-dimensional numerical models that require complex discretization of the boundary or domain.

One-dimensional models are limited to a low *ka* range, below the cut-in of the first transversal mode. They can usually give a reasonable accurate prediction of the throat impedance, and hence can be used to calculate the power response of the system. But these methods cannot predict the directivity of the horn. They are also blind to the actual cross-sectional shape of the horn, only the area change is taken into account. For applications where the directivity is of lesser importance, or where the horn can be assumed to be small enough to be omnidirectional in the frequency range of interest, these models can be surprisingly accurate. They can also take losses into account in a simple way.

Three-dimensional analytical solutions also exist for a few geometries, but the solution is very involved mathematically, if a full three dimensional solution is desired. Due to the restrictions imposed on the geometry, using this approach for analysis of practical designs is difficult, but the solutions may serve as useful references.

Numerical methods models includes the Finite Difference Method (FDM), the Finite Element Method (FEM) , and the Boundary Element Method (BEM) . They require detailed discretization of the horn walls (BEM) or the domain (FDM, FEM), and can simulate both throat impedance and directivity. These models are usually much more time consuming due to the vastly increased number of degrees of freedom, but can yield very accurate results for general geometries. The main problem with these methods, however, is how they scale with kL, where L is a measure of the size of the horn.

In between these two categories, we have the semi-analytical methods. These methods can be as accurate as element based methods, but are usually faster. The principle of the methods is to divide the horn into small segments that each have analytical solutions, and then couple these segments together. Because of this, these methods are restricted to certain cross-sectional geometries, but the shape in the axial direction is arbitrary. The methods are therefore much less restricted than the analytical methods.

3.2 ANALYTICAL METHODS

One way to simulate horns is to set up the three-dimensional wave equation in a coordinate system where the wave equation is separable, and letting the horn walls follow the coordinate surfaces. Then it is for certain cases possible to find analytical solutions. These solutions will include higher order modes of propagation, and one is therefore able to predict the sound field inside the horn. There are, however, only eleven coordinate systems where the wave equation is separable, and very few of them have surfaces that give useful horn contours [5]. Furthermore, if analytical solutions are to be found for radiation from finite horns, one is restricted to enclosures that also follow the coordinate surfaces. For instance, it would be possible to find an analytical solution for a conical horn mounted in a sphere, but not for the same horn mounted in a rectangular box. Analysis of arbitrary geometries is therefore not possible.

3.2.1 *The Horn Equation*

In order to be able to mathematically analyze sound propagation in horns of more general shape, the dimensionality of the wave equation may be reduced. By lumping all transversal variations into a function $S(x)$ describing the area variations of the horn, an essentially one-dimensional equation may be obtained. This equation is known as the horn equation, the history if which was given in Chapter 2.

The horn equation can be derived in the same manner as the one-dimensional wave equation, but using volume velocity U instead of particle velocity v, via $U = vS(x)$. The Euler equation and the linearized equation of state (mass conservation equation) then become

$$\frac{\partial U}{\partial t} = -\frac{S(x)}{\rho_0}\frac{\partial p}{\partial x}, \tag{2}$$

$$\frac{\partial p}{\partial t} = -\frac{\rho_0 c^2}{S(x)} \frac{\partial U}{\partial x}. \tag{3}$$

Differentiating the first one with respect to x and the second one with respect to t, we get

$$\frac{\partial}{\partial x} \frac{\partial U}{\partial t} = -\frac{1}{\rho_0} \left(S(x) \frac{\partial^2 p}{\partial x^2} + \frac{\partial S(x)}{\partial x} \frac{\partial p}{\partial x} \right), \tag{4}$$

$$\frac{\partial^2 p}{\partial t^2} = -\frac{\rho_0 c^2}{S(x)} \frac{\partial}{\partial t} \frac{\partial U}{\partial x}. \tag{5}$$

By combining these two equations, we get

$$\frac{\partial^2 p}{\partial t^2} = \frac{c^2}{S(x)} \left(S(x) \frac{\partial^2 p}{\partial x^2} + \frac{\partial S(x)}{\partial x} \frac{\partial p}{\partial x} \right) \tag{6}$$

or

$$\frac{\partial^2 p}{\partial x^2} + \frac{1}{S(x)} \frac{\partial S(x)}{\partial x} \frac{\partial p}{\partial x} - \frac{1}{c^2} \frac{\partial^2 p}{\partial t^2} = 0, \tag{7}$$

which is the horn equation for pressure. This equation can now be solved for different functions $S(x)$.

The horn equation is built on several assumptions, in addition to the assumption of infinitesimal amplitudes used when linearizing the wave equation. The additional assumptions are [98, 104]:

1. The walls of the horn are perfectly rigid, reflecting and smooth.
2. There are no transversal modes in the horn, i.e. the pressure and velocity is uniform over the wave front.
3. The horn axis is straight.

Assumption 1 assures that the wave front in the horn will be perpendicular to the horn walls. It can be closely approximated in practice by making the walls hard and reflective, and by avoiding material resonances.

Assumption 2 is usually dependent on a cross-section that is small in terms of wavelengths. For horns where the cross-section is not small compared to a wavelength, and especially in horns with strongly curved walls, the actual wave fronts inside the horn will deviate significantly from the assumed ones. This is also the reason for assumption 3: for a curved horn we can be certain that the wave fronts are not uniform.

Since the horn equation is not able to predict the interior and exterior sound field for horns other than true one-parameter horns (see the next section), it has been much criticized. It has however been shown [165, 206] that the approximation is not as bad as one would perhaps think in the first instance. By considering the wave front area expansion instead of the physical cross-section of the horn, the loading performance of horns of arbitrary shape can be predicted with reasonably good accuracy, and this will be discussed in Section 3.4.2.

The horn equation has been solved for several shapes, or classes of shapes. Webster himself treated the straight tube, the conical horn, $S(x) \propto x^2$, and the exponential horn, $S(x) \propto e^{-mx}$ in Webster's notation, in addition to a cursory treatment of horn profiles where $S \propto x^n$ (also known as Bessel horns) for $n = 0$ (straight tube), -2 and 2, and also horns where $S \propto e^{-mx^2}$. Ballantine considered infinite Bessel horns in greater detail [90]. In his thesis [142], Vincent Salmon developed a generalized one-dimensional horn theory, and applied it to the hyperbolic horn that had previously been treated exactly by Freehafer [109, 110]. Later, Salmon published his generalized theory [143] and used it to find a new family of horns [144, 93] known as hyperbolic-exponential horns.

Mawardi [153] gave generalized solutions of the horn equation by considering its singularities. Eisner [60] presented complete solutions of the horn equation, where the behavior of a horn for any frequency and loading can be derived from the solution for one loading, at one frequency.

Other researchers have also given more or less general solutions of the horn equation, extensions, and solutions for various specialized horn contours. For instance, Nagarkar and Finch [207] give the solutions for sinusoidal horns. These horns are in the shape of sine or cosine waves and have cusps, where the cross-sectional area becomes zero. They are not very useful for loudspeaker modeling. Nagarkar and Finch use them for instrument modeling.

Many of the solutions exist in the form of transfer matrix equations, that relate pressure and volume velocity at one end of the horn to pressure and volume velocity at the other:

$$\begin{bmatrix} p_1 \\ U_1 \end{bmatrix} = \begin{bmatrix} a_{11} & a_{12} \\ a_{21} & a_{22} \end{bmatrix} \begin{bmatrix} p_2 \\ U_2 \end{bmatrix} = T_{12} \begin{bmatrix} p_2 \\ U_2 \end{bmatrix}. \tag{8}$$

This is a very versatile approach that can either be used directly for horn shapes that have analytical solutions, or for a piecewise approximation to the actual horn contour, as described in Section 3.4.1.

The analytical solutions to the horn equation, often in the form of transfer matrices, have been used by a host of investigators, and it is futile to try to list all of them here. Of some interest is Leach's adoption of the SPICE simulation software to simulate horns [208]. It should also be mentioned that the horn equation is still an active area of research [209, 210, 211, 212].

An important concept in one-dimensional horn theory is the concept of One-Parameter (1P) horns. This idea was first presented by

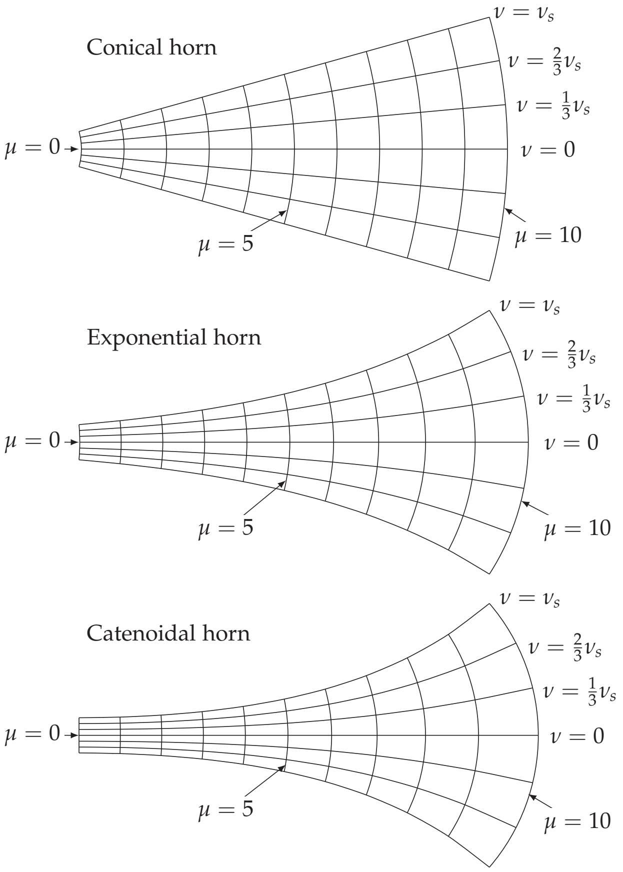

Figure 16: One-parameter coordinate systems for three horn types. Redrawn from Morse [149].

Morse [149], and can be described as follows: In a plane wave, the pressure can be expressed as

$$p = Ae^{-j(\phi - \omega t)} \tag{9}$$

i.e., it is a function only of time and the real function ϕ, which is the phase of the wave. For a plane wave, $\phi = kx$, where x is the distance from the source plane, and surfaces of constant phase (isophase surfaces) are planes, perpendicular to the x-axis. Similarly, for a spherical wave with the source at the origin, A is inversely proportional to r, the distance to the origin, and $\phi = kr$. The isophase surfaces are spheres. For both these cases, we note that both amplitude and phase are functions of only one coordinate, or *one parameter*, and time.

To apply this concept to horns, we set up an orthogonal coordinate system (μ, ν) for the horn in question, so that the horn wall is at ν_s, the axis is at $\nu = 0$, and $\mu = x$ along the axis of the horn. See

Figure 16. The μ surfaces define the isophase surfaces in our new horn-dependent coordinate system, it is the one parameter on which pressure and phase depends. We are not restricted to plane waves.

To see if a horn can be analyzed as a one-parameter (1P) horn, we may set up the wave equation in the coordinate system for the horn, and see if we can obtain a solution of the form in Eq. (9). If this can be done accurately, the horn is a 1P horn, and can be analyzed accurately by the horn equation.

However, there are very few coordinate systems where this is the case. Putland has shown [168, 170] that exactly three coordinate systems can be analyzed in this way: the Cartesian (plane waves), the cylindrical (cylindrical waves), and the spherical (spherical waves). In these systems, the horn equation is exact.

Many other horn shapes are approximately 1P, to a smaller or larger degree. Morse defined "good horns" as horns that have horn coordinate surfaces close to the surfaces of a coordinate system admitting 1P waves. Perhaps the most useful of these is the Oblate Spheroidal waveguide, which will be discussed in Section 3.2.3. Other horn shapes may also be close to 1P where the horn does not flare too rapidly.

If the horn is not 1P, the wave fronts in the horn will not correspond to the μ surfaces, and there will be be a particle velocity component parallel to these surfaces [184]. There will be reflection and scattering, giving rise to higher order modes.

3.2.2 *Three–Dimensional Solutions*

As mentioned above, there are few coordinate systems in which the full three-dimensional wave equation may be solved analytically, and even fewer of them have useful horn contours. One of them is the spherical coordinate system, where the problem of a conical horn in a sphere, the horn having its apex at the center of the sphere, may be solved analytically. No published paper showing the full solution is known to the author, but Sato [213, 101, 102] treated the problem with the simplification that no higher order modes existed inside the horn. Hoersch [79] treated the problem of higher order modes inside a conical horn, but used a pressure release boundary condition at the mouth. This makes the paper less useful as a contribution to horn simulation methods. Of interest, however, is his expansion for the Legendre polynomials $P_m(x)$ that makes it possible to find the non-integer order m of the spherical harmonics for a given cone angle.

In 1951, Stevenson [158] presented exact equations for wave propagation in horns of arbitrary shape, but the solution is in the form of an infinite set of equations. The problem has later been shown by Pagneux et al. [214] to be nearly impossible to solve in the form proposed by Stevenson.

Holtsmark et al. [159] looked at a solution for the exponential horn by setting up an orthogonal coordinate system which made the exponential horn a coordinate surface. The wave equation is not separable in this coordinate system, but by making some approximations, and by restricting the solution to the region of little flare, the wave equation is made separable, and solved. The solution is rather involved, but shows the existence of higher order modes and modal coupling.

Maezawa [160] used a perturbation method to add correction terms to the one-dimensional horn equation, and compared the mathematical results to those of Stevenson. An example was included, where an exponential horn was treated.

From the above, it is clear that deriving an analytical solution of the sound field in horns is a nearly impossible task, unless the horn follows the coordinate surfaces in a separable coordinate system. If this is not the case, further approximations must be made in order to solve the problem.

The solution of the wave equation for separable coordinate systems have been termed waveguide theory by Geddes [5], and is the topic of the next section.

3.2.3 *Waveguides*

While the concept of waveguides has been used in microwave technology for many decades, it is relatively new in audio. Although the term had occasionally been used in acoustics literature, it was not until Earl Geddes introduced the term in his 1987 AES preprint [167], and in later papers [5, 169, 215, 33], that it received widespread use in the audio community. After the turn of the millennium, many horn manufacturers started to call their products waveguides, to distinguish them from the "old fashioned" horns. Many of these devices cannot be called waveguides in the sense Geddes uses the term, since they rely on diffraction slots and similar tricks to achieve directivity control. Others are closer to wide-flaring traditional horns.

So what is a waveguide? The idea propagated by Geddes is that a true waveguide must follow the coordinate surfaces in one of the eleven coordinate systems in which the wave equation is separable. If this is the case, then the device can be analyzed exactly by the wave equation in that coordinate system. In addition to the fundamental wave, the modes can also be described. We can now describe the sound field in the device for any throat excitation, and we can find the mouth velocity distribution, which is needed for directivity calculations.

When this is done, we will find that some throat wave fronts will give a very simple sound field inside the waveguide, actually the simplest sound field we can possibly obtain. An axisymmetric conical horn, for instance, is a wave guide in spherical coordinates, and may be called a spherical waveguide. If a conical horn is inserted into a spherical sound field, and if the center of this sound field is at the apex of the cone, the presence of the cone will not disturb the sound field. Therefore, if a spherical waveguide is fed with a spherical wave at the throat, only a spherical wave is needed to describe the field inside the waveguide. The wave will follow its natural expansion through the device.

On the other hand, if the throat is excited by a plane wave, we must describe this plane wave in spherical coordinates. To do this, we have to expand it in a series of angular spherical modes, which means that infinitely many spherical modes are excited by the plane wave. These modes will propagate through the waveguide and create complex pressure distributions, and a more complex velocity distribution at the mouth. The same happens if the wave front is forced to change curvature, for instance by a change in wall slope. As we will see, this will require a new modal description after the change, and new modes will have to be generated. A true waveguide (by Geddes' definition) will try to avoid this as much as possible.

The mouth is also a point where modes always will be generated due to the large discontinuity. So while we can minimize the generation of modes inside the waveguide itself, we cannot avoid mode generation at the mouth. It can be minimized by flaring the mouth, but this mode generation will still influence the directivity pattern.

Many of the usable waveguide shapes comes from coordinate surfaces in elliptic or spheroidal coordinate systems. Figure 17 shows the the elliptic coordinate system in two dimensions. The origin here is a strip of width $2d$, not a point, and is marked by the thick line along the x-axis. If $d = 0$, we get polar coordinates, and if $d \to \infty$, we get the Cartesian coordinates. If we extend the system in and out of this figure, perpendicular to the paper, we generate the Elliptic Cylinder Coordinates. Rotating it around the line marked $\eta = 1.0$ generates the Oblate Spheroidal Coordinates, where the origin is a disc of radius d. The Prolate Spheroidal Coordinates are generated by rotating the figure around the $z = 0$ line. We can immediately see that the oblate spheroidal coordinates may make a usable waveguide, illustrated by the thick lines at $\eta = 0.87$.

This Oblate Spheroidal (OS) waveguide shape is the basis for most of Geddes' published works on waveguides [5, 33, 169, 215] (although it had previously been investigated by Freehafer [109, 110]), and appears to be an optimal solution for the transition from a plane wave at the throat to a spherical wave at the mouth. As has been shown by Geddes, however, the OS waveguide also has higher order modes, and these modes are coupled [169]. That means that even if the waveguide is excited by a perfect plane wave, higher order modes will be generated. Actually, the only coordinate systems where coupling between the modes does not exist are the ones that admit 1P waves,

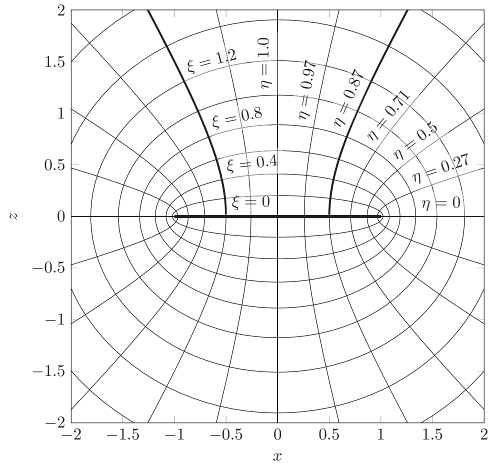

Figure 17: Two-dimensional elliptic coordinate system

and as discussed in Section 3.2.1, these are the Cartesian, cylindrical and spherical coordinate systems, given wave propagation along the proper coordinate. It is interesting to note that under these conditions, the wave front does not change its curvature. One may therefore say that it is the change of wave front curvature that generates higher order modes.

3.3 GENERAL NUMERICAL MODELS

In some cases, horns (or waveguides) that follow the coordinate surfaces of separable coordinate systems produce the desired results, but in many situations more control over horn performance is desired. Waveguides have a relatively limited range of variation in properties, and it may be desirable to design horns with a different set of properties for a given situation.

With general numerical methods, any horn shape may be analyzed and optimized to meet a certain set of criteria. A disadvantage of a purely numerical solution is that we are left with a large set of numbers, and no clue of the underlying mechanisms. Where analytical solutions provide functions and relations describing the problem, numerical methods will often only provide such insights after analysis of large data sets. Techniques like modal decomposition may be employed, but this requires at least a partial understanding of the mathematics of the problem at hand.

This chapter will give an overview of numerical methods that have been used in horn simulation. In general, many of these methods are not restricted to horn modeling, but may be used for general acoustic problems. The common approach is to discretize the problem, either

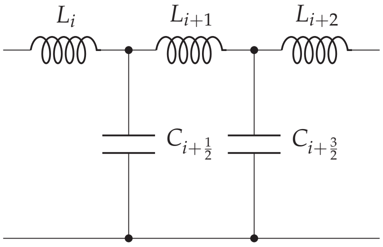

Figure 18: Lumped parameter representation of a horn.

just the structure (horn) itself, or the entire domain, and compute a numerical solution to the wave equation or Helmholtz equation for this grid or mesh. A common challenge for such approaches is that, especially for 3D domains, the number of nodes or elements increases very rapidly with frequency. The requirement of a certain maximum element size for a given wave length (commonly at least six elements per wavelength is required) can make high frequency simulation of large structures prohibitively expensive in terms of computer memory and solution time.

3.3.1 *Lumped Parameter Models*

This method was probably first used by Locanthi [151], and is based on the way transmission lines can be represented by lumped components. It may be viewed as a one-dimensional Finite Element method. Series masses and shunt compliances are used to represent the horn. Locanthi derived the values of these components by a finite difference approximation to the horn equation, resulting in (using the mobility analogy)

$$L_i = \frac{S_0 f(x_i)\Delta x}{\rho_0 c^2}$$

$$C_{i+1/2} = \frac{\rho_0 \Delta x}{S_0 f(x_i + 1/2)}$$

where $f(x)$ is the horn contour function. See Figure 18.

While this method was useful when simulation was done on analog computers, it is now rarely used, and transmission line elements are used instead, if not more accurate methods.

3.3.2 *The Finite Difference Method*

The FDM[1] is based on approximating the differential operators of the wave equation by finite differences, and is one of the most classical

---

[1] Not related to the little known Infinite Indifference Method.

numerical methods used for solving partial differential equations numerically. As an example, the one-dimensional wave equation

$$\frac{\partial^2 p}{dx^2} - \frac{1}{c^2}\frac{\partial^2 p}{\partial t^2} = 0 \tag{10}$$

is discretized in space and time with spatial steps Δx and time steps Δt. With spatial index i and time index k, the x coordinate is now given as $x_i = i\Delta x$, and the time as $t_k = k\Delta t$. The resulting discretized wave equation is then

$$\frac{p_{i+1}^k - 2p_i^k + p_{i-1}^k}{\Delta x^2} - \frac{1}{c^2}\frac{p_i^{k+1} - 2p_i^k + p_i^{k-1}}{\Delta t^2} = 0. \tag{11}$$

This equation can be solved for the next time step p_i^{k+1} to yield

$$p_i^{k+1} = 2\left(1-\alpha^2\right)p_i^k + \alpha^2\left(p_{i+1}^k + p_{i-1}^k\right) - p_i^{k-1} \tag{12}$$

where $\alpha = c\Delta t/\Delta x$. This means that we can find the pressure at the next time step from the values at the current and previous time steps, and the values at the two neighboring nodes. This is known as the Finite Difference Time Domain (FDTD) method. It can without much effort be extended to two or three dimensions. It is also possible to solve the Helmholtz equation using this method. Barjau [216] compared a one dimensional FDM to related methods; the delay line method and cellular automata method for simulation of one-dimensional flaring structures line musical instruments.

A related method, that has also been shown to be equivalent to the FDTD method, is the Transmission Line Method (TLM) [217, 218, 219], which is a method based on the Huygens' principle: that each point on a wave front is in itself a new source of waves. The TLM is based on discretization of the domain by a square grid, where each node is connected to four neighboring nodes through acoustic transmission lines that each have an impedance Z_0. A wave incident to a node through one of these transmission lines will be reflected and scattered into the neighboring nodes, where the process continues.

Another related method is the method of digital waveguides [15, 220], where the structure to be modeled is made up of a combination of delay lines, digital filters, and sometimes non-linear elements. This method has been used for modeling of wind instruments, but also other types like string instruments.

Finite difference based methods have the advantage of being relatively simple to implement. The localized updating scheme makes massive parallel processing feasible, for instance using a computer graphics card [221]. One challenge is to provide a non-reflecting termination of the domain for free field radiation problems. Another issue is that the grid in most cases is rectangular, so that a sloping and curving boundary, as found in horns, will be represented by small rectangular steps. This may introduce numerical artifacts, and a finer

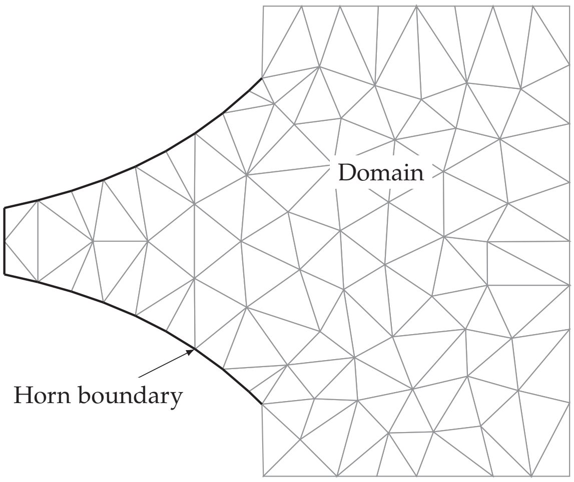

Figure 19: Discretization of the domain in the Finite Element Method.

discretization may be required than would otherwise be necessary. A solution to this problem has been presented by Noreland [222], who used an orthogonal coordinate transformation to avoid the problem.

Computer memory can also be an issue with large FDTD meshes, as the pressure at each node for several time steps has to be stored.

3.3.3 *The Finite Element Method*

The FEM was first developed for analyzing complex structures in engineering [223], but has also been applied to acoustics [224, 225]. The method is based on discretizing the domain into elements, Figure 19, impose boundary conditions, and solve for the pressure (or velocity potential) at the nodes. This makes the method well suited for interior problems like cavities. For infinite domain radiation problems (like radiation from structures like horn loudspeakers), special techniques must be used. [182] describes how spherical harmonics can be used to set the boundary conditions at a spherical outer boundary for radiation into an infinite domain. So-called *infinite elements* [226] may also be used, or a Perfectly Matcher Layer (PML) may be used to completely absorb the outward propagating wave.

The sound field in the domain must satisfy the Helmholtz equation

$$\nabla^2 p + k^2 p = 0, \tag{13}$$

subject to the boundary conditions. The domain is divided in elements, that are described by nodes, and FEM seeks to find an approximate solution to Eq. (13) at a these nodes. For the rest of the domain, the pressure is found by interpolation of *basis functions*. As an example, let us use a simple rectangular element with four nodes as our basic element. We know the pressure values at each node p_i, and each node also have a basis function N_i. The pressure inside each element can then be expressed as

$$p(x, y) = N_1(x, y)p_1 + N_2(x, y)p_2 + N_3(x, y)p_3 + N_4(x, y)p_4, \tag{14}$$

or in matrix form,

$$p(\mathbf{x}) = \mathbf{N}(\mathbf{x}) \cdot \mathbf{p}. \tag{15}$$

The basis functions satisfy the requirements that

- $N_i(x_i, y_i) = 1$ and $N_{j \neq i}(x_i, y_i) = 0$, and
- $\sum_i N_i = 1$ everywhere on the element.

We now wish to set up a system of equations including all the elements in the domain to solve for the unknown node pressures. This can be done by writing the Helmholtz equation as

$$\left(\nabla^2 + k^2\right) p(\mathbf{x}) = D_H p(\mathbf{x}) = 0 \tag{16}$$

and inserting the approximation from Eq. (15), $p(\mathbf{x}) \approx \mathbf{N}(\mathbf{x}) \cdot \mathbf{p}$, into it. This is only approximately correct, and we will get a residual $R(\mathbf{x})$:

$$D_H \left(\mathbf{N}(\mathbf{x}) \cdot \mathbf{p}\right) = R(\mathbf{x}). \tag{17}$$

We now want to set up a system of equations that can give us the set of node values that minimizes the residual. By integrating over both sides of Eq. (17), the right-hand side now describes the *average* residual over the domain:

$$\int\limits_{\Omega} D_H \left(\mathbf{N}(\mathbf{x}) \cdot \mathbf{p}\right) d\Omega = \int\limits_{\Omega} R(\mathbf{x}) d\Omega. \tag{18}$$

Minimizing the right-hand side can now result in either a good solution with small residuals everywhere, or large residuals that cancel each other. By in addition using weighting functions that are nonzero only over a small area, and by using many weighting functions so that the entire domain is covered (i.e. using a vector of weighting functions, $\mathbf{W}(\mathbf{x})$), we can set up a system of equations so that

$$\int\limits_{\Omega} \mathbf{W}(\mathbf{x}) D_H \left(\mathbf{N}(\mathbf{x}) \cdot \mathbf{p}\right) d\Omega = \int\limits_{\Omega} \mathbf{W}(\mathbf{x}) R(\mathbf{x}) d\Omega = 0. \tag{19}$$

Each row is now a single equation,

$$\int\limits_{\Omega} W_i(\mathbf{x}) D_H \left(\mathbf{N}(\mathbf{x}) \cdot \mathbf{p}\right) d\Omega = 0. \tag{20}$$

A common choice of weighting functions is to use the basis functions themselves as weighting functions. This is known as Galerkin's method. The basis functions and element types are usually chosen so that the numerical integration is efficient. To improve accuracy, higher order elements are often used, in which more nodes than corners are used. For example, triangular elements with 6 nodes, or quadrilateral elements with 8 nodes are common, and are known as quadratic elements.

The matrices that are set up to solve the system of linear equations for the FEM are usually sparse, often band diagonal. This reduces the amount of memory required, and special solution techniques adapted to sparse matrices may be used. Rotational symmetry may be used to reduce the dimensionality of the problem.

We will not go into any more mathematical details about the FEM, as this method has not been used to any great extent in this work.

3.3.4 *The Boundary Element Method*

The basis of the BEM is to replace the equations that describe the solution to the Helmholtz equation (or other partial differential equations) in the domain Ω, as in FEM, by equations that describe the solution on the boundary of the domain [225, 227]. The mathematical foundation for this is Green's second theorem:

$$\int_{\Omega} \left(u\nabla^2 v - v\nabla^2 u\right) d\Omega = \int_{\Gamma} \left(u\frac{\partial v}{\partial n} - v\frac{\partial u}{\partial n}\right) d\Gamma \tag{21}$$

where $\partial/\partial n$ is the normal derivative at the surface Γ. Both functions $u(\mathbf{x})$ and $v(\mathbf{x})$ must be continuously differentiable inside Ω.

Now let $u(\mathbf{x}) = \varphi(\mathbf{x})$ and $v(\mathbf{x}) = G(\mathbf{x})$, both solutions to the Helmholtz equation, where $\varphi(\mathbf{x})$ is the velocity potential, and $G(\mathbf{x}|\mathbf{x}_0)$ is a Green's function, i.e. the sound field at $\mathbf{x}$ due to a source at $\mathbf{x}_0$:

$$G(\mathbf{x}|\mathbf{x}_0) = \frac{e^{-jkr}}{4\pi r} \tag{22}$$

where $r = |\mathbf{x} - \mathbf{x}_0|$.

The integrand of the volume integral in Eq. (21) now becomes [225]

$$\varphi\nabla^2 G - G\nabla^2\varphi = -k^2\varphi G + k^2\varphi G = 0 \tag{23}$$

and we are left with

$$\int_{\Gamma} \left(\varphi\frac{\partial G}{\partial n} - G\frac{\partial \varphi}{\partial n}\right) d\Gamma = 0. \tag{24}$$

After some manipulation, and taking into account that when $\mathbf{x} = \mathbf{x}_0$, Eq. (22) is singular and therefore not continuously differentiable[2], we arrive at the following expression:

$$\varphi(\mathbf{x}) = \int_{\Gamma} \left(G\frac{\partial \phi}{\partial n} - \varphi\frac{\partial G}{\partial n}\right) d\Gamma, \tag{25}$$

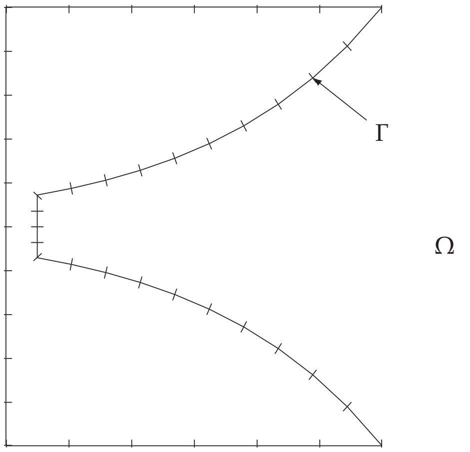

Figure 20: Example of discretized boundary for the Boundary Element Method.

which is the Kirchhoff-Helmholtz integral theorem.

To be useful, Eq. (25) must obviously be discretized, otherwise we are stuck with cases with analytical solutions. We therefore divide the surface Γ into elements Γ_i, see Figure 20, and seek to find the velocity potential and velocity at the center of each element. Using the element centers and assuming a constant value over each element is known as the collocation method.

The use of velocity potential here is to make the treatment compatible with that of Kirkup [227]. Pressure is related to the velocity potential as $p = -j\rho\omega\varphi$. For Kirkup's formulations, the surface normal is always outward *from the boundary.*

By using the operator notation used by Kirkup [227], we have

$$\{L_k\zeta\}_{\Gamma_i}(\mathbf{p}) \equiv \int_{\Gamma_i} G_k(\mathbf{p}|\mathbf{q})\,\zeta(\mathbf{q})dS_q \tag{26}$$

$$\{M_k\zeta\}_{\Gamma_i}(\mathbf{p}) \equiv \int_{\Gamma_i} \frac{\partial G_k}{\partial \mathbf{n}_q}(\mathbf{p}|\mathbf{q})\,\zeta(\mathbf{q})dS_q, \tag{27}$$

where Γ_i is (part of) a surface, $\mathbf{n}_q$ is the outward normal to Γ_i at $\mathbf{q}$, and $\zeta(\mathbf{q})$ is a function defined for $\mathbf{q} \in \Gamma_i$. The discretized Kirchhoff-Helmholtz integral theorem then becomes

$$\left[M_k + \frac{1}{2}I\right]_\Gamma \varphi(\mathbf{p}) = [L_k]_\Gamma\, v(\mathbf{p}) \tag{28}$$

where $v = \frac{\partial\varphi}{\partial n}$ is the surface normal velocity, and the brackets indicate that the operators are now matrices relating each point[3] on the surface to every other point on the surface, including itself. It is now possible to employ boundary conditions to solve for φ and v at each element, and from the values at the elements, the velocity potential in the domain can be found as

$$\varphi(\mathbf{x}) = [L_k]_\Gamma\, v(\mathbf{p}) - [M_k]_\Gamma\, \varphi(\mathbf{p}). \tag{29}$$

---

[2] We solve this by placing a small surface around $\mathbf{x}_0$ to remove it from the domain.

[3] Center point on each element.

As can be seen, the velocity potential in the domain can be found when φ and v are known on the boundary. The matrices are now relations between the field points and the elements, instead of relations between elements.

The formulation in Eq. (28) is satisfactory for interior BEM, except for the Dirichlet (pressure release) boundary condition. As this boundary condition never appears in horns (where we usually have a hard wall (Neumann) or impedance (Robin) boundary condition), we will not go into any more details on the interior problem.

If either φ or v is known at the boundary, Eq. (28) can be solved rather simply, by first a matrix-vector multiplication, followed by a matrix inversion. Sometimes, however, the more general boundary condition

$$\alpha(\mathbf{p})\varphi(\mathbf{p}) + \beta(\mathbf{p})v(\mathbf{p}) = f(\mathbf{p}), \tag{30}$$

is desired, where α, β and f are diagonal matrices. Equation 28 can now be combined with Eq. (30) to form a linear system of equations:

$$\begin{bmatrix} [M] & L_k \\ D_\alpha & D_\beta \end{bmatrix} \begin{bmatrix} \varphi \\ v \end{bmatrix} = \begin{bmatrix} 0 \\ F \end{bmatrix}, \tag{31}$$

where $[M] = -\left[M_k + \frac{1}{2}I\right]$, and D_α and D_β are diagonal matrices containing the boundary conditions. Since D_α and D_β are diagonal, Eq. (31) can be rearranged into an $N_e \times N_e$ linear system using standard methods [227], instead of the $2N_e \times 2N_e$ system shown, N_e being the number of elements.

In the case of exterior problems, application of the Kirchhoff-Helmholtz integral theorem result in the following equation

$$\left[M_k - \frac{1}{2}I\right]_\Gamma \varphi(\mathbf{p}) = [L_k]_\Gamma\, v(\mathbf{p}) \;\; (\mathbf{p} \in \Gamma) \tag{32}$$

$$\varphi(\mathbf{x}) = [M_k]_\Gamma\, \varphi(\mathbf{p}) - [L_k]_\Gamma\, v(\mathbf{p}) \;\; (\mathbf{p} \in D). \tag{33}$$

Eq. (32) is, unfortunately, unsuitable for general use, because the operator $M_k - \frac{1}{2}I$ is singular for a set of characteristic wavenumbers k^* that are the eigenfrequencies of the interior Dirichlet problem, and are ill-conditioned at wavenumbers near k^*. This is known as non-uniqueness.

Several methods have been developed to solve this problem. The method by Schenck [228], often referred to as the CHIEF method, adds interior points to make an overdetermined set of equations. The matrices are no longer square, and the system of equations must be solved by the least squares method or similar. The problem with the CHIEF method is that the optimum location of the interior points is not known, other than that they must not lie on the internal node lines, and that more and more points are necessary at higher frequencies to maintain accuracy.

Burton and Miller [229] introduced a method that is based on a hybrid between the direct formulation in Eq. (32), and the equations resulting from differentiating Eq. (32) with respect to the boundary normal. This results in the following linear system of equations:

$$\left[M_k - \frac{1}{2}I + \mu N_k\right]_\Gamma \varphi(\mathbf{p}) = \left[L_k + \mu\left(M_k^T + \frac{1}{2}I\right)\right]_\Gamma v(\mathbf{p}) \tag{34}$$

where the new operators are

$$\left\{M_k^T \zeta\right\}_{\Gamma_i}(\mathbf{p};\mathbf{u}_p) \equiv \frac{\partial}{\partial u_p}\int\limits_{\Gamma_i} G_k\left(\mathbf{p}|\mathbf{q}\right)\zeta(\mathbf{q})dS_q \tag{35}$$

$$\{N_k \zeta\}_{\Gamma_i}(\mathbf{p};\mathbf{u}_p) \equiv \frac{\partial}{\partial u_p}\int\limits_{\Gamma_i} \frac{\partial G_k}{\partial \mathbf{n}_q}\left(\mathbf{p}|\mathbf{q}\right)\zeta(\mathbf{q})dS_q, \tag{36}$$

and μ is a weighting factor such that

$$\mu = \frac{i}{k+1}.$$

The matrices are now square, but the M_k^t and N_k operators are hypersingular and difficult to discretize. However, they are available in the Fortran subroutines provided by Kirkup [227], as is an implementation of the Burton-Miller method.

A more recent solution to the problem of non-uniqueness is described by Mohsen et al. [230], and is known as the Dual Surface Method. This method adds interior points on an interior surface S located close to Γ at a distance δ along the normal to the surface, to the system of equations with a purely imaginary weighting factor α:

$$\left[M_k + \alpha\underline{M_k} - \frac{1}{2}I\right]\varphi = \left[L_k + \alpha\underline{L_k}\right]v \tag{37}$$

where the underline indicates that the operators are applied to the points in the interior domain. This method avoids the hypersingularity of the Burton-Miller method, and the matrices are square, so common solution techniques may be employed. If $k\delta < \pi$, the cavity formed between S and Γ is too small to support any resonant modes, and the solution is unique.

For completeness, the *indirect BEM* should also be mentioned. This method uses the difference of velocity and pressure (or velocity potential) across a thin surface as the variable, and is therefore able to model thin structures directly. See for instance Johansen and Kristiansen [183] and Johansen [184] for a discussion of this method.

As documented in a paper by Cheng and Cheng [231], since the early 1990s over 500 articles per year are published on BEM, so no further attempt will be made on discussing all the possible refinements and variations of the method. However, a few special cases will be mentioned.

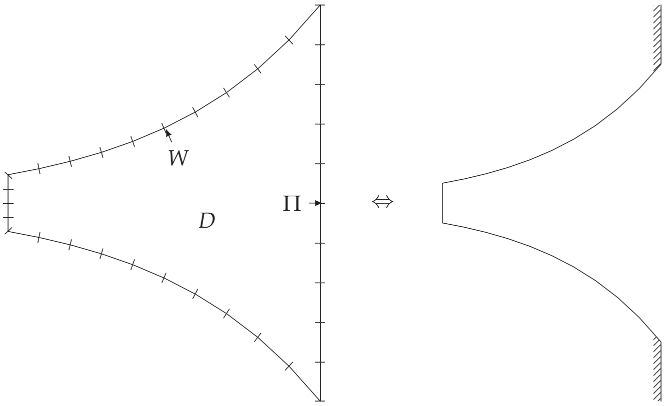

Figure 21: Principle of the Boundary Element Rayleigh Integral Method. The interior BEM domain D is bounded by surfaces W and Π, and surface Π radiates into half-space. This is equivalent to a horn mounted in an infinite baffle, right.

3.3.5 *The Boundary Element Rayleigh Integral Method*

An interesting extension or variation of BEM is the Boundary Element Rayleigh Integral Method (BERIM) developed by Stephen Kirkup [232, 191]. This method is developed to simulate cavities that open into an infinite baffle, and combines the BEM for the cavity with the Rayleigh integral for the field in front of the baffle. The basis for the method is Eq. (28), but the surface is divided into two parts (see Figure 21): the surface W belonging to the cavity, and the interface surface Π.

The radiation from Π is described by the Rayleigh integral, and this can be used to set the boundary condition here. It is now possible to set up the following systems of equations:

$$\begin{aligned}
\left[M_k + \frac{1}{2}I\right]_{WW} \varphi_W + [M_k]_{W\Pi}\,\varphi_\Pi &= [L_k]_{WW}\,v_W + [L_k]_{W\Pi}\,v_\Pi && (38)\\
[M_k]_{\Pi W}\,\varphi_W + \left[M_k + \frac{1}{2}I\right]_{\Pi\Pi} \varphi_\Pi &= [L_k]_{\Pi W}\,v_W + [L_k]_{\Pi\Pi}\,v_\Pi && (39)\\
\varphi_\Pi &= -2\,[L_k]_{\Pi\Pi}\,v_\Pi && (40)\\
[D_\alpha]_{WW}\,\varphi_W + \left[D_\beta\right]_{WW} v_W &= f_W && (41)
\end{aligned}$$

These equations are then reorganized into a linear system of equations as

$$\begin{bmatrix} [M]_{\Pi\Pi} & -M_{k,\Pi W} & L_{k,\Pi\Pi} & L_{k,\Pi W} \\ -M_{k,W\Pi} & [M]_{WW} & L_{k,W\Pi} & L_{k,WW} \\ I & 0 & 2\,[L_k]_{\Pi\Pi} & 0 \\ 0 & D_\alpha & 0 & D_\beta \end{bmatrix} \begin{bmatrix} \varphi_\Pi \\ \varphi_W \\ v_\Pi \\ v_W \end{bmatrix} = \begin{bmatrix} 0 \\ 0 \\ 0 \\ F_W \end{bmatrix}, \qquad (42)$$

where, as above, $[M] = -\left[M_k + \frac{1}{2}I\right]$, and D_α and D_β are diagonal matrices containing the boundary conditions at W.

BERIM has the advantage of not requiring the hypersingular operators M_k^T and N_k, and that the exterior of the horn does not need to be discretized. This method will be used as a reference method for much of the work in this thesis, as many of the simulations are done with the horn mounted in an infinite baffle.

A related method is presented by Post and Hixon [206], who describe a method where interior BEM is coupled to a hemisphere on which the sound field is described by spherical harmonics. The hemisphere is used as a "super-element", and the coefficients of the spherical harmonics expansion are found as part of the solution of the BEM system of equations.

3.3.6 *Fast Multipole BEM*

As traditional BEM generates dense, asymmetric matrices, requiring $\mathcal{O}(N^2)$ operations for assembly and $\mathcal{O}(N^3)$ for solving the system of equations using direct solvers ($\mathcal{O}(N^2)$ for iterative solvers like GMRES [233, 234]) , methods to accelerate the solutions have been sought. One such method is the Fast Multipole BEM (FMBEM) [235]. In this method, the BEM mesh is subdivided into clusters, and if a pair of clusters are in the far field of each other, the computations that would ordinarily have been performed on an element-to-element basis is replaced by calculations for the midpoint of the clusters. For clusters in the near field, traditional BEM is used. It is also possible to use different levels of clusters (clusters of smaller clusters) to enhance speed further.

FMBEM is mainly applied to large structures, like the sound field from submarines or planes, and it is not known if the method has been successfully applied to concave structures like horns. But as most of the elements in the interior of a horn are in the near field of each other, there may not be large savings over traditional BEM, unless a relatively large exterior mesh is needed.

3.3.7 *Other Methods*

This section will briefly mention two other numerical methods that have been used for horn simulation, and that are somewhat related to BEM.

The Source Superposition Method (SSM)

The SSM is due to Koopmann and Fahnline [236], and has been used by Morgans [237] to model and optimize horns. In this method, the surface is discretized, much as in BEM, and a combination of

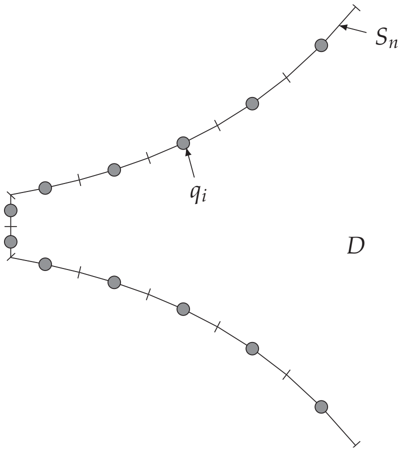

Figure 22: The principle of the source superposition method. Sources q_i are placed at the center of the elements S_n.

monopoles and dipoles are placed at the center of each element, Figure 22. The dipole is aligned normal to the element surface. The solution in the field is now found as a linear combination of these simple sources:

$$p(\mathbf{x}) = \sum_{i=1}^{N} s_i \left\{ \alpha_i G\left(\mathbf{x}|\mathbf{x}_i\right) + \beta_i \left[\nabla G\left(\mathbf{x}|\mathbf{x}_j\right) \cdot \mathbf{n}_j\right]_{\mathbf{x}_j=\mathbf{x}_i} \right\} \tag{43}$$

where s_i is the unknown strength of source i, and α_i and β_i are constants for each source type given in Table 1.

Source type	α	β
Monopole	1	0
Dipole	0	j/k
Tripole	1	j/k

Table 1: Constants α_i and β_i for monopole, dipole and tripole (combination of monopole and dipole) sources.

The source strengths are found by applying a matching technique, matching the specified normal velocity with the normal velocity due to the sources, given as

$$v(\mathbf{x}) \cdot \mathbf{n} = -\frac{1}{j\omega\rho} \sum_{i=1}^{N} s_i \nabla \left\{ \alpha_i G\left(\mathbf{x}|\mathbf{x}_i\right) + \beta_i \left[\nabla G\left(\mathbf{x}|\mathbf{x}_j\right) \cdot \mathbf{n}_j\right]_{\mathbf{x}_j=\mathbf{x}_i} \right\} \cdot \mathbf{n}, \tag{44}$$

through the volume velocity:

$$U_n = \int\int_{S_n} v(\mathbf{x}) \cdot \mathbf{n} dS(\mathbf{x}) \tag{45}$$

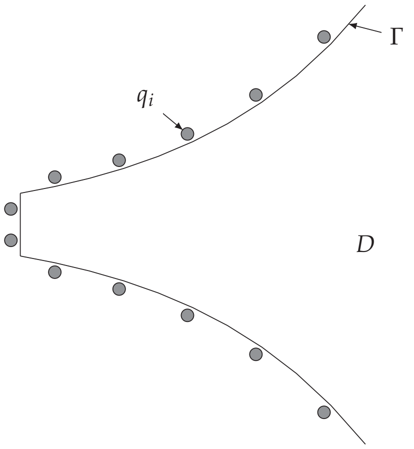

Figure 23: Principle of the Method of Fundamental Solutions. Sources q_i are placed away from the boundary Γ, outside the domain D, and their strengths Q_i are adjusted to enforce the boundary conditions at Γ.

Combining these two equations gives

$$U_n = \sum_{i=1}^{N} -\frac{s_i}{j\omega\rho} \int\int_{S_n} \nabla \left\{ \alpha_i G\left(\mathbf{x}|\mathbf{x}_i\right) + \beta_i \left[\nabla G\left(\mathbf{x}|\mathbf{x}_j\right) \cdot \mathbf{n}_j\right]_{\mathbf{x}_j=\mathbf{x}_i} \right\} \cdot \mathbf{n} dS(\mathbf{x}). \tag{46}$$

This equation is calculated for each element, and gives a system of equations

$$\mathbb{U}\vec{s} = \vec{U} \tag{47}$$

where $\vec{s}$ is a vector of source strengths, $\vec{U}$ is the vector of volume velocities, and $\mathbb{U}$ is the matrix to be inverted.

The SSM forces the volume velocity of the simple sources to match the volume velocity boundary condition, which means that the radiated power is correctly calculated (the initial goal of the method). This again means that the far field pressure is also accurate, even for coarse meshes, but the near field may not be correct, and hence the method cannot be relied on for predicting the throat impedance of horns.

The Method of Fundamental Solutions (MFS)

The MFS is related to the SSM in that it relies on computing the sound field from a distribution of simple sources. In the MFS, however, the sources are not placed on the boundary, but instead outside the domain in which the sound field is to be calculated, Figure 23. In addition, no mesh needs to be defined, only discrete points outside the domain boundary are required. The boundary conditions are then enforced and used to compute the strengths of the sources [238, 239].

Given the fundamental solutions

$$G\left(\mathbf{x}|\mathbf{x}_j\right) = \frac{1}{r}e^{-jkr} \tag{48}$$

$$H\left(\mathbf{x}|\mathbf{x}_j,\mathbf{n}\right) = \frac{1}{-j\rho\omega}\frac{-jkr-1}{r^2}e^{-jkr}\frac{\partial r}{\partial \mathbf{n}}, \tag{49}$$

and the boundary conditions for surface $\Gamma = \Gamma_1 \cup \Gamma_2$, where Γ_1 has Dirichlet, and Γ_2 has Neumann boundary conditions

$$p = p_K, \quad \text{in } \Gamma_1 \tag{50}$$

$$-\frac{1}{j\rho\omega}\frac{\partial r}{\partial \mathbf{n}} = v_K, \quad \text{in } \Gamma_2, \tag{51}$$

two sets of equations can be set up to find the source strengths Q_j:

$$\sum_{j=1}^{NS} Q_j G\left(\mathbf{x}|\mathbf{x}_j\right) = p_{K,i} \text{ for each } x_i \text{in } \Gamma_1 \tag{52}$$

$$\sum_{j=1}^{NS} Q_j H\left(\mathbf{x}|\mathbf{x}_j,\mathbf{n}\right) = v_{K,i} \text{ for each } x_i \text{in } \Gamma_2. \tag{53}$$

Here i is the index of the *collocation points*, the points distributed along the boundary where the boundary conditions are enforced. With NC collocation points and NS sources, the source strengths can now be found, either as a linear system of equations if $NC = NS$, or as an optimization problem if $NS < NC$.

Since the collocation version of the MFS does not require any integration over the surface, it can be very efficient. However, Candy [239] points out that the collocation rule used to obtain source coefficients is not unique, and prefers to use a Galerkin method with integration over the surface.

3.3.8 *Efficiency*

It is well known that when discretizing a problem, the discretization must be sufficiently fine to sample the wave field accurately. The general rule is to apply at least six elements per wavelength, although for far field calculations using BEM, sufficiently accurate results seem to be obtainable with three elements per wavelength [8]. In any case, the number of elements, N, depend on the size of the problem in wavelengths, or kL, where k is the wave number and L is the characteristic size of the problem.

For volume based elements (FDM, FEM), $N \propto \mathcal{O}\left([kL]^3\right)$. The matrices are sparse, so memory requirements are in the order of $\mathcal{O}\left(N\right)$, and the computational cost required for solving the matrices is also $\mathcal{O}\left(N\right)$ (per iteration, in the case of FDTD) due to the sparseness.

Boundary based methods (BEM) require fewer elements due to only the surface being discretized, so $N \propto \mathcal{O}\left([kL]^2\right)$, but since the matrices are full, memory requirements are in the order of $\mathcal{O}\left(N^2\right)$, and the computational cost for the solution is $\mathcal{O}\left(N^3\right)$. FMBEM can achieve $\mathcal{O}\left(N^{3/2}\right)$ or $\mathcal{O}\left(N \log N\right)$.

The SSM appears to have similar requirements as BEM, but may work well also with fewer elements than BEM due to the matching of surface volume velocity. Morgans [8] reports increased efficiency over BEM.

For the MFS, no definite number of sources for a given frequency limit is given in the references cited, so it is hard to judge the efficiency of this method directly. The study in [238], however, indicates a rather large increase in efficiency over BEM.

From this quick overview of memory requirements and computation cost, it is clear that both increase quite rapidly with frequency. For a large constant directivity horns, with mouth size in the order of one meter, and considering an upper frequency limit of 20 kHz, kL is in the order of 365. Simulation of such a horn with FEM or BEM can be very demanding, and the time required can be prohibitive if computer optimization is desired.

3.4 SEMI-ANALYTICAL MODELS

So far, the methods discussed have been either analytical or numerical. Analytical methods give up flexibility (or accuracy, in the case of one-dimensional models) to achieve exact solutions that may give new insights into the problem. These solutions are in many cases are rather computationally efficient. Numerical methods give up the exact mathematical description to achieve flexibility. The price is usually increased computational cost, and that it is harder to get fundamental insights into the problem at hand. Where analytical solutions may suggest certain solutions to a problem based on the mathematical formulation, this is very seldom found in purely numerical methods.

In between these two approaches is what can be termed *semi-analytical* methods[4]. In these methods, the problem is only partially solved analytically, and these partial analytical solutions are combined numerically. When applied to horns, an often used approach is to divide the horn into small sections or elements that each have an analytical solution, Figure 24, and then to match the sound fields at the interfaces, or discontinuities, between the element. If each element is one-dimensional, the cross-sectional area can be arbitrary. The

---

[4] When numerical output is desired from an analytical method, for instance to plot curves, numerical calculations are necessary. These methods are still not considered semi-analytical, as they provide a solution in the form of equations that adequately describe the solution without the need for numerical evaluation.

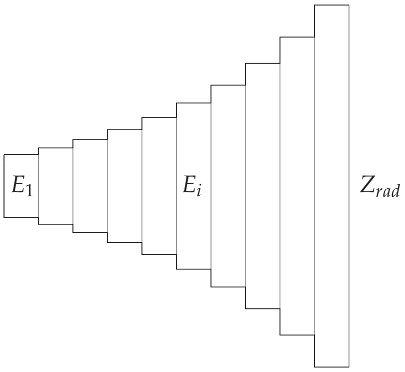

Figure 24: Principle of semi-analytical methods. The horn is divided into elements E_i that can be (depending on the model used) cylindrical, conical, exponential, or other shapes that have analytical solutions. A radiation impedance Z_{rad} defines the boundary condition at the mouth.

elements can for instance be cylindrical, conical [240] or exponential [241].

Conical elements may also include transversal modes, and may be used for 3D models of axisymmetric horns. If the elements are straight ducts, a modal description based only on the cross-sectional shape of each element is required. This is a more flexible approach than using conical elements, as now both cylinders, annular cylinders and rectangular ducts may be used. The cross-sectional shape is still restricted compared to purely numerical methods, but now the axial shape of the horn can be arbitrary. This approach is the basis for the work in this thesis and will be discussed in general terms in Section 3.4.3 and in detail in Chapter 4.

3.4.1 *Transmission Line Elements*

This method must not be confused with the Transmission Line Method (TLM) described in Section 3.3.2. The principle of the transmission line elements method was first described by Olson [138, 140]. He describes how the throat impedance of a horn of any shape can be found by dividing the horn into segments. The throat impedance of the last segment is used as the mouth impedance of the second last segment, and so on, from the mouth to the throat. Young [242] used a similar method for computing the resonance of musical instruments. Plitnik and Strong used straight cylindrical segments and introduced losses into the model [243].

A more elegant method is to express each segment by it's transfer matrix (also known as four-pole parameters, two-port elements, transmission matrices, T-matrices[5] or ABCD-matrices), and find a complete matrix for the horn by multiplying together the matrices for all the segments. The method originated in the analysis of electrical circuits, and an early reference in electroacoustics on this method is a paper by Molloy [244] from 1957, where T-matrices were used for lumped and distributed parameter analysis of vibrational systems, including loudspeakers. Lampton [245], in a paper from 1978, showed more advanced applications of T-matrices, and he also referred to it as being a common method in the analysis of electromagnetic waveguides. The method was used by Kergomard and Caussé [246] for simulation of musical instruments, and they also introduced losses, something also done by Keefe [247]. McLean et al. [248] used a series of straight elements to simulate constant directivity horns. The method is described in detail by Mapes-Riordan [240], with applications to electroacoustics.

Thanks to the computational efficiency and simplicity of the method, it has found much use in the simulation of musical instruments [249].

The T-matrix method has the advantage that the T-matrix for any horn shape can be found, and from this, the response to any mouth radiation impedance, and the mouth pressure and volume velocity for any excitation, can easily be found. The complete T-matrix H for the series of matrices can be found by multiplying the transfer matrices. For a horn consisting of $n-1$ elements,

$$\begin{bmatrix} p_1 \\ U_1 \end{bmatrix} = H \begin{bmatrix} p_n \\ U_n \end{bmatrix} = T_{12} \cdot T_{23} \cdot \ldots \cdot T_{n-2,n-1} \cdot T_{n-1,n} \begin{bmatrix} p_n \\ U_n \end{bmatrix} \tag{54}$$

where $T_{n-1,n}$ is the T-matrix of element $n-1$.

3.4.2 *Advanced One-Dimensional Models*

When using transmission line elements, it is not uncommon to use a combination of uniform tubes and conical elements; the uniform tubes are used for the straight portion of the horn, while the conical elements are used in the flaring sections. Wave fronts in horns are not either plane or spherical, however; they are often in the form of flattened spherical caps [241]. Also by simple reasoning, as long as the sound speed is constant in the horn, the distance between each successive wavefront must be constant over the wave front. If the horn, assuming axisymmetry, is not conical or of uniform cross-section, this leads to wave fronts that are neither spherical nor plane, but that are again flattened spherical caps. Using conical elements with spherical wave fronts also brings up the issue of the discontinuity created between the mouth wave front of one conical element and the throat

---

[5] Not to be confused with the T-matrix method in scattering theory.

wave front of the next, if these two elements don't share a common apex [250].

For wind instruments, where radiation directivity is of minor importance, there has been much research into one-dimensional models for predicting their resonance frequencies [251, 250, 252]. The use of spherical, or even oblate ellipsoidal, wave fronts have been used, together with a proper choice of radiation impedance model, to improve accuracy [253, 254, 255]. It appears that for improved accuracy in these models, the radiation impedance should change with the horn profile, as discussed in [254].

3.4.3 *Mode Matching Methods*

Traditionally, sound in ducts was treated one-dimensionally, assuming that the cross-section of the duct was smaller than a wavelength. That the wave equation also has solutions that can expressed as a sum of eigenfunctions, or *modes*, that can be found based on the boundary conditions imposed, has been known for a long time. An early, perhaps the earliest, example in acoustics comes from Rayleigh [256], paragraph 267, where he treats the sound in a rectangular enclosure by the familiar sum of cosine modes, and paragraph 268, where one of the enclosure dimensions is extended to infinity. Here, Rayleigh also discuss the phenomenon of mode cutoff and evanescent waves:

> *"If we fix our attention on any particular simple mode of vibration (for which p and q [mode indices] do not not both vanish), and conceive the frequency of vibration to increase from zero upwards, we see that the effect, at first confined to the neighbourhood of the source, gradually extends further and further and, after a certain value is passed, propagates itself to an infinite distance, the critical frequency being that of the two dimensional free vibrations of the corresponding mode."*

While Hoersch [79] probably was the first to analyze higher order modes in horns, it seems that Miles [257, 258, 259] was the first to analyze the generation of modes at a discontinuity, and using the method of matching of the fields. Miles was, however, mainly interested in a better lumped parameter model of the discontinuity, and he also treated right-angled joints [260] and bifurcations [261] this way.

The analytical treatments by Stevenson [158] and Holtsmark et al. [159] have already been mentioned, but while these treatments take modes into account, they are not directly related to mode matching as such. It should, however, be mentioned that mode matching has a long tradition in modeling of electromagnetic waveguides [262, 263].

The first complete *implementation* of a Mode Matching Method (MMM) for horns is probably due to Alfredson [36]. Here many of the elements used in this thesis are in place: discretization of the horn into short, cylindrical ducts, a step-by-step iteration down the horn, and matching of the sound fields, described by modes, at each discontinuity. Alfredson used an iterative technique to compute the sound field radiated from an axisymmetric exponential horn, first assuming no reflected wave, and working from a plane wave at the throat towards the mouth. At the mouth the boundary condition of an unflanged circular duct was used to obtain the reflected wave, which was then propagated back to the throat. The procedure was repeated to convergence. The method is a bit unwieldy in that the calculations are performed iteratively directly on the pressure field.

Roure [37] pioneered the method as used in the present thesis (the mathematical description will be presented in the following chapters), where he showed that by propagating the impedance at the mouth back to the throat, only a single iteration is necessary, and no assumptions about the source need to be made[6]. The method was applied to a muffler expansion chamber by Kergomard et al. in 1989 [264], where it was also compared to other mode matching formulations.

From about 1996, several papers from Laboratorie d'Acoustique, France, were published, where Roure's method was used. These papers describe the model in detail. Pagneux et al. [214] give a detailed treatment of the discrete model described by Roure, a version of the discrete model carried to the limit of infinitesimal segment length, and a purely continuous model. Amir et al. [265] have verified experimentally and numerically that the discrete model carried to the limit is able to predict both the sound field inside the horn, and the input impedance of the horn. Amir and Starobinski [266] also describe how the method may be used to find the eigenmodes of two-dimensional cavities.

The discrete model is also used by Kemp [267]. Kemp has also demonstrated that the discrete model is able to predict the input impedance of wind instruments with good accuracy. In both Kemp's and Amir's studies, the horn was assumed mounted in an infinite baffle.

Further work on the mode matching methods described by Pagneux et al. have been done by many (the 1996 paper has been cited over 140 times), but in particular the work by for instance Felix [19, 20, 268, 269, 21] and Braden [22] to extend the method to include bends, could be mentioned.

An alternative matrix formulation of the method is given by Shindo et al. [188] and Schuhmacher and Rasmussen [270], who simulated rectangular horns. Here the amplitudes of the propagating and reflected waves in each section were found by solving a linear system of equations. Shindo et al. used the Boundary Element Method in the narrow parts of the horn, claiming that MMM had numerical chal-

---

[6] Roure's thesis is in French, and is in general hard to obtain. The reference is provided to give proper credit for the origin of the method.

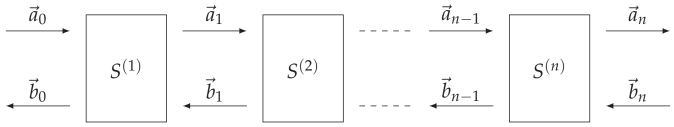

Figure 25: Principle of the Scattering Matrix approach. $\vec{a}$ represents a vector of incoming wave mode amplitudes, $\vec{b}$ represent the mode amplitudes of the scattered wave.

lenges when dealing with evanescent waves, but Schuhmacher and Rasmussen show no problems in this regard. They did not, however, use more than four modes.

Other mode based methods are also presented by Ando [55] and Oie et al. [56].

A different approach to the mode matching method is the scattering matrix method. This method has been used in modeling of electromagnetic waveguides [262], but also in modeling the ear canal [4, 271, 272] (including non-rigid walls) or ventilation systems [273, 274, 275]. Here a matrix is defined that relates waves in the two directions of propagation at the two sides of a duct element, see Figure 25. The relations are

$$\begin{bmatrix} \vec{a}_n \\ \vec{b}_{n-1} \end{bmatrix} = \begin{bmatrix} S_{11}^{(n)} & S_{12}^{(n)} \\ S_{21}^{(n)} & S_{22}^{(n)} \end{bmatrix} \begin{bmatrix} \vec{a}_{n-1} \\ \vec{b}_n \end{bmatrix} = \begin{bmatrix} T & R \\ R & T \end{bmatrix} \begin{bmatrix} \vec{a}_{n-1} \\ \vec{b}_n \end{bmatrix} \tag{55}$$

where T and R are $N \times N$ matrices specifying the modal transmission and reflection characteristics of the segment. For a straight segment, $R = \mathbf{0}$ and $T = \operatorname{diag}\left[e^{-jk_m L}\right]$ where k_m is the modal wave number of mode m.

The matrices can be multiplied together to form a composite scattering matrix for the entire duct system, but this may lead to instability due to evanescent modes, as T now will contain exponential numbers that may become very large.

It appears that the scattering matrix method can more easily be employed to compute the characteristics of bends (Furnell [273]) and junctions and right angle joints (Muehleisen [275]) than the formulation by Roure.

A final mode matching variant that should be mentioned, is the one described by Geddes [33]. Here the horn is discretized into conical elements approximating the contour. The sound field inside each cone is described by spherical Hankel functions. As the cones will have different angles, the spherical mouth surface of one cone will not match the throat surface of the next. The sound field is therefore matched at a plane surface perpendicular to the horn axis at the point where the two cones join. A simple example of a cone in a sphere is given in the Appendix of [33].

Similar to the one-dimensional horn models, the mode-matching models also require a good model for the radiation impedance. Fortunately, the dependence of the radiation impedance on the shape of the horn, as discussed in [254], is now expressed by coupling between pressure and velocity modes. Now the radiation impedance model can be computed based only on the cross-sectional shape of the horn mouth, and possibly other external influences, like diffraction and reflections.

3.5 SUMMARY

Acoustic modeling of duct-like structures can be roughly divided into three areas: loudspeaker horns, musical instrument horns, and ventilation systems, acoustic filters and similar. These three areas have different requirements: for loudspeaker horns, directivity and to a degree throat impedance are important factors. As horns for loudspeakers are mainly used to control directivity, accurate computation of this quantity is very important. For musical instruments, accurate computation of the resonance frequencies is the main goal. And for the last category, transmission and attenuation characteristics usually take on great importance.

Methods employed for these categories may have many similarities, and many of the methods can be used for all three. Benefits may be had from studying methods originally developed for a different purpose than the problem at hand.

The methods can be divided into three groups: analytical, numerical, and semi-analytical methods.

Analytical methods can give exact solutions, but only for a very small set of geometries. Numerical efficiency of the analytical methods (as numerical values are almost always required in the end) is usually high, although problems may be encountered for some cases where, for instance, a convergent series expansion that is analytically convergent may not converge numerically. Analytical methods (if we disregard the final numerical implementation) do not have frequency limitations, if we disregard low- or high frequency asymptotic methods.

For numerical methods, a discretization (meshing) of the problem must be made, and an approximation to the true solution is computed over the elements. This mesh must be sufficiently fine to sample the wave field accurately. The general rule is to apply at least six elements per wavelength, although for far field calculations using BEM, sufficiently accurate results seem to be obtainable with three elements per wavelength [8]. Creating an optimal mesh is not entirely straightforward [276].

Semi-analytical methods are based on breaking up a problem into elements, or subdomains, that each have analytical solutions. In the case of horns, this can be a series of straight or conical elements. These piecewise analytical solutions are then combined numerically using matching techniques. These methods are more restricted in choice of geometry than fully numerical methods, but more flexible than analytical methods. The numerical efficiency is somewhere between the two.

In this thesis, one of the semi-analytical methods will be used: the discrete segment mode matching method pioneered by Roure and further developed by Kergomard, Pagneux, Amir and others. There are several reasons for the choice of this method.

- The method is relatively easy to implement,
- It is efficient, both in terms of memory usage, and computation time,
- It is easily scalable,
- Discretization of the horn is very simple.
- By describing the sound field in the horn in terms of modes, new insights into the behavior of horns may be found,

In many of the references by Pagneux, Kergomard, Felix and others, a discrete method carried to the limit of infinitesimal step size is used (see for instance [214]), and here the impedance along the horn is expressed in the form of a Riccati differential equation that is integrated numerically. The infinitesimal step size method method has not been used in this thesis mainly due to the somewhat higher implementation complexity, but also since the discrete model makes it easier to experiment with the step size and other parameters. In addition, the extension described in Chapter 11 would not be possible.

In contrast to the Mode Matching Methods, analytical methods are mathematically very complicated, the allowable geometries are very few, and solution of any problem of practical interest would probably require significantly more mathematical training than the author has.

General numerical methods are already developed to a high state of perfection, with many commercial packages available. It does not seem to be much left to do here for someone primarily interested in horns; horns can be simulated, but that is hardly something to write a PhD thesis on. Gaining new insights into horn behavior is also not so easy with purely numerical methods.

Due to the apparent advantages of the MMM, this method was taken as a starting point for the work in this thesis; as the fundamental building block. The main work has then been to extend the applicability of the method to new areas, either by direct extension, or by combination with other methods.

Part II

THE MODE MATCHING METHOD

In this part, the Mode Matching Method is described in detail. Three cross-sectional geometries are covered: circular, annular circular, and rectangular. The method is applied to simulation of horns under three common conditions: mounted in a large (infinite) baffle, radiating into free space, and placed close to reflecting boundaries. Experimental verification of the three cases is presented. In addition, the multimodal radiation impedance seen by horns radiating into rooms is briefly covered.

4

THE MODE MATCHING METHOD

The general idea and historical background of the Mode Matching Method (MMM) was presented in Section 3.4.3. This chapter will give a more detailed overview of the theory of the MMM, and formulations for several possible geometries.

The method described here is the method developed by Roure [37], and later studied and further developed by Kergomard, Amir, Pagneux, Kemp and others. See Section 3.4.3 for a more detailed listing of references.

This chapter is mainly based on the references given in Section 3.4.3. In addition, the work by Evensen [44, 277] has been included, extending the MMM to annular geometries. The new contribution to the method itself, is the slight change of the algorithm to reduce memory requirements, as first presented in [45].

4.1 MODAL DESCRIPTION OF THE SOUND FIELD

A time harmonic factor of $e^{j\omega t}$ is implicitly assumed throughout this thesis.

The wave equation and the Helmholtz equation can be solved in terms of expansions of eigenfunctions. This enables the pressure and velocity in a duct to be expressed as a weighted sum of orthogonal eigenfunctions appropriate for the coordinate system used [267, 278, 279].

Starting with the Helmholtz equation for pressure, we have

$$\Delta p = -k^2 p \tag{56}$$

where $\Delta = \nabla^2$ is the Laplacian operator.

There are now two possible approaches for a modal solution. The first option is to describe the sound field solely by modes, which is appropriate for a closed volume:

$$p(x, y, z) = \sum_{n=0}^{\infty} P_n \psi_n(x, y, z). \tag{57}$$

This approach is not suitable for describing wave propagation. Therefore, for our purpose is more convenient to describe the sound field as a sum of two components; the component in the z-direction, and the component in the (x, y) plane perpendicular to the z-direction:

$$\Delta = \Delta_{\perp} + \frac{\partial^2}{\partial z^2}. \tag{58}$$

We can then solve the Helmholtz equation by separation of variables, by describing the pressure as

$$p(x,y,z) = \sum_{n=0}^{\infty} P_n(z)\psi_n(x,y). \tag{59}$$

Inserting this expression for p into Eq. (56) we get

$$\frac{1}{\psi_n}\Delta_\perp \psi_n + \frac{1}{P_n}\frac{\partial^2 P_n}{\partial z^2} = -k^2. \tag{60}$$

Since each term is a function of a separate variable, each term must be constant, giving

$$\frac{\partial^2}{\partial z^2}P_n(z) = -k_n^2 P_n(z) \tag{61}$$

$$\Delta_\perp \psi_n(x,y) = -\alpha_n^2 \psi_n(x,y), \tag{62}$$

which again are linked through the wavenumber k

$$k^2 = k_n^2 + \alpha_n^2. \tag{63}$$

α_n is the wavenumber in the $x - y$ plane.

Along a uniform pipe of arbitrary, but uniform, cross-section, solution of Eq. (61) gives

$$P_n(z) = A_n e^{-jk_n z} + B_n e^{jk_n z}. \tag{64}$$

Using the relation

$$\rho\frac{\partial v_z}{\partial t} = -\frac{\partial p}{\partial z}, \tag{65}$$

a similar expression can be found for the volume velocity

$$U_n(z) = \frac{k_n S}{k\rho c}\left(A_n e^{-jk_n z} - B_n e^{jk_n z}\right). \tag{66}$$

We also have the relation

$$U_n = Z_{c,n}P_n(z) \tag{67}$$

where Z_c is the characteristic impedance, which for the multimodal case is

$$Z_{c,n} = \frac{k\rho c}{k_n S}. \tag{68}$$

Strictly speaking, only the first (plane wave) term U_0 can rightly be called the volume velocity. However, since the $\vec{U}$ vector can be expressed as $S\vec{v}$, where $\vec{v}$ is a vector of particle velocity mode amplitudes, we will refer to the entire $\vec{U}$ vector as the volume velocity.

Solution of Eq. (62) with the appropriate boundary conditions (for our case, the Neumann (hard wall) boundary condition would be the most appropriate in most cases) gives the mode functions $\psi_n(x, y)$. These can be found analytically for certain geometries (rectangular, circular, annular and elliptic), but may also be found by numerical methods. The α_n values will turn out to be the eigenvalues of the mode functions. Given the eigenvalues, k_n is determined from Eq. (63). When $k < \alpha_n$, k_n will be imaginary, and the mode is said to be in cutoff. The pressure will decay exponentially when propagating away from the source, it is evanescent, and the sign of the root is chosen so that this is the case:

The term 'cut-on' is also often used for the phenomenon happening at the cutoff frequency. A mode is cut-on above this frequency, and in cutoff below it. What term to use depends on what direction along the frequency axis one considers. Moving from a low to a high frequency, the modes "cut on", while moving from a high to a low frequency, the modes "cut off".

$$k_n = \begin{cases} -\sqrt{k^2 - \alpha_n^2} & : \ k < \alpha_n \\ \sqrt{k^2 - \alpha_n^2} & : \ k > \alpha_n \end{cases}. \tag{69}$$

With the expressions given above, any sound field in a uniform duct can be described. If we know the pressure or velocity distribution, we can find the mode amplitudes P_n or U_n as follows:

P_n is found by multiplying both sides of Eq. (59) by ψ_n and integrating over S, giving

$$\int_S p(x, y)\psi_n(x, y)dS = \sum_{m=0}^{\infty} \int_S P_m \psi_m(x, y)\psi_n(x, y)dS = P_n S, \tag{70}$$

where the last equality comes from the orthogonality relation

$$\int_S \psi_n \psi_m dS = S\delta_{nm}. \tag{71}$$

We may notice that the modes are not orthonormal, in which case the integral would be unity, but the formulation used here can often be more convenient [266]. Note that Braden [22] uses orthonormal mode functions.

Rearranging, we get

$$P_n = \frac{1}{S} \int_S p(x, y)\psi_n(x, y)dS. \tag{72}$$

Similarly, we have, for velocity,

$$v_\perp(x, y) = \frac{1}{S} \sum_{m=0}^{\infty} U_m \psi_m(x, y), \tag{73}$$

$$U_m = \int_S v_\perp(x, y)\psi_m(x, y)dS, \tag{74}$$

were $v_\perp$ is the velocity normal to the x, y-plane, and U_m is the modal volume velocity amplitude of mode m.

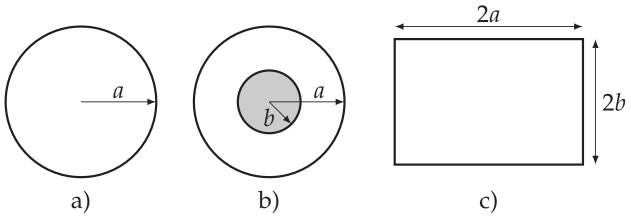

Figure 26: Duct geometries treated in this thesis.

In addition, it is possible to describe pressure mode amplitudes in terms of a matrix of modal acoustic impedances, and the volume velocity mode amplitudes,

$$P_n = \sum_{m=0}^{\infty} Z_{nm} U_m, \tag{75}$$

or, in vector notation,

$$\vec{P} = \mathbb{Z}\vec{U}. \tag{76}$$

How to compute the $\mathbb{Z}$-matrix will be discussed in more detail in connection with radiation impedance in Section 5.2, but in principle each column of the matrix consists of the pressure mode amplitudes due to volume velocity mode U_m, scaled by the amplitude of U_m.

For a field decomposed into modes and a subsequently reconstructed to be identical to the original field, i.e.

$$p(x,y,z) = \sum_{n=0}^{\infty} \psi_n(x,y) \frac{1}{S} \int_S p(x,y,z) \psi_n(x,y) dS \tag{77}$$

the mode functions must be scaled so that the following relation holds:

$$\int_S (\psi_n)^2 \, dS = S. \tag{78}$$

Therefore the mode functions must be normalized, although they do not have to be orthonormal.

4.2 MODE FUNCTIONS

The mode functions depend on the geometry and the boundary conditions. For horns, we usually assume rigid walls, as treating ducts with a general impedance condition at the wall complicates things somewhat. Here follows the mode functions for some useful geometries, Figure 26.

4.2.1 *Cylindrical Geometry*

In cylindrical coordinates, $\Delta_\perp$ in Eq. (58) is

$$\Delta_\perp = \left(\frac{\partial^2}{\partial r^2} + \frac{1}{r}\frac{\partial}{\partial r} + \frac{1}{r^2}\frac{\partial^2}{\partial \theta^2} \right), \tag{79}$$

or, assuming axisymmetry,

$$\Delta_\perp = \left(\frac{\partial^2}{\partial r^2} + \frac{1}{r}\frac{\partial}{\partial r} \right), \tag{80}$$

which gives

$$\left(\frac{\partial^2}{\partial r^2} + \frac{1}{r}\frac{\partial}{\partial r} \right) \psi_n(r) = -\alpha_n^2 \psi_n(r) \tag{81}$$

for Eq. (62). This equation can be turned into Bessel's equation of order zero with some manipulation, the the general solution of which is

$$\psi_n(r) = c_1 J_0\left(\alpha_n r\right) + c_2 Y_0\left(\alpha_n r\right). \tag{82}$$

If the horn has no central member, $c_2 = 0$, since Y_0 is singular at the origin. With the boundary condition

$$\frac{\partial \psi_n}{\partial r} = 0, \qquad r = a, \tag{83}$$

where a is the radius of the duct, Figure 26a, it can be shown that the mode function is

$$\psi_n = \frac{J_0(\mu_n r/a)}{J_0(\mu_n)} \tag{84}$$

where μ_n are the successive zeros of J_1, which is the the derivative of J_0.

The case of non-axisymmetry will not be treated in this thesis, but see [22] for the relevant expressions.

4.2.2 *Annular Geometry*

In the case of a structure with central member of radius b, Figure 26b, we have to retain c_2 in Eq. (82). By again applying the hard wall boundary condition, we get the mode function [280, 281]

$$\psi_n(r) = c_1 \left\{ J_0\left(\varphi_n \frac{r}{b}\right) - \frac{J_1\left(\varphi_n\right)}{Y_1\left(\varphi_n\right)} Y_0\left(\varphi_n \frac{r}{b}\right) \right\} \tag{85}$$

where φ_n are the zeros of the characteristic equation

$$J_0'(\varphi_n) Y_0'\left(\varphi_n \frac{a}{b}\right) - J_0'\left(\varphi_n \frac{a}{b}\right) Y_0'(\varphi_n) = 0, \tag{86}$$

which is slightly easier (and more efficient) to handle in the form

$$J_1(\varphi_n) Y_1\left(\varphi_n \frac{a}{b}\right) - J_1\left(\varphi_n \frac{a}{b}\right) Y_1(\varphi_n) = 0. \tag{87}$$

The zeros of Eq. (87) have to be found numerically, but a useful approximation [282] for the higher order zeros is

$$\varphi_n \approx \beta + \frac{p}{\beta} + \frac{q-p^2}{\beta^3} + \frac{r-4pq+2p^3}{\beta^5} \tag{88}$$

where

$$\begin{aligned}
\beta &= \frac{n\pi}{\lambda-1}, \\
\lambda &= a/b, \\
\\
p &= \frac{3}{8\lambda}, \\
q &= \frac{-63\left(\lambda^3-1\right)}{6(4\lambda)^3(\lambda-1)} \\
r &= \frac{1899\left(\lambda^5-1\right)}{5(4\lambda)^5\left(\lambda-1\right)}.
\end{aligned}$$

This approximation can be used as the basis for a root finding algorithm. It should, however, be noted that for large values of λ the first zeros from the approximation are not usable.

In addition, we need to know the normalization factor $\eta_n = 1/c_1$ so that

$$\begin{aligned}
&\int\limits_S \left(\psi_n\right)^2 dS = \\
&c_1^2 2\pi \int\limits_b^a \left\{ J_0\left(\varphi_n \frac{r}{b}\right) - \frac{J_1\left(\varphi_n\right)}{Y_1\left(\varphi_n\right)} Y_0\left(\varphi_n \frac{r}{b}\right) \right\}^2 r dr \\
&= \pi\left(a^2-b^2\right)
\end{aligned} \tag{89}$$

Performing the integration, using relation 11.4.2 from [282], we get

$$\eta_n^2 = \frac{2}{a^2-b^2}\left[\frac{1}{2} r^2 \left(\psi_n^2\left(\varphi_n \frac{r}{b}\right) + \psi_n'^2\left(\varphi_n \frac{r}{b}\right)\right)\right]_{r=b}^{r=a}$$

which, when written out, becomes

$$\begin{aligned}
\eta_n^2 \;=\; & \frac{1}{\left(a^2-b^2\right) Y_1^2\left(\varphi_n\right)} \\
& \times \left\{ a^2 \left[Y_1^2\left(\varphi_n\right)\left(J_0^2(\zeta) + J_1^2(\zeta)\right) \right.\right. \\
& -2 J_1\left(\varphi_n\right) Y_1\left(\varphi_n\right)\left(J_0(\zeta) Y_0(\zeta) + J_1(\zeta) Y_1(\zeta)\right) \\
& \left.\left. + J_1^2\left(\varphi_n\right)\left(Y_0^2(\zeta) + Y_1^2(\zeta)\right)\right] - \left(\frac{2b}{\pi\varphi_n}\right)^2 \right\}
\end{aligned} \tag{90}$$

where $\zeta = \varphi_n \frac{a}{b}$.

n	(n_x, n_y)	n	(n_x, n_y)
1	(0,0)	9	(2,2)
2	(0,1)	10	(0,3)
3	(1,0)	11	(3,0)
4	(1,1)	12	(1,3)
5	(0,2)	13	(3,1)
6	(2,0)	14	(2,3)
7	(1,2)	15	(3,2)
8	(2,1)	16	(3,3)

Table 2: Mode pairs sorted in increasing order.

For the plane wave mode $\varphi_0 = 0$, which means that we must normalize this mode separately. The result is

$$\eta_0^2 = \frac{2}{a^2 - b^2}\left[\frac{1}{2}u^2\left(J_0^2(u) + J_0'^2(u)\right)\right]_{u=\varphi}^{u=\varphi a/b} = 1$$

as one would expect.

4.2.3 *Rectangular, Quarter Symmetric Geometry*

The results for this case are well known [267]. Since we now have modes it two directions, it is advantageous to separate ψ_n into two parts, one dependent on x, and the other on y:

$$\psi_n = \phi_{n_x}\sigma_{n_y}. \tag{91}$$

Here n is used as a short hand index for n_x, n_y, and the modes are sorted in increasing order, see Table 2.

It would also be possible to sort the modes by cutoff wave number, but as the aspect ratio may change through the horn, the sorting would have to change trough the horn as well.

In a quarter symmetric duct having hard wall boundary conditions, width $2a$ and height $2b$, Figure 26c, the mode functions in Eq. (91), are [279]

$$\phi_{n_x} = \begin{cases} 1 & : n_x = 0 \\ \sqrt{2}\cos\left(\frac{n_x \pi x}{a}\right) & : n_x > 0 \end{cases} \tag{92}$$

$$\sigma_{n_y} = \begin{cases} 1 & : n_y = 0 \\ \sqrt{2}\cos\left(\frac{n_y \pi y}{b}\right) & : n_y > 0. \end{cases} \tag{93}$$

The corresponding eigenvalues are

$$\alpha_n = \sqrt{\left(\frac{n_x \pi}{a}\right)^2 + \left(\frac{n_y \pi}{b}\right)^2} \tag{94}$$

We have here made use of the fact that asymmetric modes are not excited in a symmetrical duct, so that the actual mode functions

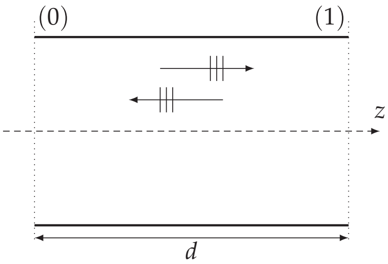

Figure 27: Propagation along a uniform tube.

$\sqrt{2}\cos\left(\frac{n_x \pi x}{2a}\right)$ have been changed to $\sqrt{2}\cos\left(\frac{n_x \pi x}{a}\right)$ by replacing n_x and n_y by $2n_x$ and $2n_y$. This is done in Equations Eq. (92) through Eq. (94).

4.2.4 *Rectangular, Asymmetric Geometry*

If the horn is geometrically symmetric, the source is symmetric, and there is no asymmetry introduced by external factors like asymmetric baffles or reflectors, only symmetric modes propagate in the horn. If asymmetry is introduced, for instance if the horn expands more upwards than downwards, referred to the horn axis, asymmetric modes will be introduced.

For asymmetric ducts extending from a_- to a_+, and from b_- to b_+, the mode functions in Eq. (91) become

$$\phi_{n_x} = \begin{cases} 1 & : n_x = 0 \\ \sqrt{2}\cos\left(\frac{n_x \pi (x - a_-)}{a_+ - a_-}\right) & : n_x > 0 \end{cases} \tag{95}$$

$$\sigma_{n_x} = \begin{cases} 1 & : n_y = 0 \\ \sqrt{2}\cos\left(\frac{n_y \pi (y - b_-)}{b_+ - b_-}\right) & : n_y > 0 \end{cases} \tag{96}$$

The corresponding eigenvalues are

$$\alpha_n = \sqrt{\left(\frac{n_x \pi}{a_+ - a_-}\right)^2 + \left(\frac{n_y \pi}{b_+ - b_-}\right)^2} \tag{97}$$

Note that the mode numbers are not the same as for a symmetric duct; in the symmetric case all odd modes are zero, and can consequently be removed. Therefore n_x and n_y in Eq. (94) will correspond to $2n_x$ and $2n_y$ in Eq. (97).

4.3 PROPAGATION ALONG A UNIFORM DUCT – GENERAL

If we know the pressure and volume velocity at the far end of a duct of length d, Figure 27, the pressure and volume velocity at the near end can be found as

$$P_n^{(0)} = \cos(k_n d) P_n^{(1)} + j \sin(k_n d)\, Z_{c,n} U_n^{(1)} \tag{98}$$

$$U_n^{(0)} = j \sin(k_n d) Z_{c,n}^{-1} P_n^{(1)} + \cos(k_n d)\, U_n^{(1)}. \tag{99}$$

By defining column vectors $\vec{P}$ and $\vec{U}$ containing the modal pressure and volume velocity amplitudes P_n and U_n, respectively, we can rewrite in matrix notation

$$\vec{P}^{(0)} = D_1 \vec{P}^{(1)} + D_2 Z_c \vec{U}^{(1)} \tag{100}$$

$$\vec{U}^{(0)} = D_2 Z_c^{-1} \vec{P}^{(1)} + D_1 \vec{U}^{(1)} \tag{101}$$

where D_1, D_2 and Z_c are diagonal matrices defined as

$$D_1(n,m) = \begin{cases} \cos(k_n d) & : \ n = m \\ 0 & : \ n \neq m \end{cases} \tag{102}$$

$$D_2(n,m) = \begin{cases} j \sin(k_n d) & : \ n = m \\ 0 & : \ n \neq m \end{cases} \tag{103}$$

$$Z_c(n,m) = \begin{cases} k\rho c / k_n S & : \ n = m \\ 0 & : \ n \neq m \end{cases} \tag{104}$$

If the impedance at end (1) of the tube is known, the input impedance at end (0) can be calculated as

$$\mathbb{Z}^{(0)} = (jD_3)^{-1} Z_c - D_2^{-1} Z_c \left(\mathbb{Z}^{(1)} + (jD_3)^{-1} Z_c \right)^{-1} D_2^{-1} Z_c \tag{105}$$

where

$$D_3(n,m) = \begin{cases} \tan(k_n d) & : \ n = m \\ 0 & : \ n \neq m \end{cases} \tag{106}$$

Subsequently, the modal volume velocity at end (1) can be calculated as

$$\vec{U}^{(1)} = \left(-D_2 Z_c^{-1} \left(\mathbb{Z}^{(0)} - Z_c \right) + E \right) \vec{U}^{(0)} \tag{107}$$

where the extra diagonal matrix is:

$$E(n,m) = \begin{cases} e^{-jk_n d} & : \ n = m \\ 0 & : \ n \neq m \end{cases} \tag{108}$$

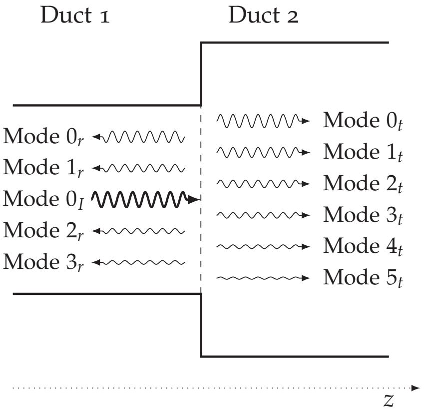

Figure 28: Multimodal reflection at a discontinuity. The incident plane wave (Mode 0_I) creates transmitted modes in duct 2 (subscript t) as well as reflected modes (subscript r).

These are the general equations for multimodal propagation along a uniform duct, and are independent of the mode functions. In passing, it should be noted that Eq. (107) is a matrix-vector multiplication, a fact we will later use to our advantage in reducing the memory requirement of the MMM over that of previous implementations.

4.4 PROPAGATION ACROSS A DISCONTINUITY – GENERAL

At a discontinuity in a duct, the sound field will be disturbed, and additional modes must be used to describe this disturbance. At the discontinuity there is an edge that will produce diffraction; the edge can be viewed as a source of the diffracted waves, and this source is driven by the incident waves. The diffracted waves will propagate in all directions (with a certain directivity [49]), both into the space after the discontinuity, but also in the reverse direction of the incident wave. The diffracted wave thus alters the field at both sides of the discontinuity, and both fields will thus contain a sum of modes, even if only a single mode was incident. We therefore have both reflected modes and transmitted modes, Figure 28. In order to take this into account in the MMM, we need a description of what happens at the discontinuity.

Refer to Figure 29. Denoting the pressure at surface 1 $p^{(1)}$ and the pressure at surface 2 $p^{(2)}$, if If $S_1 < S_2$, we must have that

$$p^{(1)} = p^{(2)} \text{ on } S_1,\ S_1 \leq S_2. \tag{109}$$

If $S_1 > S_2$, the pressure is matched over S_2.

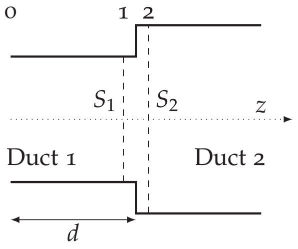

Figure 29: Two ducts joined by a discontinuity.

The modes are orthogonal, so that

$$\int_S \psi_n \psi_m dS = S\delta_{nm}, \tag{110}$$

where ψ_n is the eigenfunction of mode n. Multiplying the pressure field p with the nth eigenfunction and integrating of the area will extract the nth mode component from the field. Since pressure may be also expressed as a sum of modes, we can write

$$\int_S \psi_n p dS = \int_S \psi_n \sum_{m=0}^{\infty} \psi_m P_m dS, \tag{111}$$

where P_m is the amplitude of the mth pressure mode. In the following, $P_n^{(1)}$ and $P_m^{(2)}$ will be the complex mode amplitudes at surfaces 1 and 2, respectively, and $\psi_n^{(1)}$ and $\psi_m^{(2)}$ will be the corresponding mode profiles on these surfaces.

Combining (109) and (111), we get

$$\begin{aligned} P_n^{(1)} = \frac{1}{S_1} \int_{S_1} \psi_n^{(1)} p^{(1)} dS &= \frac{1}{S_1} \int_{S_1} \psi_n^{(1)} p^{(2)} dS \\ &= \frac{1}{S_1} \int_{S_1} \psi_n^{(1)} \sum_{m=0}^{\infty} \psi_m^{(2)} P_m^{(2)} dS, \end{aligned} \tag{112}$$

which we can write as

$$P_n^{(1)} = \sum_{m=0}^{\infty} F_{nm} P_m^{(2)} \tag{113}$$

where

$$F_{nm} = \frac{1}{S_1} \int_{S_1} \psi_n^{(1)} \psi_m^{(2)} dS. \tag{114}$$

In matrix notation:

$$\vec{P}^{(1)} = F\vec{P}^{(2)}. \tag{115}$$

Because of continuity, the velocities on the surfaces S_1 and S_2 must match as well. It is also clear that the velocity into the part of S_2 that is larger than S_1, denoted $S_2 - S_1$, must be zero for a hard-walled duct with no wall vibration. For the case where the velocity on $S_2 - S_1 \neq 0$, see Chapter 11 on page 227.

$$v_z^{(1)} = v_z^{(2)} \text{ on } S_1,\ S_1 < S_2 \tag{116}$$

$$v_z^{(2)} = 0 \text{ on } S_2 - S_1,\ S_1 < S_2. \tag{117}$$

In terms of volume velocities, we have that $U^{(1)}/S_1 = U^{(2)}/S_2$, and $U^{(2)} = 0$ on $S_2 - S_1$. Again using the orthogonality of the modes, we can set up the following:

$$\begin{aligned} U_n^{(2)} = \int\limits_{S_2} \psi_n^{(2)} v_z^{(2)} dS = \int\limits_{S_1} \psi_n^{(2)} v_z^{(1)} dS + \int\limits_{S_2 - S_1} \psi_n^{(2)} 0 dS \\ = \frac{1}{S_1} \int\limits_{S_1} \psi_n^{(2)} \sum_{m=0}^{\infty} \psi_m^{(1)} U_m^{(1)} dS, \end{aligned} \tag{118}$$

which we can write as

$$U_n^{(2)} = \sum_{m=0}^{\infty} F_{mn} U_m^{(1)}. \tag{119}$$

In matrix notation:

$$\vec{U}^{(2)} = F^T \vec{U}^{(1)}. \tag{120}$$

If $S_1 > S_2$, the relations are

$$\vec{P}^{(2)} = V \vec{P}^{(1)} \tag{121}$$

and

$$\vec{U}^{(1)} = V^T \vec{U}^{(2)}, \tag{122}$$

where the elements of the matrix V are defined as

$$V_{nm} = \frac{1}{S_2} \int\limits_{S_2} \psi_n^{(2)} \psi_m^{(1)} dS. \tag{123}$$

The V-matrix is thus computed in the same way as the F-matrix, even using the same functions, but with the (1) and (2) indices swapped.

Pressure and volume velocity are related through the modal impedances, Eq. (75). This relation, together with Eq. (115) and Eq. (120), or Eq. (121) and Eq. (122), can be used to express how the modal impedances are coupled across the discontinuities:

$$\mathbb{Z}^{(1)} = F \mathbb{Z}^{(2)} F^T,\ S_1 < S_2 \tag{124}$$

$$\mathbb{Z}^{(1)} = V^{-1} \mathbb{Z}^{(2)} (V^T)^{-1},\ S_1 > S_2. \tag{125}$$

There may be numerical problems involved in inverting the V-matrix, as it may be close to singular. The larger the discontinuity, and the higher the number of modes, the more problematic is this problem. Roure [283], Amir and Starobinski [266] and Pagneux et at. [214] suggests using using the admittance matrix $\mathbb{Y}$ instead of $\mathbb{Z}$, where $\mathbb{Y}$ is defined by

$$\vec{U} = \mathbb{Y}\vec{P},$$

and

$$\mathbb{Y} = \mathbb{Z}^{-1}.$$

Then the V-matrix can be used directly, without inversion, to find the admittance at (1) from the admittance at (2) as[1]

$$\mathbb{Y}^{(1)} = V^T\mathbb{Y}^{(2)}V,\ S_1 > S_2. \tag{126}$$

If the mode functions have been be found numerically, a challenge is to find the F-matrix. In the case of analytically derived modes, the F-matrix can usually be found analytically.

The next section will detail how to compute the F and V matrices and their combinations for the geometries treated in this thesis.

4.5 *F*-MATRICES

In this section, the expressions for the F-matrices for geometries treated above, are given. The matrices are frequency independent, and will only need to be computed once for a given horn.

4.5.1 *Cylindrical Geometry*

For axisymmetric polar coordinates, (114) can be written as[2]

$$F_{nm} = \frac{1}{\pi R_1^2}\int\limits_0^{a_1}\int\limits_0^{2\pi} \psi_n^{(1)}\psi_m^{(2)} r d\theta dr \tag{127}$$

Inserting the mode functions,

$$\psi_n = \frac{J_0(\mu_n r/a)}{J_0(\mu_n)} \tag{128}$$

and integrating with respect to θ, we get [267]

$$F_{nm} = \frac{2}{a_1^2 J_0(\mu_n)J_0(\mu_m)}\int\limits_0^{a_1} rJ_0(\mu_n r/a_1)J_0(\mu_m r/a_2)dr, \tag{129}$$

---

[1] Another possible approach would be check the condition number of the V-matrix, and then partition the discontinuity into several smaller discontinuities that each had an invertible V-matrix. The inverted V-matrices are then multiplied together.

[2] This derivation is taken from Kemp [267].

which is a standard integral of the form

$$\int xJ_p(\alpha x)J_p(\beta x) = \frac{\beta x J_p(\alpha x)J_{p-1}(\beta x) - \alpha x J_{p-1}(\alpha x)J_p(\beta x)}{\alpha^2 - \beta^2}. \tag{130}$$

With some variable substitution, we arrive at

$$F_{nm} = \left(\frac{2}{a_1^2 J_0(\mu_n)J_0(\mu_m)}\right) \times \left[\frac{(\mu_m r/a_2)J_0(\mu_n r/a_1)J_{-1}(\mu_m r/a_2) - (\mu_n r/a_1)J_{-1}(\mu_n r/a_1)J_0(\mu_m r/a_2)}{(\mu_n r/a_1)^2 - (\mu_m r/a_2)^2}\right]_{r=0}^{r=R_1} \tag{131}$$

The contribution from $r = 0$ is zero, and $J_{-1}(x) = -J_1(x)$. Since μ_n is a zero of J_1, some terms vanish. This gives us

$$F_{nm} = \left(\frac{2}{a_1^2 J_0(\mu_n)J_0(\mu_m)}\right)\frac{(\mu_m a_1/a_2)J_0(\mu_n)J_1(\mu_m a_1/a_2)}{(\mu_n/a_2)^2 - (\mu_m/a_1)^2} \tag{132}$$

If we now set $\beta = a_1/a_2$, we get

$$F_{nm}(\beta) = \frac{2\beta\mu_m J_1(\beta\mu_m)}{(\beta^2\mu_m^2 - \mu_n^2)\,J_0(\mu_m)} \tag{133}$$

and

$$V_{nm}(\beta) = F_{nm}(1/\beta). \tag{134}$$

4.5.2 *Annular Cylindrical Geometry*

For the annular geometry, there are two types of discontinuity to be considered. The first type of discontinuity for which we need to find the F-matrix, is the annular-to-annular type, shown in Figure 30a. From the definition in Eq. (114), we must solve the integral

$$\begin{aligned} F_{nm} &= \frac{2\pi}{S_1\eta_n^{(1)}\eta_m^{(2)}}\int_{b_1}^{a_1}\left\{J_0\left(\varphi_n\frac{r}{b_1}\right) - \frac{J_1(\varphi_n)}{Y_1(\varphi_n)}Y_0\left(\varphi_n\frac{r}{b_1}\right)\right\} \\ &\quad \times\left\{J_0\left(\varphi_m\frac{r}{b_2}\right) - \frac{J_1(\varphi_m)}{Y_1(\varphi_m)}Y_0\left(\varphi_m\frac{r}{b_2}\right)\right\}rdr \end{aligned} \tag{135}$$

which can be expressed as a sum of four integrals, and results in [44]

$$\begin{aligned} F_{nm} &= \frac{2\pi}{S_1\eta_n^{(1)}\eta_m^{(2)}}\left\{[I_1(r)]_{r=b_1}^{r=a_1} - \frac{J_1(\varphi_m)}{Y_1(\varphi_m)}[I_2(r)]_{r=b_1}^{r=a_1}\right. \\ &\quad \left. - \frac{J_1(\varphi_n)}{Y_1(\varphi_n)}[I_3(r)]_{r=b_1}^{r=a_1} + \frac{J_1(\varphi_m)J_1(\varphi_n)}{Y_1(\varphi_m)Y_1(\varphi_n)}[I_4(r)]_{r=b_1}^{r=a_1}\right\} \end{aligned} \tag{136}$$

with the functions

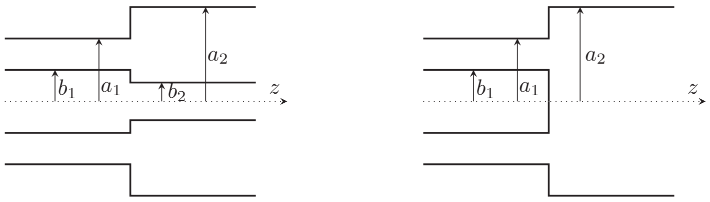

(a) (b)

Figure 30: The two types of discontinuities

$$I_1(r) = r\frac{\alpha_n J_1(\alpha_n r) J_0(\alpha_m r) - \alpha_m J_0(\alpha_n r) J_1(\alpha_m r)}{\alpha_n^2 - \alpha_m^2}$$

$$I_2(r) = r\frac{\alpha_n J_1(\alpha_n r) Y_0(\alpha_m r) - \alpha_m J_0(\alpha_n r) Y_1(\alpha_m r)}{\alpha_n^2 - \alpha_m^2}$$

$$I_3(r) = r\frac{\alpha_m J_1(\alpha_m r) Y_0(\alpha_n r) - \alpha_n J_0(\alpha_m r) Y_1(\alpha_n r)}{\alpha_m^2 - \alpha_n^2}$$

$$I_4(r) = r\frac{\alpha_n Y_1(\alpha_n r) Y_0(\alpha_m r) - \alpha_m Y_0(\alpha_n r) Y_1(\alpha_m r)}{\alpha_n^2 - \alpha_m^2}$$

where $\alpha_m = \varphi_m / b_1$, $\alpha_n = \varphi_n / b_1$, and η_n is defined in Eq. (90). Eq. (136) is valid for $m \neq 0$ and $n \neq 0$. If $m = n = 0$, the integral reduces to an integral over r, and $F_{00} = 1$. The case where either m or n are zero must be treated separately, because in this case, $\varphi_0 = 0$, and $Y_0(0)$ is singular. It can be shown that

$$\lim_{\varphi_n \to 0} \psi_n(r) = J_0\left(\varphi_n \frac{r}{b}\right).$$

This results in following expressions:

$$\begin{aligned} F_{n0} &= \frac{2\pi}{S_1 \eta_n^{(1)}} \frac{a_1 b_1}{\varphi_n Y_1(\varphi_n)} \\ &\quad \times \left(J_1(\alpha_n a_1) Y_1(\varphi_n) - J_1(\varphi_n) Y_1(\alpha_n a_1)\right), \end{aligned} \tag{137}$$

$$\begin{aligned} F_{0m} &= \frac{2\pi}{S_1 \eta_m^{(2)}} \frac{b_2}{\varphi_m Y_1(\varphi_m)} \\ &\quad \times \left\{Y_1(\varphi_m)\left(a_1 J_1(\alpha_m a_1) - b_1 J_1(\alpha_m b_1)\right)\right. \\ &\quad \left. - J_1(\varphi_m)\left(a_1 Y_1(\alpha_m a_1) - b_1 Y_1(\alpha_m b_1)\right)\right\}. \end{aligned} \tag{138}$$

For an annular-to-circular transition, shown in Figure 30b, the integral is

$$\begin{aligned} F_{nm} &= \frac{2\pi}{S_1 \eta_n^{(1)} J_0(\mu_m)} \\ &\quad \times \int_{b_1}^{a_1} \left[\left\{ J_0\left(\varphi_n \frac{r}{b_1}\right) - \frac{J_1\left(\varphi_n\right)}{Y_1\left(\varphi_n\right)} Y_0\left(\varphi_n \frac{r}{b_1}\right) \right\} \right. \\ &\quad \left. \times\ J_0\left(\mu_m \frac{r}{a_2}\right) \right] r dr \\ &= \frac{2\pi}{S_1 \eta_n^{(1)} J_0(\mu_m) \left\{\alpha_n^2 - \beta_m^2\right\}} \\ &\quad \times \left\{ \left[I_5(r)\right]_{r=b_1}^{r=a_1} - \frac{J_1\left(\varphi_n\right)}{Y_1\left(\varphi_n\right)} \left[I_6(r)\right]_{r=b_1}^{r=a_1} \right\} \end{aligned} \tag{139}$$

with

$$I_5(r) = r\left\{\alpha_n J_1\left(\alpha_n r\right) J_0\left(\beta_m r\right) - \beta_m J_0\left(\alpha_n r\right) J_1\left(\beta_m r\right)\right\}$$

$$I_6(r) = r\left\{\alpha_n Y_1\left(\alpha_n r\right) J_0\left(\beta_m r\right) - \beta_m Y_0\left(\alpha_n r\right) J_1\left(\beta_m r\right)\right\}$$

where $\beta_m = \mu_m / a_2$. Again we need to treat the case $n = 0$ separately:

$$F_{0m} = \frac{2\pi}{S_1 J_0(\mu_m) \beta_m} \left(a_1 J_1\left(\beta_m a_1\right) - b_1 J_1\left(\beta_m b_1\right)\right) \tag{140}$$

As before, the V-matrices are computed the same way as the F-matrices, but with arguments changed so that a_1 is used instead of a_2 and so on.

As can be seen, the mode functions and F-matrices are significantly more complex for the annular case than for the ordinary circular geometry. The computational load is, however, not materially increased, and although the $F-$matrices and the roots of Eq. (87) have to be found for each combination of a and b, this only has to be done once for the entire structure, as both are frequency independent. In the programming of the method, the only change from the ordinary circular geometry case, is calling different subroutines a few places.

4.5.3 *Rectangular, Quarter Symmetric Geometry*

The general geometry for a rectangular duct is illustrated in Figure 29 and Figure 31. For two symmetric ducts, $a_- = -a$, $a_+ = a$, $b_- = -b$ and $b_+ = b$.

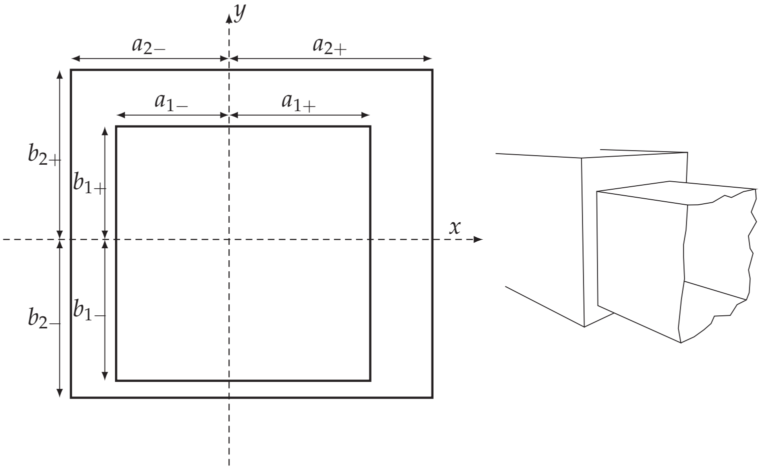

Figure 31: General discontinuity between two rectangular ducts.

For a rectangular duct, it is most convenient to express Eq. (114) as an *element-wise* multiplication of two matrices:

$$\begin{aligned} F_{nm}(\beta_x, \beta_y) &= \frac{1}{S_1} \int\limits_{S_1} \psi_n^{(1)} \psi_m^{(2)} dS \\ &= \frac{1}{2a_1} \int\limits_{-a_1}^{a_1} \phi_{n_x}^{(1)} \phi_{m_x}^{(2)} dx \frac{1}{2b_1} \int\limits_{-b_1}^{b_1} \sigma_{n_y}^{(1)} \sigma_{m_y}^{(2)} dy \\ &= X_{n_x m_x} Y_{n_y m_y} \end{aligned} \tag{141}$$

where $\beta_x = a_1/a_2$ and $\beta_y = b_1/b_2$, and

$$X_{n_x m_x} = \begin{cases} 1 & : \quad n_x = m_x = 0, \\ \sqrt{2}\text{sinc}\left(m_x \pi \beta_x\right) & : \quad n_x = 0,\ m_x > 0, \\ 2\text{sinc}\left(\pi(m_x\beta_x - n_x)\right) \frac{m_x\beta_x}{m_x\beta_x + n_x} & : \quad n_x > 0 \end{cases} \tag{142}$$

$$Y_{n_y m_y} = \begin{cases} 1 & : \quad n_y = m_y = 0, \\ \sqrt{2}\text{sinc}\left(m_y \pi \beta_y\right) & : \quad n_y = 0,\ m_y > 0, \\ 2\text{sinc}\left(\pi(m_y\beta_y - n_y)\right) \frac{m_y\beta_y}{m_y\beta_y + n_y} & : \quad n_y > 0 \end{cases} \tag{143}$$

The V matrix then becomes

$$V_{nm} = F_{nm}(1/\beta_x,\ 1/\beta_y) \tag{144}$$

4.5.4 *Rectangular, Asymmetric Geometry*

The geometry is illustrated in Figure 31. It is again most convenient to express the F matrix as an element-wise product of two terms:

$$\begin{aligned}
F_{nm} &= \frac{1}{S_1}\int\limits_{S_1} \psi_n^{(1)}\psi_m^{(2)} dS \\
&= \frac{1}{a_{1+}-a_{1-}}\int\limits_{a_{1-}}^{a_{1+}} \phi_{n_x}^{(1)}\phi_{m_x}^{(2)} dx \frac{1}{b_{1+}-b_{1-}}\int\limits_{b_{1-}}^{b_{1+}} \sigma_{n_y}^{(1)}\sigma_{m_y}^{(2)} dy \\
&= X_{n_x m_x} Y_{n_y m_y}
\end{aligned} \tag{145}$$

where $X_{n_x m_x}$ and $Y_{n_x m_x}$ now are

$$X_{n_x m_x} = \begin{cases}
1 & : \; n_x = m_x = 0, \\
\sqrt{2}\mathrm{sinc}\left(\frac{m_x\pi}{2}\beta_{x,t}\right)\cos\left(\frac{m_x\pi}{2}\beta_{x,a}\right) & : \; n_x = 0,\, m_x > 0, \\
\quad \mathrm{sinc}\left(\frac{\pi}{2}\left(n_x - m_x\beta_{x,t}\right)\right)\cos\left(\frac{\pi}{2}\left(n_x - m_x\beta_{x,a}\right)\right) & \\
\quad +\mathrm{sinc}\left(\frac{\pi}{2}\left(n_x + m_x\beta_{x,t}\right)\right)\cos\left(\frac{\pi}{2}\left(n_x + m_x\beta_{x,a}\right)\right) & : \; n_x > 0
\end{cases} \tag{146}$$

$$Y_{n_y m_y} = \begin{cases}
1 & : \; n_y = m_y = 0, \\
\sqrt{2}\mathrm{sinc}\left(\frac{m_y\pi}{2}\beta_{y,t}\right)\cos\left(\frac{m_y\pi}{2}\beta_{y,a}\right) & : \; n_y = 0,\, m_y > 0, \\
\quad \mathrm{sinc}\left(\frac{\pi}{2}\left(n_y - m_y\beta_{y,t}\right)\right)\cos\left(\frac{\pi}{2}\left(n_y - m_y\beta_{y,a}\right)\right) & \\
\quad +\mathrm{sinc}\left(\frac{\pi}{2}\left(n_y + m_y\beta_{y,t}\right)\right)\cos\left(\frac{\pi}{2}\left(n_y + m_y\beta_{y,a}\right)\right) & : \; n_y > 0
\end{cases} \tag{147}$$

Here the ratio

$$\beta_{x,t} = \frac{a_{1+} - a_{1-}}{a_{2+} - a_{2-}} \tag{148}$$

describes the symmetrical part of the field at the junction, and corresponds to β_x in the symmetrical case.

$$\beta_{x,a} = \frac{a_{1+} + a_{1-} - 2a_{2-}}{a_{2+} - a_{2-}} \tag{149}$$

describes the asymmetry. The V-matrix is again $V_{nm} = F_{nm}(1/\beta_x, 1/\beta_y)$.

4.5.5 *Complex Discontinuities*

In certain cases it may be difficult to describe the discontinuity analytically. An example is rectangular horns where the profile expands in one direction and contracts in the other, Figure 32. This can be solved in an elegant way if one is prepared to compute two matrices instead of one. Since the F matrices are computed only once for each horn

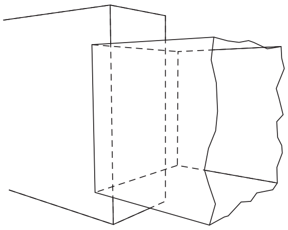

Figure 32: Discontinuity with both expansion and contraction.

profile, the extra computational cost is small. The idea is to split the discontinuity into two or more successive discontinuities, each with its own F-matrix. The F-matrices are then multiplied together at the end to describe the actual discontinuity.

Another reason for doing it this way, is convenience. For discontinuities in annular ducts, there are 8 possible combinations of expanding and contracting inner and outer radii, but all can be created from combinations of four different F-matrices.

The following example focus on rectangular horns, but the principle is the same in every case. In this example, the discontinuity is split in two, where first discontinuity expands in only one direction, with no change in the other, and the second contracts in the other direction, with no change in the first. See Figure 33. For instance, $\beta_x < 1$, $\beta_y = 1$ for the first, and $\beta_x = 1$, $\beta_y > 1$ for the second.

For velocity propagation across these two discontinuities, which we will call a and b, we have that

$$\vec{U}^{(2)} = F_a^T \vec{U}^{(1)} \tag{150}$$

$$\vec{U}^{(3)} = F_b^T \vec{U}^{(2)} \tag{151}$$

so that

$$\vec{U}^{(3)} = F_b^T F_a^T \vec{U}^{(1)}. \tag{152}$$

Since $(AB)^T = B^T A^T$, we can form a composite matrix $F_C = F_a F_b$ that replaces the two F matrices. Actually, one of the matrices will be a V matrix, since there is a contraction in one plane. If this is the second matrix, $F_C = F_a V_b^{-1}$. However, this introduces the same issues with inversion of the V-matrix as discussed in 4.4.

That this also works for impedances, can be seen from the following:

$$\mathbb{Z}^{(1)} = F_a \mathbb{Z}^{(2)} F_a^T \tag{153}$$

$$\mathbb{Z}^{(2)} = F_b \mathbb{Z}^{(3)} F_b^T \tag{154}$$

$$\mathbb{Z}^{(1)} = F_a F_b \mathbb{Z}^{(3)} F_b^T F_a^T \tag{155}$$

where we again can form the composite matrix $F_C = F_a F_b$.

The case of a skewed duct where, for instance, $a_{1+} < a_{2+}$ while at the same time $a_{1-} < a_{2-}$, can also be solved using this technique, by splitting the discontinuity into more than two successive ones.

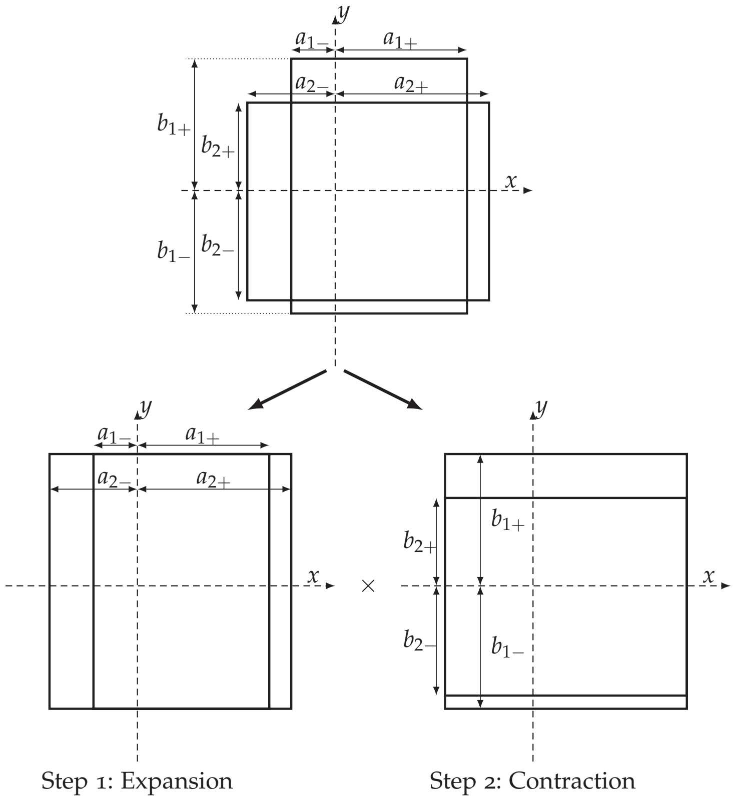

Figure 33: Partitioning of a discontinuity.

4.6 SUMMARY OF THE METHOD

The radiation impedance at the mouth end of the horn needs to be known in order to specify the boundary conditions at this end of the horn [214].

Together with Eq. (120), Eq. (107) can be used to calculate the volume velocity mode amplitudes at the mouth of the horn, given the volume velocity amplitudes at the throat.

The traditional method to do this is outlined in [267], and is summarized as follows:

1. Calculate the impedance matrices at all points in the horn, starting from the mouth, using equations (124) or (125), and (105).
2. Excite the throat end with a given vector of volume velocity amplitudes, and propagate it to the mouth using equations (107), and (120) or (122), and the impedance matrices from step 1.

This procedure requires storage of a large number of impedance matrices per frequency, one for each end of each duct element, which can be prohibitive if many modes and many duct elements are used. In addition, step 2 above must be repeated for each new throat velocity distribution. As the method has previously primarily been used for impedance calculations, this drawback may not have been of any great concern. For loudspeaker simulations, however, one often need to change other parameters while the horn is kept constant.

However, inspection of equations (122) and (107) shows that both are matrix-vector multiplications. Therefore, a single matrix for the entire horn, relating mouth volume velocity to throat volume velocity, can be found by multiplying together the matrices from these equations. What is more, this matrix can be built up from either end of the horn. The result is that the volume velocity transfer matrix can be built up simultaneously with the impedance matrix, from the mouth through to the throat, without storing the impedance values through the horn. This will result in a significant saving of computer memory. The fact that the diagonal matrices D_2 and Z_c only have to be calculated once per frequency and position will also reduce the computation time slightly. The revised procedure will then be:

1. Start with mouth impedance $\mathbb{Z}^{(N)} = \mathbb{Z}_{end}$ (which could be the radiation impedance) and volume velocity transfer matrix $\mathbb{U}^{(N,N)} = I$, the identity matrix.

2. For a straight duct element between positions $n-1$ and n, calculate $\mathbb{Z}^{(n-1)}$ from Eq. (61) and $Z^{(n)}$.

3. Calculate
$$\mathbb{M}^{(n-1,n)} = \left(-D_2 Z_c^{-1}\left(\mathbb{Z}^{(n-1)} - Z_c\right) + E\right)$$
and
$$\mathbb{U}^{(n-1,N)} = \mathbb{U}^{(n,N)} \times \mathbb{M}^{(n-1,n)}.$$

4. For a discontinuity between positions $m-1$ and m, calculate $\mathbb{Z}^{(m-1)}$ from Eq. (124) or (125), and $\mathbb{Z}^{(m)}$.

5. Calculate
$$\mathbb{U}^{(m-1,N)} = \mathbb{U}^{(m,N)} \times F^{T(m-1,m)}$$
from Eq. (120) or (122), and $\mathbb{Z}^{(m)}$.

The results from these operations are a throat impedance matrix $\mathbb{Z}^{(0)}$ and a volume velocity transfer matrix $\mathbb{U}^{(0,N)}$, that can be used to evaluate the performance of the horn.

In the case where the sound field inside the horn is to be computed, the traditional method must be used.

4.7 PRACTICAL NOTES

There are a few practical issues to keep in mind when implementing and using the MMM. A common question is the number of modes required, and this factor is addressed in the next section. A discussion of the number of modes in terms of accuracy of the far field pressure can also be found in Section 5.1.5. The issue of element length is addressed in Section 4.7.2.

A more hidden potential problem is what happens if the calculation frequency coincides with the cutoff frequency of one mode in one of the elements. In this case, $k_n = 0$, as can be seen from Eq. (63), and from Eq. (68), this results in a characteristic impedance Z_c that is infinite for that particular mode.

4.7.1 *Convergence: Number of Modes*

An interesting question for the practical use of the MMM is the number of modes required for a given accuracy. Kergomard and Garcia investigated the convergence for a single discontinuity [284]. Some tests on entire horns have been previously been performed by the author [285]. In these tests, average and maximum error over a frequency range as a function of the number of modes was computed for several types of horns. The results do not, unfortunately, give concrete guidelines for choosing the number of modes to use in a certain case.

In order to arrive at a better estimate of how many modes to use, tests were run to look at the error as a function of the ratio of the cutoff frequency of the highest mode used in the simulation, to the calculation frequency. This way, the curves also apply to rectangular horns, where the modes are not equally spaced, which they approximately are in an axisymmetric horn. In the following, the cutoff frequencies of the modes will be referred to the mouth radius, so that the cutoff wavenumber of mode n is $k_{c,n} = \mu_n / a_m$. In the narrower parts of the horn, the cutoff frequencies will be higher.

A conical horn, an exponential horn, and a tractrix horn, all having a length of 50 cm, and throat and mouth areas of $10\ \text{cm}^2$ and $1250\ \text{cm}^2$, respectively, were used. The horns were axisymmetric and mounted in an infinite baffle. 1000 elements per wavelength were used in all horns, for all frequencies. The reference was simulation results using 192 modes. A series of simulations were run at a few selected frequencies, some well below the first cut-on frequency of the lowest mode, and some right above the cut-on frequencies of the first few modes, varying the number of modes. The result is a family of curves, one for each calculation frequency, that show how the error decreases as the number of modes is increased.

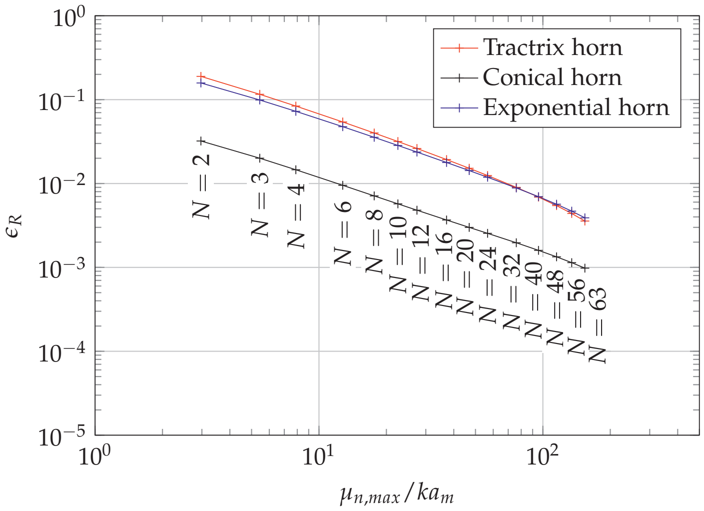

Figure 34: Relative error in mouth plane wave volume velocity amplitude as a function of the ratio of the cutoff frequency of the highest mode used to the frequency used in the calculations. Single frequency, $ka_m = 1.29$.

The results are plotted as $k_{c,max}/k = \mu_{n,max}/ka_m$. A single curve, with N, the total number of modes used in the simulation (including the plane wave mode) indicated along the line, is shown in Figure 34. This curve requires a few comments. First of all, the curve shows how the error for a single frequency decreases as the number of modes increases. The discrepancy between the curves for the conical horn and for the exponential and tractrix horns requires a comment. As can be seen from the curves in Appendix A, the first resonance frequency of the horns differ between the plane wave approximation and the MMM simulations. The frequency in Figure 34 is close to the first resonance peak for the exponential and tractrix horns, and the error is in this case greater due to slight shifts in the location of the peak. The conical horn is large enough to not have a clear peak near this frequency.

Plotting the similar curves for different frequencies, a clear trend emerges, see Figure 35. The curves group into two categories, where the curves for frequencies where all modes are in cutoff everywhere in the horn behave differently from the curves for frequencies where one or more propagating mode exist. For the last case, the curves are practically overlapping, and the slope of error vs. $\mu_{n,max}/ka_m$ is -1. When all modes are in cutoff, the slope appears to be the same, but with an additional factor that causes an offset that is dependent on the frequency. From the curves, it appears that to achieve an error of less than 1%, the cutoff of the highest mode used must be 10-20 times

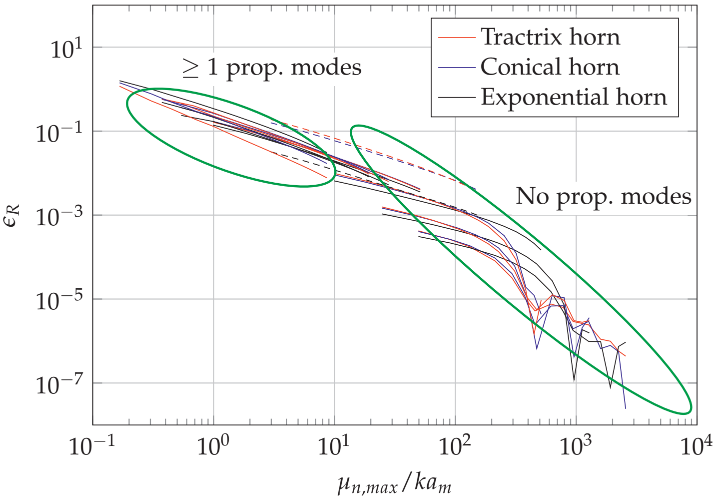

Figure 35: Relative error in mouth plane wave volume velocity amplitude as a function of the ratio of the cutoff frequency of the highest mode used to the frequency used in the calculations. Note that each triplet of curves is for a single frequency, see previous figure, which shows the dashed curves in detail.

the calculation frequency. An exception is around the first resonance peak of the horn, as commented above.

The results differ slightly between the three horn types: for the conical horn more modes will be cut-on in a larger part of the horn, while for the exponential and tractrix horns, fewer modes are cut-on close to the throat.

4.7.2 *Convergence: Element Length*

The number of elements per wavelength required for a given accuracy was investigated by simulating the conical horn used above for a certain number of elements per wavelength, compared to a reference simulation using 1000 elements per wavelength. All simulations were run using 64 modes. The resulting relative error in mouth plane wave volume velocity is shown in Figure 36. Δz is the length of each element. Convergence is rather slow; the slope of the curves is approximately -1, corresponding to $\mathcal{O}(n)$. While this may seem a bit depressing, it should be remembered that a in terms of error, 1 dB equals 12%, and 0.5 dB 6%. 0.5 dB error in the plane wave mouth volume velocity requires about 40 elements per wavelength, and for a 50 cm long horn operating at 5 kHz, this corresponds to about 2900 elements. The requirement is relaxed as frequency is lowered.

The very high errors for long elements for the lowest frequencies in Figure 36 comes from numerical problems that occurs for evanescent

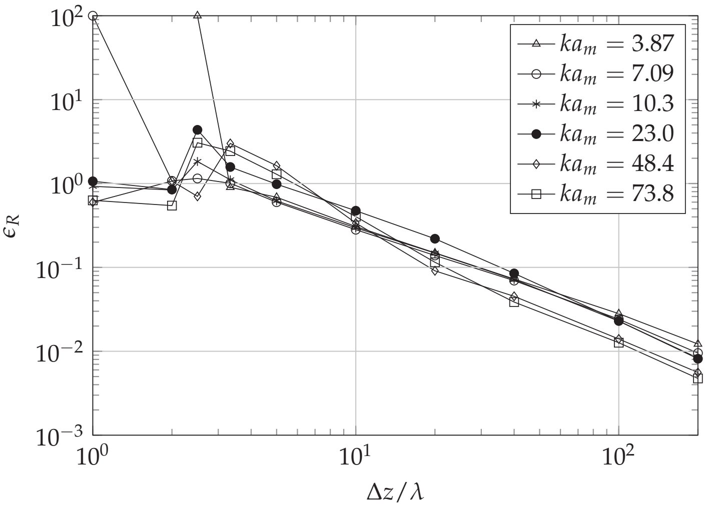

Figure 36: Relative error in mouth plane wave volume velocity amplitude as a function of the number of elements per wavelength. 64 modes were used in the simulations.

modes if an element is to long. There is no problem in computing the projected impedance matrix, using Eq. (105), the error comes from the propagation of the volume velocity down the horn using Eq. (107). As the wavenumber for an evanescent mode is imaginary, the complex exponentials become real, and this will produce very large or very small values in the matrix E, causing underflow or overflow. An absolute minimum length for an element is therefore set by making sure that

$$e^{-jk_n\Delta z}$$

is a representable number for the highest mode in the element with the smallest dimensions. This is because the cutoff frequency of the modes depend on the transversal size of the element, and high order modes are more likely to cause trouble in elements of small cross section.

As the throat impedance approaches $\rho_0 c$ at high frequencies, accurate computation of this quantity does not require as many elements. This fact causes the error in impedance to decrease with frequency, and 3 elements per wavelength is sufficient to achieve less than 10% error for the two highest frequencies in this test. For the lowest frequency, 20 elements per wavelength is required for 10% error.

5

RADIATION FROM HORNS IN HALF-SPACE

The most commonly treated case for horns is radiation into half-space (2π solid angle). This is also a very important case, as it is part of all other radiation cases, as will be discussed in section 6.2.

The previous chapter outlined the basics of the Mode Matching Method (MMM), and as mentioned in Section 4.6, the impedance at the mouth end of the horn must be known in order to compute the impedances at all points in the horn, and the volume velocity transfer matrix. This impedance can be the radiation impedance, either into half-space, or into other solid angles, or it can be the throat impedance of another horn, or the characteristic impedance of an infinite duct, Z_c. In this chapter, we will look in more detail into the multimodal radiation impedance and its physical meaning. In addition, expressions for radiation impedance for axisymmetric and rectangular geometries will be given for the infinite baffle (IB) case. For detailed derivations of the expressions, please see the references. This chapter will instead focus on how to improve the computational efficiency.

With the volume velocity transfer matrix, the modal volume velocity amplitudes at the mouth of the horn can be found, given a vector of throat volume velocity amplitudes. This chapter will also look at the basic methods to compute the radiated pressure from the horn mouth.

An experimental verification of the MMM applied to a horn mounted in an infinite baffle is given in Section 9.2 on page 195.

The main contributions in this chapter are the improvements in efficiency for calculating the modal radiation impedance matrix for circular and rectangular geometries. In addition, a derivation of the equations for far field radiation from asymmetric rectangular horns is presented, and the relation between the reflectance matrix and the radiation impedance is discussed in terms of the physical meaning of modal radiation impedance and the influence of the reflected modes.

Computation times in this and subsequent chapters are given for comparison only, the absolute values have little significance. All the computations have been performed on a computer that had an Intel i7-2600 CPU running at 3.4 GHz, and 8 GB RAM.

5.1 CALCULATION OF THE PRESSURE RESPONSE

Calculation of the pressure radiated from the horn is also necessary if the model is to be used for directivity predictions. One way to do this, for a radiator in an infinite baffle, is to use the Rayleigh integral [286, 174], mapping the velocity profile in the mouth of the horn to the pressure response. From a throat volume velocity vector $\vec{U}^{(1)}$ and the volume velocity transfer matrix $\mathbb{U}^{(1,N)}$, the mouth volume velocity mode amplitude vector $\vec{U}^{(N)}$ can be found as $\vec{U}^{(N)} = \mathbb{U}^{(1,N)}\vec{U}^{(1)}$. From this, the radiated pressure, p_{IB}, can be calculated using a multimodal variant of the Rayleigh integral over the mouth area S:

$$p_{IB}(\mathbf{x}) = \frac{j\omega\rho}{2\pi S} \int_S \sum_{m=0}^{\infty} \psi_m(x_0, y_0) U_m^{(N)} \frac{e^{-jkr}}{r} dS_0 \tag{156}$$

where $\mathbf{x} = (x, y, z)$ and

$$r = \sqrt{(x - x_0)^2 + (y - y_0)^2 + z^2}.$$

This expression is valid for the case of an infinite baffle, as indicated by the subscript IB for p. The Rayleigh integral is accurate for any distance to the source.

5.1.1 *Far Field Approximation*

If only the far field pressure is required, the pressure can be calculated directly from the amplitudes of the velocity modes at the mouth. This method was first described for circular geometries by Morse [149], and later for circular and rectangular geometries by Geddes [33]. The derivation is somewhat involved, and outside the scope of this text, but can be found in the references. The basic idea is that in the far field, the distance r to the observation point is much greater than the size of the source, and the factor e^{-jkr}/r can be moved outside the integral:

$$p(r, \theta_x, \theta_y) = j\rho ck \frac{e^{-jkr}}{2\pi r} \sum_{m_x, m_y} \int\int_S v(x, y) e^{jk_x x} e^{jk_y y} dx dy \tag{157}$$

where

$$k_x = k \sin\theta_x$$
$$k_y = k \sin\theta_y$$

and θ_x and θ_y describe the angle between source surface normal and the line from the source to the observation point in the x and y directions, respectively.

In the following sections, the results for three geometries will be presented: cylindrical axisymmetric, rectangular symmetric, and rectangular asymmetric.

5.1.2 *Cylindrical Geometry*

The result for the axisymmetric case is [149]

$$p(r,\theta) = j\rho ck \frac{e^{-ikr}}{2\pi r} \sum_n U_n \Theta_n(ka\sin\theta) \tag{158}$$

where

$$\Theta_n(s) = \frac{2sJ_1(s)}{s^2 - \mu_n^2}. \tag{159}$$

The function Θ_n is plotted in Figure 37 as a function of the argument $ka\sin\theta$. It is clear that as the frequency increases, a larger range of the argument is used.

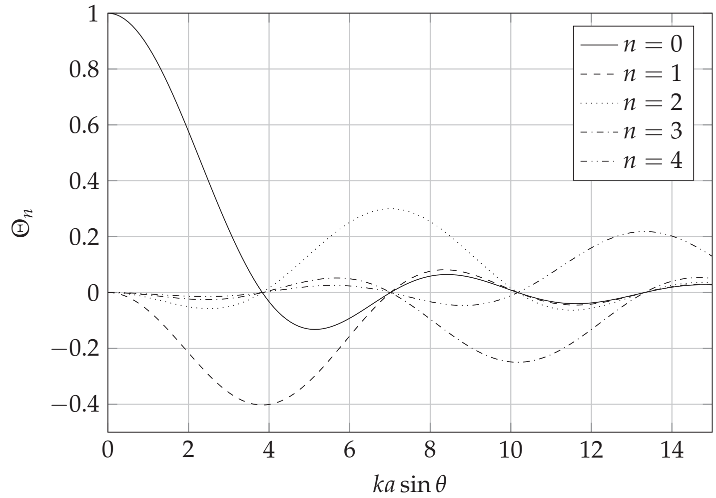

Figure 37: The function Θ_n for some radiation modes for an axisymmetric horn.

5.1.3 *Rectangular, Quarter Symmetric Geometry*

Given a rectangular radiator with half-width a and half-height b, with a velocity profile is given as

$$\psi_m(x,y) = A_{m_x} \cos\left(\frac{m_x \pi x}{a}\right) \cdot B_{m_y} \cos\left(\frac{m_y \pi y}{b}\right) \tag{160}$$

the pressure can be found as [33]

$$p(r,\theta_x,\theta_y) = j\rho ck \frac{e^{-jkr}}{2\pi r} \sum_{m_x,m_y} A_{m_x} B_{m_y} \times \int_{-b}^{b}\int_{-a}^{a} \cos\left(\frac{m_x \pi x}{a}\right) \cos\left(\frac{m_y \pi y}{b}\right) e^{-jk_x x} e^{-jk_y y} dx dy. \tag{161}$$

By solving the integral

$$\int_{-a}^{a} \cos\left(\frac{n\pi x}{a}\right) e^{-jk_x x} = 2a^2(-1)^n \frac{k_x \sin(ak_x)}{(ak_x)^2 - (n\pi)^2} \tag{162}$$

we can express the radiated pressure as

$$p(r, \theta_x, \theta_y) = j\rho ckS \frac{e^{-jkr}}{2\pi r} \sum_{m_x, m_y} A_{m_x} B_{m_y} G_{m_x}(ka \sin\theta_x) \cdot G_{m_y}(kb \sin\theta_y) \tag{163}$$

where

$$G_n(s) = (-1)^n \frac{s \sin(s)}{s^2 - (n\pi)^2}, \tag{164}$$

which reduces to the familiar sinc function for $n = 0$. The function is plotted for a few modes in Figure 38, and is symmetric with respect to the argument.

A_{m_x} and B_{m_y} can be found from modal decomposition of the velocity profile, but when the modal amplitudes already are known from the modal propagation through the horn, we have

$$A_{m_x} B_{m_y} = N_{m_x} N_{m_y} u_{m_x m_y} \tag{165}$$

where

$$N_{m_x} = \begin{cases} 1 & m_x = 0 \\ \sqrt{2} & m_x > 0 \end{cases} \tag{166}$$

and similarly for N_{m_y}, and $u_{m_x m_y}$ are the modal velocity amplitudes.

5.1.4 *Rectangular, Asymmetric Geometry*

For the asymmetric case, the radiator having half-width a and half-height b, the velocity profile is given as (see Section 4.2.4)

$$\psi_m(x, y) = A_{m_x} \cos\left(\frac{m_x \pi (x - a)}{2a}\right) \cdot B_{m_y} \cos\left(\frac{m_y \pi (y - b)}{2b}\right). \tag{167}$$

By using the same procedure as above,

$$\begin{aligned} p(r, \theta_x, \theta_y) &= j\rho ck \frac{e^{-jkr}}{2\pi r} \sum_{m_x, m_y} A_{m_x} B_{m_y} \\ &\times \int_{-b}^{b} \int_{-a}^{a} \cos\left(\frac{m_x \pi (x - a)}{2a}\right) \cos\left(\frac{m_y \pi (y - b)}{2b}\right) e^{-jk_x x} e^{-jk_y y} dx dy, \end{aligned} \tag{168}$$

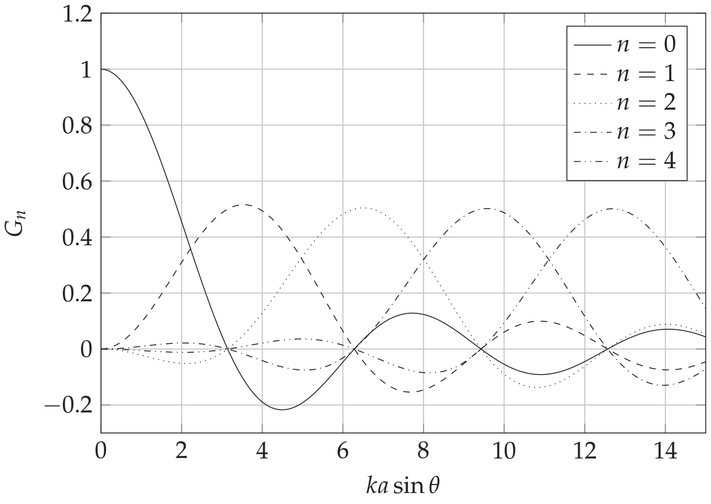

Figure 38: The function G_n for some radiation modes for a symmetric rectangular horn.

and we need to solve the integral

$$\int_{-a}^{a} \cos\left(\frac{n\pi(x-a)}{2a}\right) e^{-jk_x x} dx$$

$$= -4ja^2 \frac{e^{-jak_x}\left((-1)^n e^{2jak_x} - 1\right)}{4(ak_x)^2 - (n\pi)^2}. \quad (169)$$

Now we can express the radiated pressure as

$$p(r, \theta_x, \theta_y) = j\rho ckS \frac{e^{-jkr}}{2\pi r} \sum_{m_x, m_y} A_{m_x} B_{m_y} G^A_{m_x}(ka\sin\theta_x) \cdot G^A_{m_y}(kb\sin\theta_y) \quad (170)$$

with the function $G^A_n(s)$ defined as

$$G^A_n(s) = -2j \frac{e^{-js}\left((-1)^n e^{2js} - 1\right)}{4s^2 - (n\pi)^2}. \quad (171)$$

This function can be simplified somewhat, to remove the complex exponentials. For even modes, it reduces to a function very similar to the G-function for symmetric modes:

$$G^A_{n,even}(s) = \frac{s\sin(s)}{s^2 - (n\pi/2)^2}, \quad (172)$$

which again reduces to the sinc function for $n = 0$. For odd modes,

$$G^A_{n,odd}(s) = -4j \frac{s\cos(s)}{(n\pi)^2 - 4s^2}. \quad (173)$$

The function is plotted in Figure 39 for a few odd modes. Note the asymmetry of the function with respect to the argument. For the even modes, see Figure 38.

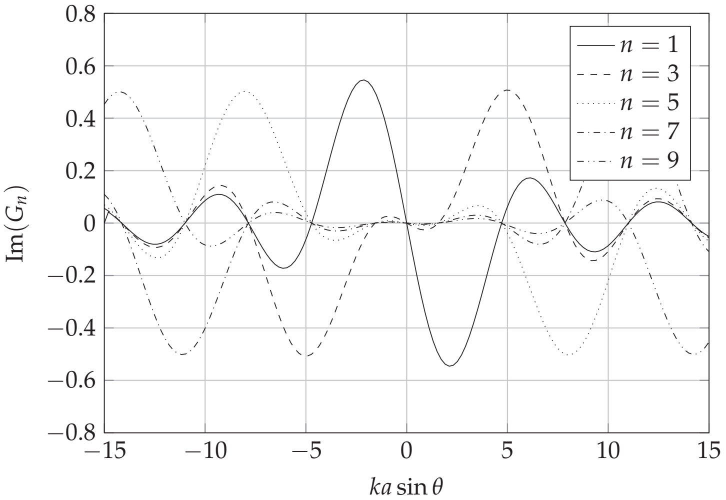

Figure 39: The function G_n for odd radiation modes for an asymmetric rectangular horn from Eq. (173) (imaginary part plotted).

5.1.5 *Convergence: Far Field Pressure*

Inspection of the plots of the directivity functions, Figures 37, 38 and 39, show that all functions have certain values of the argument where only one mode contributes. For instance, in Figure 37, at $ka\sin\theta=10.2$ only the mode with $n=3$ contributes. If this mode is not present, there will be a null in the response for this value of the argument.

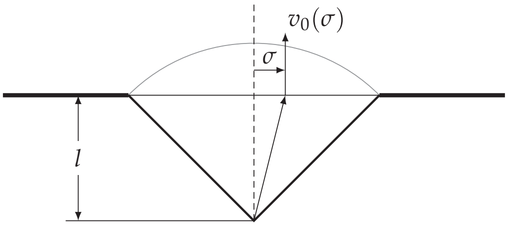

Figure 40: Spherical wave front in an aperture.

To illustrate the effect of this, the velocity distribution of a shaded spherical wave front in the aperture, Figure 40, was computed from the following equation [33]:

$$v(\sigma)=wv_0\frac{l^2}{l^2+\sigma^2}e^{-jk\left(\sqrt{\sigma^2-l^2}-l\right)} \tag{174}$$

where

$$w = e^{-0.7^{-1}\sigma^2}$$

is the shading function, and l and σ are defined in Figure 40. The aperture velocity distribution was decomposed into a number of modes, which were then propagated to the far field using Eq. (158).

The results are shown in Figure 41. The lower halves of the plots (negative angles) show the reference polar response, computed using the Rayleigh integral directly on the velocity distribution, while the upper halves (positive angles) show the polar responses for a plane wave (Figure 41a) and for five modes included (plane wave and four higher modes, Figure 41b). By comparing the upper and lower halves of the plots, it is possible to judge the accuracy of the approximations.

The plane wave polar plot has a series of null lines (due to the finite resolution of the plot they are not continuous lines in the figures), and four of these null lines are gone when the four first higher modes are added. Adding successive modes will remove additional null lines. Also note that the polar response at smaller angles and lower frequencies (lower $ka \sin\theta$) approaches the correct shapes fairly quickly.

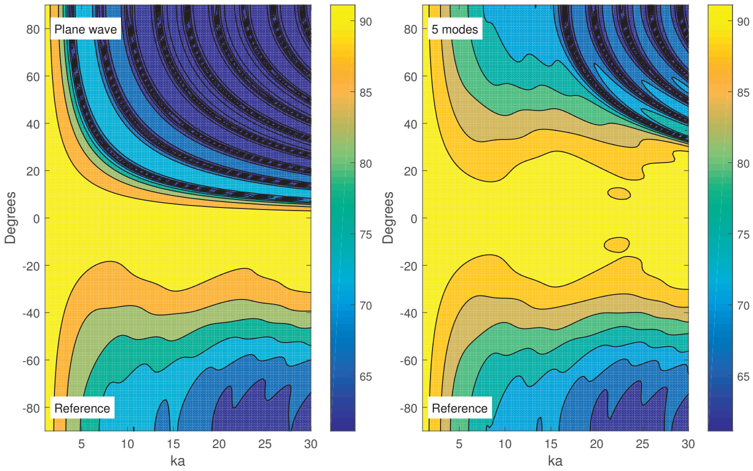

(a) Polar response for a plane wave (upper).

(b) Polar response for 5 modes (upper).

Figure 41: Normalized polar responses for a shaded spherical wave front described by a plane wave or by 5 modes (including the plane wave). Upper half of the plots (positive angles) are shows the truncated modal description, lower half (negative angles) shows the reference polar response computed from the Rayleigh integral.

Figure 42 shows the relative error in the far field as a function of $ka \sin\theta$ for a number of added modes, compared to a reference solution using 100 modes. The results were computed for $\theta = 90°$. It can

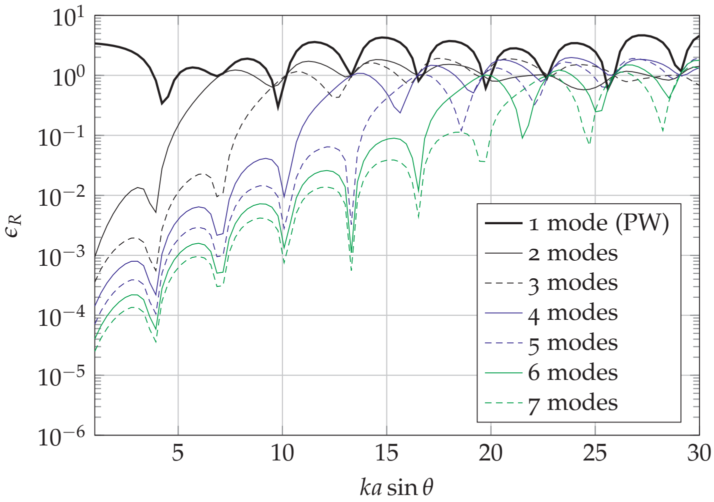

Figure 42: The relative error in far field pressure various number of modes. The reference is a solution with 100 modes.

be seen that the error is reduced significantly at frequencies below the cutoff frequency of the highest mode included. Unfortunately, the number of modes required for a given error increases at higher frequencies, but it is clear that at least the mode with a cutoff identical to the highest *ka* value in use should be included, and preferably a few extra. This, of course, assumes that the mode amplitudes are correct in the first place, and this also depends on the number of modes used in the simulation of the horn, see Section 4.7.

One should also note that only the plane wave mode contributes to the on-axis response, and that the higher modes becomes more important as one moves off-axis.

5.2 GENERALIZED MODAL RADIATION IMPEDANCE

In general, the mechanical radiation impedance is defined as the area integral of the specific radiation impedance $p/v_\mathbf{n}$, where $v_\mathbf{n}$ is the normal surface velocity [279]. The acoustic radiation impedance, Z_{rad}, for a surface S in an infinite baffle, is thus defined as

$$Z_{rad} = \frac{j\omega\rho}{2\pi S^2} \int\limits_S \int\limits_S \frac{e^{-jkh}}{h} dS_0 dS \tag{175}$$

where $h = \sqrt{(x - x_0)^2 + (y - y_0)^2}$.

In the multimodal case, the radiation impedance for a given velocity distribution is more complicated. Now, the radiation impedance must be expressed as [287]

$$Z_{rad} = \frac{W}{S^2 \left\langle |v_{\mathbf{n}}|^2 \right\rangle} \tag{176}$$

where $\left\langle |v_{\mathbf{n}}|^2 \right\rangle = \frac{1}{S} \int_S v_{\mathbf{n}} v_{\mathbf{n}}^* dS$ is the mean square normal velocity, and $W = \int_S p v_{\mathbf{n}}^* dS$ is the radiated power. However, this is not a formulation that can be used directly with the MMM. What we need is a relation between each pressure mode and each velocity mode, so that the radiation impedance can be described as a matrix in the form of Eq. (75). The physical meaning of this is discussed in the next chapter. By combining Eq. (70) with the orthogonality relation [267]

$$\int\limits_S \psi_m \psi_n dS = S\delta_{mn},$$

we can find the amplitude of the nth pressure mode as

$$P_n = \frac{1}{S} \int\limits_S p(x,y,0) \psi_n(x,y) dS. \tag{177}$$

By substituting Eq. (156), page 98, into Eq. (177), we can find the amplitude of the nth pressure mode due to all velocity modes as

$$P_n = \frac{j\omega\rho}{2\pi S^2} \sum_{m=0}^{\infty} U_m \int\limits_S \int\limits_S \frac{e^{-jkh}}{h} \cdot \psi_m(x_0,y_0) \psi_n(x,y) dS_0 dS. \tag{178}$$

The factor $2e^{-jkh}/h$ in Eq. (178) is the infinite-baffle Green's function, but other Green's functions can be inserted instead, if the surroundings are not represented by an infinite baffle. So, for the general case,

$$P_n = \frac{j\omega\rho}{4\pi S^2} \sum_{m=0}^{\infty} U_m \int\limits_S \int\limits_S G(\mathbf{x}|\mathbf{x}_0) \cdot \psi_m(x_0,y_0) \psi_n(x,y) dS_0 dS, \tag{179}$$

where $\mathbf{x}_0 = (x_0, y_0)$. This equation assumes that there are no independent sources outside S, i.e. that $G(\mathbf{x}|\mathbf{x}_0)$ vanishes outside S. Secondary sources, like image sources, or edge sources due to diffraction of the pressure radiated from S, however, may be included.

Comparing Eq. (75), page 74, to Eq. (179), we see that we can express the elements of the Z_{rad} as

$$Z_{nm} = \frac{j\omega\rho}{4\pi S^2} \int\limits_S \int\limits_S G(\mathbf{x}|\mathbf{x}_0) \cdot \psi_m(x_0,y_0) \psi_n(x,y) dS_0 dS \tag{180}$$

The Green's function in Eq. (180) can include the contribution to the self impedance (the ordinary infinite baffle radiation impedance), contributions from image sources, and contributions from edge diffraction [45]. See Section 6.2 for details.

5.3 PHYSICAL MEANING OF THE MODAL RADIATION IMPEDANCE

The radiation impedance describes the reaction on the wave propagating to the mouth of the horn by the medium outside: the resistive part describes the dissipation of power into the medium, the reactive part describes the oscillating air mass (radiation mass). As can be seen from Eq. (176), there is a direct relation between the radiation impedance and power radiated by each mode. This relation can also be found from the Bouwkamp integral, where the radiation impedance is found directly from integration over the far field pressure [288]:

$$R_s = \frac{k^2 \rho c}{4\pi^2} \int_0^{2\pi} \int_0^{\frac{\pi}{2}} |D(\theta, \phi)|^2 \sin\theta d\theta d\phi \tag{181}$$

$$X_s = -j\frac{k^2 \rho c}{4\pi^2} \int_0^{2\pi} \int_{\frac{\pi}{2}+j0}^{\frac{\pi}{2}+j\infty} |D(\theta, \phi)|^2 \sin\theta d\theta d\phi \tag{182}$$

This leads to the definition in Eq. (176), which, as mentioned, does not produce the desired impedance matrix in Eq. (75). What we require is a matrix that will give us the modal amplitudes of the pressure, given the modal amplitudes of the volume velocity. What is the physical meaning of such a matrix?

To get insight into this problem, let us take a closer look at what physically happens when a multimodal wave encounters a discontinuity, which can be either a step in the duct, or the radiation into free field at the mouth. As we have seen in Section 4.4 on page 80, an incident mode at a discontinuity produces an infinite number of reflected modes, see, Figure 28, and the same applies to the duct exit, Figure 43.

There must therefore be a matrix that relates the modal amplitudes of the incident wave $\vec{P}_+$ to the modal amplitudes of the reflected wave $\vec{P}_-$, so that

$$\vec{P}_- = \mathbb{R}\vec{P}_+. \tag{183}$$

The matrix $\mathbb{R}$ is called the reflectance matrix [267]. In the case where only plane waves are considered, this is simply the reflection factor, given by

$$R = \frac{Z_2 - Z_1}{Z_2 + Z_1} \tag{184}$$

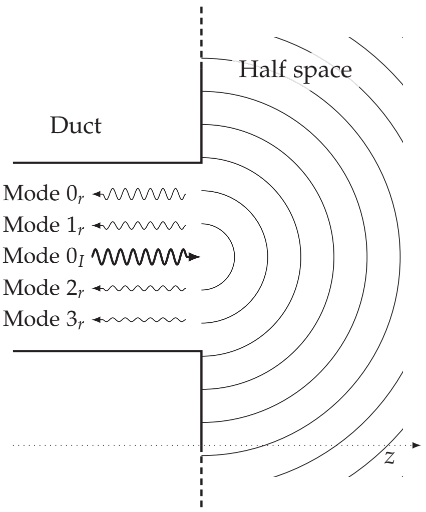

Figure 43: Multimodal reflection at the duct exit. The incident plane wave (Mode 0_I) creates a radiated wave as well as reflected modes (subscript r).

where Z_1 and Z_2 are the impedances of the medium before and after the discontinuity, respectively.

To derive[1] the multimodal reflectance matrix, we make use of the relations

$$\begin{aligned} \vec{P} &= \vec{P}_+ + \vec{P}_- & \vec{U} &= \vec{U}_+ + \vec{U}_- \\ \vec{U}_+ &= Z_c^{-1}\vec{P}_+ & \vec{U}_- &= -Z_c^{-1}\vec{P}_- \end{aligned}$$

where Z_c is the characteristic impedance given by Eq. (104). By combining these relations, we have that

$$\vec{P}_+ + \vec{P}_- = \mathbb{Z}Z_c^{-1}\left(\vec{P}_+ - \vec{P}_-\right) \tag{185}$$

or

$$\left(\mathbb{Z}Z_c^{-1} + I\right)\vec{P}_- = \left(\mathbb{Z}Z_c^{-1} - I\right)\vec{P}_+. \tag{186}$$

Using Eq. (183), we find that

$$\mathbb{R} = \left(\mathbb{Z}Z_c^{-1} + I\right)^{-1}\left(\mathbb{Z}Z_c^{-1} - I\right). \tag{187}$$

Similarly,

$$\mathbb{Z}Z_c^{-1} = (I + \mathbb{R})(I - \mathbb{R})^{-1}. \tag{188}$$

A factor that we encounter here, and which will prove to be important when considering circular, unflanged ducts, is the intermingling of the reflection factors for individual modes, when computing the

---

[1] This derivation is due to Kemp [267].

impedance. This intermingling is not immediately apparent due to the matrix formalism used above, but as is well known, matrix inversion and multiplication never leaves a single element untouched by the others. This can easily be ascertained by writing out Eq. (188) term by term. This means that all reflected modes have influence on all elements in the impedance matrix, there is no one-to-one correspondence between the elements of the reflectance matrix and the impedance matrix, and thus it is not possible to correctly calculate the plane wave impedance Z_{00} from R_{00} alone.

The effect of not including higher order modes in the reflectance matrix will now be examined. For this example, the radiation impedance matrix for a duct ending in an infinite baffle, as given by Zorumski [280], has been used. For each frequency, an impedance matrix of 64 modes was calculated and converted into a reflectance matrix using Eq. (187). This reflectance matrix was then truncated to a specific number of modes, and thereafter converted back into an impedance matrix using Eq. (188), from which the Z_{00} impedance was extracted. The results are shown in Figure 44. The reference is the radiation impedance of a piston.

The curves have the following interesting properties:

- Using only R_{00}, both the resistance and reactance components of the radiation impedance are a little too low in the $ka = 1 - 3$ region.
- The resistance has a peculiar "jumpy" behavior near the cut-in wavenumbers of the modes.
- The reactance has a discontinuous derivative at the cut-in wavenumbers.
- As one mode is added, the curve smooths out near the first mode cut-in wavenumber, but the discontinuities at higher wave numbers remain.
- Each mode added smooths out the discontinuity near its own cut-in wavenumber.

We can now clearly see the reason for the ripple in the radiation impedance for a circular piston: the ripple peaks correspond to the cut-in of the successive modes in the pressure distribution across the piston. This is also why there is no ripple for the radiation impedance for a pulsating sphere: in this case only the zeroth order mode is excited, and no higher order modes are involved. This is illustrated in Figure 45, where the pressure in front of a piston with is compared to the piston in front of a pulsating sphere. For the piston, there is a discontinuity in velocity at the edge; this results in a complex pressure distribution that indicates the presence of higher order modes in the

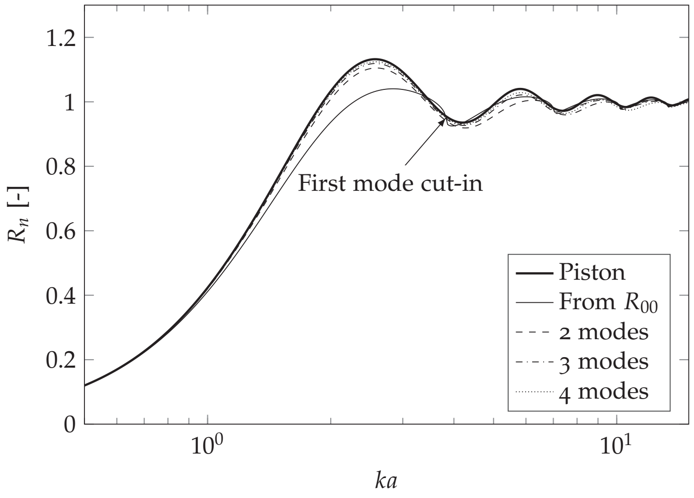

(a) Radiation resistance.

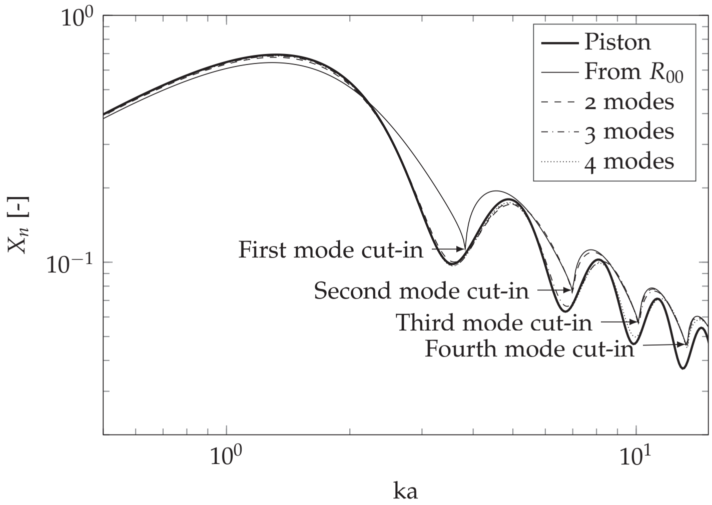

(b) Radiation reactance. Note that the ordinate axis is logarithmic to enhance readability of low level artifacts.

Figure 44: Normalized radiation impedance for a duct ending in an infinite baffle (see Figure 46), calculated from reflectance matrix. 2 modes indicate that a 2×2 reflectance matrix was used, and so on.

pressure field. For the pulsating sphere, the velocity is constant with angle, and consequently the pressure distribution is too.

It is also clear that the higher order modes must be included to produce the smooth behavior of the radiation impedance curves. Even when a mode is evanescent, as all modes are below $ka = 3.83$, it contributes to the impedance. This is because the impedance is the

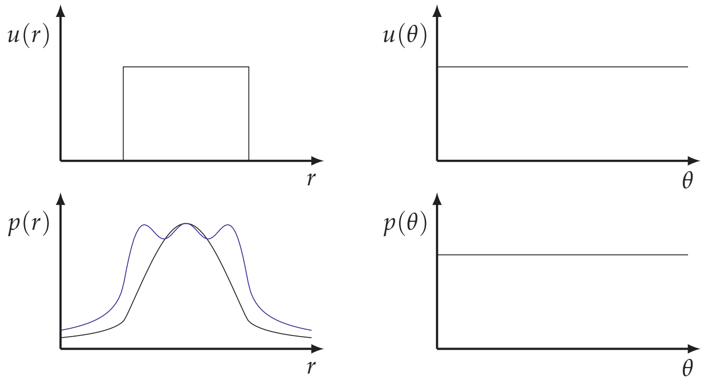

Figure 45: Velocity and pressure distribution for a piston (left) and a pulsating sphere (right). For the piston, the pressure distributions for $ka = 3$ (black) and $ka = 5$ (blue) are shown.

quotient of the near field pressure to the velocity, and even evanescent modes may contribute significantly to the near field pressure.

Therefore, in order to produce smooth impedance curves from a reflectance matrix, enough modes must be included that at least one mode is in cutoff at the highest wavenumber of interest.

5.4 RADIATION IMPEDANCE, AXISYMMETRIC DUCT

The radiation impedance of a circular duct ending in an infinite baffle, Figure 46, has been derived by Zorumski [280], with a simplification to axisymmetric excitation by Kemp [267].

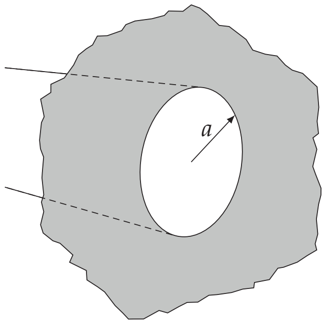

Figure 46: Geometry of a circular duct ending in an infinite baffle.

Starting from Eq. (180), $G(\mathbf{x}|\mathbf{x}_0) = 2e^{-jkh}/h$ for the axisymmetric case, where

$$h = \left[r^2 + r_0^2 - 2rr_0\cos(\theta - \theta_0)\right]^{\frac{1}{2}} \tag{189}$$

is the distance between the points (r_0, θ_0) and (r, θ). The mode functions are given in Eq. (84). After some extensive manipulation of the integrals, the result, as given by the references, is reduced to two single integrals:

$$Z_{nm} = \frac{\rho c}{S} \int_0^{\pi/2} \sin\phi D_n(\sin\phi) D_m(\sin\phi) d\phi \\ + \frac{j\rho c}{S} \int_0^{\infty} \cosh\xi D_n(\cosh\xi) D_m(\cosh\xi) d\xi \quad (190)$$

where

$$D_n(\tau) = \frac{-\sqrt{2}\tau J_1(\tau ka)}{\left(\frac{\mu_n}{ka}\right)^2 - \tau^2} \quad (191)$$

These integrals are then numerically integrated. According to Kemp, the integrand of the reactance function decays exponentially quite fast to about 10^{-6} around $\xi = 10$, so the integration can be terminated here without much error. It turns out, however, that a larger integration range is needed for very low ka values due to the decay behavior of the integrand.

For the plane wave mode, an analytical expression can be found, this is the well known relation first derived by Rayleigh [256]:

$$Z_{00} = \frac{\rho c}{S}\left[1 - \frac{J_1(2ka)}{ka} + j\frac{H_1(2ka)}{ka}\right], \quad (192)$$

where $H_1(x)$ is the Struve function.

5.4.1 *Polynomial Approximation*

At low frequencies, it is possible to make polynomial approximations for the radiation resistance. By expanding Eq. (191) around $ka = 0$, we get

$$D_n \approx -\frac{\tau^2 (ka)^3}{\sqrt{2}\mu_n^2} + \frac{(-8+\gamma_n^2)\tau^4 (ka)^5}{8\sqrt{2}\mu_n^4} \\ - \frac{((192 - 24\mu_n^2 + \mu_n^4)\tau^6)(ka)^7}{192\sqrt{2}\mu_n^6} + \mathcal{O}(ka)^9 \quad (193)$$

This expression can be integrated by term by term to give an analytical polynomial expression for R_{nm}. Using only the first term, the expression for the normalized radiation resistance becomes

$$R_{LF} \approx \frac{4\,(kR)^6}{15\mu_n^2\mu_m^2} \quad (194)$$

which clearly cannot be used for $m = 0$ or $n = 0$. In the case $\mu_n = 0$, we have

$$D_0 \approx \frac{ka}{\sqrt{2}} - \frac{\tau^2 (ka)^3}{8\sqrt{2}} + \frac{\tau^4 (ka)^5}{192\sqrt{2}} - \frac{\tau^6 (ka)^7}{192\sqrt{2}} + \mathcal{O}(ka)^9 \tag{195}$$

Which gives the following expression for $m = 0$, $n \neq 0$:

$$R_{LF} \approx \frac{(ka)^4 \left((ka)^2 - 10\right)}{30\mu_n^2} \tag{196}$$

For $m = n = 0$:

$$R_{LF} \approx \frac{(ka)^2}{240}(120 - 20\,(ka)^2 - (ka)^4) \tag{197}$$

which corresponds to the traditional normalized value $R_{LF} = 0.5(ka)^2$ when using only the first term. As can be seen from the approximations, and also from Figure 47 below, the low frequency slope of the radiation resistance is different for the different combination of orders. For mode (0,0), the slope is second order, and it is fourth order for $(0, m)$ and $(n, 0)$ modes. For (n, m) modes, it is sixth order. This means that the radiation resistance for most higher modes is very low at low frequencies. The modes merely add a little to the radiation mass.

Using more terms in $(ka)^2$, the polynomial coefficients are given in Table 20 and Table 21 in Appendix B on page 275. For R_{00}, the expression in Eq. (192) is usually used, but it may be advantageous to use the polynomial expression for very low values of ka, depending on the accuracy of the Bessel and Struve function algorithms for small arguments.

These polynomial coefficients may be precomputed and stored in a data file, which makes for a very efficient computation of the multimodal radiation resistance at low frequencies.

A similar approach was tried for the reactance, but the resulting integrals did not have any analytical solutions, and an alternative method was sought. Numerical evaluation indicated that the slope of the reactance curves is independent of mode order and combination; it is always a mass reactance with a first order slope. This was also brought out by making a polynomial approximation for the modal radiation impedance of a rectangular duct (Section 5.5.2), where the first polynomial coefficient always was non-zero, indicating a mass term. By computing the reactance integral in Eq. (190) for a few frequencies well below $ka = 1$, a constant can be found, which, when multiplied with ka, gives the reactance at low frequencies. Below $ka = 0.5$, this gives an error smaller than 10%.

For the modal impedances on the diagonal of the impedance matrix, from now on called diagonal modes, it was found that the reactance is represented fairly well by the characteristic impedance of a duct the same radius as the opening, Z_c, as defined in Eq. (68). Thus the low frequency reactance for diagonal modes can be found as

$$X_m \approx \frac{\rho c k}{S k_m} = \frac{j\rho\omega}{S\sqrt{\left(\frac{\mu_m}{a}\right)^2 - k^2}}. \tag{198}$$

For low mode numbers, there is some discrepancy between this value and the true value, so a correction factor must be found based on the true value from Eq. (190).

5.4.2 *A High Frequency Approximation*

At high *ka* values, numerical integration is slow, due to the oscillatory integrals. However, looking at the impedance curves in Figure 47, we notice the following:

- At wave numbers higher than the highest mode cutoff, all curves converge to one of three shapes; one shape for the reactance, and for the resistance, one for diagonal modes and one for off-diagonal modes.
- These shapes appear to be scaled versions of the plane wave radiation impedance curves.

An experimental scaling function applied to the plane wave radiation impedance appears to give good agreement for values 2-3 times the highest mode cutoff, $\mu_q = \max(\mu_n, \mu_m)$. The scaling function gives the following expressions:

$$R_{mn,HF} \approx \frac{R_{00,HF} - 1}{1 - \left(\frac{\mu_q}{ka}\right)^2}, \tag{199}$$

$$X_{mn,HF} \approx \frac{X_{00,HF}}{1 - \left(\frac{\mu_q}{ka}\right)^2}. \tag{200}$$

Using these approximations for $ka > 2\mu_q$ yields a maximum error of approximately 10%, decreasing approximately as $1/\omega^2$ with increasing frequency.

This method does not work well for the diagonal modes, however. But here a very good approximation can be found by exploiting the fact that above mode cutoff, the radiation resistance oscillates around the characteristic impedance Z_c. In addition, these oscillations are very close to the oscillations in the plane wave mode impedance. Thus,

$$R_{mm,HF} \approx R_{00} \frac{k}{\sqrt{k^2 - \left(\frac{\mu_m}{a}\right)^2}}. \tag{201}$$

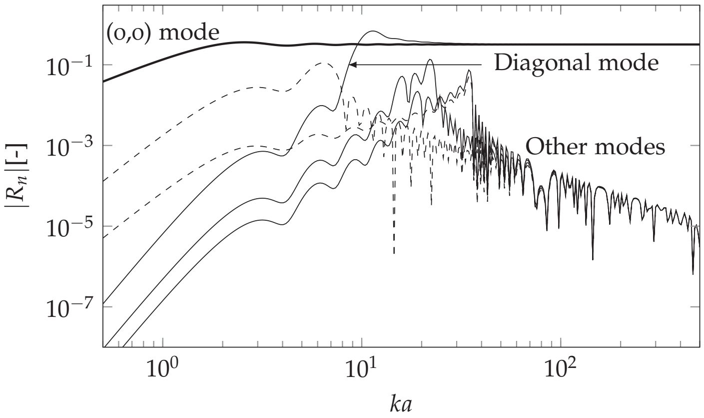

(a) Radiation resistance for some modes.

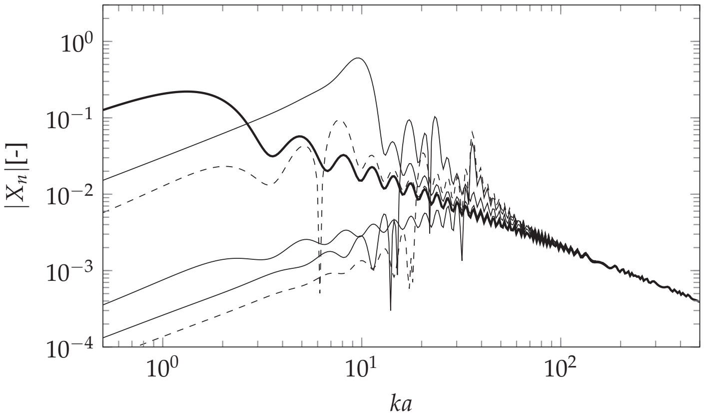

(b) Radiation reactance for some modes.

Figure 47: Radiation impedance for a few selected modes. Note that the curves converge, for large *ka*, to two shapes for resistance and one shape for reactance. The term "diagonal mode" refers to an element from the diagonal of the impedance matrix.

In between the ranges where the above approximations are possible, the simplest approach is interpolation of precomputed data. It has been found advantageous to use linearly spaced frequency points for the precomputed data, in order to make the error fairly constant with frequency.

5.4.3 *Performance*

A few examples of the error resulting from application of all the techniques outlined above are shown in Figure 48. The transition wave numbers are 0.5 and 26.6. Mostly the error is below 1% (which was the target accuracy), except for the high frequency approximation. The noise in the error for low frequency reactance comes from inaccuracies in the integration of Eq. (190) for low frequencies.

As for timing, using the Matlab `quadv` function with a tolerance of $1 \cdot 10^{-8}$ for the integration of Eq. (190), takes about 6.8 s for a single mode, for 1500 frequencies. By using the techniques described in this section, computation time is down to about 3.4 ms. In addition comes computation of the tabulated data for interpolation, and computation of the polynomial coefficients, which have also been tabulated. But this computation is only done once.

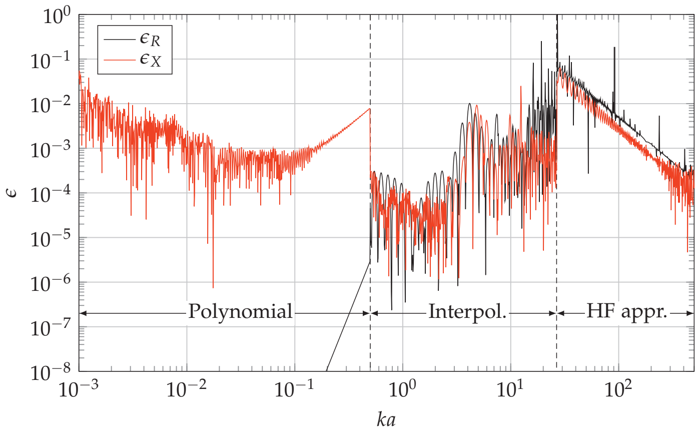

(a) Relative error for mode (2,4).

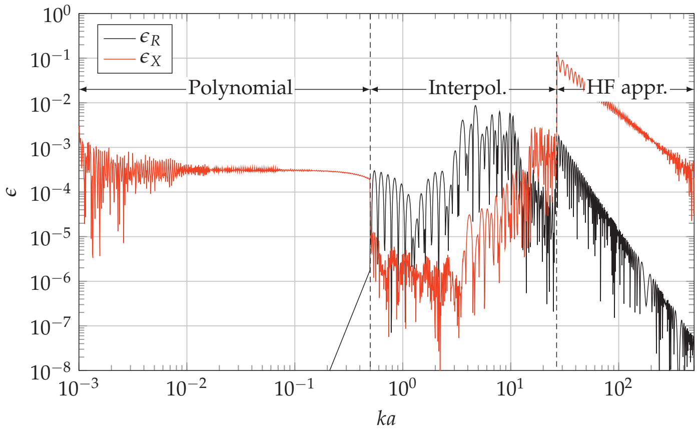

(b) Relative error for mode (4,4).

Figure 48: Relative error for approximation and interpolation of circular duct radiation impedance.

5.5 RADIATION IMPEDANCE, RECTANGULAR DUCT

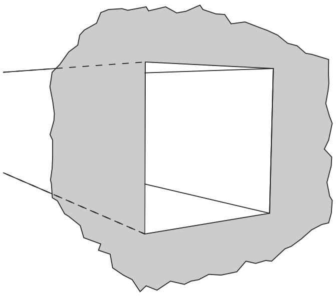

Figure 49: Geometry of a rectangular duct ending in an infinite baffle.

The radiation impedance for a rectangular duct ending in an infinite baffle, Figure 49, has been given by Kemp for symmetric [267] and asymmetric [11] modes. To sum up, the equations given by Kemp are, for duct with only symmetrical modes:

$$Z_{mn} = \frac{j\omega\rho}{2\pi S^2} \int_0^{2a} d\xi \int_0^{2b} d\zeta \frac{e^{-jkh}}{h} G(n_x, m_x\xi, a) G(n_y, m_y, \zeta, b) \tag{202}$$

where

$$h = \sqrt{\xi^2 + \zeta^2}, \tag{203}$$

and

$$\begin{aligned} G(n_x, m_x, \xi, a) = {} & N_{n_x} N_{m_x} (2a - \xi) \times \\ & \left[\operatorname{sinc}\left((n_x + m_x)\,\pi \left(1 - \frac{\xi}{2a}\right)\right) \cos\left(\frac{(n_x - m_x)\,\pi\xi}{2a}\right) + \right. \\ & \left. \operatorname{sinc}\left((n_x - m_x)\,\pi \left(1 - \frac{\xi}{2a}\right)\right) \cos\left(\frac{(n_x + m_x)\,\pi\xi}{2a}\right) \right] \end{aligned} \tag{204}$$

with

$$N_{n_x} = \begin{cases} 1 & : n_x = 0 \\ \sqrt{2} & : n_x > 0 \end{cases}. \tag{205}$$

Kemp then does a change of variables to express the integrals in terms of dimensionless variables $u = k\xi$ and $v = k\zeta$, giving

$$Z_{mn} = \frac{j\rho c}{2\pi S} \int_0^{2ka} du \int_0^{2kb} dv \frac{e^{-j\sqrt{u^2+v^2}}}{\sqrt{u^2+v^2}} G(n_x, m_x \frac{u}{2ka}, \frac{1}{2}) G(n_y, m_y, \frac{v}{2kb}, \frac{1}{2}). \tag{206}$$

This equation has a singularity at the origin if $n_x = m_x$ and $n_y = m_y$, which Kemp removes by splitting up the integral:

$$\begin{aligned}
Z_{nm} = {} & \frac{j\rho c}{2\pi S}\int_0^{2ka} du \int_0^{2kb} dv \frac{\left(1-\frac{u}{2ka}\right)\left(1-\frac{v}{2kb}\right)}{\sqrt{u^2+v^2}} \times \\
& \left[e^{-j\sqrt{u^2+v^2}} \frac{G(n_x, m_x, \frac{u}{2ka}, \frac{1}{2})}{1-\frac{u}{2ka}} \frac{G(n_y, m_y, \frac{v}{2kb}, \frac{1}{2})}{1-\frac{v}{2kb}} - f(n,m)\right] \\
& + \frac{j\rho c}{2\pi S}\int_0^{2ka} du \left(1-\frac{u}{2ka}\right) \times \\
& \left[\ln\left(2kb+\sqrt{u^2+(2kb)^2}\right) + \frac{u}{2kb} - \frac{1}{2kb}\sqrt{u^2+(2kb)^2}\right] f(n,m) \\
& + \frac{j\rho c}{2\pi S}\left[-ka\ln(2ka) + \frac{3}{2}ka\right] f(n,m),
\end{aligned} \tag{207}$$

where

$$\begin{aligned}
f(n,m) = {} & N_{n_x} N_{m_x} N_{n_y} N_{m_y} \times \\
& \left[\operatorname{sinc}\left(n_x+m_x\right)\pi + \operatorname{sinc}\left(n_x-m_x\right)\pi\right] \times \\
& \left[\operatorname{sinc}\left(n_y+m_y\right)\pi + \operatorname{sinc}\left(n_y-m_y\right)\pi\right].
\end{aligned} \tag{208}$$

Similarly, the expressions for ducts where asymmetric modes are included, are given by Kemp in [11]. Apart from a different G function, the basic equation is identical to 202 with integration limits a and b, respectively. The dimensionless equation is identical to Eq. (206) except that the integration limits are now ka and kb, respectively, and the handing of the singularity for $n_x = m_x$ and $n_y = m_y$ results in a slightly different equation:

$$\begin{aligned}
Z_{nm} = {} & \frac{j\rho c}{2\pi S}\int_0^{ka} du \int_0^{kb} dv \frac{\left(1-\frac{u}{2ka}\right)\left(1-\frac{v}{2kb}\right)}{\sqrt{u^2+v^2}} \times \\
& \left[e^{-j\sqrt{u^2+v^2}} \frac{G(n_x, m_x, \frac{u}{ka}, 1)}{1-\frac{u}{2ka}} \frac{G(n_y, m_y, \frac{v}{kb}, 1)}{1-\frac{v}{2kb}} - f(n,m)\right] \\
& + \frac{j\rho c}{2\pi S}\int_0^{ka} du \left(1-\frac{u}{2ka}\right) \times \\
& \left[\ln\left(kb+\sqrt{u^2+(kb)^2}\right) + \frac{u}{2kb} - \frac{1}{2kb}\sqrt{u^2+(kb)^2}\right] f(n,m) \\
& + \frac{j\rho c}{2\pi S}\left[-\frac{3}{4}ka\ln(ka) + \frac{7}{8}ka\right] f(n,m),
\end{aligned} \tag{209}$$

where $f(n,m)$ is given as before, but

$$\begin{aligned} G(n_x, m_x, \xi, a) = {} & N_{n_x} N_{m_x} \times \\ & \left\{ \cos\left((n_x - m_x)\, \pi \frac{\xi}{2a} \right) \times \right. \\ & \frac{1}{2} \left[(2a - \xi)\, \mathrm{sinc}\left((n_x + m_x)\, \pi \left(1 - \frac{\xi}{2a} \right) \right) \right. \\ & \left. - \xi \mathrm{sinc}\left((n_x + m_x)\, \pi \frac{\xi}{2a} \right) \right] \\ & + \cos\left((n_x + m_x)\, \pi \frac{\xi}{2a} \right) \\ & \frac{1}{2} \left[(2a - \xi)\, \mathrm{sinc}\left((n_x - m_x)\, \pi \left(1 - \frac{\xi}{2a} \right) \right) \right. \\ & \left. \left. - \xi \mathrm{sinc}\left((n_x - m_x)\, \pi \frac{\xi}{2a} \right) \right] \right\}. \end{aligned} \tag{210}$$

When $n_x = m_x = 0$, then

$$G\left(n_x, m_x, \xi, a\right) = 2\left(a - \xi\right) \tag{211}$$

which gives the radiation impedance of a piston in an infinite baffle.

5.5.1 *Improving the Computational Efficiency*

When computing the terms in the radiation impedance matrix, the dimensionless equations given by Kemp do not give optimum efficiency, because all terms, including the arguments to the G function, are frequency dependent. If we, however, look at the basic equations, before the change of variables, we see that the only frequency dependent part of the integral is the complex exponential. The arguments for the G functions depend on mode index and position, but are not frequency dependent. This realization will make it possible to improve the computation efficiency significantly if a fixed number of integration points are used (e.g. by using Gauss-Legendre integration). The method works as follows:

1. The number of integration points are determined based on the frequency, the highest mode to be computed, and on the accuracy needed.

2. A matrix of the complex exponential and h is computed for all integration points.

3. Matrices of the two G functions are computed for the various mode combinations and integration points along the two axes.

4. The most expensive part of the computation is now done, and the elements of the $\mathbb{Z}$ matrix are then computed by combining the precomputed data.

By taking advantage of the frequency independence of parts of the integral, a speedup of 4-6 times has been observed in the C++ implementation.

The singularity at $n_x = m_x$ and $n_y = m_y$ still exist, though. If a similar procedure as employed by Kemp is used, the following sum of integrals result, first for the symmetrical case:

$$\begin{aligned}
Z_{mn} &= \frac{j\rho\omega}{2\pi S^2}\int_0^{2a} d\xi \int_0^{2b} d\zeta \frac{(a-\xi/2)\,(b-\zeta/2)}{\sqrt{\xi^2+\zeta^2}} \\
&\quad \times \left\{ e^{-jk\sqrt{\xi^2+\zeta^2}} \frac{G(m_x,n_x,\xi,a)G(m_y,n_y,\zeta,b)}{(a-\xi/2)\,(b-\zeta/2)} - f(m,n) \right\} \\
&+ \frac{j\rho\omega f(m,n)}{2\pi S^2} \int_0^{2a} d\xi\,(a-\xi/2) \\
&\quad \times \left\{ b\ln\left(2b+\sqrt{\xi^2+4b^2}\right) + \frac{1}{2}\left(\xi - \sqrt{\xi^2+4b^2}\right) \right\} \\
&- \frac{j\rho\omega f(m,n)}{2\pi S^2} ab \left(a\ln(2a) - \frac{3}{2}a \right)
\end{aligned} \tag{212}$$

and for the asymmetrical case:

$$\begin{aligned}
Z_{mn} &= \frac{j\rho\omega}{2\pi S^2}\int_0^{a} d\xi \int_0^{b} d\zeta \frac{(a-\xi/2)\,(b-\zeta/2)}{\sqrt{\xi^2+\zeta^2}} \\
&\quad \times \left\{ e^{-jk\sqrt{\xi^2+\zeta^2}} \frac{G(m_x,n_x,\xi,a)G(m_y,n_y,\zeta,b)}{(a-\xi/2)\,(b-\zeta/2)} - f(m,n) \right\} \\
&+ \frac{j\rho\omega f(m,n)}{2\pi S^2} \int_0^{a} d\xi\,(a-\xi/2) \\
&\quad \times \left\{ b\ln\left(b+\sqrt{\xi^2+b^2}\right) + \frac{1}{2}\left(\xi - \sqrt{\xi^2+b^2}\right) \right\} \\
&- \frac{j\rho\omega f(m,n)}{2\pi S} \left(\ln a\left(1-\frac{a}{4}\right) + \frac{a}{8} - 1 \right)
\end{aligned} \tag{213}$$

Note that the single integrals and final constants in Equations (212) and (213) are frequency independent, apart from the factor $j\rho\omega/2\pi S^2$ that is common for all the parts.

It should also be noted that the function $f(m,n)$ can be significantly simplified, based on the fact that $\mathrm{sinc} n\pi = 0$, $n \neq 0$. In fact, the function is only non-zero if $n_x = m_x$ and $n_y = m_y$, in which case it equals 4. Therefore,

$$f(m,n) = 4\delta_{n_x m_x}\delta_{n_y m_y}, \tag{214}$$

where δ_{nm} is the Kronecker delta, that is zero except when $n = m$, in which case it is 1.

Two other factors will also contribute to improving the efficiency of the computations: symmetry and sparseness. This is especially true for the asymmetric modes.

Where the impedance matrix for the axisymmetric case is only diagonally symmetric, the rectangular case has more symmetries that reduce the number of elements needed significantly:

$$Z_{n_x n_y m_x m_y} = \begin{cases} Z_{m_x m_y n_x n_y}, \\ Z_{n_x m_y m_x n_y}, \\ Z_{m_x n_y n_x m_y}. \end{cases} \tag{215}$$

For symmetric modes, the matrix is full, but for asymmetric modes, modal coupling only occurs between mode pairs that have the same parity indices in both directions, with the result that only one fourth of the modes are non-zero [289]. A few examples of the reduction in matrix elements that must be computed are given in Table 3.

N_{modes}	Total	Symmetric	Asymmetric
9	81	36	16
16	256	100	36
256	65536	18496	5184

Table 3: Number of radiation impedance matrix elements necessary to compute when the symmetry of the matrix is taken into account.

5.5.2 *Polynomial Approximation*

As for the axisymmetric case, employing a polynomial approximation for the low frequency impedance values is possible, and also extremely efficient, much more so than interpolation. Tests indicates that due to finite numerical precision, the absolute limit for the polynomial approximation is for $ka \approx 15$ (assuming $ka \geq kb$), regardless of the number of terms.

Repeating Eq. (202),

$$Z_{nm} = \frac{j\omega\rho}{2\pi S^2} \int_0^{2a} d\xi \int_0^{2b} d\zeta \frac{e^{-jk\sqrt{\xi^2+\zeta^2}}}{\sqrt{\xi^2+\zeta^2}} G(n_x, m_x, \xi, a) G(n_y, m_y, \zeta, b),$$

the basic idea is to express the exponential as a series expansion:

$$e^x = 1 + x + \frac{x^2}{2!} + \frac{x^3}{3!} + ...$$

By inserting this expansion into Eq. (202), and simplifying the notation by setting $G_x = G(n_x, m_x, \xi, a)$, etc, we get

$$Z_{nm} = \frac{j\omega\rho}{2\pi S^2}\left\{\int_0^{2a} d\xi \int_0^{2b} d\zeta \frac{1}{\sqrt{\xi^2+\zeta^2}} G_x G_y + \int_0^{2a} d\xi \int_0^{2b} d\zeta (-jk) G_x G_y \right.$$
$$\left. + \int_0^{2a} d\xi \int_0^{2b} d\zeta \frac{(-jk)^2}{2!}\sqrt{\xi^2+\zeta^2} G_x G_y + ...\right\}, \quad (216)$$

or

$$Z_{nm} = \frac{j\omega\rho}{2\pi S^2}\left\{\int_0^{2a} d\xi \int_0^{2b} d\zeta \frac{1}{\sqrt{\xi^2+\zeta^2}} G_x G_y - jk \int_0^{2a} d\xi \int_0^{2b} d\zeta G_x G_y \right.$$
$$\left. + k^2 \int_0^{2a} d\xi \int_0^{2b} d\zeta \frac{1}{2!}\sqrt{\xi^2+\zeta^2} G_x G_y - ...\right\}, \quad (217)$$

i.e. we get a polynomial in $-jk$ with the coefficients

$$K_{nm}^p = \int_0^{2a} d\xi \int_0^{2b} d\zeta \frac{(\xi^2+\zeta^2)^{\frac{p-1}{2}}}{p!} G_x G_y,\ p = 0, 1, 2... \quad (218)$$

The first term is the mass reactance. For higher order modes, the low frequency slope of the radiation resistance is very steep (4th to 10th order), and the mass term will dominate up to a fairly ka value.

It is of course possible to split the expression into real and imaginary parts [290]:

$$R_{nm} = -\frac{\omega\rho}{2\pi S^2}\int_0^{2a} d\xi \int_0^{2b} d\zeta \frac{\sin\left(k\sqrt{\xi^2+\zeta^2}\right)}{\sqrt{\xi^2+\zeta^2}} G(n_x, m_x, \xi, a) G(n_y, m_y, \zeta, b) \quad (219)$$

$$X_{nm} = \frac{j\omega\rho}{2\pi S^2}\int_0^{2a} d\xi \int_0^{2b} d\zeta \frac{\cos\left(k\sqrt{\xi^2+\zeta^2}\right)}{\sqrt{\xi^2+\zeta^2}} G(n_x, m_x, \xi, a) G(n_y, m_y, \zeta, b) \quad (220)$$

and then approximate the sine and cosine functions as power series [291]:

$$\sin x = x - \frac{x^3}{3!} + \frac{x^5}{5!} - ...$$
$$\cos x = 1 - \frac{x^2}{2!} + \frac{x^4}{4!} - ...$$

Due to the steep slope of the radiation resistance for many of the higher order modes, the polynomial approximation will be more accurate than numerical integration for low frequencies. For instance, for mode (3,5)(3,5), the radiation resistance is $1 \cdot 10^{-21}$ at $ka = 0.1$, and numerical integration can be quite inaccurate.

5.5.3 *A High Frequency Approximation*

As for the axisymmetric case, it is possible to make a high frequency approximation based on the plane wave impedance. Unfortunately the rectangular opening does not have the same high frequency asymptotes for all modes. But for the diagonal mode radiation resistance, the following approximation works well for symmetric modes:

$$R_{mm,HF} = R_{00} \frac{k}{\sqrt{k^2 - \left(\frac{m_x \pi}{a}\right)^2 - \left(\frac{m_y \pi}{b}\right)^2}}. \tag{221}$$

Note that for diagonal modes, $m_x = n_x$ and $m_y = n_y$.

5.5.4 *Impedance Impulse Response*

As is well known, it is possible to express the radiation impedance in the time domain, as an impulse response [292, 293]. For many piston shapes, an analytical expression for the impulse response can be found. For the multimodal case, numerical integration is necessary. The most straightforward way to implement this, is to replace the complex exponential with the Dirac delta function in Eq. (202). We can then express the radiation impedance as a frequency dependent constant multiplied by the Fourier transform of an impulse response:

$$Z = \frac{j\omega\rho}{2\pi S^2} \mathcal{FT}\left\{h(t)\right\}$$

where

$$h(t) = \int_0^{2a} d\xi \int_0^{2b} d\zeta \frac{\delta\left(t - \frac{\sqrt{\xi^2+\zeta^2}}{c}\right)}{\sqrt{\xi^2 + \zeta^2}} G(n_x, m_x, \xi, a) G(n_y, m_y, \zeta, b). \tag{222}$$

The length of the impulse response is given by the maximum distance between two points on the baffle, which is the length of the diagonal, and the sampling frequency. Computing the radiation impedance is now a simple Fourier transform of the (tabulated) impulse response, followed by a multiplication. While using FFT may seem like a good idea, it requires very many bins to get good low frequency resolution, and the high frequency resolution is then much too high. In most cases, DFT is more efficient, since relatively few frequency points are usually needed, and these are typically logarithmically spaced.

Examples of the resulting impulse response for three modes for a square piston are given in Figure 50. The integral has been computed using Gauss-Legendre quadrature rule, with 1000 points for Figure 50a and 3000 points for Figures 50c and d. The sampling frequency corresponds to $ka = 1460$.

In addition, the numerically differentiated impulse response is compared with Lindemann's analytical result, Figure 50b. The agreement is good, but shows some numerical noise in the numerically differentiated impulse response. The original impulse response was computed with 3000 integration points, but is otherwise identical to Figure 50a.

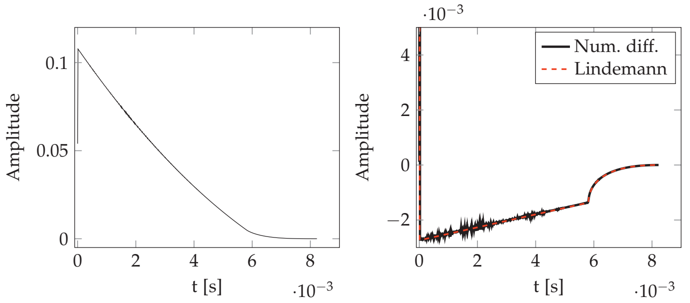

(a) Mode (0,0,0,0)

(b) Mode (0,0,0,0), differentiated impulse response compared with Lindemann's analytical expression.

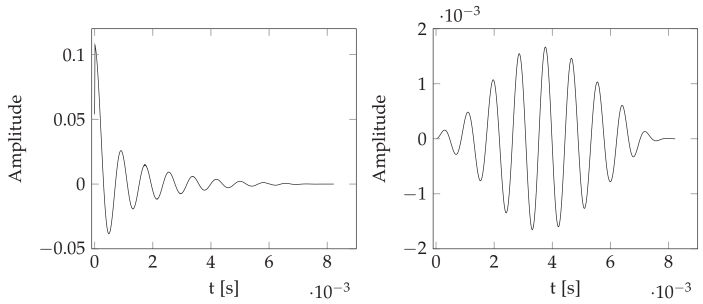

(c) Mode (5,5,5,5)

(d) Mode (5,5,4,4)

Figure 50: Example impulse responses

The resulting impedance curves for the two cases in Figure 50a and Figure 50c are given in Figure 51, plotted up to $ka = 730$. In the same plots, the impedance computed by the numerical integration methods are given. Several comments are in order.

- The impulse response based impedance is computed using a 2048-point FFT, which gives a rather poor low frequency resolution. This illustrates the comment given above.

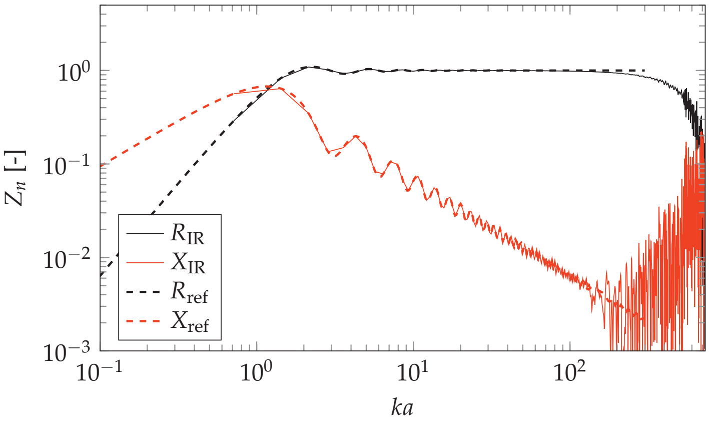

(a) Mode (0,0,0,0)

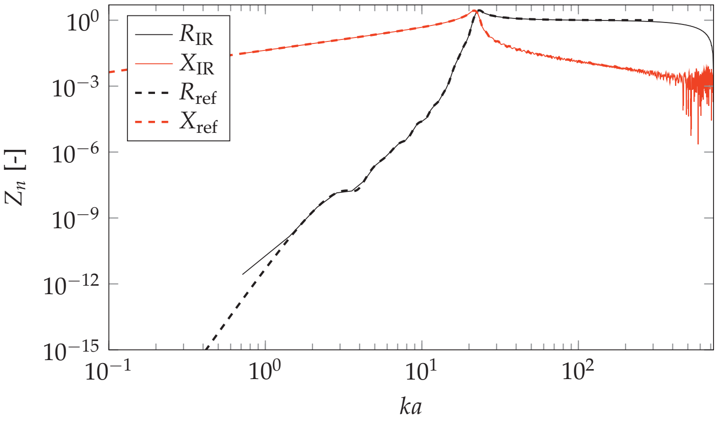

(b) Mode (5,5,5,5)

Figure 51: Impedance computed from the impulse responses in Figure 50a and Figure 50c.

- Some high frequency noise is apparent, and it is more obvious when fewer integration points are used. For the (0,0,0,0)-mode, the noise can also be seen by looking closely at the impulse response, especially around $t = 2 \cdot 10^{-3}$s.

- There is a high frequency droop in the radiation resistance. This is only a problem for the diagonal modes, where the impulse response starts with a step, and is not so obvious for other modes, where the impulse response starts from zero. The cause is most likely an error in the initial sample of the impulse response.

- Due to the very steep slope of the radiation resistance curve at low frequencies for higher order modes, the resistance values are very small. Numerical errors then result in large relative errors at low frequencies. The error that can be seen in Figure 51b below $ka = 1$ is not due to the small FFT-size; the slope of the curve is wrong.

Fortunately, there are ways to overcome these problems, as outlined above. The droop in the diagonal mode radiation resistance for large ka can be circumvented by using the high frequency approximation here, and the low frequency error can be avoided by using the polynomial approximation below $ka = 2$ or so. The high frequency noise is reduced by increasing the number of integration points, and this is most likely most critical for the first part of the impulse response.

5.5.5 *Performance*

Mean and maximum errors for three different methods are shown in Figure 52. Here the radiation impedance for 256 mode combinations at 300 frequencies have been computed. The reference is numerical integration of Eq. (202) using Gauss-Legendre integration. The impulse response has been computed using 3000 Gauss-Legendre points in each direction, and the legend *IR, D* indicates that for this case, the impedance of the diagonal modes has been computed using the high frequency asymptote above $1.75k_c$. The basis for the interpolation is impedance values computed using the reference method, using 525 linearly spaced frequency values ($N_k = 1.75 \cdot k_{a,max}$), and interpolation is by the cubic spline method. Note that the error is rather large at some individual frequencies; this is close to the zero-crossings of the oscillating functions.

Using the high frequency approximation for the diagonal modes for the impulse response does not improve the mean or maximum error for the impulse response method, as the error for the other modes follow the same behavior. Low/mid frequency error is rather good for the impulse response method, but the error increases with frequency and goes over 1% at around $f_s/20$. This could probably be improved by a better integration scheme for this method.

Interpolation performance is rather uniform over the frequency range covered, and has lower high frequency error. The low frequency error can easily be improved by adding a few more data points here.

Both methods could clearly be improved, and it should also be noted that relative error can be misleading in cases where the values in question are very small. In some frequency ranges, certain mode impedances are very small, and contributes very little to the total error in practical use, but may give a large contribution to a mean or maximum relative error calculation.

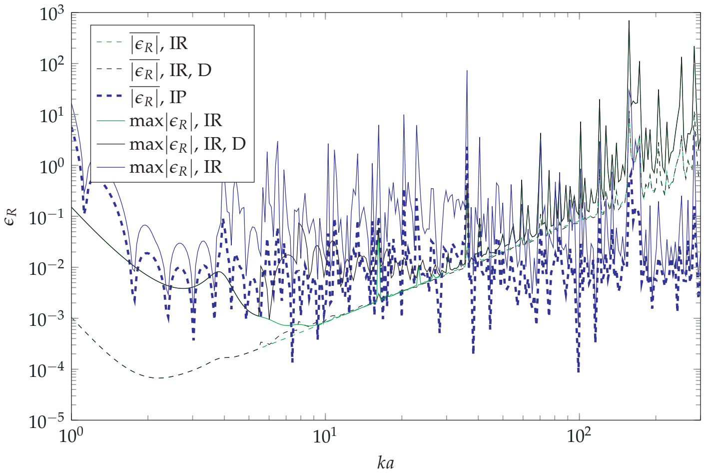

(a) Resistance error.

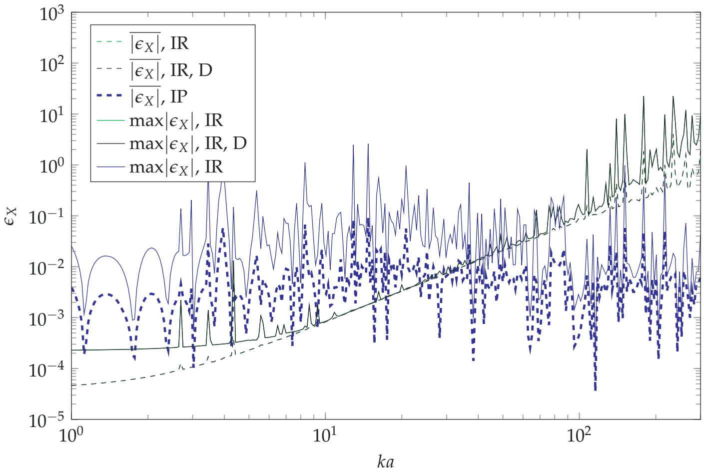

(b) Reactance error.

Figure 52: Mean and maximum relative error for three methods for computing the radiation impedance for rectangular ducts. *IR* indicates impedance calculated from the impulse response. *IR, D* indicates that the impedance of the diagonal modes has been computed using the high frequency asymptote above $1.75k_c$. *IP* indicates interpolation.

5.5.6 *Aspect Ratio Transformation*

For axisymmetric ducts, the radiation impedance can be tabulated once and for all, and interpolation, polynomial approximations etc can be used for all future calculations. For rectangular ducts, there is one additional variable: the aspect ratio. Horns come in all sorts of aspect ratios, although ratios between 1:1 and 1:5 are probably most common. Tables can be computed for a set of aspect ratios, but what to do when the aspect ratio is between two of the tabulated ratios? Interpolation between normalized impedance curves for two aspect ratios is possible, but usually results in low accuracy since the oscillations of the curves often are more or less out of phase.

Perhaps the most elegant transformation of aspect ratios is to use the same method as is used for a discontinuity in MMM: using the F-matrix (seeEq. (124)):

$$Z^{(1)} = \frac{S_1}{S_2} F Z^{(2)} F^T. \tag{223}$$

In this way, the radiation impedance for any aspect ratio can be found with two matrix multiplications. Note that it is only necessary to have a dimensional change in one plane, either x or y.

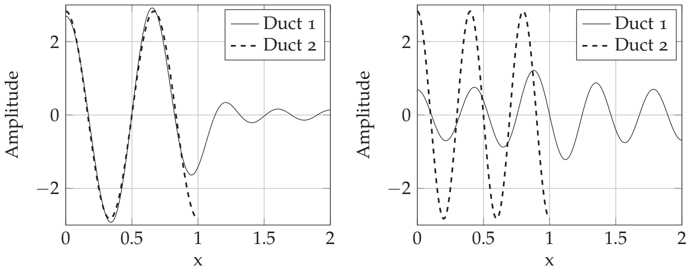

(a) Mode 3 in duct 2.

(b) Mode 5 in duct 2.

Figure 53: Mode resolution in F-matrix aspect ratio transformation. Duct 1 belongs to the tabulated impedance, Duct 2 belongs to the transformed impedance. 10 modes are used.

One should be aware, however, that to get an accurate transformed impedance, there must be enough modes in the original impedance matrix to describe the highest mode to be used in the transformed impedance matrix. This assumes that the impedance is transformed from a larger to a smaller area so that F-matries can be used. Figure 53 illustrate the idea. Here a rather large aspect ratio transform takes place, from 1:2 to 1:1, so the width of the duct is reduced by a factor of two. A total of 10 modes are used in the computation. As can be seen, the lower order modes in the narrow duct can (duct 2) be sufficiently represented by the modes in the wide duct (duct 1) to represent the sound field with reasonable accuracy, Figure 53a. But as the higher modes in duct 2 will have a higher spatial frequency than the highest mode in duct 1, these modes can no longer be represented by the modes in duct 1.

Based on the above, and on the periodic nature of the mode functions for rectangular ducts, the number of possible modes in the original and transformed impedance matrices can be found from

$$\frac{A_1}{A_2} = \frac{n_2}{n_1} \tag{224}$$

where A_1 and A_2 are the two aspect ratios, assuming that change occurs by changing only one of the dimensions, and n_1 and n_2 are the highest indices of the modes in the direction of change. As an example, if the transformation ratio is 2, and 10 modes (the highest mode index is 9) are used in the original impedance matrix, we find that $n_2 = \frac{A_1}{A_2} n_1 = \frac{1}{2} 9 = 4.5 = 4$. That is, the highest mode index that can be used in the transformed matrix is 4, which verifies the examples in Figure 53. The other way around, if mode 5 is to be represented, the highest mode index is $n_1 = \frac{A_2}{A_1} n_2 = \frac{2}{1} 5 = 10$, i.e. 11 modes must be used.

Figure 54 shows two example of the results. In Figure 54a, enough modes are present to adequately describe the field in duct 2, and the impedance is correct up to $ka = 26$. In Figure 54b, there are no longer enough modes (the mode index in the y-direction is one higher than in the previous example), and the transformed impedance values deviates rather much from the actual values.

The deviation above $ka = 26$ in Figure 54a needs commenting. The exact origin of this deviation is hard to determine due to the complexity of the interaction between the modes through the matrix multiplications. But the magnitude of the deviation is to a degree dependent on the transformation ratio, and the frequency at which it appears depends on the number of modes in the transformation. Tests indicates that the error increases above the cutoff frequency of the highest mode of the transformed impedance[2] up to the cutoff frequency of the highest mode in the original impedance matrix. These values are approximate, but seem to given an indication of where the error can be expected to be large.

If the aspect ratio is just the inverse of the aspect ratio of the precomputed data, the transformation can be performed without loss of accuracy by rearranging the radiation impedance matrix. All that needs to be done is to interchange elements so that

$$Z_{n_x n_y m_x m_y} \to Z_{n_y n_x m_y m_x}, \tag{225}$$

---

[2] Each modal impedance describes a relation between a pressure mode and a velocity mode, which each have their own cutoff frequency. The cutoff frequency mentioned is the highest of these.

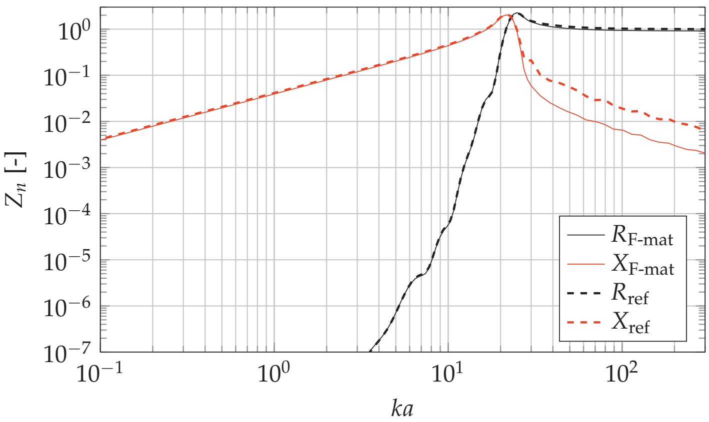

(a) Mode (4,3,4,3)

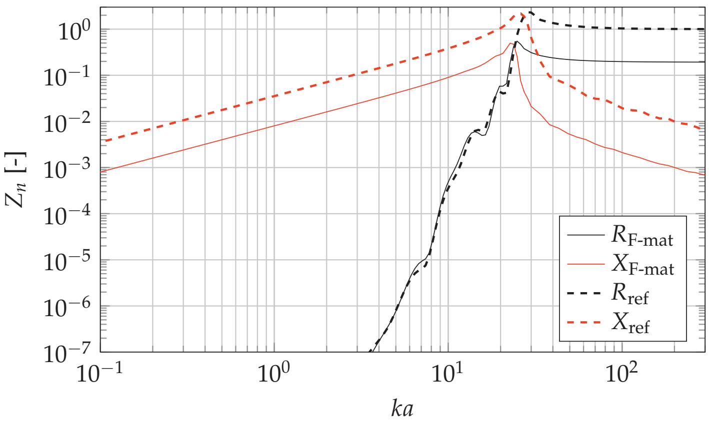

(b) Mode (3,4,3,4)

Figure 54: Aspect ratio impedance transformation, using a total of 64 symmetric modes in the transformation. Aspect ratio changes from 1:1 to 2:1.

i.e. the indices corresponding to x are exchanged for those corresponding to y. This means that the impedance for Z_{1234} for the new aspect ratio can be found at the place of Z_{2143} in the table of the inverse aspect ratio.

5.6 SUMMARY

This chapter has shown several methods to speed up the calculation of the infinite baffle radiation impedance. While not radically new methods, some work has been put into determining the appropriate frequency ranges and conditions for the various methods. These ranges must necessarily be approximate, based on a judgment of what is adequate accuracy.

For the axisymmetric case, interpolation in the middle frequency range, combined with a simple high frequency approximation above the highest mode cutoff and a polynomial approximation for low frequencies appears to be the most appropriate.

For the rectangular case, it has been shown that a reformulation of the equations given by Kemp offers a computational advantage when the impedances for many modes and frequencies are to be computed. Tabulation and interpolation of impedance is also an option in the rectangular case, although instead tabulating the impulse response is also an option. However, a definite upper frequency limit is now imposed, and if this limit is, say, doubled, the number of data points is also doubled. For tabulation/interpolation, one is able to get away with the high frequency approximation for the diagonal matrix elements, and would have no upper frequency limit here. For the other elements, a few sample points for, say, $ka > 300$, could give a good enough approximation, since the impedance elements on the diagonal of the matrix dominate in this range.

Unless the high frequency performance of the impulse response method can be improved, interpolation with a somewhat denser sampling in the region of maximum modal contribution, is probably the method of choice.

For low frequencies, again the polynomial approximation is the most suitable.

To be able to simulate horns with aspect ratios that are not tabulated, a transformation using the F-matrix is suitable for low and medium frequencies, up to approximately the cutoff frequency of the highest mode in the original impedance matrix. Above this frequency, some error begin to creep in, and interpolation between two aspect ratios may be a better option, in particular for reactance and off-diagonal elements. Although this method will not give the exact shape of the curves, the error may be less than for the F-matrix transformation. The high frequency approximation may be used for the resistance for the diagonal elements.

No horn example is given in this chapter, as the infinite baffle model has been evaluated and verified numerically in previous work [38]. But an experimental verification is provided in Section 9.2.

6

HORNS IN FULL-SPACE

In many cases the horn is not mounted in an infinite baffle. More common is that the horn is either free standing or mounted in a box, the width of the box often being not much larger than that of the horn. In order to simulate horns under such conditions, the influence of the pressure diffracted from the edges on the radiation impedance and radiated pressure, must be taken into account. Two methods will be presented: the method developed by Snakowska [287] for multimodal radiation from a circular unflanged duct, and the Edge Diffraction Method (EDM) due to Svensson [49], which is usable for general geometries including the enclosure. The methods will be discussed separately.

An experimental verification of the EDM as applied to horns, as outlined in this chapter, is given in Section 9.3 on page 198.

The contributions in this chapter are the application of Snakowska's method to an unflanged circular horn, and the application of the EDM to rectangular horns with small flanges, including how to compute the radiation impedance for a horn with a small flange, and investigating the contribution of diffraction to the total radiation impedance. The work on rectangular horns has previously been published in [45].

6.1 AXISYMMETRIC GEOMETRY

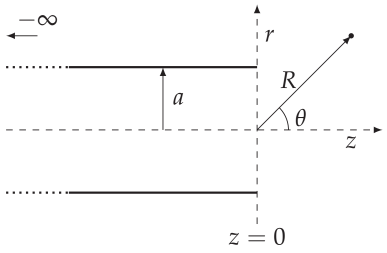

Figure 55: Geometry of the circular unflanged duct problem.

The problem of an unflanged circular duct is much more complicated than the flanged duct problem. The reasons include the diffraction at the open end, and the presence of the duct in the sound field, which introduces a discontinuity of the field. The problem was investigated by Levine and Schwinger [294] for the plane wave mode, and by Weinstein [295] for all propagating modes. The solution arrived at by Weinstein was later taken up by Snakowska [46, 296, 297, 298], who also expanded the work to include non-axisymmetric modes. The theory presented in this section is based on their work. For a more complete summary of the derivation, see Appendix C.

The geometry of the circular unflanged duct problem is shown in Figure 55. With an incident mode of order l, the total sound field inside the duct, expressed in terms of the velocity potential, is given as

$$\Phi_l(r,z) = \frac{J_0\left(r\frac{\mu_l}{a}\right)}{J_0(\mu_l)}e^{ik_l z} + \sum_{n=0}^{N} R_{ln}\frac{J_0\left(r\frac{\mu_n}{a}\right)}{J_0(\mu_n)}e^{-ik_n z}. \tag{226}$$

The reflection factor R_{ln} can be expressed as

$$R_{ln} = -\frac{2k_l}{k_l+k_n}\left[\prod_{i=0,i\neq l}^{N_m}\frac{k_i+k_l}{k_i-k_l}\prod_{i=0,i\neq l}^{N_m}\frac{k_i+k_n}{k_i-k_n}\right]^{\frac{1}{2}} e^{\frac{1}{2}(S(k_l)+S(k_n))}. \tag{227}$$

It may be more convenient to express R_{ln} as modulus and phase,

$$R_{ln} = -\left|R_{ln}\right| e^{i\theta_{ln}},$$

in which case

$$\left|R_{ln}\right| = \frac{2k_l}{k_l+k_n}\left[\prod_{i=0,i\neq l}^{N_m}\left|\frac{k_i+k_l}{k_i-k_l}\right|\prod_{i=0,i\neq l}^{N_m}\left|\frac{k_i+k_n}{k_i-k_n}\right|\right]^{\frac{1}{2}} e^{\frac{1}{2}(X(k_l)+X(k_n))} \tag{228}$$

and

$$\theta_{ln} = \begin{cases} Y(k_l)+Y(k_n), & l+n \text{ even}, \\ Y(k_l)+Y(k_n)+\pi, & l+n \text{ odd}. \end{cases} \tag{229}$$

The functions $X(w)$ and $Y(w)$ are defined as

$$X(w) = \frac{1}{\pi}P\int_{-k}^{k}\frac{\Omega(v'a)}{w'-w}dw' \tag{230}$$

$$Y(w) = \frac{2wa}{\pi} - \Omega(va) - i\lim_{M\to\infty}\left[\sum_{n=N_m+1}^{M}\frac{k_n+w}{k_n-w} - \frac{1}{\pi}\int_{-k_N}^{k_N}\frac{\Omega(v'a)}{w'-w}dw'\right], \tag{231}$$

where

$$\Omega(v'a) = \arg H_1^{(1)}(v'a) - \frac{\pi}{2}. \tag{232}$$

From these functions, it is possible to compute the reflectance matrix $\mathbb{R}$, and from Eq. (188) the radiation impedance can be found.

However, these functions are only valid above the mode cutoff frequency.

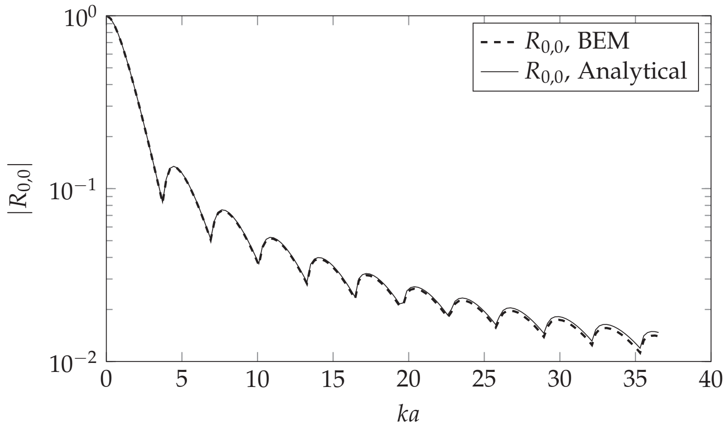

(a) Modulus

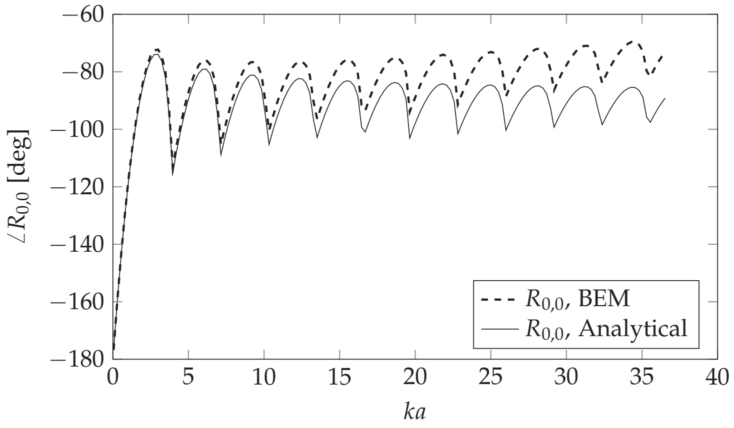

(b) Phase

Figure 56: Plane wave reflection factor for an unflanged circular duct, comparison of BEM and analytical method.

6.1.1 *Reflection Factor*

For the examples in this section and the next, a reference result for the radiation impedance was computed using BEM for a range of *ka* up to 36. The structure was a cylinder with a radius $a = 0.5\,\mathrm{m}$ and a length $4a$, where the rear half had an absorbing boundary condition (surface impedance $Z = \rho_0 c$). The sound field at the end surface of this cylinder was decomposed into modes, creating a matrix of modal impedances, as described in Section 10.1 on page 215. This matrix was converted to a matrix of reflection factors using Eq. (187), and the results compared to the results computed from Eq. (227) above. The comparison for the plane wave reflection factor is shown in Figure 56.

The results are reasonably similar for the modulus Figure 56a, but more different for the phase angle, Figure 56b, since the phase is more sensitive to small numerical errors. As the differences increase with frequency, it may be suspected that this is a discretization issue.

The equations given in Section 6.1 are not applicable when any of the modes are in cutoff, as mentioned above. The strategy was therefore adopted to use the BEM results for frequencies where one or both modes are in cutoff, and the analytical expressions for the higher frequencies. The modulus and phase of the reflection factor for a few mode combinations are given in Figure 57. As can be seen, the reflectance matrix is not symmetrical, $R_{0,3}$ differs from $R_{3,0}$. What is interesting is that below cutoff, the reflection factor is very small, and increasing to a maximum at the cut-in frequency of the reflected mode.

6.1.2 *Radiation Impedance*

Examples of radiation impedance computed from a 16-mode reflectance matrix that is a hybrid between BEM for evanescent modes and analytical functions for propagating modes, are shown in figures 58 and 59. The fundamental mode impedance, Figure 58, which in this case corresponds to a piston in the end of an infinite tube, is similar to the radiation impedance of a piston in an infinite baffle for $ka > 2$, except for a slightly higher radiation mass. When many modes are included in the reflectance matrix, the oscillations are smooth, and the curves lack the odd discontinuous behavior seen when the impedance is calculated from the R_{00} reflection factor only (see also Figure 44). For lower frequencies, the radiation resistance is half of the infinite baffle resistance, as expected. Radiation mass is also slightly lower than for an infinite baffle.

For higher order modes, there is even more similarity between curves for infinite baffle and the unflanged duct, and again there is a difference in low frequency radiation resistance. The slope of the resistance curve for the unflanged duct for $ka < 1$ is less steep than for the infinite baffle case, and this is most likely an artifact from the BEM computations. Similar phenomena appear in other computations where low level modal information is numerically extracted from a sound field.

6.1.3 *Directivity*

The far field pressure of a single mode l radiated from an unflanged duct [48] is

$$p_l(R,\theta) = -\frac{ka}{2} P_l \sin\theta J_1(ka\sin\theta) F_l\left(-k\cos\theta\right)\frac{e^{ikR}}{R} = P_l d_l(\theta)\frac{e^{ikR}}{R}, \tag{233}$$

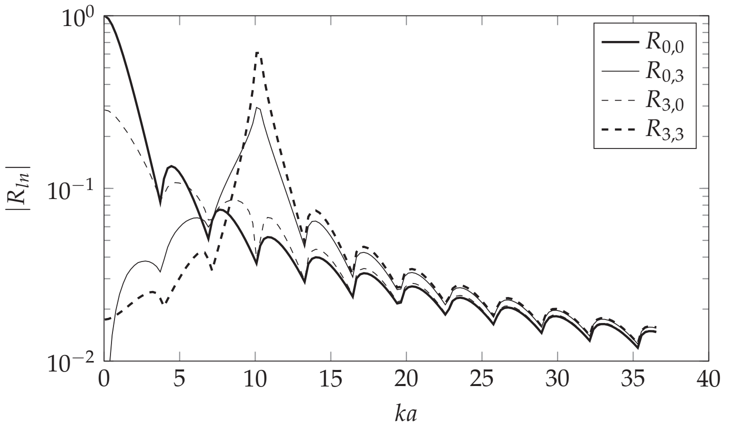

(a) Modulus

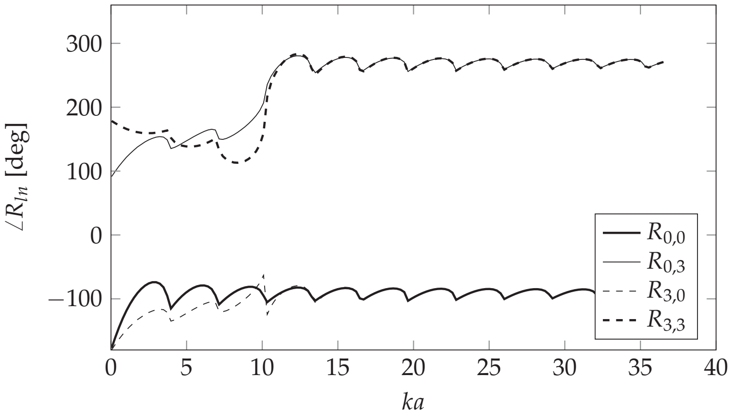

(b) Phase

Figure 57: Reflection factor for an unflanged circular duct, for a few mode combinations.

as outlined in Appendix C on page 277. P_l is pressure amplitude of mode l at the outlet.

A comparison was made with BEM, using the same geometry as in Section 6.1.1, only that the boundary condition at the radiating end was set to a constant pressure of 1 Pa. This would then correspond to the plane wave mode being radiated. Results for this case are given in figures 60 and 61. The directivity results (Figure 60) are reasonably close in the front hemisphere, in particular within 60° off axis, but the BEM results have more lobes for larger angles. This may be due to the fact that the BEM geometry is not infinitely long, and that there is a rear edge that causes diffraction that may disturb the sound field.

The frequency response, plotted in Figure 61, shows good agreement for $ka > 1$, however, there is significant discrepancy at low fre-

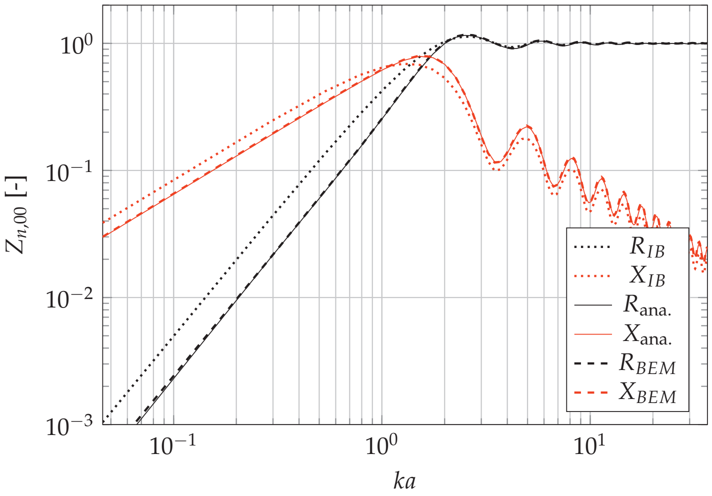

Figure 58: Fundamental mode radiation impedance, Z_{00}, normalized, for infinite baffle (subscript *IB*) and unflanged duct, using either a full BEM solution (subscript *BEM*) or the analytical solution for the cut-on region (subscript *ana.*).

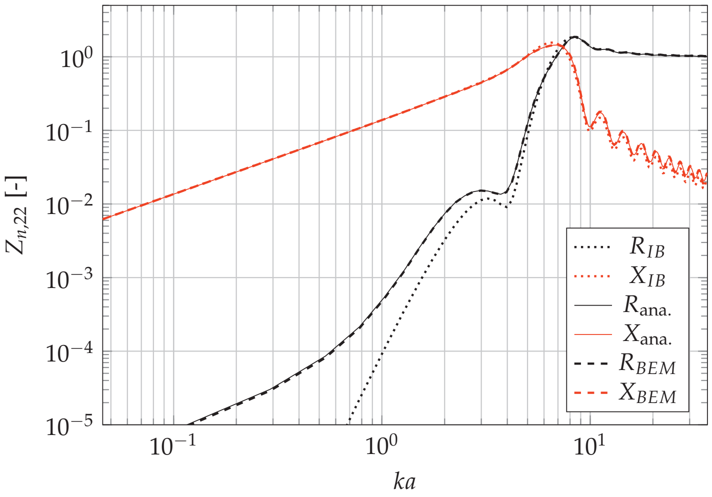

Figure 59: Radiation impedance for mode combination (2,2), Z_{22}, normalized, subscripts as above.

quencies. The analytical solution shows a rising on-axis response at all frequencies, while the BEM solution shows a nearly flat response at low frequencies. That this is the correct response for a pressure

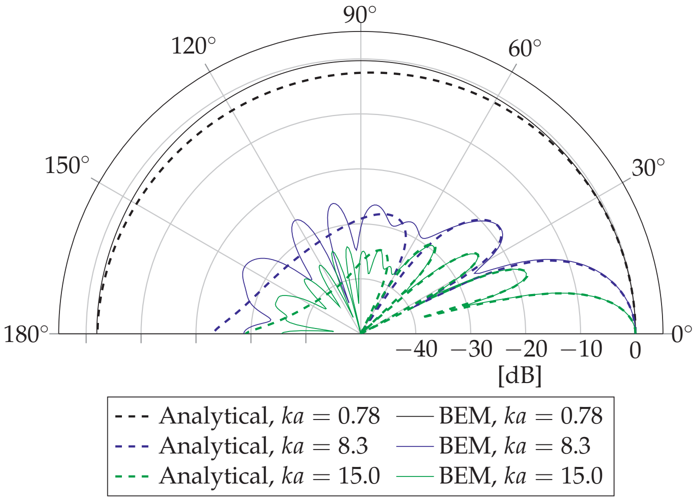

Figure 60: Polar response for a few values of *ka*.

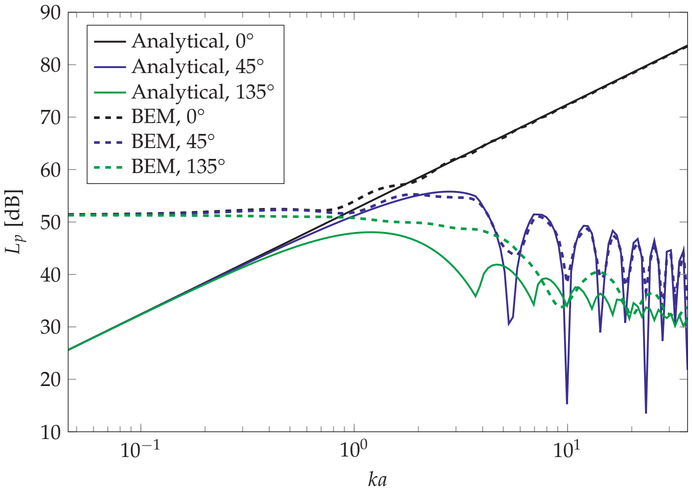

Figure 61: Frequency response for the plane wave mode, comparison with BEM.

monopole can be shown as follows: for a pulsating sphere, the radiated pressure is

$$p(r) = -jk\rho_0 c U_0 \frac{1}{1 + jka} \frac{e^{-jk(r-a)}}{4\pi r}.$$

Given that the acoustic radiation impedance of the sphere is

$$Z_{r,a} = \frac{\rho_0 c}{4\pi a^2} \frac{jka}{1 + jka}$$

and that $U = p/Z_a$, the radiated pressure for a sphere with a specified surface pressure p_s is

$$p(r) = -jk\rho_0 c p_s \frac{4\pi a^2}{\rho_0 c} \frac{1 + jka}{jka} \frac{1}{1 + jka} \frac{e^{-jk(r-a)}}{4\pi r} = -p_s \frac{a}{r} e^{-jk(r-a)},$$

which is a function of constant amplitude for all frequencies.

6.1.4 *A Horn Example*

As an example of the application of the theory outlined above, a horn mounted in a long tube was simulated. The horn was a tractrix horn, with a throat area of 10 cm², a mouth area of 1250 cm², and a length of 43 cm. The geometry is shown in Figure 62. A tractrix horn [89, 156] was chosen since the mouth flare tangent angle approaches 90°, which makes it possible to avoid very sharp angles between the elements in the BEM mesh near the edge of the horn mouth.

The radiation impedance was computed using a hybrid of BEM (below mode cutoff) and the analytical equations (above mode cutoff). The radiated pressure was found by calculating the mouth pressure mode amplitudes from the mouth velocity mode amplitudes and the radiation impedance, and then summing the contribution from each mode calculated from Eq. (233).

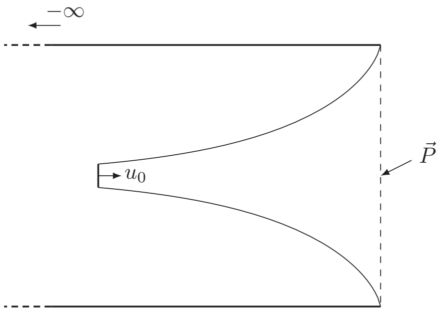

Figure 62: Horn geometry for a tractrix horn in a semi-infinite unflanged duct. The vector of mouth pressure mode amplitudes, $\vec{P}$, are used to determine the radiated pressure.

The throat impedance of the horn, compared to BEM, is shown in Figure 63. Agreement is fairly good between 200 Hz and 3 kHz. If radiation impedance is computed by BEM for all frequencies, the MMM results improve above 3 kHz, this indicates that the error exists in the analytical computations. The discrepancy below 200 Hz still exists, though, and may be due to the absorption applied to the rear end of the enclosing tube used in the BEM simulations.

The frequency response for a few angles is shown in Figure 64. We notice that:

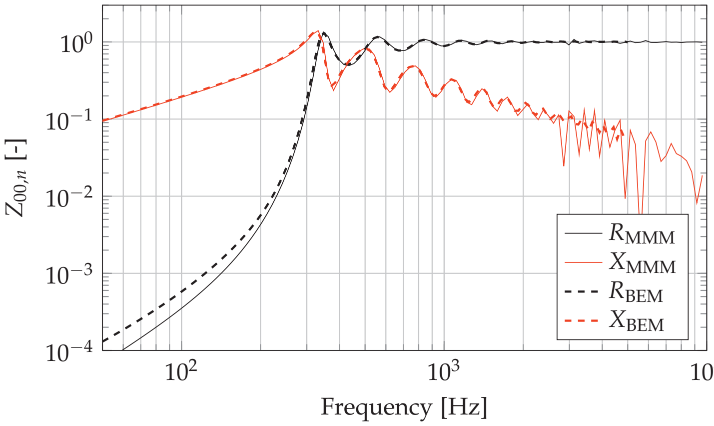

Figure 63: Throat impedance for the unflanged axisymmetric horn.

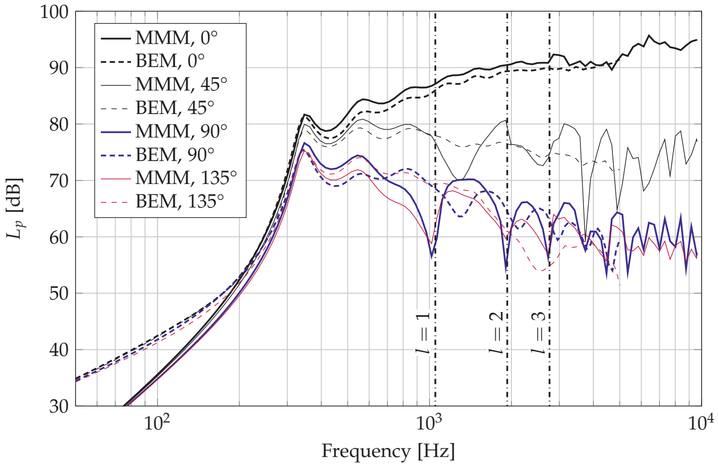

Figure 64: Frequency response for the unflanged axisymmetric horn. The vertical dash-dotted lines indicate the cutoff frequencies of the first three modes.

- The same low frequency behavior as observed in Section 6.1.3 can be seen for the horn: the low frequency slope for $ka < 1$ (in this case 275 Hz) is too steep.

- The shape of the on-axis response is fairly close, but there is a level difference of about 2.5 dB. Only the plane wave mode contributes to the on-axis response, as all the higher order modes have a zero in this direction [47].

- The off-axis response is much more ragged for MMM than for BEM. A possible explanation is that the higher order modes are ignored below their cutoff frequencies, and that this may

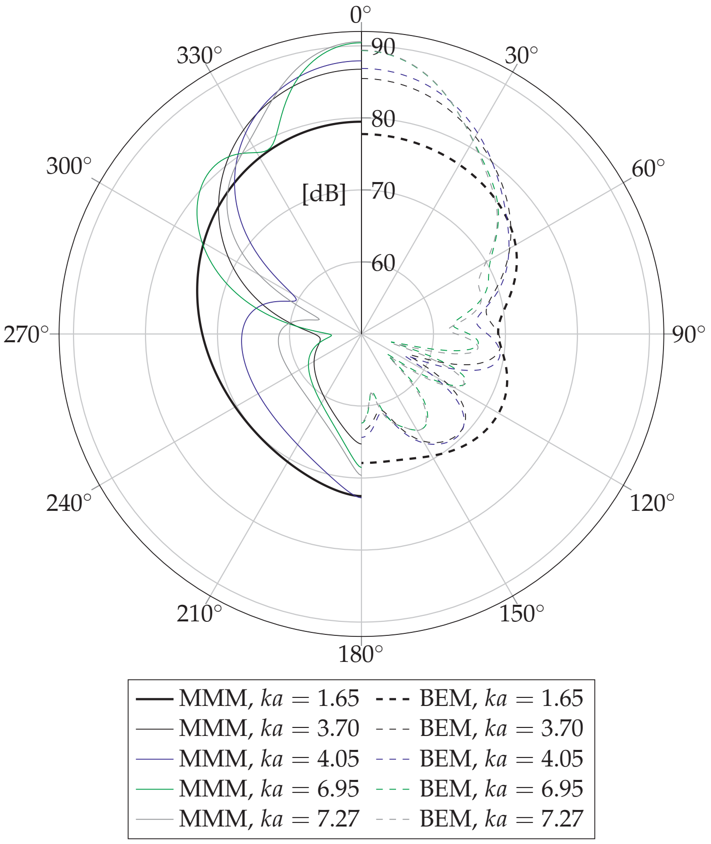

Figure 65: Polar response for the unflanged axisymmetric horn. The *ka* values correspond to 454 Hz, 1.02 kHz, 1.11 kHz, 1.91 kHz and 1.99 kHz.

create a sudden change in the response when each new mode is introduced. The cut-off frequencies for the first few modes are 1.05 kHz, 1.93 kHz and 2.76 kHz. Especially the 90° and 135° curves show large changes around these frequencies.

Figure 65 show the polar response for a few frequencies, expressed in terms of *ka*. Below the cutoff of the first mode, the reduced response at 90° is missing in the MMM results. The following pairs of frequencies show the polar response just below and just above the first and second mode cutoff frequencies. One notices the rather abrupt change in polar response, which is absent in the BEM results. The BEM results for the frequency pairs are nearly overlapping, while for the MMM results it is hard to see which curves are at nearly the same frequencies without consulting the legend.

6.1.5 *Summary*

The equations for the reflection factor and directivity for an unflanged semi-infinite duct, as described by Snakowska [46] have been implemented and applied to an axisymmetric horn. The equations, as presently developed, ignore evanescent modes. This makes it necessary to use BEM (or other numerical methods) for the frequency range where the modes are evanescent, in order to properly compute the reflectance matrix. This approach turned out to be fairly successful, although there are some discrepancies at both low and high frequencies. It should be possible to eliminate these discrepancies by a careful study of their origin.

Some comments on the results:

- Evanescent modes are ignored in the radiated pressure, and this makes the resulting response rather ragged, especially around the mode cutoff frequencies.
- It is clear that the contribution of the evanescent modes just below their cutoff frequencies should not be underestimated.
- There is an error in the low frequency slope of the analytical expression. The origin of this error is uncertain, but probably derives from the approximations used in deriving Eq. (233). In any case, this error makes Eq. (233) unsuitable for calculating the radiated pressure below $ka = 1$.

The analytical expressions for the reflection factor for an unflanged duct would be useful if they could be expanded to include evanescent modes. In horns, evanescent modes will be generated also close to the mouth, and it is not possible to make the assumption that they have died out before they reach the mouth, an assumption used in deriving the expressions used in this Section. The need for using BEM to obtain a full reflectance matrix makes the computations unnecessary complex. The analytical expression for directivity should also be modified to include the evanescent modes, in order to have a hope of producing correct results. In addition, the low frequency error must be corrected. As the equations currently stand, they are not entirely suitable for loudspeaker response calculations.

6.2 SUPERPOSITION

The principle of superposition will be important in the following section and in subsequent chapters. The basic principle, which is also the foundation of MMM, is that a sound field can be described as a linear combination of component sound fields, Figure 66. This may be a sum of the sound field from simple sources, from modes, or from direct and reflected sound. This, of course, requires that we operate

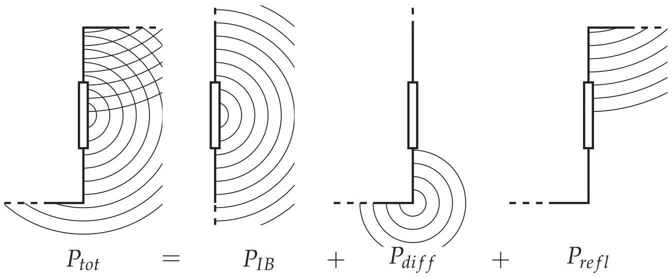

Figure 66: Principle of superposition.

in the region of linear acoustics, which is by no means given in horn loudspeakers. However, linearity will be assumed here, due to the much simpler equations that result, and since the results are applicable to most cases. Also, in situations where non-linearity is prominent in parts of the domain, typically close to the sound generation, the radiation might be adequately described by linear conditions [299].

Superposition may be applied to both the radiation impedance and the radiated pressure, and we may set up

$$\begin{aligned} p_{tot}(\mathbf{x}) &= p_{IB} + p_{diff} + p_{refl} \\ &= Q\left[G_{IB}(\mathbf{x}|\mathbf{x}_0) + G_{diff}(\mathbf{x}|\mathbf{x}_0) + G_{refl}(\mathbf{x}|\mathbf{x}_0)\right] \end{aligned} \tag{234}$$

where

p_{tot} is the total sound pressure at $\mathbf{x}$ due to a monopole source at $\mathbf{x}_0$,

p_{IB} is the direct, or geometrical, sound pressure due to the source, IB indicates Infinite Baffle.

p_{diff} is the sound pressure at $\mathbf{x}$ that has been diffracted on its way from the source, and

p_{refl} is the sound pressure at $\mathbf{x}$ that has been reflected on its way from the source.

We have that

$$G_{IB} = 2\frac{e^{-jkr}}{r} \tag{235}$$

is the infinite-baffle Green's function, for a monopole source signal $Q = j\omega\rho U/4\pi$, U is the volume velocity and

$$r = \sqrt{(x - x_0)^2 + (y - y_0)^2 + (z - z_0)^2}. \tag{236}$$

G_{diff} and G_{refl} are the Green's functions for diffracted and reflected sounds, respectively. For a velocity distribution in the mouth of a horn, specified by the volume velocity distribution, $U(x_0, y_0)$, the radiated sound pressure is then given by a surface integration over this velocity distribution,

$$p_{tot}(\mathbf{x}) = \frac{j\omega\rho}{4\pi S} \int_S U(x_0, y_0) \cdot \left[G_{IB}(\mathbf{x}|\mathbf{x}_0) + G_{diff}(\mathbf{x}|\mathbf{x}_0) + G_{refl}(\mathbf{x}|\mathbf{x}_0) \right] dS_0. \quad (237)$$

The G_{IB}-term yields the Rayleigh integral in Eq. (156) (page 98), so the sound pressure for the general case of a horn near reflecting boundaries and diffracting edges is

$$p_{tot}(\mathbf{x}) = p_{IB}(\mathbf{x}) + \frac{j\omega\rho}{4\pi S} \int_S U(x_0, y_0) \cdot \left[G_{diff}(\mathbf{x}|\mathbf{x}_0) + G_{refl}(\mathbf{x}|\mathbf{x}_0) \right] dS_0. \quad (238)$$

From Eq. (238) and Eq. (180) (page 105), it is clear that

$$Z_{rad,tot} = Z_{IB} + Z_{diff} + Z_{refl}. \quad (239)$$

Note that p_{IB} and Z_{IB} are always included in the total, and as we will see, dominate at high frequencies. At lower frequencies, the contributions from diffraction and reflection play a greater part, and act as correction terms to the infinite baffle terms. Depending on the relative magnitude of these extra terms, it may not be necessary to compute them with as high precision as the direct sound.

6.3 EDGE DIFFRACTION METHOD

In Section 6.1, analytical expressions for the radiation impedance and directivity of a semi-infinite, unflanged circular duct were presented. While it may be possible to employ a similar method for rectangular ducts, the procedure is complex, and the geometry is fairly restricted. And, as pointed out in Section 6.1.5, there are some problems with this method that must be solved before it can be applied to horn speakers.

In order to simulate more general structures external to the horn, like flanges and cabinets, the Edge Diffraction Method (EDM) due to Svensson et al. [49] may be used. This method is based on the analytical solution of the problem of diffraction from an infinite wedge as given by Biot and Tolstoy [301], where the diffracted wave is described in terms of a line integral. A frequency-domain formulation for the first-order diffraction term was presented by Svensson et al. [50] in the form of a line integral along the edges of a scattering object. An efficient method for computing the resulting integrals was later presented by Asheim and Svensson [302]. For a finite edge, the

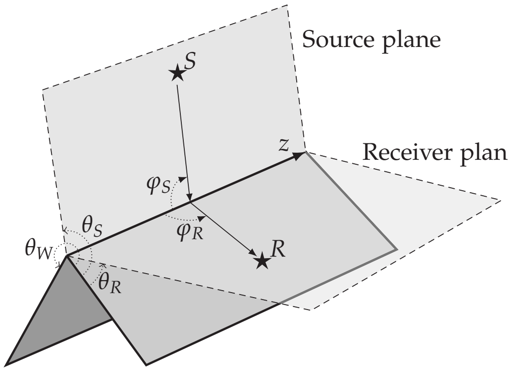

Figure 67: A wedge, where sound from the source at S is diffracted and received at R. Redrawn from [300].

integration is performed only over the physical edge. Using the notation that $r_{a,b}$ represents the distance between points a and b, the diffracted field at receiver position R is expressed as [300]

$$p_{diff} = -\frac{\nu}{4\pi}\int_{z_1}^{z_2} \frac{e^{-jkr_{R,z}}}{r_{R,z}}\frac{e^{-jkr_{z,S}}}{r_{z,S}}\beta(R,z,S)dz \tag{240}$$

where z describes the edge, and ν is a wedge index defined as

$$\nu = \frac{\pi}{\theta_W}$$

where θ_W is defined as in Figure 67. The function $\beta(R,z,S)$ is a directivity function of the diffracted field, given as

$$\beta(R,z,S) = \sum_{i=1}^{4} \frac{\sin(\nu\phi_i)}{\cosh(\nu\eta) - \cos(\nu\phi_i)}, \tag{241}$$

where ϕ_i are defined, for the Neumann boundary condition, as

$$\phi_1 = \pi + \theta_S + \theta_R, \qquad \phi_2 = \pi - \theta_S + \theta_R,$$
$$\phi_2 = \pi - \theta_S - \theta_R, \qquad \phi_4 = \pi + \theta_S - \theta_R,$$

and

$$\eta = \cosh^{-1}\frac{\cos\varphi_S\cos\varphi_R + 1}{\sin\varphi_S\sin\varphi_R}. \tag{242}$$

The angles θ_R, θ_S, φ_R and φ_S are defined in Figure 67.

If there is more than one edge, or the edge is not straight, there will be higher order diffraction. These higher order diffraction components could be represented by higher order integrals [49], with double integrals for second order diffraction and so on, but in [300] a formulation is described which avoids this exponential increase in computation cost. There the first order diffraction is computed separately, and a special integral equation is used for second and higher order diffraction. The total sound field is then the sum of the geometric field (direct sound) first order and higher order diffraction, using the principle outlined in Section 6.2.

The methods described in the papers referred to above are, or will be, implemented in a freely available Matlab toolbox [303].

Considering a sound field where only diffraction and direct sound is taken into account, the sound pressure radiated by a monopole, p_0, in a position $\mathbf{x}_0$, on a finite baffle [300] in $z = 0$, is:

$$\begin{aligned} p_0(\mathbf{x}) &= p_{IB} + p_{d1} + p_{hod} \\ &= Q\left[G_{IB}(\mathbf{x}|\mathbf{x}_0) + G_{d1}(\mathbf{x}|\mathbf{x}_0) + G_{hod}(\mathbf{x}|\mathbf{x}_0)\right] \end{aligned} \quad (243)$$

where G_{IB} is, as in Section 6.2, the infinite-baffle Green's function, $Q = j\omega\rho U/4\pi$ is the monopole strength, and U is the volume velocity. G_{d1} is the corresponding Green's function for the first-order diffraction waves off the edges of the finite baffle, and G_{hod} represents the second order and all higher orders of diffraction.

Proceeding as in Section 6.2, and further splitting p_{diff} up into first order and higher order diffraction, the radiated sound pressure from a radiator with the velocity distribution given by $U(x_0, y_0)$ is

$$\begin{aligned} p_{fb}(\mathbf{x}) = p_{IB}(\mathbf{x}) + \frac{j\omega\rho}{4\pi S} \int_S & U(x_0, y_0) \\ & \cdot \left[G_{d1}(\mathbf{x}|\mathbf{x}_0) + G_{hod}(\mathbf{x}|\mathbf{x}_0)\right] dS_0. \end{aligned} \quad (244)$$

The first-order diffraction term G_{d1} and the higher order diffraction term, G_{hod}, can be computed for convex, rigid scattering objects via an integral equation, as described in [300].

From Eq. (239), we see that we can find the total radiation impedance as

$$Z_{rad,tot} = Z_{IB} + Z_{d1} + Z_{hod}, \quad (245)$$

where Z_{d1} and Z_{hod} are impedances due to the diffracted pressure.

To compute Z_{d1} and Z_{hod}, we must perform the double surface integral (see Eq. (180), on page 105)

$$Z_{mn} = \frac{j\omega\rho}{4\pi S^2} \int\limits_S \int\limits_S G(\mathbf{x}|\mathbf{x}_0) \cdot \psi_m(x_0, y_0)\, \psi_n(x, y)\, dS_0 dS \quad (246)$$

over the horn mouth surface, using the edge diffraction Green's functions G_{d1} and G_{hod}, respectively, from Eq. (243), for $G(\mathbf{x}|\mathbf{x}_0)$.

In this study, a simplified geometry has been used, where the exterior of the horn is represented only by an infinitely thin plate corresponding to the flange. This simplified geometry reduces both the number of edges that have to be discretized, and the number of paths for higher order diffraction, hence reducing computation time. A grid of 24 by 24 points distributed according to the Gauss-Legendre quadrature rule was placed over the area of the horn mouth on one side of the plate, see Figure 68. Each point was used both as source and as receiver. Since the direct sound is computed separately, no singularity occurs when $\mathbf{x} = \mathbf{x}_0$.

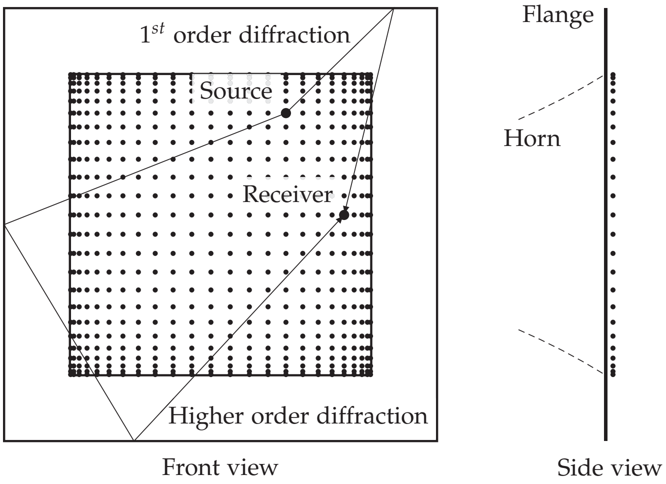

Figure 68: Geometry of horn flange, with the placement of source and receiver points for edge diffraction calculation. The sources and receivers are placed a short distance in front of the flange, which is modeled as a thin rigid plate. The horn, indicated by dashed lines, is not part of the EDM geometry. Example paths for first order and higher order diffraction are indicated.

The method to compute G_{hod} encounters singularities when a receiver point, $\mathbf{x}$, in free space is co-planar with two edges. However, for the impedance computation all receiver points are on the baffle, and no such singularity problems occur. A final singularity occurs when $\mathbf{x}$ is very close to an edge, but for the horns studied here, a part of the flange always extends beyond $\mathbf{x}$ and $\mathbf{x}_0$ when calculating the radiation impedance. Even for horns with no flange, this singularity is easily avoided by employing integration schemes that do not require evaluation of the function at the endpoints.

The transfer functions between all combinations of sources and receivers were calculated separately. First order and higher order diffraction terms were also kept separate in the calculations, to investigate their effects separately.

When all transfer functions had been computed, the integral of Eq. (180) was performed for each combination of modes, using the Gauss-Legendre rule. This produced an impedance matrix giving the contribution of the edge diffraction, which was then added to the radiation impedance for a duct in an infinite baffle to produce the total radiation impedance.

The radiated pressure was computed by Eq. (244), using the same source positions, but placing the receiver points in front of the horn.

The EDM simplifies the discretization of the boundary in that only the edges need to be discretized. For convex geometries, only diffraction and direct sound need to be computed, but in the case of concave geometries, specular reflections must also be taken into account, which may be challenging due to the high order that may be required.

6.3.1 *Diffraction Contribution to Radiation Impedance*

The pressure diffracted from the flange edges back into the horn mouth, or into the far field, can also be described by modes. Each mouth velocity mode will produce a different excitation of the edges, and the resulting diffracted pressure will modify both the radiation impedance seen by the horn, and the field point pressure.

This section will study how much the diffracted pressure contributes to the radiation impedance. This will be done using a few examples, focusing mainly on the plane wave radiation impedance, since this is an important component, and is familiar to most readers.

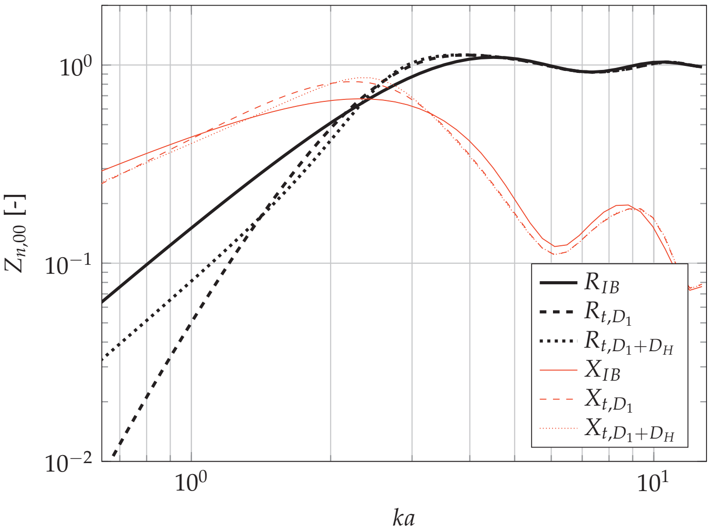

Figure 69: Contribution of higher order diffraction to the fundamental mode radiation impedance.

In the computations, higher order diffraction up to order 20 has been included. The ratio of flange size to horn mouth size is 1.44.

Figure 69 shows the total radiation impedance when including direct sound, direct sound and first order diffraction, and direct sound

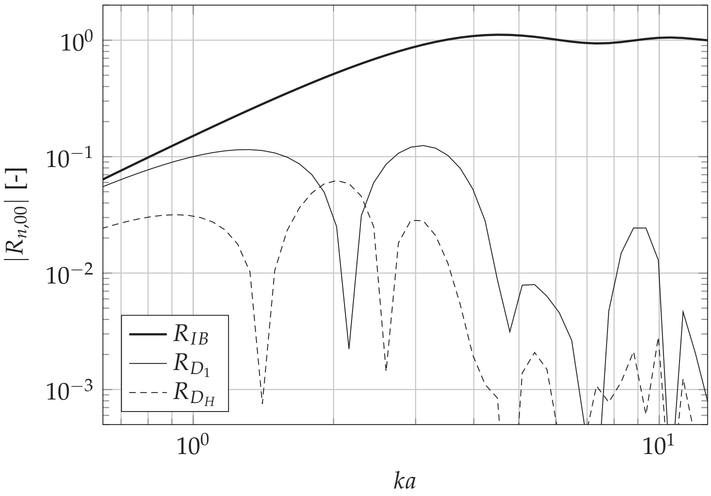

(a) Resistance

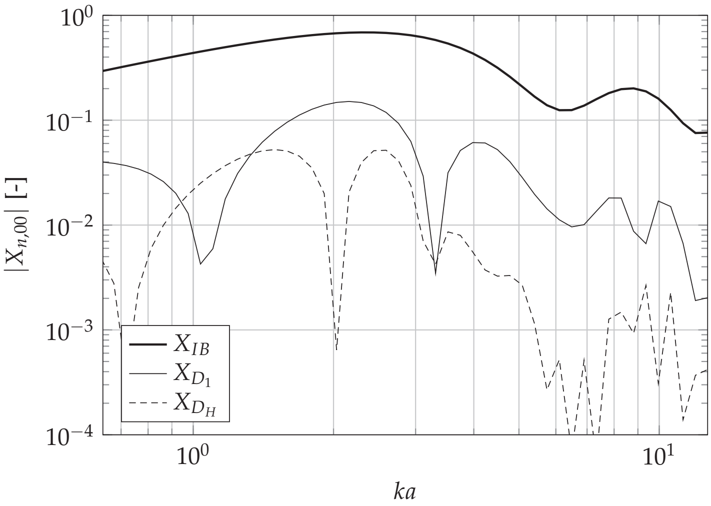

(b) Reactance

Figure 70: The components of the diffraction contribution to fundamental mode radiation impedance.

and all diffraction. It can be seen from the figure that at low frequencies, higher order diffraction is important, as using only first order diffraction creates a rather large error in the radiation resistance below $ka = 1.5$. This is because the resistance due to the first order diffraction is negative and almost as large as the infinite baffle resistance. Higher order diffraction is needed to return the resistance value to the correct $R_{IB}/2$ value. The magnitude, but not the sign, can be seen from Figure 70a.

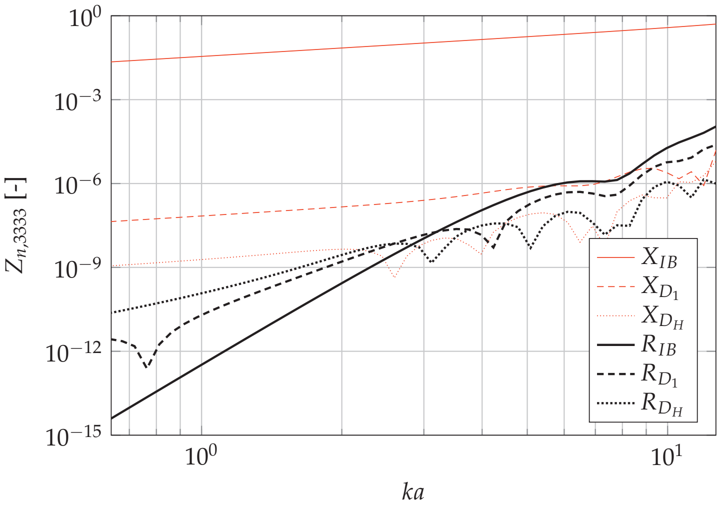

Figure 71: The components of the diffraction contribution to mode (3,3)(3,3) radiation impedance.

Above $ka \approx 4.5$, the contribution from the first order diffraction to the radiation resistance falls below 1%, and becomes insignificant, Figure 70. The contribution from higher order diffraction falls away at a lower frequency, around $ka \approx 3.5$.

The contribution of diffraction to radiation reactance is rather more constant with frequency, approximately 10% of the infinite baffle reactance. Also here the higher order diffraction is needed to produce the correct results at low frequencies, but has little significance above $ka \approx 4$, as for resistance.

Since the higher order modes have directivity patterns different from that of the plane wave, the resulting contribution from edge diffraction on the the radiation impedance will also be different. Figure 71 shows the components of the impedance for mode (3,3)(3,3). Diffraction contributes very little to the reactance, but the contribution to resistance is significant over much of the frequency range.

6.3.2 *A Horn Example*

As an example of application of the EDM to horn loudspeakers, the horn described in Appendix D has been simulated using this method. An illustration of the horn is shown in Figure 72. Some results are given in this section. Section 9.3 compares the simulation results to measurements, and to results from a BEM model, so the verification of the model will not be treated here.

Throat impedance is shown in Figure 73, and compared to the throat impedance for the horn mounted in an infinite baffle. As

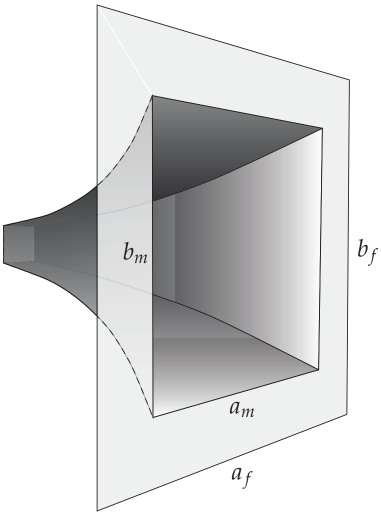

Figure 72: Geometry of the horn with a small flange. Mouth dimensions $a_m = b_m = 0.345\,\mathrm{m}$, flange dimensions $a_f = b_f = 0.5\,\mathrm{m}$. The horn is described in Appendix D.

expected, the lower impedance at low frequencies caused by the doubled solid angle of radiation causes larger peaks in the throat impedance near cutoff.

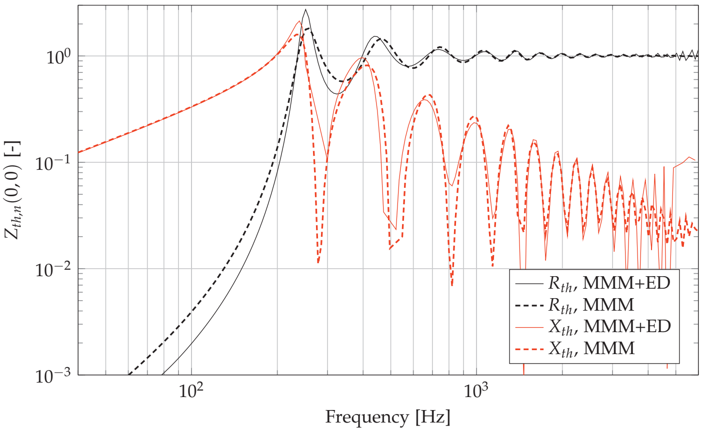

Figure 73: Throat impedance for the rectangular horn in Figure 72.

Figure 74 shows the frequency response, both the direct sound (denoted IB), the diffracted pressure alone, and the total pressure. As expected, due to the increased solid angle of radiation, the total low frequency sound pressure level is lower than that of the direct sound alone. At higher frequencies, however, the total on-axis pressure is higher. The same can be seen in Figure 75, where the two components of the sound field and the total are plotted in polar coordinates for two frequencies. Note that the response at 135° and 180° would be identical to the response of the diffracted pressure alone for 45° and 0° respectively.

Figure 75 also illustrates the problem of the singularities mentioned above, when the field points are nearly coplanar with the edges, this is evident from the "spikes" in the angular response near 90° off-axis.

There are two possible solutions to this problem:

- Increase the number of discretization points along the edges. However, the equations are converging extremely slowly near the singularities.
- Use a hybrid EDM/BEM method, where the pressure at the surface is computed using EDM, and the far field pressure is computed using BEM techniques [304].

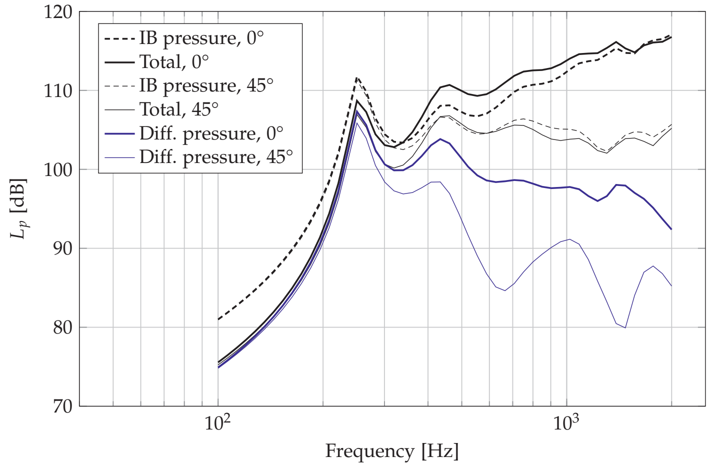

Figure 74: Frequency response for the rectangular horn with a small flange.

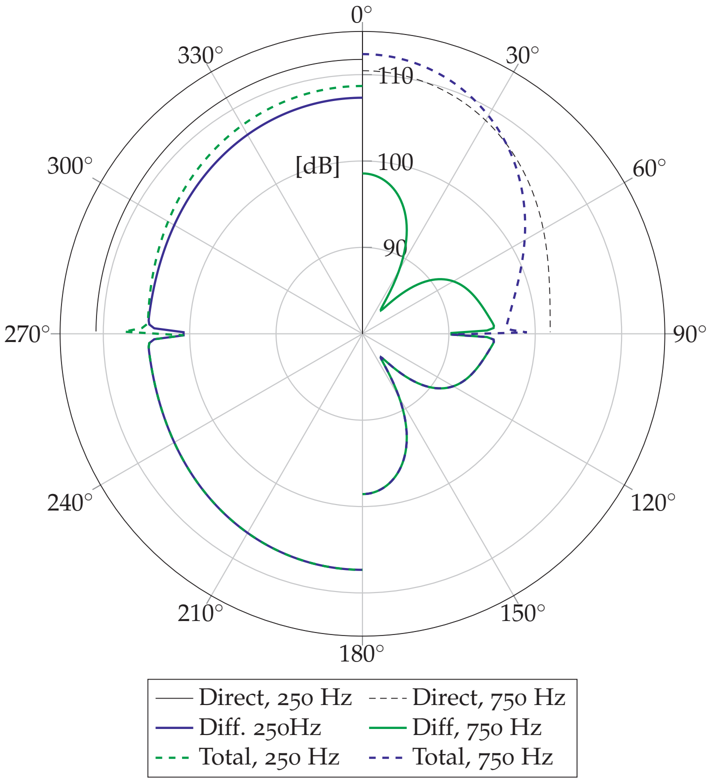

Figure 75: Polar response for the rectangular horn with a small flange.

6.3.3 *Dependence on Number of Modes in Diffraction Calculations*

Higher order velocity modes usually have both lower amplitude than the plane wave mode, and directivity patterns that make their contribution to the edge terms different from that of the plane wave mode. Since computing the contribution of the diffracted pressure to the radiation impedance involves the quadruple integral of Eq. (246) for each mode, it would be advantageous if the number of modes could be reduced. It is the purpose of this section to investigate the resulting error if only a small number of modes is used to describe the contribution of the diffracted pressure.

In the following, the simulations were performed with 144 modes. A frequency range of 100 Hz to 2 kHz was used for this study. The diffraction contribution to the radiation impedance was decomposed into a number of modes and added to the modal radiation impedance for an opening in an infinite baffle. For the reference simulation, all 144 modes were used. For other simulations, 144 modes were still used in total, the diffraction contribution is only added up to mode $N_{m,diff}$. I.e. in the 144×144 impedance matrix, entries (1,1) to

$(N_{m,diff}, N_{m,diff})$ contained $Z_{IB} + Z_{d1} + Z_{hod}$, while the other entries only contained Z_{IB}. A test was also done using only the diffraction impedance terms along the diagonal of the impedance matrix, i.e. where a velocity mode couples to a pressure mode of the same shape. Since the diagonal terms are dominating in the infinite baffle radiation impedance matrix, the question was raised if this was also the case for the diffraction contribution.

The test was performed on a numerical model of the horn described in Appendix D. The reason for using a horn to evaluate the influence of diffraction was that this reduces the radiation impedance matrix (20736 elements) to a single value (the fundamental mode throat impedance) in a way that is relevant to the problem at hand.

Figure 76 shows the relative error in throat impedance as function of frequency for a few cases: no diffraction included in the radiation impedance, plane wave mode diffraction only, and 2 and 64 modes included. Also the results obtained using only the diagonal terms of the impedance matrix are plotted. In this case, all the results are identical, regardless of the number of modes, and are represented by a single curve. Figure 77 shows the same data as function of the number of modes included in the diffraction contribution. Please note that the values are plotted in terms of $\sqrt{N_{m,diff}}$ to improve readability.

Generally, the error decreases monotonically when more modes are included in the diffraction computation, as expected, see Figure 77 on the next page. A maximum error of 10^{-3} is reached for $N_{m,diff} = 16$. This could suggest that including only 16 of the 144 modes would give quite an adequate accuracy for many purposes, in the frequency range evaluated here, up to 2 kHz. Modal coupling is clearly important, as adding only the diagonal terms does not reduce the error beyond the first mode, see Figures 76 and 77

To see the reason for the modal coupling through diffraction, we may inspect the pressure distribution in front of the horn, for three cases: infinite baffle, the diffracted pressure only, and the sum of the two, which corresponds to a horn with a small flange. In the example, the mouth of the horn was given a velocity distribution corresponding to symmetric mode (1,0), which has two minima across the horn mouth in the x-direction (see the definition of mode functions in Section 4.2.3 on page 77). The three cases are plotted in Figure 78, where the pressures along a line across the center of the horn mouth and 1 mm in front of it, are plotted. The horn mouth itself extends from -0.174 m to 0.174 m on the x-axis, indicated by the dash-dotted vertical lines in the figures. In Figures 78a and 78b, it can be seen that the infinite baffle pressure follows the shape of the velocity distribution closely, with minima that move only slowly with frequency. The number of minima inside the horn mouth is the same as for the excitation. This means that the dominant pressure mode is the same as the ve-

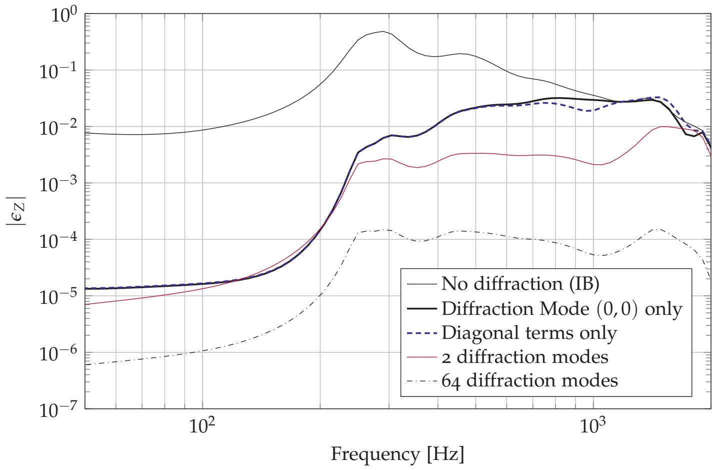

Figure 76: Relative error in Z_{th} for the small-flange example. Note that the curve for "Diagonal terms only" is the same regardless of the number of modes.

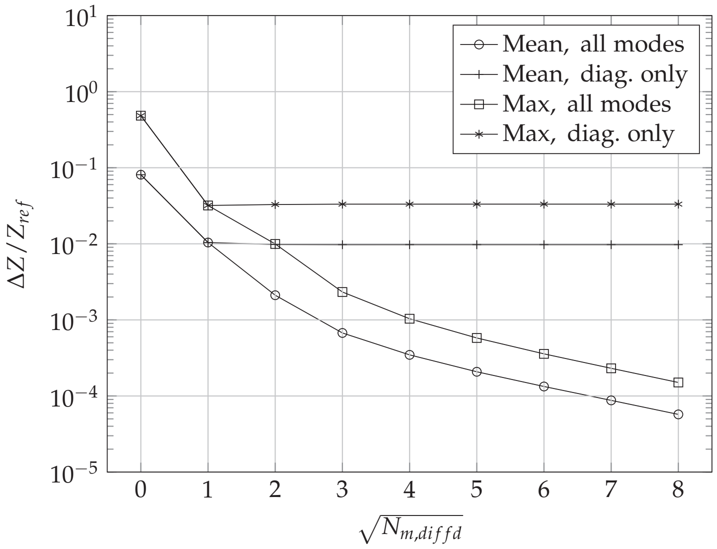

Figure 77: Relative error in Z_{th} as function of number of modes used in the diffraction impedance for the small-flange example. Mean and maximum values have been computed over the 100 Hz to 2 kHz range.

locity mode, and the radiation impedance matrix will be diagonally dominant.

The matter is quite different for the diffracted pressure alone, Figure 78c. Here the number of minima varies strongly with frequency.

The radiation impedance matrix due to diffraction will therefore not be diagonally dominant in general.

By comparing the plots in Figure 78, one notices that the magnitude of the diffracted pressure is well below the magnitude of the infinite baffle pressure. At low frequencies, the contribution to the total pressure is negligible, which can be seen by comparing the infinite baffle pressure with the total pressure in Figure 78a. One does, however, notice that the dips at 500 Hz are shallower with diffraction included. One may ask why the contribution of the diffracted pressure seems to be so small, when we know that the effect of diffraction is greatest at low frequencies. A look at the radiation impedance with and without diffraction, Figure 69, may clarify the matter. Although this figure shows the radiation impedance of a piston, the trend is similar for other modes. At low frequencies, the diffraction has very little influence on the reactance, but quite a large influence on the radiation resistance. Since the reactive part of the pressure dominates the near field at these frequencies, and since only the magnitude of the pressure is plotted in Figure 78, the influence of the diffraction seems small.

At middle frequencies, we can see from both Figure 78b and Figure 69 that the contribution of diffraction to the total pressure is greater (600 Hz to 1 kHz curves), until the effect is again negligible at 2 kHz. The larger contribution from diffraction in the 500 Hz to 1 kHz range can also be seen from Figure 78c.

In Figure 78c, for positions close to the baffle edge ($\mathbf{x} \approx \pm 0.25\,\mathrm{m}$), numerical challenges, as described in section Section 6.3, lead to reduced accuracy. Therefore, the apparent dip near those baffle edges might be a numerical artifact.

6.3.4 *First Order and Higher Order Diffraction*

Usually the most dominant part of the diffracted field comes from the first order diffraction term, as long as the diffracting edge is visible from both the source and the receiver positions. Since computing the higher order diffraction term is time consuming, it is interesting to see how large a contribution the higher order term makes to radiation impedance and radiated pressure. Several simulations were run, where the number of first order diffraction impedance modes (D1ZM), N_{D_1}, was varied from 0 to 64, and the number of higher order diffraction impedance modes (HDZM) was varied from 0 to N_{D_1}. The case of zero diffraction impedance modes corresponds to the infinite baffle case. Otherwise the test was identical to the test in the previous section, including the stepping of N_{D_1} and N_{HOD}.

The results for relative impedance error and relative pressure error are presented in Figures 79 and 80, respectively. Again, the values are plotted against $\sqrt{N_{HOD}}$ to improve readability when N_{HOD} is low,

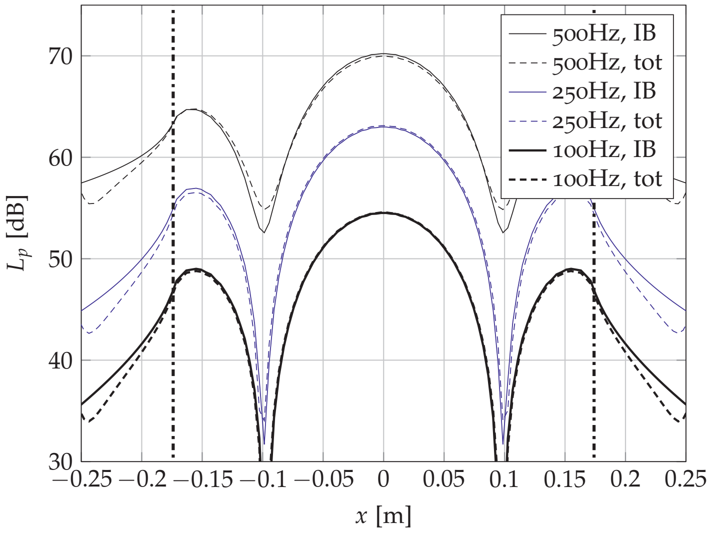

(a) Infinite baffle pressure and total (infinite baffle and diffraction) pressure, low frequencies.

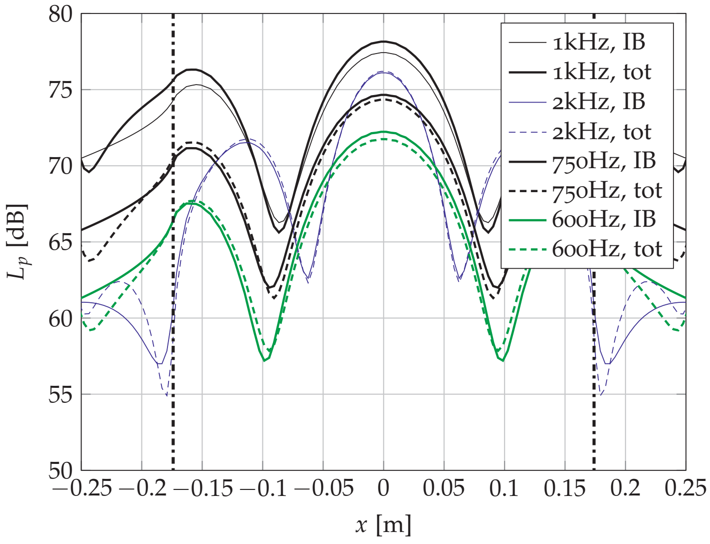

(b) Infinite baffle pressure and total (infinite baffle and diffraction) pressure, middle to high frequencies.

Figure 78: Pressure across horn mouth for velocity mode (1,0). The horn mouth extends between the dash-dotted lines. Please note the different vertical scales. (Cont. next page.)

due to the many data points in this region. The trends are similar for both impedance and pressure. It is clear that including no more than the part of the diffraction pressure that corresponds to a plane piston

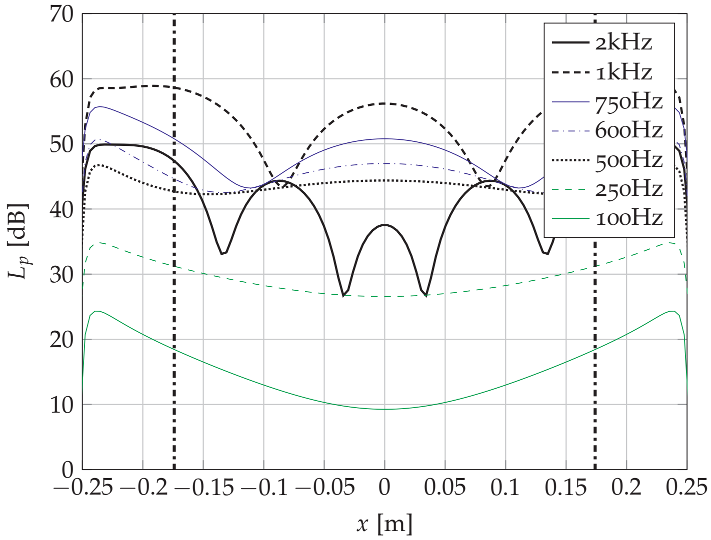

(c) Diffraction contribution to pressure.

Figure 78: (Cont.) Pressure across horn mouth for velocity mode (1,0). The horn mouth extends between the dash-dotted vertical lines. Please note the different vertical scales.

source, gives a significant reduction in error: the error in impedance is halved if a single D1ZM is included. However, unless higher order diffraction is included, adding more D1ZM has little effect. A further significant reduction of error results by including one or more HDZM. The large reduction in error from no HDZM to a single HDZM shows that higher order diffraction is important in establishing the correct zeroth order mode radiation impedance. The influence on the radiation impedance can be seen in Figure 69. The influence is clearly largest for the radiation resistance, the reactance being substantially the same in all three cases.

A reduction of the mean relative error to 0.1% can be achieved with three D1ZM and two HDZM. About 25 to 36 D1ZM and 9 to 16 HDZM are required to reduce the maximum error to the same level.

This distinction between first order and higher order diffraction is largely of academic interest, though, as in practice the D1ZM and HDZM would not be calculated separately. One would rather calculate the modal diffraction impedances from the total diffracted pressure, and it is then logical to use the same number of modes in each term.

The frequency dependence of the error is shown in Figure 81 for the throat impedance. The main contribution of higher order diffraction is at low frequencies, and becomes less significant at higher frequencies. The plane wave HDZM reduces the low frequency error sig-

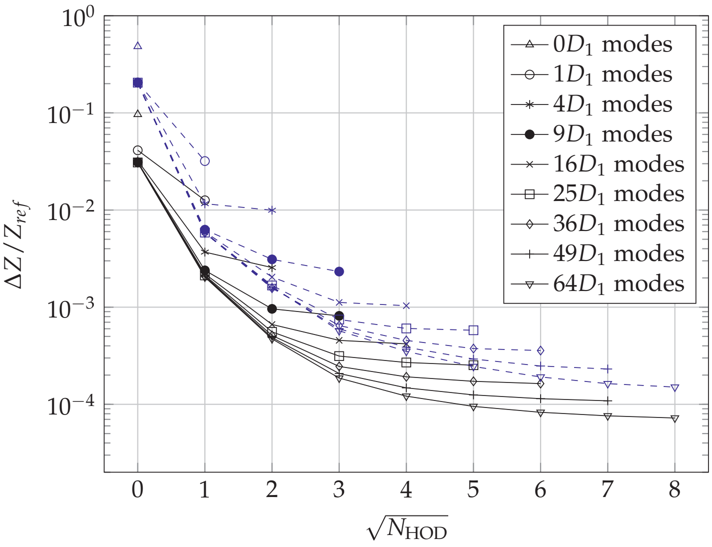

Figure 79: Error in throat impedance as function of number of modes in diffracted pressure. The number of modes in first order diffraction impedance are indicated by the markings on the lines. Solid lines indicate mean error, dashed lines indicate maximum error.

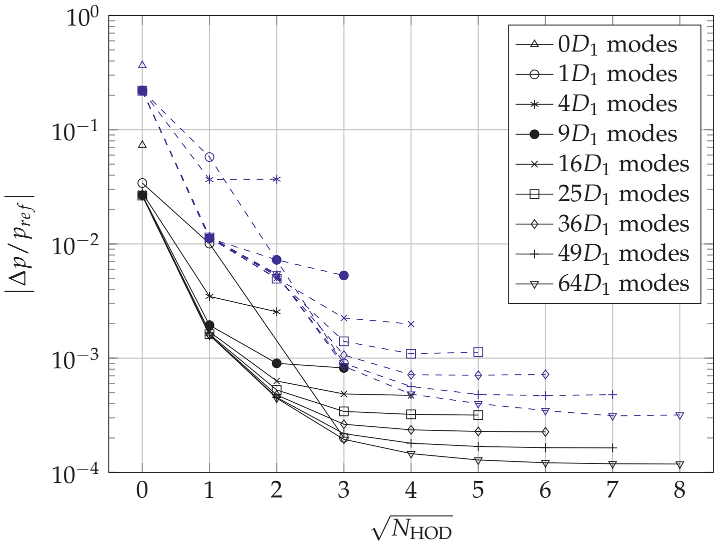

Figure 80: Error in radiated far-field pressure as function of number of modes in diffracted pressure. Legend as in Figure 79.

nificantly, while subsequently adding more modes from the HDZM reduces the error at all frequencies, and the effect is to more or less shift the error curve downward.

As shown above, a general truncation of the number of HDZM to be less than the number of D1ZM is of little value. Of greater interest, however, is to limit the calculation of higher order diffraction to low frequencies.

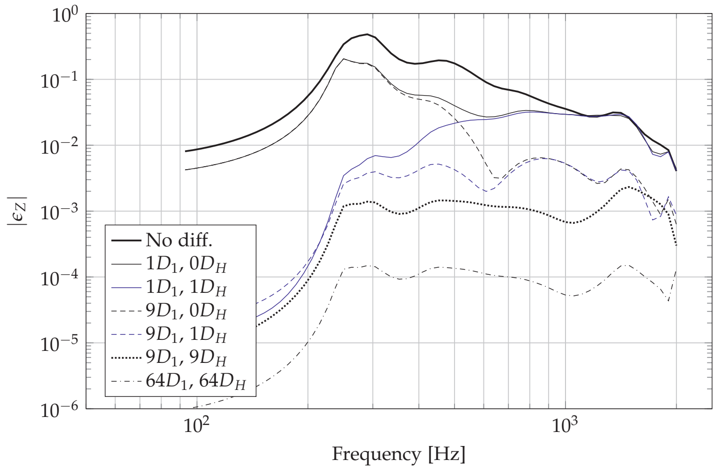

Figure 81: Error in throat impedance as function of frequency, for a few of the combinations in Figure 79.

6.3.5 *Summary*

This section has shown how the Edge Diffraction Method can be combined with the MMM to simulate horns with small flanges, i.e. free standing horns. A verification of the performance of the example horn from Section 6.3.2 is given in Section 9.3, where comparisons with both BEM and with measurements show excellent agreement. Further discussions of the results are given there.

This section has also investigated the influence of number of modes in the diffraction contribution to the radiation impedance and if, and to what extent, higher order diffraction needs to be taken into account. The results can be summarized as follows:

- The EDM has some numerical challenges due to singularities when the receiver point is coplanar with the edges of the model, causing inaccurate results at some receiver positions. While this is not an issue for computing the radiation impedance, a solution must be found in order to provide accurate directivity calculations.

- Including just the plane wave mode in the diffraction impedance gives a great improvement in accuracy, reducing the error by an order of magnitude compared to just including the infinite baffle radiation impedance.

- There is significant modal coupling between the modes in the diffraction impedance, and just using the diagonal of the diffraction impedance matrix does not improve the results over that of using the plane wave mode only.

- Higher order diffraction is required at low frequencies. At least the plane wave mode of the higher order diffraction must be included to for any reasonable accuracy.

- Unless more modes are added from the higher order diffraction, little is to be gained by adding more modes from the first order diffraction.

- Limiting the calculation of higher order diffraction to low frequencies, on the other hand, appears to be feasible, and since this part of the diffraction calculation is the most time consuming, this would make it possible to reduce the computational load at higher frequencies.

7

HORNS NEAR REFLECTING BOUNDARIES

When the space the horn radiates into is reduced from the full 4π steradians solid angle by the introduction of one or more (semi-)infinite planes, see Figure 82, we say that the horn radiates into fractional space. Half-space is a common case, and has been treated separately in Chapter 5. If the solid angle is further reduced, the problem can in many cases be solved by image source based methods, which is the approach used in this chapter. The chapter is based on [51].

The contributions in this chapter are the formulation of the computation of the modal mutual radiation impedance matrix as a matrix operation, and the demonstration of the influence of the distance to reflecting walls on the performance of horns.

7.1 SOURCES IN FRACTIONAL SPACE

When two or more acoustic sources radiate into the same space, there will be a mutual interaction between them due to the fact that the pressure from each source will change the pressure on all the others. All sources will therefore experience a different reaction force to its vibration velocity than if it was radiating alone, and hence a different radiation impedance. This impedance is dependent on the spacing in terms of wavelengths, and the relative placement of the sources.

Expressions for the mutual impedance between circular pistons in an infinite baffle are given by Klapman [305] and others, and Arase [306] gives expressions for rectangular pistons. Sha et al. [307] give a review of previous work on mutual modal radiation impedance, and also give expressions for computing the mutual impedance matrix. The results, however, do not agree with other numerical solutions, including direct numerical integration. Because of this, the author decided to instead develop another method to compute the mutual modal radiation impedance.

The method is based on direct numerical integration of the double surface integral (see also Eq. (180), on page 105)

$$Z_{mn} = \frac{j\omega\rho}{4\pi S^2} \int\limits_S \int\limits_S G(\mathbf{x}|\mathbf{x}_0) \cdot \psi_m\left(x_0, y_0\right) \psi_n\left(x, y\right) dS_0 dS \tag{247}$$

with $G(\mathbf{x}|\mathbf{x}_0) = 2e^{-jkh}/h$, $\mathbf{x}$ and $\mathbf{x}_0$ now being points on two different radiators that belong to the same plane. Designating $\mathbf{x}$ to be the mirror source, and $\mathbf{x}_0$ the actual horn opening, Eq. (247) describes the

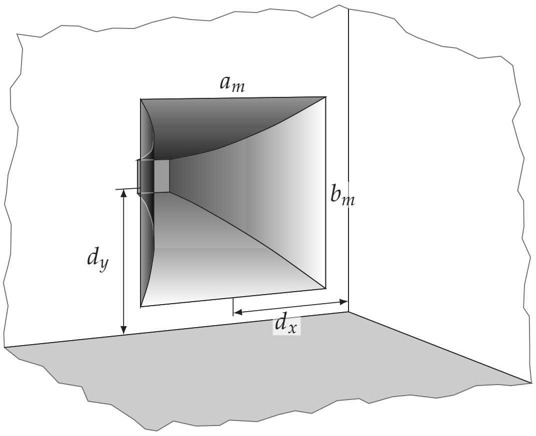

Figure 82: Horn placed near boundaries. The boundaries are planes that extend outward to infinity.

mutual impedance seen by the horn opening. Due to the mirroring, the mode functions $\psi_n(x, y)$ must be symmetric with respect to the reflecting wall. With more than one reflecting wall, there will be more than one image source $\mathbf{x}_i$, and it is the superposition of all the pressure fields from the image sources on the actual horn opening that is of interest. We may thus write the Green's function as

$$G(\mathbf{x}|\mathbf{x}_0) = \sum_{i=1}^{N} G(\mathbf{x}_i|\mathbf{x}_0) \tag{248}$$

This Green's function can then be inserted into Eq. (180) on page 105 to give the mutual radiation impedance.

7.2 MUTUAL RADIATION IMPEDANCE

The radiation impedance for the infinite baffle case is computed from the equations given in Chapter 5 for the asymmetric case. Even if the horn in question is quarter symmetric, asymmetry in the sound field is introduced due to the presence of the reflecting surfaces.

From the relation in Eq. (248), and from superposition as outlined in Section 6.2, we see that we can then find the total radiation impedance as

$$Z_{rad,tot} = Z_{IB} + Z^{(M)}, \tag{249}$$

where $Z^{(M)}$ is the total mutual impedance. $Z^{(M)}$ can thus be computed separately, independently from Z_{IB}. Using direct Gauss-

Legendre numerical integration [308], for clarity only shown for one image source,

$$\begin{aligned} Z_{nm}^{(M)} &= \frac{j\omega\rho}{2\pi S^2}\sum_{p=1}^{N_x}\sum_{q=1}^{N_y}\sum_{r=1}^{N_x}\sum_{s=1}^{N_y}\frac{e^{-jk\sqrt{(x_p-x_r)^2+(y_q-y_s)^2}}}{\sqrt{(x_p-x_r)^2+(y_q-y_s)^2}} \\ &\times \quad \psi_m\left(x_p,y_q\right)\psi_n\left(x_r,y_s\right)w_p w_q w_r w_s. \end{aligned} \tag{250}$$

The indices p and q loop over the positions of the image source surface, while r and s loop over the positions at the receiving surface, both defined by the abscissas in the Gauss-Legendre rule. w_p etc. are the corresponding weights.

This expression is computationally heavy, and has to be repeated for every mode in the impedance matrix, for each frequency. There are some things to note, however:

- The argument $h = \sqrt{(x_p-x_r)^2+(y_q-y_s)^2}$ for the Greens function is independent of frequency and mode number.
- The Green's function is independent of the mode number.
- The mode functions are independent of frequency.

One should also note that the computation of the radiation impedance is actually a two-stage process: first finding the pressure distribution for each velocity mode of the source (this corresponds to the column index m of the matrix) using Eq. (156) and assuming unit volume velocity, then decomposing each of these pressure distributions into modes using Eq. (177).

It is evident that when using a fixed number of integration points, Eq. (156) can be computed for one point and one mode as the inner product

$$p_m(x,y,z) = \frac{j\omega\rho}{2\pi S}\vec{G}^T\vec{\psi}_m^w \tag{251}$$

where $\vec{G}$ is a vector of the Green's function from all source points on the radiator to $\mathbf{x} = (x,y,z)$, and $\vec{\psi}_m^w$ is a vector of the values of the mode function for mode m at all points on the radiator. The w indicates that the mode function has been multiplied by the weights of the employed integration scheme. The volume velocity is assumed to be unity. By expanding $\vec{G}$ into a matrix that contains the Green's functions from all N_s source points (columns) to all N_r receiver points (rows), and expanding $\vec{\psi}_m^w$ to a matrix that contains all used modes, one obtains the pressure at all receiver points for all source modes by a single matrix-matrix multiplication:

$$\mathbb{P} = \frac{j\omega\rho}{2\pi S}\mathbb{G}\Psi^w \tag{252}$$

Here $\mathbb{G}$ is an $N_r \times N_s$ matrix of Green's functions, and Ψ^w is an $N_s \times N_{modes}$ matrix of mode functions multiplied by integration weights.

This gives $\mathbb{P}$ as an $N_r \times N_{modes}$ matrix. The pressure matrix is then decomposed into modes by another matrix-matrix multiplication by Ψ^w. This process gives

$$\mathbb{Z} = \frac{j\omega\rho}{2\pi S^2} \left(\Psi^w\right)^T \mathbb{G}\Psi^w \tag{253}$$

which is the desired $N_{modes} \times N_{modes}$ impedance matrix. If $N_r = N_s$, $\mathbb{G}$ is symmetric, and only half of the entries need to be calculated, the rest can be copied. Depending on the integration scheme, more symmetries may be found, further speeding up calculations.

The advantage of this method of computing the mutual radiation impedance is that the integration is now expressed in terms of matrix-matrix multiplications, which is a standard operation that has been highly optimized in linear algebra libraries like BLAS [309].

It should be noted that this method cannot be used directly for the self impedance Z_{IB}, as the Green's function becomes singular when $h = 0$. But since the self impedance is computed by the methods presented in Chapter 5, this poses no problem.

The influence of the mutual radiation impedance is small at high frequencies [310], as we will see, so it is not necessary to compute Eq. (253) to very high frequencies.

7.3 RADIATED PRESSURE

The radiated pressure is computed from the Rayleigh integral in Eq. (177) on page 105. By employing the same reasoning as in the previous section, it is evident that the integral can also be performed by matrix-matrix multiplication as in Eq. (252), with an additional multiplication with the vector of mouth volume velocity mode amplitudes:

$$p(x, y, z) = \frac{j\omega\rho}{2\pi S} \mathbb{G}\Psi^w \vec{U} \tag{254}$$

The pressure is computed for both ordinary receiver points and for the mirror receiver points, and then summed afterwards. An alternative is to let the mirror receivers be included in the Green's functions when computing $\mathbb{G}$. What is most efficient is a matter of the shape and size of the matrices.

7.4 RADIATION IMPEDANCE FOR A PISTON NEAR ONE OR TWO WALLS

From Waterhouse [40] we know that at low frequencies, the power of a source is doubled if it is placed near a wall, quadrupled if it is placed near two walls, and eight times as large if it is placed near three walls. In our case, the source is already placed in an infinite baffle, and we can only consider the cases of one and two extra walls.

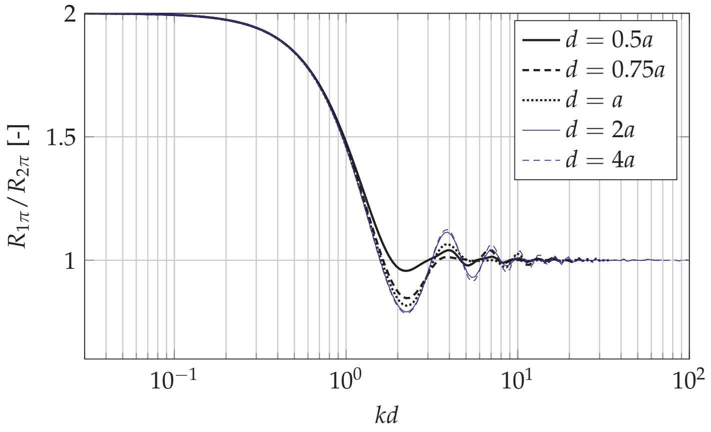

(a) Relative radiation resistance.

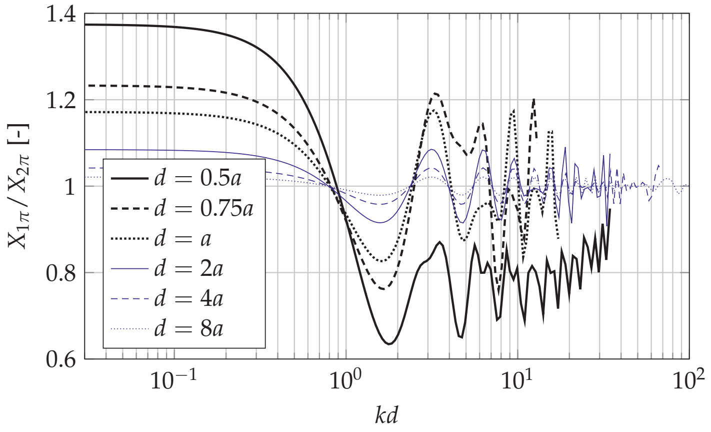

(b) Relative radiation reactance.

Figure 83: Relative radiation impedance for a square piston at a distance d from a single wall.

Since the radiated power is proportional to the real part of the radiation resistance, we expect the resistance at low frequencies to either double or quadruple.

The first example considers a square piston of sides a, placed at various distances from a single wall, the center-to-wall distance being d. As we can see from Figure 83a, the shape of the relative radiation resistance, $R_{1\pi}/R_{2\pi}$, is very nearly independent of kd up to $kd \approx 1$, above which the relative distance in terms of the piston size begins to play a role. One may recognize the dip around $kd \approx 2.25$ from the study by Waterhouse, this corresponds to $x/\lambda = 0.358$ in Waterhouse's notation. The consequence of this dip for horns will be discussed in more detail in Section 7.5. It is also interesting to note that power output is doubled even when the distance between the sources is very large. This is perhaps counter-intuitive, as the pressure from the mirror source becomes small when the distance is large. But at low frequencies, where the radiation impedance is mainly reactive, the pressure from the mirror source arrives almost in-phase with the primary source velocity even if the propagation distance is large. So even if this contribution is small in absolute terms, it adds up to double the radiation resistance [311].

The radiation mass shows quite a different behavior, see Figure 83b, but the reason is the same as for the doubling of the resistance: at large relative distances, the pressure from the mirror source is more in-phase with the primary source velocity than at smaller relative distances. The contribution to the radiation impedance is resistive rather than reactive, and the contribution to the radiation mass becomes smaller as d increases.

The total radiation resistance is shown in Figure 84, and the doubling at low frequencies is readily seen. For larger distances, the doubling is only approached at low frequencies, and above that, the curve oscillates around the curve for the infinite baffle resistance.

When two walls are involved, things get more complicated, as there is one more degree of freedom. A few examples are given in figures 85 and 86. The shape of the curves at low frequencies depend mainly on the two relative distances, and their relative ratio. If the d_y/d_x ratio is large, for instance 16 as in two of the examples, there will be two transitions, first to a doubling, then to a quadrupling of the resistance, as frequency is reduced. The dip around $kd_x \approx 2 - 2.5$ is also deeper, meaning a larger reduction of the radiated power in this region.

As for the one-wall case, the resistance has a transitional region where it oscillates around the infinite baffle or quarter-space curve, before finally reaching a quadrupling at low frequencies, Figure 86.

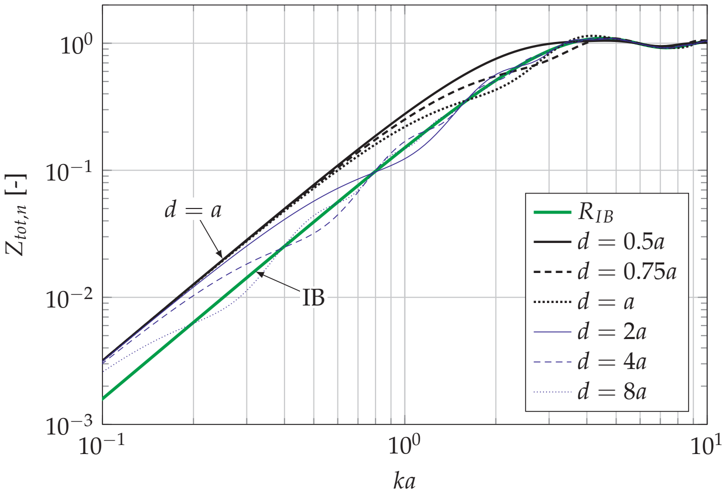

Figure 84: Total radiation resistance for a square piston at a distance d from a single wall.

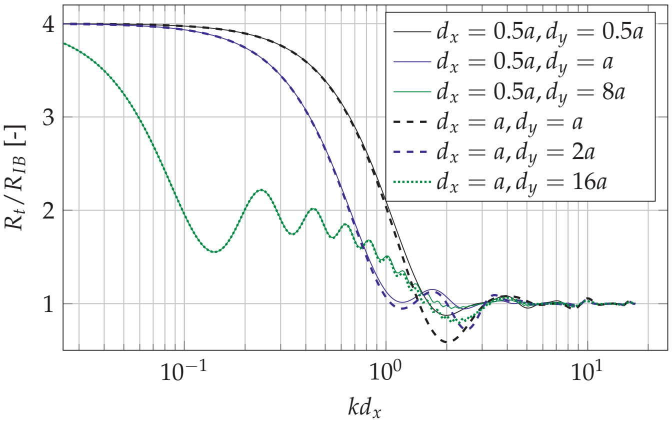

Figure 85: Relative radiation resistance for a square piston near two walls, d_x and d_y indicate the distances in the two directions.

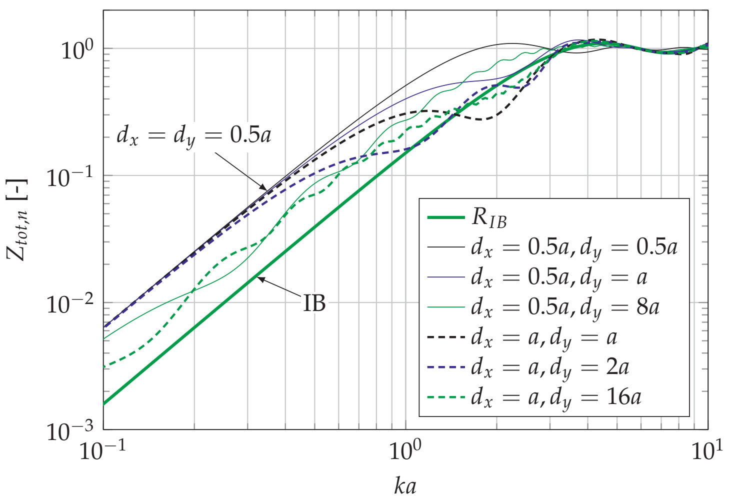

Figure 86: Total radiation resistance for a square piston near two walls, d_x and d_y indicate the distances in the two directions.

7.5 CASE STUDIES

In this section, a few examples of the effect of mutual radiation impedance on the total radiation impedance and on the performance of horns will be given. For horns, the focus will be on the throat impedance, as in the frequency range where the mutual coupling is significant, the image sources are so close as not to cause significant lobing in the directivity response.

The horns used in this case study are shown in Figure 87, and the dimensions are given in Table 4. Horn 1 has the same size and shape as the horn used in the measurements in Chapter 9, and the dimensional details are also listed in Appendix D. The other horns are exponential horns.

Horn	S_{th} [cm^2]	S_m [cm^2]	L [cm]	T
1	42.25	1188.8	50.0	0.7
2	5.0	1180.0	74.8	1.0
3	5.0	590.0	65.3	1.0
4	5.0	295.0	55.8	1.0

Table 4: Dimensions of the horns used in the case studies

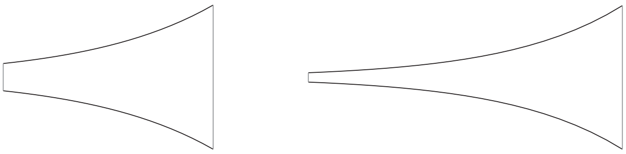

(a) Horn 1 (b) Horn 2

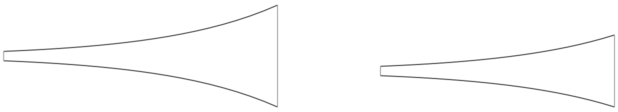

(c) Horn 3 (d) Horn 4

Figure 87: The horns used in the case studies.

7.5.1 *Constant Mouth Size, Varying Distance*

Horn 1 from Figure 87 is used in this example. 50 elements and 64 modes were used in the MMM simulations.

The distance d is the distance from the center of the horn mouth to the wall, and is indicated in the figures in terms of mouth size. The frequency axis is in terms of the non-dimensional parameter k/k_c, where k_c is the cutoff wave number of the horn.

Figure 88 shows the throat resistance as the distance to a single wall is varied. The thickest green curve is the throat resistance for the horn mounted in an infinite baffle. One notes that the distance does not need to be increased much before the results are very similar to the infinite baffle case from approximately the cutoff frequency and up. A tight coupling (horn very close to the wall) reduces the ripple significantly, but for distances larger than $0.75a_m$, the ripple is similar to, or larger than, the infinite baffle case. Below the cutoff frequency, it is evident that the power is increased, but since this is outside the pass band of the horn, it is not very useful.

In the case of a horn placed in the corner, the behavior is similar, see Figure 89. As with the single-wall case, a significant reduction of ripple is found when the horn is placed in the corner, with increasing ripples as it is moved away. The worst placement of the cases plotted for this horn is at $d_x = d_y = a_m$.

7.5.2 *Varying Mouth Size and Distance*

Now what happens if the horn's mouth size is reduced, but the horn is placed near a wall or a corner? In this study, three exponential horns as listed in Table 4 were used. Horn 2 was used for the infinite baffle mounting, the mouth area of this horn corresponds to $k_c a_m = 0.71$. Horn 3 was used for the baffle/wall placement, and horn 4 for corner placement.

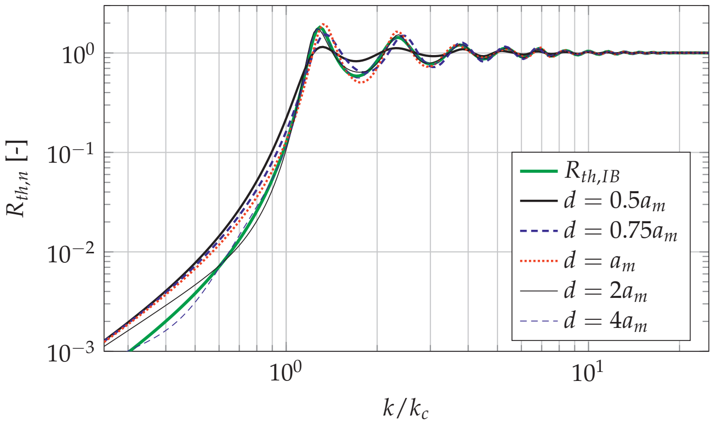

Figure 88: Throat resistance, horn 1, quarter space. Note that $d = 0.5a_m$ means that the wall is immediately next to the horn mouth.

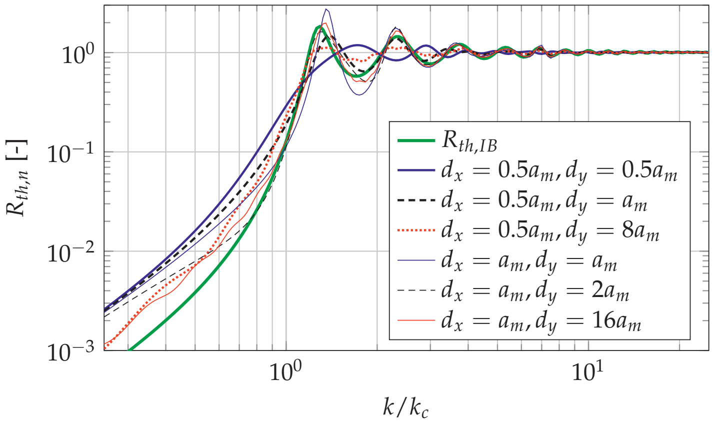

Figure 89: Throat resistance, horn 1, eighth space.

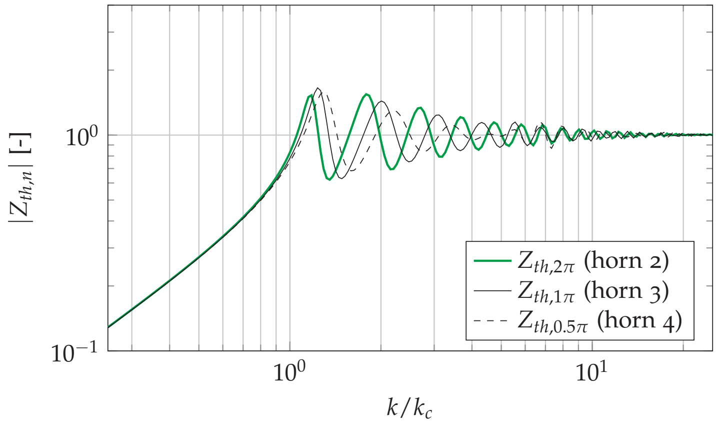

Figure 90: The effect on the throat impedance of reducing mouth size, while placing the horn as close as possible to one or two walls, for the horns in Figure 90.

The resulting throat impedance magnitude curves for the horns when placed as close as possible to the reflecting surface(s) are shown in Figure 90. Since the length of the horn is not kept constant, the curves mostly do not overlap, but the ripple magnitude is approximately constant. If the horn is made to have a constant length, adjusting the throat area when the mouth area is reduced (i.e. linearly scaling the entire horn), the resulting curves do overlap to a much larger degree. But usually, when making a horn with reduced mouth size, the purpose is to make the horn significantly smaller. In addition, one usually does not want to employ a smaller driver, so the throat size should be kept constant. One should, however, keep in mind that the frequencies of the resonance peaks are shifted when the length is changed. The most important peak is the first one, where a shift will produce a similar shift in the lower corner frequency of the system.

The reason for the similar throat impedance curves for the three horns can be understood by looking at the radiation impedance at the mouth. The radiation resistance for several cases is plotted in Figure 91. The thick gray lines show the radiation resistance for the horn mouths without any support from the walls. Adding one or more wall(s) close to the horn increases the radiation resistance to the value for the largest horn mouth, which is what we want. For quarter space the shape of the curve is slightly different; since the horn mouth itself is square, the total effective mouth surface corresponds to a rectangle of twice the size and with an aspect ratio of 2. For eighth space, the effective mouth surface is again square, with four times the area of the physical mouth.

If the same horns are placed further away from the walls, the throat ripple increases significantly, as shown in Figure 92. Here the effect

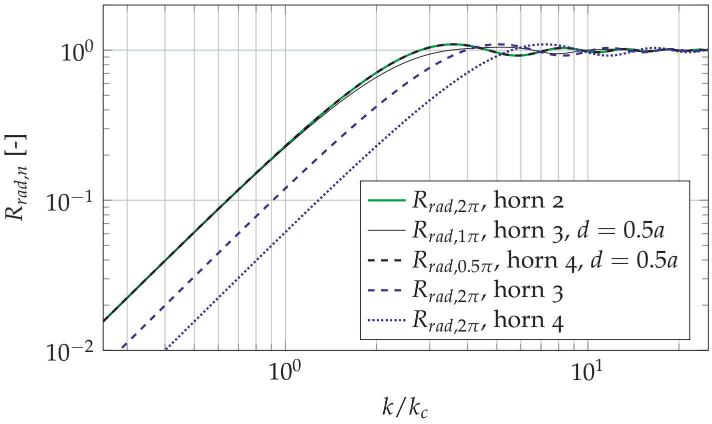

Figure 91: Radiation resistance for the horns in Figure 87 under the conditions used in Figure 90. In addition, the infinite baffle radiation resistance curves for horns 3 and 4 are shown.

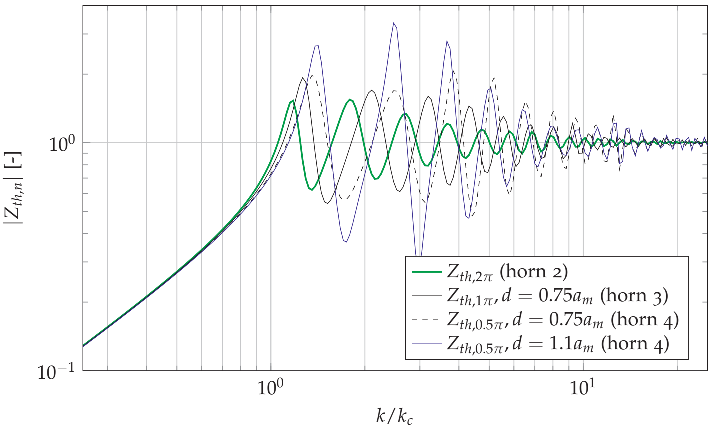

Figure 92: The effect on the throat impedance of reducing mouth size, while placing the horn at a distance from one or two walls.

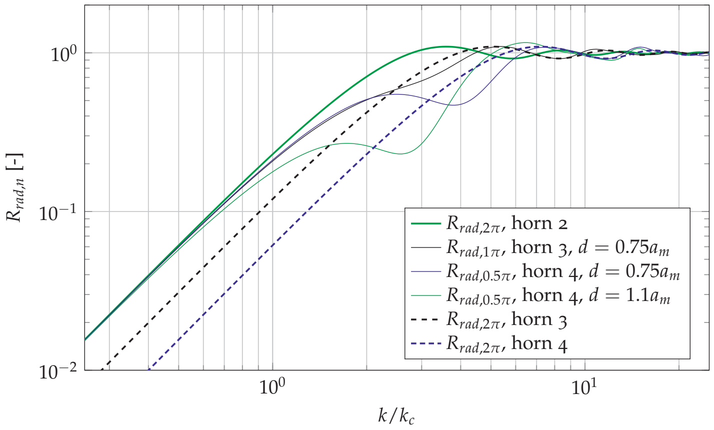

Figure 93: Radiation resistance for the horns in Figure 87 under the conditions used in Figure 92. In addition, the infinite baffle radiation resistance curves for horns 3 and 4 are shown.

of placing the horn at a distance $d = 0.75a_m$ from the wall is marked, and even more so at higher frequencies; the peaks do not decrease in magnitude as fast as in Figure 90. If the eighth space horn is moved even further away from the corner, to a distance that corresponds to $0.75a_{m,1\pi}$, even more ripple results, as expected. The distances in cutoff wave lengths for the three cases are $0.21\lambda_c$, $0.15\lambda_c$ and $0.21\lambda_c$, respectively. So even if the horn is within a quarter cutoff wavelength of its image(s) at the low end, this is not enough to provide the needed reinforcement.

The fundamental mode radiation impedance for the four cases is plotted in Figure 93, and can explain the behavior in Figure 92. First, at low frequencies, the curves overlap, and as we can see from Figure 92, the horns behave very similarly at the lowest frequencies, approximately up to the cutoff frequency. Second, the curves do not reach their asymptotic values at the same low frequency as for the previous case, which creates problems in a fairly large frequency range above cutoff. Even worse, the phase relations between the horn mouth and its image(s) create dips in the radiation resistance that further increase the problem. The location of these dips can be seen to correlate well with the increased ripple in Figure 92.

Figure 94 shows how the throat impedance ripple changes with the distance from the wall(s) for the horns described above. The ratio $\max|Z_{th}|/\min|Z_{th}|$, i.e. the ratio between the highest impedance peak and the lowest impedance dip (after the first peak), is plotted as a function of wall distance to give an indication of the ripple magnitude. it is clear that for a horn designed to be placed near a wall or in a corner, d/a_m ratios in the range 1.2 to 3 are especially unfavorable. For horns originally designed for infinite baffle mounting,

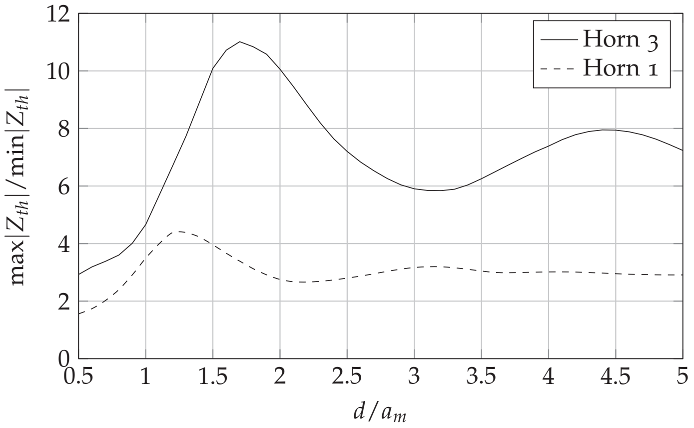

(a) Peak-to-dip ratio as a function of center-to-wall distance d for horns close to a single wall.

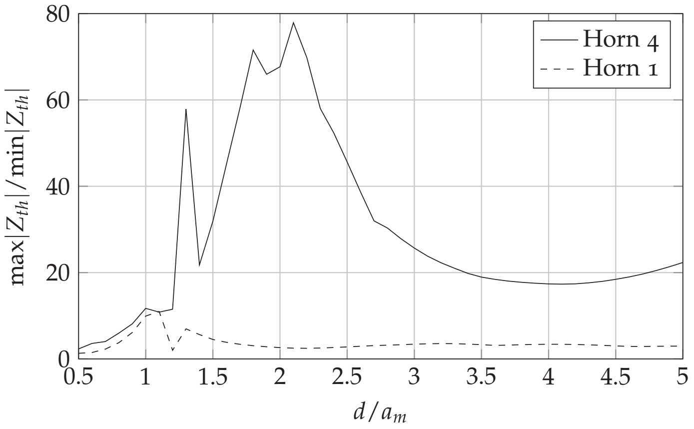

(b) Peak-to-dip ratio as a function of center-to-wall distance $d = d_x = d_y$ for horns close to two walls. The large peak at $d/a_m = 1.3$ is caused by a particularly deep dip for this distance.

Figure 94: The peak-to-dip ratio $\max|Z_{th}|/\min|Z_{th}|$ for horns place near walls.

d/a_m ratios in the range 0.75 to 1.5 are unfavorable. The curves also show that when the horn is designed for infinite baffle mounting, they approach their infinite baffle performance quickly for distances larger than $1.5a_m$. For distances where $d < 0.7a_m$, there is a general reduction in ripple for all horns. It should be noted that these curves applies specifically to the square horns described above, and will vary when horn profile and aspect ratio are varied. Still, the curves indicate the variation in performance to be expected when the distance from the reflecting surfaces are varied.

It is also interesting to look at the differences between horns and direct radiators. If k_c, the cutoff wave number, is taken as the lower limit of the pass band, horns are used from $k_c a = 1$ and up, a now being the effective mouth radius, including the mirror sources. For direct radiators, $ka = 1$ marks the upper limit of the piston range, and much of the utilized pass band is below this frequency. In other words, horns are used in a frequency range where they are large compared to the wavelength, while the opposite is true for direct radiators. As we can see from Figure 93, the help from the mutual impedance rapidly moves out of the pass band of the horn as the horn moves away from the wall(s). For a direct radiator, however, the increased radiation resistance will still be in the pass band, especially near the low frequency end where it is most needed, for even larger distances than shown in Figure 93. Another factor is that horns will exhibit large resonant peaks when presented with a low impedance load at the mouth (e.g., a small mouth away from reflecting boundaries), something that does not happen for direct radiators.

7.6 SUMMARY

When horns are placed near reflecting surfaces, the mutual impedance cannot be neglected, and it is important to be able to calculate this quantity in an efficient manner. This chapter has developed a method where the mutual impedance is computed by matrix multiplication, making it possible to exploit the highly efficient optimized BLAS libraries available.

Simulations of horns show the influence of the mutual radiation impedance due to wall reflections on the throat impedance. The results show that:

- The reflections are beneficial if the distances from the horn to the walls are small (less than $0.7a_m$ for square horns), providing either a reduction in impedance ripple, or the opportunity to shorten the horn and reducing the mouth size without increasing the ripple.

- As the distances are increased beyond $0.7a_m$, the benefit is reduced, actually resulting in a notable worsening of the performance at certain distances.
- At large distances, the performance approaches that of a horn in an infinite baffle, as expected.
- Horns designed for near-wall or corner placement typically have mouth areas that are half or one quarter of the mouth area for a horn designed for infinite baffle mounting. They can therefore not be used too far from the supporting surfaces, as the horn mouth is then too small for good performance with the resulting infinite baffle radiation condition.

An experimental verification of the method presented in this chapter is given in Chapter 9, Section 9.4 on page 205.

8

HORNS IN ROOMS

The previous chapters have dealt with free standing horns, horns in infinite baffles, and baffled horns near one or two infinite boundaries, i.e. horns near corners. These approximations are useful when the horn is small compared to the room it is placed in.

If the horn is not small, or the room is not well damped, a better approximation needs to take the room modes into account. One may of course use MMM for the room directly, as is done in Chapter 12, but if the room is shoebox-shaped, more efficient methods can be used.

In this chapter, two methods are presented; the first method is based on the familiar mode sum for a rectangular room, and the second is based on expressions given by Beranek and Mellow [288] for the input impedance of a closed box with an impedance rear wall.

Part of the work in this work has been presented in [52]. The contributions in this chapter is the derivation of analytical expressions for the radiated pressure from, and the modal radiation impedance of, a distributed source in the wall of a shoebox shaped room with uniform damping, and in the wall of a room with hard walls, except for the wall opposite the source.

8.1 METHOD 1: MODE SUM METHOD

The geometry is shown in Figure 95. Method 1 is based on the transfer function in a room expressed as a mode sum. The pressure at $\mathbf{x}$ due to a source at $\mathbf{x}_0$ is [312, 313]

$$p(\mathbf{x}) = \frac{j\omega\rho U_0 c^2}{V} \sum_N \varepsilon_x \varepsilon_y \varepsilon_z \frac{\psi_N(\mathbf{x}_0)\psi_N(\mathbf{x})}{\omega^2 - \omega_N^2 - 2j\delta_N\omega_N} \tag{255}$$

where $N = (m, n, q)$ is the mode index for the room,

$$\varepsilon_x = \begin{cases} 1 & : m = 0, \\ 2 & : \text{otherwise}, \end{cases}$$

and similar for the other modes.

$$\psi(\mathbf{x}) = \cos\frac{m\pi x}{l_x} \cos\frac{n\pi y}{l_y} \cos\frac{q\pi z}{l_z}$$

is the ordinary mode function for a rectangular room with rigid walls, and

$$\omega_N = c\sqrt{k_{mx}^2 + k_{ny}^2 + k_{qz}^2},$$

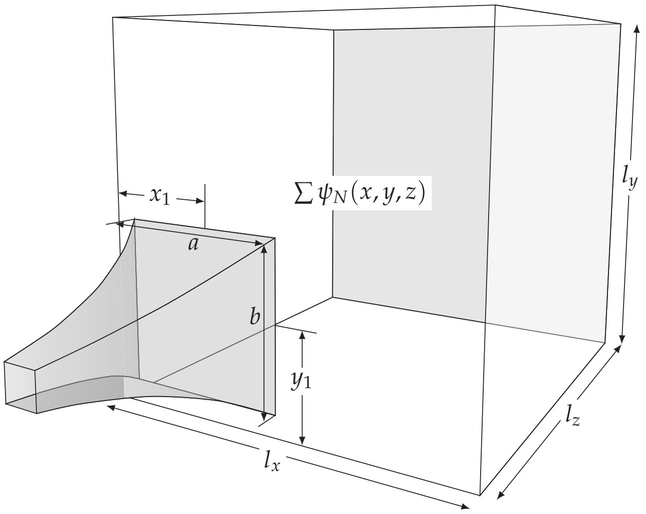

Figure 95: Geometry for a horn in the wall of a room.

where

$$k_{mx} = \frac{m\pi}{l_x},$$

etc, where $\delta_N = 6.91/T_{60}$ [33].

Let $\Omega_N = \frac{\varepsilon_x \varepsilon_y \varepsilon_z}{\omega^2 - \omega_N^2 - 2j\delta_N \omega_N}$ to simplify notation. Assume then a source velocity distribution $u(x_0, y_0, z_0)$, and assume z_0 to be constant. The pressure in the room is then

$$p(x,y,z) = \frac{j\omega\rho c^2}{V} \int\limits_{S_0} u(x_0,y_0,z_0) \sum_N \Omega_N \psi_N(x_0,y_0,z_0) \psi_N(x,y,z) dS_0. \tag{256}$$

8.1.1 *Plane Wave Excitation*

The plane wave (piston) mechanical radiation impedance is given as (see also Section 5.2)

$$Z_m = \frac{1}{u} \int\limits_S p(x,y,z_0) dS, \tag{257}$$

which when applied to Eq. (256), gives the integral

$$Z_m = -\frac{j\omega\rho c^2}{V} \int\limits_{S_0} \int\limits_S \sum_N \Omega_N \psi_N(x_0,y_0,z_0) \psi_N(x,y,z_0) dS_0 dS. \tag{258}$$

By changing the order of summation and integration, and letting the source extend from x_a to x_b and y_a to y_b, we get

$$Z_m = -\frac{j\omega\rho c^2}{V}\sum_N \Omega_N \int\limits_{x_a}^{x_b}\int\limits_{y_a}^{y_b} \psi_N(x_0, y_0, z_0)dx_0dy_0 \int\limits_{x_b}^{x_b}\int\limits_{y_a}^{y_b} \psi_N(x, y, z_0)dxdy. \tag{259}$$

Given the source geometry in Figure 95, Eq. (259) can be solved analytically by using the relation

$$\int\limits_{x_1-a/2}^{x_1+a/2} \cos\left(\frac{m\pi x}{l_x}\right)dx = \begin{cases} a, & m = 0 \\ \frac{2l_x}{m\pi}\cos\left(\frac{m\pi x_1}{l_x}\right)\sin\left(\frac{m\pi a}{2l_x}\right) & m \neq 0 \end{cases} \tag{260}$$

to give

$$Z_m = -\frac{j\omega\rho c^2}{V}\sum_N \Omega_N \cos^2\left(\frac{q\pi z_0}{l_z}\right)\frac{16l_x^2l_y^2}{n^2m^2\pi^4}$$
$$\times\left(\cos\left(\frac{m\pi x_1}{l_x}\right)\sin\left(\frac{m\pi a}{2l_x}\right)\right)^2\left(\cos\left(\frac{n\pi y_1}{l_y}\right)\sin\left(\frac{n\pi b}{2l_y}\right)\right)^2 \tag{261}$$

for the general case and

$$Z_m = -\frac{j\omega\rho c^2}{V}\sum_N \Omega_N \cos^2\left(\frac{q\pi z_0}{l_z}\right)\frac{4l_y^2}{n^2\pi^2}$$
$$\times a^2\left(\cos\left(\frac{n\pi y_1}{l_y}\right)\sin\left(\frac{n\pi b}{2l_y}\right)\right)^2 \tag{262}$$

for $m = 0$. Similar expressions are found for $n = 0$ and for $m = n = 0$.

8.1.2 *Multimodal Excitation*

When the source is a rectangle with multimodal excitation, the source velocity distribution is given by the mode functions given in Section 4.2.4. Given that the source has dimensions a, b, and is parallel to the xy-plane with the center at the position (x_1, y_1) in room coordinates, the mode functions are

$$\phi_{m_x} = N_{m_x}\cos\left(m_x\pi(x - x_1 + \frac{a}{2})/a\right) \tag{263}$$

where $N_{m_x} = 1$ for $m_x = 0$ and $\sqrt{2}$ otherwise, and similar for the y-direction.

It is now useful to define a function Y that expresses the integral in one dimension over the the source mode function multiplied with the room mode function. This integral can be found analytically as

$$
\begin{aligned}
&\Upsilon_{m_x}^{m}(a, x_1, l_x)\\
&\quad = \int\limits_{x_1-a/2}^{x_1+a/2} N_{m_x} \cos\left(m_x\pi(x - x_1 + \frac{a}{2})/a\right) \cos\left(m\pi x/l_x\right) dx\\
&\quad = \begin{cases} a, & m = 0,\, m_x = 0\\ \frac{2l_x}{m\pi} \cos\left(\frac{m\pi x_1}{l_x}\right) \sin\left(\frac{m\pi a}{2l_x}\right) & m > 0,\, m_x = 0\\ 0 & m = 0,\, m_x > 0\\ \frac{\sqrt{2}a^2 l_x m\left(\sin\left(\frac{\pi m(a-2x_1)}{2l_x}\right)+(-1)^{m_x}\sin\left(\frac{\pi m(a+2x_1)}{2l_x}\right)\right)}{\pi(ma-m_x l_x)(ma+m_x l_x)} & m > 0,\, m_x > 0 \end{cases}
\end{aligned} \tag{264}
$$

where m is the room mode index, and m_x is the mode index of the excitation.

The pressure in the room is now found from

$$
\begin{aligned}
p(x, y, z) = \frac{j\omega\rho c^2}{V} \int\limits_{x_1-a/2}^{x_1+a/2} \int\limits_{y_1-b/2}^{y_1+b/2} u(x_0, y_0, z_0)&\\
\times \sum_N \Omega_N \psi_N(x_0, y_0, z_0)\psi_N(x, y, z) dx_0 dy_0&
\end{aligned} \tag{265}
$$

where

$$
u(x_0, y_0, z_0) = \frac{1}{S} \sum_{m_x, m_y} \psi_{m_x, m_y}(x_0, y_0) U_{m_x, m_y} \tag{266}
$$

and U_{m_x,m_y} is the mode amplitude. By changing positions of the integral and the summation,

$$
\begin{aligned}
&p(x, y, z) = \frac{j\omega\rho c^2}{V} \sum_N \Omega_N\\
&\quad\times \int\limits_{x_1-a/2}^{x_1+a/2} \int\limits_{y_1-b/2}^{y_1+b/2} \psi_N(x_0, y_0, z_0) u(x_0, y_0, z_0) dx_0 dy_0 \psi_N(x, y, z).
\end{aligned} \tag{267}
$$

Then for a single excited mode of amplitude $U_{m_x m_y}$, the pressure in the room is

$$
\begin{aligned}
&p(x, y, z) = \frac{j\omega\rho c^2}{abV} U_{m_x, m_y} \sum_N \Omega_N\\
&\quad\times \int\limits_{x_1-a/2}^{x_1+a/2} \int\limits_{y_1-b/2}^{y_1+b/2} \psi_N(x_0, y_0, z_0) \psi_{m_x, m_y}(x_0, y_0) dx_0 dy_0 \psi_N(x, y, z).
\end{aligned} \tag{268}
$$

By using Eq. (264), this integral can be solved analytically, giving

$$p(x,y,z) = \frac{j\omega\rho c^2}{abV} U_{m_x,m_y} \sum_N \Omega_N \cos\left(\frac{q\pi z_0}{l_z}\right) \times \mathrm{Y}^m_{m_x}(a,x_0,l_x)\mathrm{Y}^n_{m_y}(b,y_0,l_y)\psi_N(x,y,z) \quad (269)$$

The radiation impedance for a single mode is found by

$$Z_m = \frac{1}{v} \int\limits_{x_1-a/2}^{x_1+a/2} \int\limits_{y_1-b/2}^{y_1+b/2} p(x,y,z)\psi_{n_x,n} dxdy. \quad (270)$$

By again applying Eq. (264), an analytical expression for the radiation impedance can be found:

$$Z_m = -\frac{j\omega\rho c^2}{V} \sum_N \Omega_N \cos^2\left(\frac{q\pi z_0}{l_z}\right) \times \mathrm{Y}^m_{m_x}(a,x_0,l_x)\mathrm{Y}^n_{m_y}(b,y_0,l_y)\mathrm{Y}^m_{n_x}(a,x_0,l_x)\mathrm{Y}^n_{n_y}(b,y_0,l_y) \quad (271)$$

Note that a non-zero value for z_0, the source z-position, has been used. If z_0 is different from 0 or l_z, the source is placed inside the room, and corresponds to a monopole source with a given velocity distribution. This is not appropriate for a horn, which is a one-sided radiator, but the expression may be used by setting z_0 to 0 or l_z, indicating a horn mounted in the wall.

In an attempt to find a method to compute the radiation impedance of a horn placed at a given position in the room, with a given angle to the z-axis, angled multimodal source distributions were investigated both for monopole and dipole sources. The results of these investigations are summarized in Appendix E.

8.2 METHOD 2: TERMINATED DUCT METHOD

In [288], Beranek and Mellow presented a two-port network for bass reflex enclosures where both the port and the driver are mounted in the front wall of the enclosure, and the rear wall is lined, having a *specific* impedance Z_s. Figure 96 shows the principle, modified to show a horn radiating into an enclosure with a lined rear wall, and with asymmetry in the x-direction added.

The expressions give the impedances seen by each of the pistons alone, and a coupling impedance, making it possible to compute the transmission through the system. If only a single piston is used, it is possible to compute the impedance looking into a closed box with an impedance at the opposite wall. The method seems like a good starting point for computing the radiation impedance of a horn mounted in the wall of a room if it is extended to include asymmetry in both

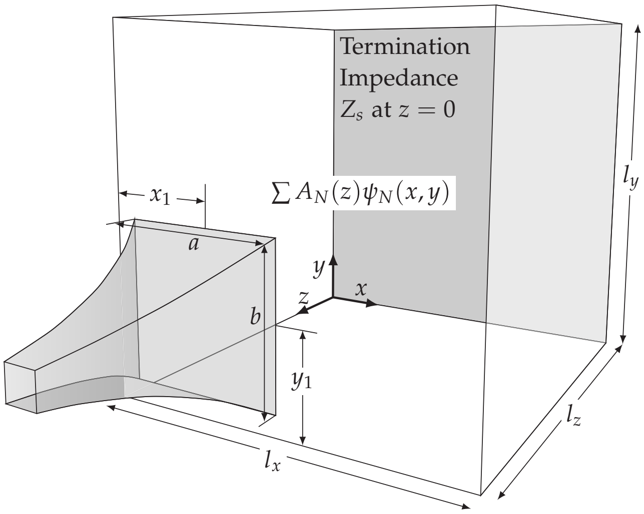

Figure 96: The geometry of a horn in the wall of a room for Method 2. All damping is now at the rear wall.

directions (the Beranek and Mellow solution assumes symmetry in the x-direction), and multimodal excitation.

8.2.1 *Basic Equations*

From [288], the pressure field inside the room can be found from

$$p(x,y,z) = \rho_0 c u_0 \sum_{m=0}^{\infty}\sum_{n=0}^{\infty}\left(A_{mn}e^{-jk_{mn}z} + B_{mn}e^{jk_{mn}z}\right) \times \cos\left(\frac{m\pi x}{l_x}\right)\cos\left(\frac{n\pi y}{l_y}\right) \quad (272)$$

and the velocity in the z direction is found from

$$\begin{aligned} u_z(x,y,z) &= \frac{1}{-jk\rho_0 c}\frac{\partial}{\partial z}p(x,y,z) \\ &= \frac{1}{k}u_0 \sum_{m=0}^{\infty}\sum_{n=0}^{\infty}\left(A_{mn}e^{-jk_{mn}z} - B_{mn}e^{jk_{mn}z}\right) \\ &\qquad \times \cos\left(\frac{m\pi x}{l_x}\right)\cos\left(\frac{n\pi y}{l_y}\right). \end{aligned} \quad (273)$$

The boundary condition at $z = 0$ (rear wall) is

$$p(x,y,z) = -Z_s u_z(x,y,0) \quad (274)$$

giving

$$B_{mn} = \frac{k_{mn}Z_s + k\rho_0 c}{k_{mn}Z_s - k\rho_0 c}A_{mn}. \quad (275)$$

The boundary condition at $z = l_z$ is found by

$$u_z(x,y,l_z) = \begin{cases} u_0, & x_1 - \frac{a_1}{2} \leq x \leq x_1 + \frac{a_1}{2},\ y_1 - \frac{b_1}{2} \leq y \leq y_1 + \frac{b_1}{2} \\ 0, & \text{otherwise.} \end{cases} \tag{276}$$

Now, with multimodal excitation,

$$u_0 = u_{m_x m_y} = N_{mx} \cos\left(m_x \pi (x - x_1 + \frac{a_1}{2})/a_1\right) \times N_{my} \cos\left(m_y \pi (y - y_1 + \frac{b_1}{2})/b_1\right) \tag{277}$$

where

$$\begin{cases} N_{m_x} = 1, & m_x = 0 \\ N_{m_x} = \sqrt{2}, & m_x > 0, \end{cases} \tag{278}$$

and similar for N_{m_y}, $u_{m_x m_y}$ is the velocity amplitude of the exciting mode. We must now also include the mode indices for the excitation in the labeling of A_{mn}, which from now will be designated $A_{mn}^{m_x,n_x}$.

Assuming the same mode functions for the horn opening as in Method 1, Eq. (263), we find $A_{mn}^{m_x,n_x}$ using

$$\begin{aligned} u_z(x,y,l_z) &= \frac{2}{k} u_0 \sum_{m=0}^{\infty} \sum_{n=0}^{\infty} k_{mn} A_{mn}^{m_x,n_x} \frac{k\rho c \cos k_{mn} l_z + j k_{mn} Z_s \sin k_{mn} l_z}{k\rho c - k_{mn} Z_s} \\ &\times \int_0^{l_x} \cos(m\pi x/l_x) \cos(p\pi x/l_x)\, dx \int_0^{l_y} \cos\left(n\pi y/l_y\right) \cos\left(q\pi y/l_y\right) dy \\ &= u_{m_x m_y} \int_{x_1 - a_{1/2}}^{x_1 + a_{1/2}} N_{m_x} \cos\left(m_x \pi (x - x_1 + \frac{a_1}{2})/a_1\right) \cos(p\pi x/l_x)\, dx \\ &\times \int_{y_1 - b_{1/2}}^{y_1 + b_{1/2}} N_{my} \cos\left(m_y \pi (y - y_1 + \frac{b_1}{2})/b_1\right) \cos\left(q\pi y/l_y\right) dy \end{aligned} \tag{279}$$

Then we apply orthogonality and the integral solutions as in Method 1:

$$\int\limits_{x_1-a/2}^{x_1+a/2} N_{m_x} \cos\left(m_x\pi(x - x_1 + \frac{a_1}{2})/a_1\right) \cos\left(m\pi x/l_x\right) dx$$
$$= \begin{cases} a_1, & m = 0,\, m_x = 0 \\ \frac{2l_x}{m\pi} \cos\left(\frac{m\pi x_1}{l_x}\right) \sin\left(\frac{m\pi a_1}{2l_x}\right) & m > 0,\, m_x = 0 \\ 0 & m = 0,\, m_x > 0 \\ \frac{\sqrt{2}a_1^2 l_x m\left(\sin\left(\frac{\pi m(a_1-2x_1)}{2l_x}\right)+(-1)^{m_x}\sin\left(\frac{\pi m(a_1+2x_1)}{2l_x}\right)\right)}{\pi(ma_1-m_x l_x)(ma_1+m_x l_x)} & m > 0,\, m_x > 0 \end{cases} \tag{280}$$

We now define a new function $\Upsilon_{m_h}^{m_r}(a_1, \xi_1, l_\xi)$ (note the italics) that differs from the previously defined Y only in that l_x/π has been moved out of the function:

$$\Upsilon_{m_h}^{m_r}(a_1, \xi_1, l_\xi) = N_{m_h} \frac{a_1^2 m_r}{a_1^2 m_r^2 - l_\xi^2 m_h^2} \left\{ \sin\left(\frac{\pi m_r\,(a_1 - 2\xi_1)}{2l_\xi}\right) + (-1)^{m_h} \sin\left(\frac{\pi m_r\,(a_1 + 2\xi_1)}{2l_\xi}\right) \right\} \tag{281}$$

where

$$\begin{cases} N_{m_h} = 1, & m_h = 0 \\ N_{m_h} = \sqrt{2}, & m_h > 0 \end{cases} \tag{282}$$

and the subscripts r and h indicates the mode index of the room and the horn, respectively.

Υ also has the following properties:

$$\Upsilon_{m_h}^{0}(a_1, \xi_1, l_\xi) = 0 \tag{283}$$

$$\Upsilon_{0}^{m_r}(a_1, \xi_1, l_\xi) = \frac{2\cos\left(\frac{m_r\pi\xi_1}{l_\xi}\right)\sin\left(\frac{m_r\pi a_1}{2l_\xi}\right)}{m_r} \tag{284}$$

We can now find the following definitions of $A_{mn}^{m_x,n_x}$, including special cases when some of the mode indices are zero:

Coefficient $A_{00}^{m_x,n_x}$ is zero for all excitation modes except the plane wave mode, so all we have left is A_{00}^{00}:

$$A_{00}^{00} = \frac{a_1 b_1}{2l_x l_y} \frac{\rho c - Z_s}{\rho c \cos kl_z + jZ_s \sin kl_z} \tag{285}$$

The other coefficients for plane wave mode excitation are the same as given in [288], except that symmetry in the y direction is not assumed:

$$A_{0n}^{00} = \frac{2a_1}{n\pi l_x}\cos\left(\frac{n\pi y_1}{l_y}\right)\sin\left(\frac{n\pi b_1}{2l_y}\right) \times \frac{k}{k_{0n}}\frac{k\rho c - k_{0n}Z_s}{k\rho c\cos k_{0n}l_z + jk_{0n}Z_s\sin k_{0n}l_z} \tag{286}$$

$$A_{m0}^{00} = \frac{2b_1}{m\pi l_y}\cos\left(\frac{m\pi x_1}{l_x}\right)\sin\left(\frac{m\pi a_1}{2l_x}\right) \times \frac{k}{k_{m0}}\frac{k\rho c - k_{m0}Z_s}{k\rho c\cos k_{m0}l_z + jk_{m0}Z_s\sin k_{m0}l_z} \tag{287}$$

$$A_{mn}^{00} = \frac{8}{nm\pi^2}\cos\left(\frac{n\pi y_1}{l_y}\right)\sin\left(\frac{n\pi b_1}{2l_y}\right)\cos\left(\frac{m\pi x_1}{l_x}\right)\sin\left(\frac{m\pi a_1}{2l_x}\right) \times \frac{k}{k_{mn}}\frac{k\rho c - k_{mn}Z_s}{k\rho c\cos k_{mn}l_z + jk_{mn}Z_s\sin k_{mn}l_z} \tag{288}$$

As for the other coefficients,

$$A_{0n}^{0,m_y} = \frac{a_1\Upsilon_{m_y}^{n}(b_1,y_1,l_y)}{\pi l_x}\cdot\frac{k}{k_{0n}}\frac{k\rho c - k_{0n}Z_s}{k\rho c\cos k_{0n}l_z + jk_{0n}Z_s\sin k_{0n}l_z} \tag{289}$$

$$A_{m0}^{m_x,0} = \frac{b_1\Upsilon_{m_x}^{m}(a_1,x_1,l_x)}{\pi l_y}\cdot\frac{k}{k_{m0}}\frac{k\rho c - k_{m0}Z_s}{k\rho c\cos k_{m0}l_z + jk_{m0}Z_s\sin k_{m0}l_z} \tag{290}$$

$$A_{0n}^{m_x,0} = A_{0n}^{m_x,m_y} = 0 \tag{291}$$

$$A_{m0}^{0,m_y} = A_{m0}^{m_x,m_y} = 0 \tag{292}$$

$$A_{mn}^{m_x,m_y} = \frac{\Upsilon_{m_x}^{m}(a_1,x_1,l_x)\Upsilon_{m_y}^{n}(b_1,y_1,l_y)}{4\pi} \times \frac{k}{k_{mn}}\frac{k\rho c - k_{mn}Z_s}{k\rho c\cos k_{mn}l_z + jk_{mn}Z_s\sin k_{mn}l_z} \tag{293}$$

8.2.2 *Impedance*

The modal radiation impedance $Z_{m_x m_y n_x n_y}$ is found by integrating over the opening and multiplying with the mode functions as usual:

$$Z_{m_x m_y n_x n_y} = \frac{1}{-U_m}\int_{x_1-a_{1/2}}^{x_1+a_{1/2}}\int_{y_1-b_{1/2}}^{y_1+b_{1/2}} N_{n_x}\cos\left(n_x\pi(x-x_1+\frac{a_1}{2})/a_1\right) \times N_{ny}\cos\left(n_y\pi(y-y_1+\frac{b_1}{2})/b_1\right)p(x,y,l_z) \tag{294}$$

We also get that

$$\frac{k\rho c - k_{mn}Z_s}{k\rho c\cos k_{mn}l_z + jk_{mn}Z_s\sin k_{mn}l_z} \times \left(e^{-jk_{mn}l_z} + \frac{k_{mn}Z_s + k\rho c}{k_{mn}Z_s - k\rho c}e^{jk_{mn}l_z}\right)$$
$$= -2\frac{\frac{k_{mn}Z_s}{k\rho c} + j\tan k_{mn}l_z}{1 + j\frac{k_{mn}Z_s}{k\rho c}\tan k_{mn}l_z}$$

so we can define a factor C_{mn} as

$$C_{mn} = \frac{\frac{k_{mn}Z_s}{k\rho c} + j\tan k_{mn}l_z}{1 + j\frac{k_{mn}Z_s}{k\rho c}\tan k_{mn}l_z}$$

For every duct mode combination $m_x m_y n_x n_y$, the total impedance is the sum of four factors:

$$Z_{tot}^{m_x m_y n_x n_y} = Z_{00}^{m_x m_y n_x n_y} + \sum_{n=1}^{\infty} Z_{0n}^{m_x m_y n_x n_y} + \sum_{m=1}^{\infty} Z_{m0}^{m_x m_y n_x n_y} + \sum_{n=1}^{\infty}\sum_{m=1}^{\infty} Z_{mn}^{m_x m_y n_x n_y}.$$

This occurs because it is necessary to treat the cases where the room mode indices are zero separately.

The general expression for the modal impedances is

$$Z_{mn}^{m_x,m_y,n_x,n_y} =$$
$$\frac{4l_x l_y}{\pi^4} Y_{m_x}^{m}(a_1, x_1, l_x) Y_{m_y}^{n}(b_1, y_1, l_y) Y_{n_x}^{m}(a_1, x_1, l_x) Y_{n_x}^{n}(b_1, y_1, l_y) \frac{k}{k_{mn}} C_{mn} \tag{295}$$

For the plane wave impedance, great simplifications can be made since $A_{m0}^{0,m_y} = A_{0n}^{m_x,0} = A_{0n}^{m_x,m_y} = A_{m0}^{m_x,m_y} = 0$, and we get

$$Z_{00}^{0000} = \frac{a_1^2 b_1^2}{l_x l_y} C_{mn} \tag{296}$$

The impedance for $Z_{00}^{m_x m_y n_x n_y} = 0$ for all other combinations of duct modes.

For the plane wave duct mode, the resulting expressions are the same as given in [288] except that no symmetry is assumed:

$$Z_{0n}^{0,0,0,0} = \frac{8a_1^2}{l_x n^2 \pi^2} \frac{k}{k_{0n}} \cos^2\left(\frac{n\pi y_1}{l_y}\right) \sin^2\left(\frac{n\pi b_1}{2l_y}\right) C_{mn} \tag{297}$$

$$Z_{m0}^{0,0,0,0} = \frac{8b_1^2}{l_y m^2 \pi^2} \frac{k}{k_{m0}} \cos^2\left(\frac{m\pi x_1}{l_x}\right) \sin^2\left(\frac{m\pi a_1}{2l_x}\right) C_{mn} \tag{298}$$

$$Z_{mn}^{0,0,0,0} = \frac{64 l_x l_y}{m^2 n^2 \pi^4} \frac{k}{k_{mn}} \cos^2\left(\frac{m\pi x_1}{l_x}\right) \sin^2\left(\frac{m\pi a_1}{2l_x}\right)$$
$$\times \cos^2\left(\frac{n\pi y_1}{l_y}\right) \sin^2\left(\frac{n\pi b_1}{2l_y}\right) C_{mn} \tag{299}$$

Parameter	Case 1	Case 2	Parameter	Case 1	Case 2
T_{60}	0.5 s	1.5 s	a_1	1.0 m	1.0 m
Z_s	$4\rho_0 c$	$12\rho_0 c$	b_1	1.0 m	1.0 m
l_x	4.0 m	4.0 m	x_1	0.5 m	0.5 m
l_y	2.4 m	2.4 m	y_1	0.5 m	0.5 m
l_z	6.0 m	6.0 m	$N_{tot,1}$	42875	42875
ϵ_w	∞	∞	$N_{tot,2}$	900	900

Table 5: Parameters for the test cases.

A few other combinations can also be simplified:

$$Z_{m0}^{m_x,0,n_x,0} = \frac{2b_1^2 l_x Y_{m_x}^m(a_1, x_1, l_x) Y_{n_x}^m(a_1, x_1, l_x)}{l_y \pi^2} \frac{k}{k_{m0}} C_{mn} \tag{300}$$

$$Z_{0n}^{0,m_y,0,n_y} = \frac{2a_1^2 l_y Y_{m_y}^n(b_1, y_1, l_y) Y_{n_y}^n(b_1, y_1, l_y)}{l_x \pi^2} \frac{k}{k_{0n}} C_{mn} \tag{301}$$

Finally, some combinations are zero: $Z_{0n}^{0,0,n_x,0}$, $Z_{m0}^{0,0,0,n_y}$,$Z_{0n}^{0,0,n_x,n_y}$, $Z_{m0}^{0,0,n_x,n_y}$, $Z_{0n}^{m_x,0,0,0}$, $Z_{0n}^{m_x,0,n_x,0}$, $Z_{0n}^{m_x,0,0,n_y}$, $Z_{m0}^{m_x,0,0,n_y}$, $Z_{0n}^{m_x,0,n_x,n_y}$, $Z_{m0}^{m_x,0,n_x,n_y}$, $Z_{m0}^{0,m_y,0,0}$, $Z_{0n}^{0,m_y,n_x,0}$, $Z_{m0}^{0,m_y,n_x,0}$, $Z_{m0}^{0,m_y,0,n_y}$, Z_{0n}^{0,m_y,n_x,n_y}, Z_{m0}^{0,m_y,n_x,n_y}, $Z_{0n}^{m_x,m_y,0,0}$, $Z_{m0}^{m_x,m_y,0,0}$, $Z_{0n}^{m_x,m_y,n_x,0}$, $Z_{m0}^{m_x,m_y,n_x,0}$, $Z_{0n}^{m_x,m_y,0,n_y}$, $Z_{m0}^{m_x,m_y,0,n_y}$, $Z_{0n}^{m_x,m_y,n_x,n_y}$, $Z_{m0}^{m_x,m_y,n_x,n_y}$. The rest is covered by Eq. (295).

8.3 RESULTS AND COMPARISONS

The two methods outlined above are somewhat different, and the results will not be completely comparable. Method 1 assumes that the damping is uniformly distributed in the room, while in Method 2 all damping is placed on the wall opposite the horn mouth. For Method 1, therefore, all room modes will experience damping, while in Method 2, the modes that do not have a z component will not experience damping.

In this section, a few modal impedances will be computed using the two methods, and with two different amounts of damping. The parameters for the test cases are given in Table 5. The value of Z_s has been adjusted to make the results of Method 2 roughly similar to the results from Method 1 by matching the level of the first resistance peak for the plane wave impedance. N_{tot} is the total number of room modes, the number indicates which method.

With the indicated number of modes, the computation time for Method 1 is 4.2 s, and for Method 2, 0.06 s. If the number of modes is reduced to 2750 for Method 1, the computation time is 0.32 s, while Method 2 takes 0.15 s with 2756 modes.

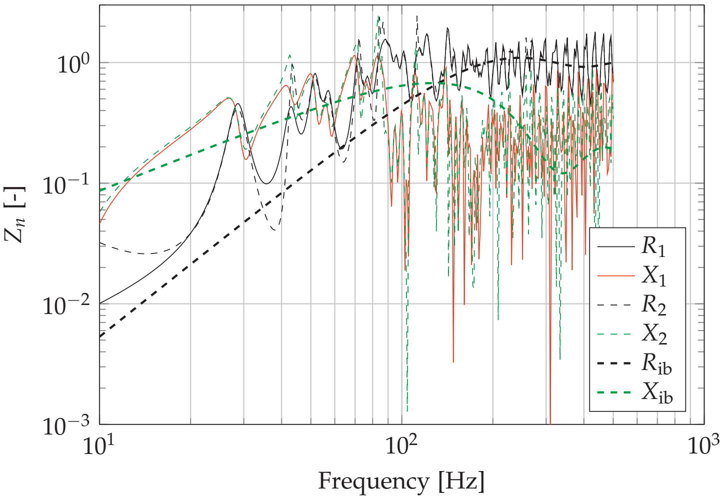

Figure 97: Plane wave impedance, test case 1.

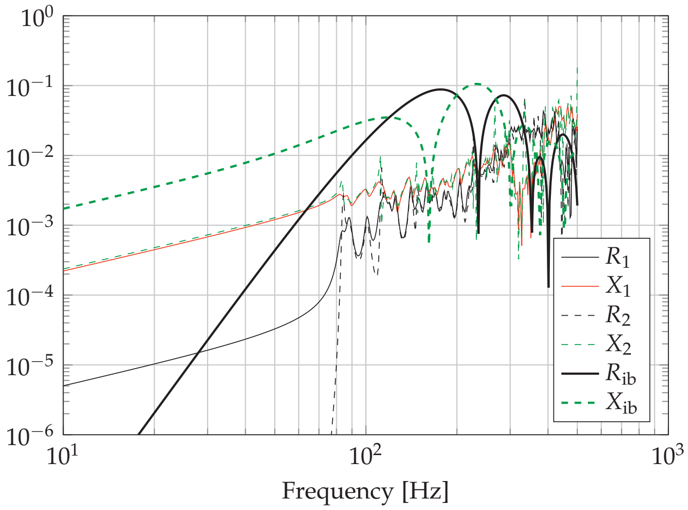

Figure 98: Impedance for mode (2,2,0,0), test case 1.

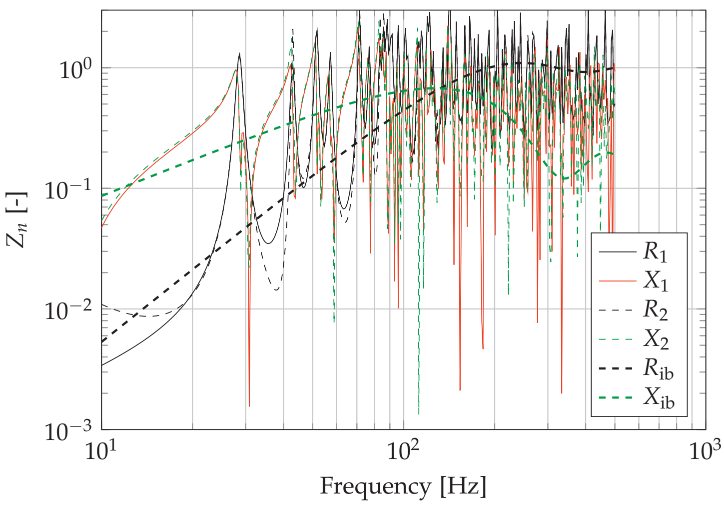

Figure 99: Plane wave impedance, test case 2.

The plane wave mode impedance for case 1 is shown in Figure 97. The effect of uniformly distributed damping can be seen in that some modes are more damped for Method 1 than for Method 2. At high frequencies, the curves overlap to a large degree, especially for the resistance. There is less overlap for reactance. As can be seen from Table 5, very many modes are used in Method 1 compared to Method 2. The reason is that for Method 1, the reactance will droop slightly at high frequencies, especially if there is much damping in the room. For instance, if the number of modes is reduced to 2750 for case 1, the reactance for the plane wave mode will oscillate around a line that slopes from about zero at 150 Hz down to -1 (normalized) at 400 Hz. This may be due to that when the modes are heavily damped, they influence the results over a much larger frequency range than when they are less damped.

Figure 97 also plots the corresponding plane wave mode impedance for the infinite baffle case. Comparing this impedance with the room impedance, it looks like the low frequency room impedance oscillates around a line with four times the value of the infinite baffle impedance. Looking at Figure 86, this would be the curve for a radiator placed tightly into a corner, which actually is the case here. Thus the increase in low frequency resistance is due to the mutual coupling to the nearest walls.

A cross-modal impedance, mode (2,2,0,0), for case 1 is shown in Figure 98. Here there is less resemblance to the infinite baffle impedance, which is probably due to how this mode couples to the room modes.

Finally, the plane wave mode impedance for case 2, which has less damping than case 1, is shown in Figure 99. Naturally, the oscillations are greater, but the agreement between the two methods is actually better. The less damping in the room, the more similar the methods should be.

8.4 SUMMARY

Two methods to find the modal impedance seen by a horn or other duct exiting in the wall of a room, have been outlined in this chapter. Both methods are based on a modal description of the sound field in a room, and on finding the radiation impedance for a distributed source with a modal excitation by analytically solving the integrals. The methods are quite different in how damping is applied to the room, Method 1 has the damping uniformly distributed in the room, while Method 2 has all damping at one wall. Despite this difference, the two methods do give reasonably similar results if the values of reverberation time and wall impedance is properly adjusted, and both methods can be applied to the problem at hand. Which model to use depends mostly on what is known about the distribution of damping in the room. If the damping mainly is at the wall opposite the source (not an unreasonable assumption in a dedicated listening room), Method 2 can be used. If the reverberation time is known, and the damping of the room is more uniformly applied, Method 1 is probably a better choice.

9

EXPERIMENTAL VERIFICATION

This chapter is based on work published in the papers [45] and [51].

The horn used in the experiments is described in Appendix D. Measurements were made in an anechoic chamber of both throat impedance and of the frequency response at various points in front of the horn.

Some of the MMM simulation results were also compared to results obtained by BEM or BERIM. By using mirroring of the elements, symmetries could be exploited. Either the mesh size could be reduced, or the effect of introducing one or two infinitely large walls could be simulated.

The mesh bandwidth used in the BEM and BERIM simulations is stated in each case, and the Boundary Element results therefore do not extend beyond this frequency.

The mesh bandwidth *is understood as the frequency where the largest element of the mesh is not larger than* 1/6*th of a wavelength.*

9.1 SETUP

The setup is shown in Figure 100. The loudspeaker unit, a SEAS 11F-GX 4″ mid-range unit, was mounted in a small closed cabinet (gray) filled with acoustic foam. This combination was connected to the horn through a 100 mm long impedance tube (black) in which two Brüel & Kjær 4149 microphones, M1 and M2, were mounted. The loudspeaker was driven by a signal from the WinMLS measurement system through a Lynx sound card and a Quad 50E power amplifier.

The radiated pressure was measured with a Brüel & Kjær 4190 microphone.

The mountings used are indicated in Figure 100, and described in Table 6. The extra reflecting walls used for the fractional space cases are described in Sections 9.4.1 and 9.4.2.

Mounting type	Size [mm]	Offset [mm]
Large baffle	1255 × 1361	(107.5, 81.5)
Small flange	500 × 500	(0, 0)

Table 6: The mounting arrangements for the horn when mounted in a large or small baffle. *Offset* is the position of the center of the horn mouth relative to the center of the baffle/flange.

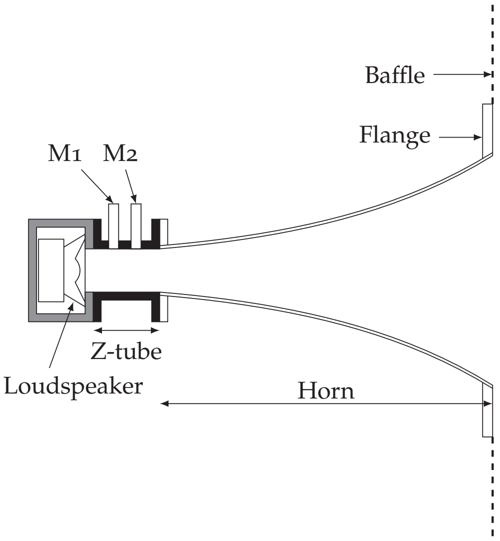

(a) Setup for small flange or infinite baffle.

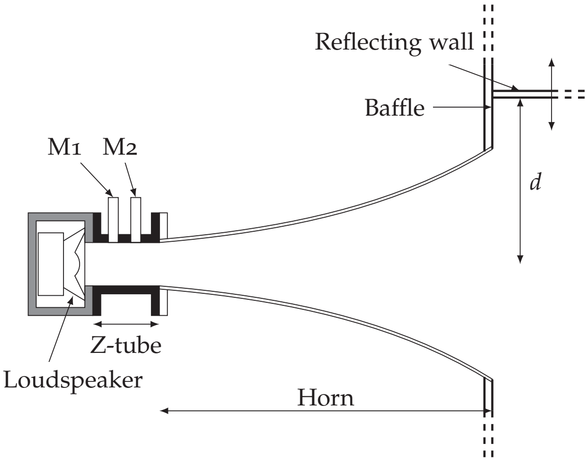

(b) Setup for reflecting walls.

Figure 100: Measurement setup.

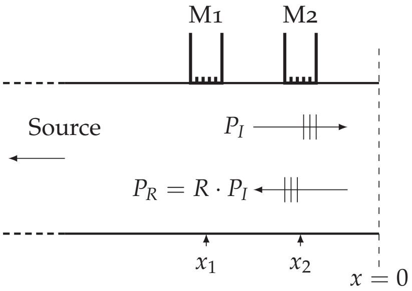

Figure 101: Principle of the two-microphone method of measuring acoustical impedance. The sound source is to the left, the sample (in this case the horn) is connected to the end where $x = 0$.

9.1.1 *Throat Impedance*

The throat impedance was measured using the conventional two-microphone method, which is the standard method of measuring the acoustical impedance of absorbing material, mufflers and horns. The method, including the calibration, is described in detail in ISO 10534-2 [314].

See Figure 101. In short, the transfer function $\frac{p_2}{p_1} = H_{12}$ between the two microphones is measured, and the reflection factor is found as

$$R = \frac{P_R}{P_I} = \frac{H_{12} - e^{-jk\Delta x}}{e^{jk\Delta x} - H_{12}} e^{2jkx_1} \tag{302}$$

where $\Delta x = x_1 - x_2$, and x_1 and x_2 are the distances from the horn throat surface to microphones 1 and 2, respectively. From this, the normalized throat impedance is found as

$$Z_A = \frac{1+R}{1-R}$$

It is known that the measurement results become unreliable above the first mode cutoff frequency, and at frequencies where the microphone spacing $\Delta x = n\lambda/2$, $n = 1, 2, \ldots.$ The first mode cuts in at about 2.6 kHz, and the microphones are one-half wavelength apart at 5.0 kHz.

It should be noted that the impedance tube is much shorter than the length recommended in the standard, and the distance between the microphones is also small (33.7 mm), considering the low frequencies measured. It has been found, however, that it is still possible to achieve good signal-to-noise ratios down to fairly low frequencies using short impedance tubes [206], and the experiments presented here confirms this. However, the calibration procedure, to take differences between the two microphones into account, turned out to be very important when using short impedance tubes. Calibration is done by

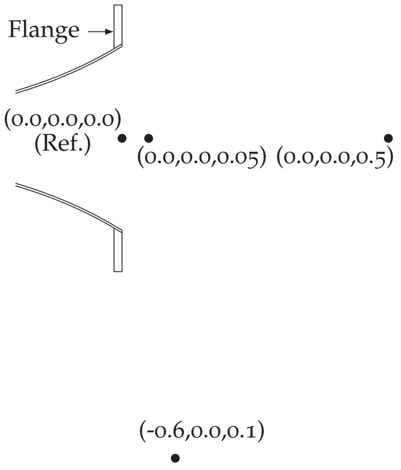

Figure 102: Placement of field points. Units in meters.

first measuring the transfer function H_{12}^{F} between the microphones in their ordinary positions, then reversing the positions and measuring the transfer function H_{12}^{B}. A calibration factor H_c is then found as

$$H_c = \left(\frac{H_{12}^{F}}{H_{12}^{B}} \right)^{1/2} . \tag{303}$$

The corrected transfer function used in further measurements is then

$$H_{12} = \frac{\hat{H}_{12}}{H_c} \tag{304}$$

where $\hat{H}_{12}$ is the uncorrected transfer function.

In the BERIM and BEM simulations, the magnitude of the impedance does not completely reach the asymptotic ρc impedance value unless the mesh is very fine. This may be related to the collocation used in the method, or to numerical dispersion as discussed by Bängtson et al. [315]. It has been found necessary to increase the impedance by an empirical factor of 4.2% to compensate for this.

9.1.2 *Frequency Response*

The frequency response was measured at several points in front of the horn, both on- and off-axis, with the impedance tube in place. Measurements were done relatively close to the horn, compared to typical directivity measurements. The purpose of the measurements was, however, the comparison with simulations, and the simulations should be valid for any distance, as the far field approximations were not used for the cases considered here.

To make comparisons between simulations and measurements that are relatively independent of the behavior of the loudspeaker driver used, a point at the center of the horn mouth has been used as reference. This point has been designated as the origin, and the pressures at all other points are compared to the pressure here. See Figure 102.

9.2 HALF-SPACE

Amir et al. [265] have verified experimentally and numerically that the discrete model carried to the limit is able to predict both the sound field inside the horn, and the input impedance of the horn. Kemp has also demonstrated that the discrete model is able to predict the input impedance of wind instruments with good accuracy. In both these studies, the horn was assumed mounted in an infinite baffle, although Amir et al. also tested the horn without baffle and with a closed end. The half-space case is therefore in principle verified. It is still useful to measure the half-space case for three reasons: first, the verifications of Amir and Kemp are based on a musical instrument bore, which is a long tube with large resonant peaks (at the fundamental resonance these peaks have normalized impedance values larger than 20). While it is challenging to accurately model the exact resonance frequencies of musical instruments, it is also interesting to see how well the method works for horns that do not have large resonant peaks, and where the higher order modes are cut-on in a larger part of the horn's high frequency range. Second, these former verifications have not looked at the radiated field. While this has been done by Schuhmacher and Rasmussen [270], these authors used no more than four modes, and the agreement with experiment was only fair. Third, the half-space case also serves as a reference point for the other cases to follow.

9.2.1 *Throat Impedance*

The throat impedance for the test horn mounted in a large baffle is shown in Figure 103. Measurements (solid lines) are compared to MMM (dashed) and BERIM (dotted).

The introduction of the first mode in the measurement setup at approx. 2.6 kHz can be seen, and one notices the increased deviation from the simulated values above this frequency. The measurements break down completely above approximately 4.2 kHz, as opposed to the theoretical 5 kHz. This is, however, most likely due to the finite dimensions of the 0.5″ microphones, since the 33.7 mm distance is the center-center spacing.

256 modes were used in this simulation, and the horn consisted of 100 duct elements. For the BERIM simulation, a mesh bandwidth of 3kHz was used, and the symmetry of the geometry was exploited.

The maximum and mean errors, computed from $\epsilon_{\mathcal{M}} = |Z - Z_{\mathcal{M}}| \,/\, |Z_{\mathcal{M}}|$, are low, as listed in Table 7, and confirm the data

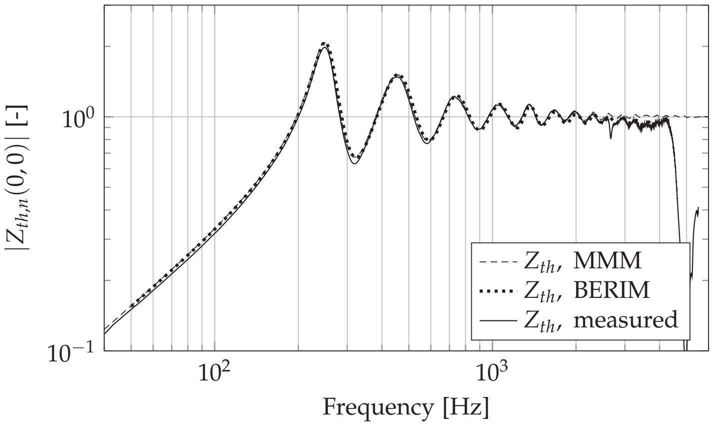

(a) Magnitude (normalized)

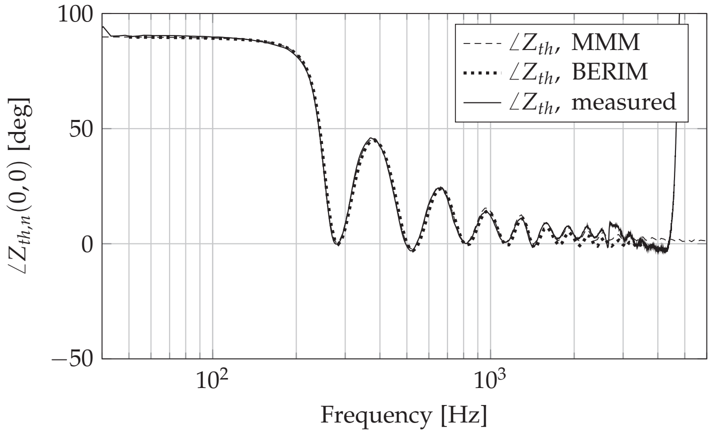

(b) Phase

Figure 103: Throat impedance for the test horn in a large/infinite baffle.

in Figure 103. Z and $Z_{\mathcal{M}}$ indicate the simulated and measured impedance, respectively.

9.2.2 *Radiated Pressure*

Figure 104 shows the relative responses at three different points in front of the horn with a large baffle: one very close, one at a distance on the principal axis, and one that is out to the side and fairly close to the plane of the baffle. It can be seen that the MMM and BERIM simulations follow each other well, and both capture the principal features of the measurements. The deviation at low frequencies is most likely due to the influence of the finite baffle used in the measurements. This is also most likely the cause of the deviation at 1kHz

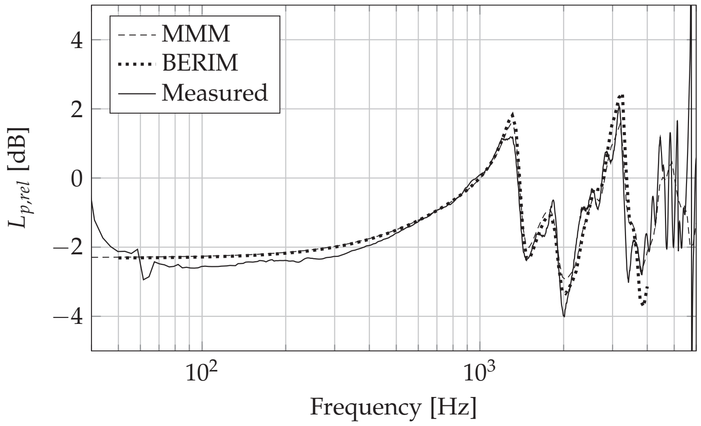

(a) Case 1B: $p(0.0, 0.0, 0.05)/p(0.0, 0.0, 0.0)$.

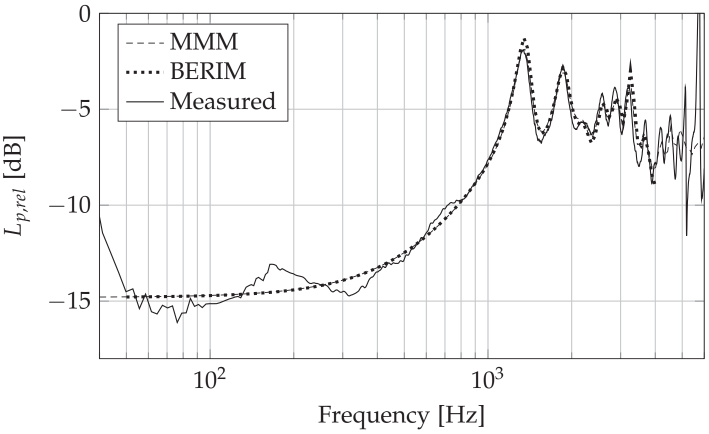

(b) Case 2B: $p(0.0, 0.0, 0.5)/p(0.0, 0.0, 0.0)$.

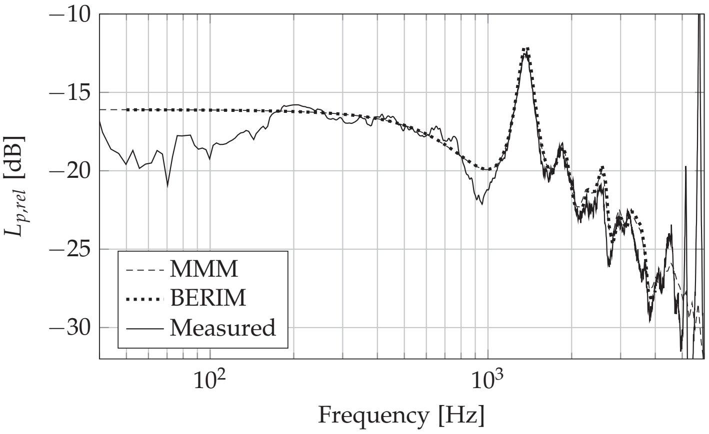

(c) Case 3B: $p(-0.6, 0.0, 0.1)/p(0.0, 0.0, 0.0)$.

Figure 104: Radiated pressure for the test horn in a large baffle.

$\max \epsilon_{\mathcal{M}}$	$\overline{\epsilon_{\mathcal{M}}}$
0.066	0.0123

Table 7: Normalized throat impedance error, horn with large baffle, in the frequency range 40 Hz to 2.5 kHz.

Case	$\max\lvert\Delta L_{p,2\pi}\rvert$ [dB]	$\overline{\lvert\Delta L_{p,2\pi}\rvert}$ [dB]	$\max\lvert\Delta L_{p,BERIM}\rvert$ [dB]	$\overline{\lvert\Delta L_{p,BERIM}\rvert}$ [dB]
1B	1.1	0.31	1.1	0.29
2B	1.4	0.36	1.5	0.37
3B	2.6	0.65	3.5	0.71

Table 8: Frequency response error, horn with large baffle. Error computed in the frequency range 100 Hz to 3 kHz.

in Figure 104c, since this point is quite close to the baffle edge. The maximum and mean errors in frequency response, computed in the frequency range 100 Hz to 3 kHz, are listed in Table 8.

9.3 FULL SPACE

For full space (4π), the measurements were compared to both the MMM, MMM with Edge Diffraction (MMM+ED), and BEM. Ordinary BEM was used [227], with a simple pyramid-shaped enclosure around the horn, see Figure 105. A simplified geometry was used to avoid discretizing the thin flange and the many small details on the outside of the actual horn. Discretizing these thin objects would result in many small surface elements and extended computation time, without giving any clear benefit.

The influence of edge diffraction was calculated for the frequency range 100 Hz–2 kHz. Extrapolation of the data was used below this range, but above 2 kHz the diffraction contribution was ignored.

As with the large baffle case, increased deviation above 2.6 kHz can be seen in Figures 106 and 107b. 196 modes have been used for the simulation, as the modal decomposition of the diffraction-related radiation impedance with the given number of integration points did not allow for modes of higher order to be reliably resolved. As in the large baffle case, the horn consisted of 100 duct elements. For the BEM simulation, a mesh bandwidth of 2 kHz was used, and the symmetry of the geometry was exploited. The geometry used is illustrated in Figure 105.

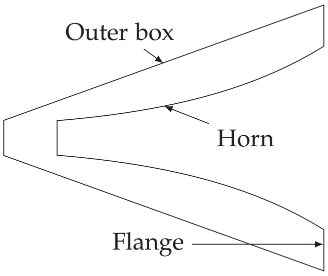

Figure 105: BEM geometry for the horn with flange.

9.3.1 *Throat Impedance*

The throat impedance for the test horn with the small flange, is shown in Figure 106 on the next page.

As expected, the impedance ripple is higher for the horn with a flange than for the horn in the large baffle. This is mainly due to the reduced value of the radiation impedance at low frequencies for the flanged case, see Figure 69. The MMM+ED overestimates the first impedance peaks somewhat. The most likely reason for this is that the geometry of the horn is approximated by a single thin plate representing the flange, and the rear side of the horn is ignored.

In Figure 107 the measured throat impedance for the flanged horn is compared to simulations using MMM and MMM+ED. In Figure 107b the relative error is shown for the two cases, in addition to the BEM simulation. For this figure, the simulated impedance values have been interpolated to the frequency values in the measurements, before computing the error.

9.3.2 *Radiated Pressure*

Figure 108 shows the response at the same points in front of the horn with a small flange as for the infinite baffle. Again, both MMM+ED and BEM capture the principal features of the measurements. Above 2kHz the BEM simulation experiences problems with eigenfrequencies, so results for frequencies above 2kHz are not shown. Since the edge diffraction terms are only calculated in the range 100Hz to 2kHz, only this range is shown for MMM+ED. The deviation of the MMM+ED results in the 200–600Hz range in Figure 108c could be due to the approximate geometry used in the edge diffraction simulation, since at this point the rear of the horn is visible from the receiver position.

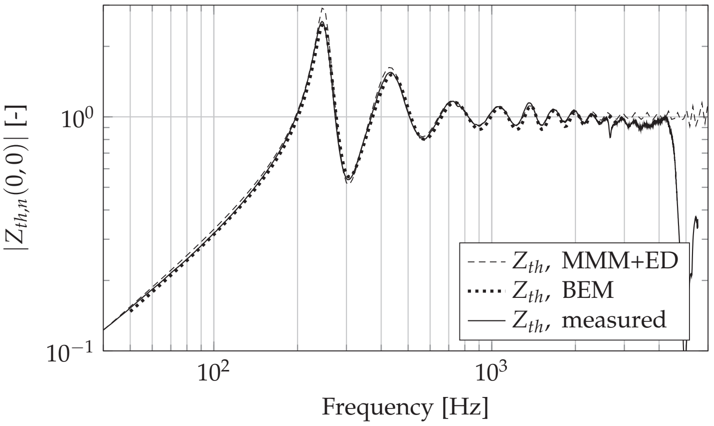

(a) Magnitude (normalized)

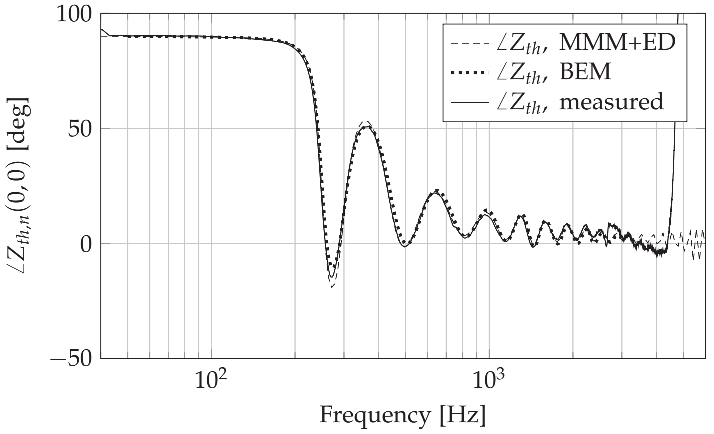

(b) Phase

Figure 106: Throat impedance for the test horn with a small flange.

9.3.3 *Comments*

Table 9 shows the maximum and mean relative error for the throat impedance, computed as $\epsilon_{\mathcal{M}} = |Z - Z_{\mathcal{M}}| / |Z_{\mathcal{M}}|$, in the range between 100 Hz and 2 kHz, which is where the first mode in the impedance tube starts to influence the results. Z and $Z_{\mathcal{M}}$ indicate the simulated and measured impedance, respectively. In addition, the throat impedance simulated by MMM for half-space is compared to the measurements, and the relative error in this case is calculated as $\epsilon_{2\pi} = |Z_{2\pi} - Z_{\mathcal{M}}| / |Z_{\mathcal{M}}|$. As can be seen, the maximum error is significantly reduced by including edge diffraction.

Figure 109 and Table 10 summarize the responses computed with MMM, MMM+ED and BEM, relative to the measurements for the

$\max \epsilon_{\mathcal{M}}$	$\overline{\epsilon_{\mathcal{M}}}$	$\max \epsilon_{2\pi}$	$\overline{\epsilon_{2\pi}}$
0.22	0.027	0.45	0.067

Table 9: Normalized throat impedance error, horn with small flange, in the frequency range 100 Hz to 2 kHz.

Case	$\max\lvert\Delta L_{p,4\pi}\rvert$ [dB]	$\overline{\lvert\Delta L_{p,4\pi}\rvert}$ [dB]	$\max\lvert\Delta L_{p,2\pi}\rvert$ [dB]	$\overline{\lvert\Delta L_{p,2\pi}\rvert}$ [dB]
1F	0.66	0.17	0.70	0.25
2F	0.81	0.83	2.67	0.95
3F	1.7	0.67	6.9	4.0

Table 10: Frequency response error, horn with small flange.

horn with a small flange. Also here, the simulated values have been interpolated to match the frequencies in the measurements.

It is clear from these comparisons that

- Close to the horn mouth (Figures 108a and 109a) the contribution from edge diffraction is small, even at low frequencies, since the direct sound is strong there. Still, the methods that take the finite size of the baffle into account (MMM+ED, BEM) are more accurate.
- On-axis, but further from the horn mouth (Figures 108b and 109b), edge diffraction contributes significantly below approximately 1.5 kHz, but above this frequency the difference between a finite and infinite baffle is small. The reason for this is most likely the directivity of the horn.
- Off-axis (Figures 108c and 109c), the edge diffraction alters the directivity pattern significantly over a large frequency range, causing large errors at all frequencies for the MMM without ED. The difference between the MMM+ED and BEM results are probably due to the different geometries for the two methods.

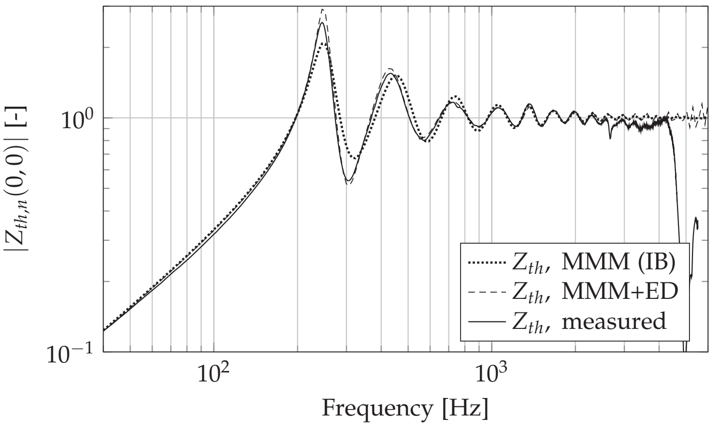

(a) Magnitude

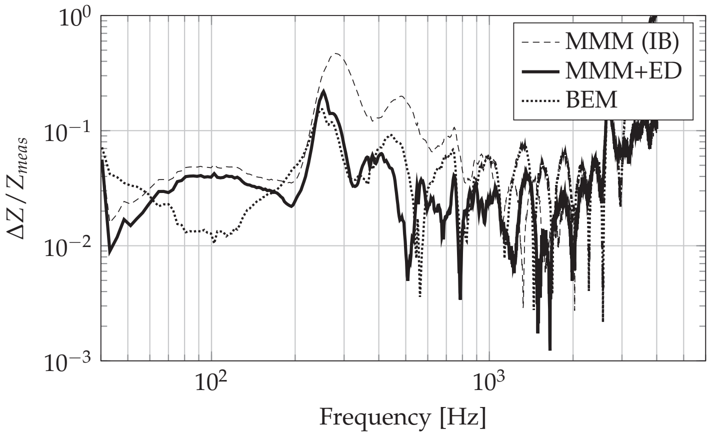

(b) Relative difference (comparison with measurements).

Figure 107: Throat impedance from MMM simulations compared to measured values for the test horn with a small flange, with and without edge diffraction.

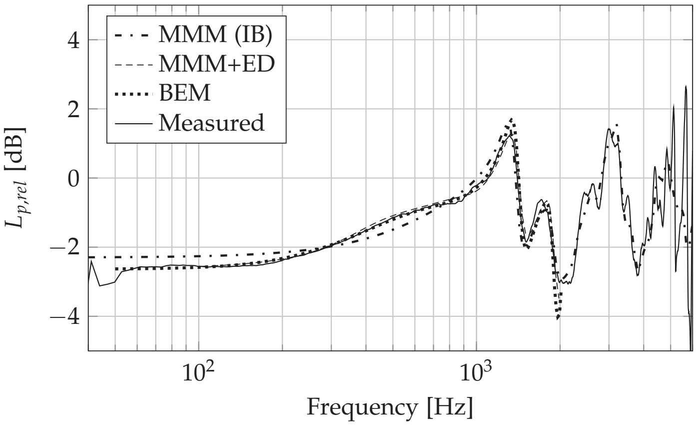

(a) Case 1F: $p(0.0, 0.0, 0.05)\,/\,p(0.0, 0.0, 0.0)$.

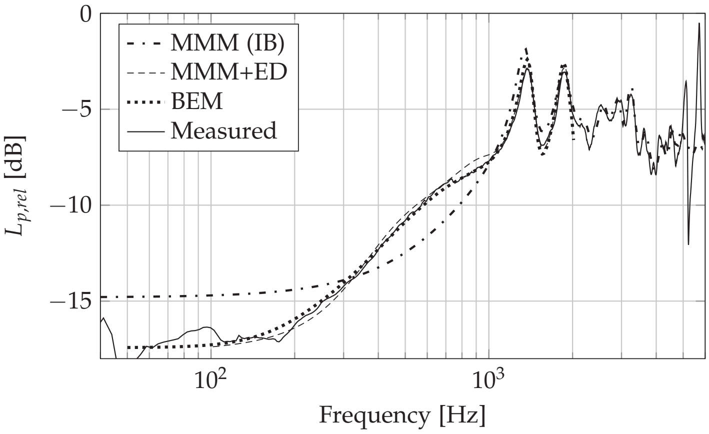

(b) Case 2F: $p(0.0, 0.0, 0.5)\,/\,p(0.0, 0.0, 0.0)$.

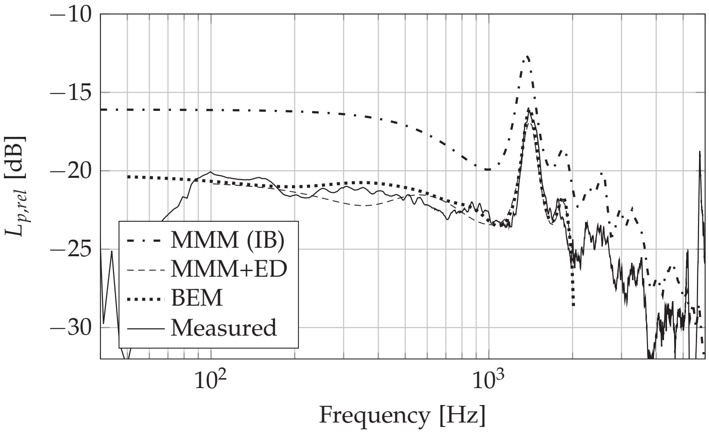

(c) Case 3F: $p(-0.6, 0.0, 0.1)\,/\,p(0.0, 0.0, 0.0)$.

Figure 108: Radiated pressure for the test horn with a small flange.

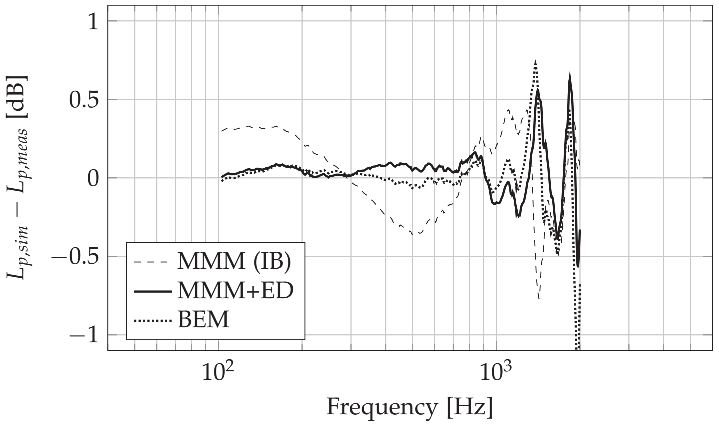

(a) Case 1F: $p(0.0, 0.0, 0.05) / p(0.0, 0.0, 0.0)$.

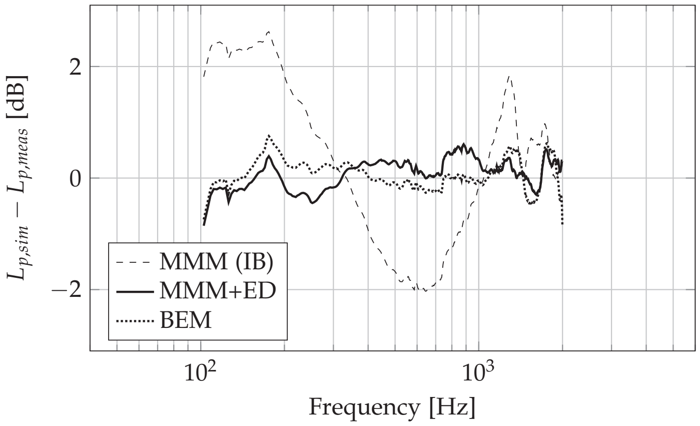

(b) Case 2F: $p(0.0, 0.0, 0.5) / p(0.0, 0.0, 0.0)$.

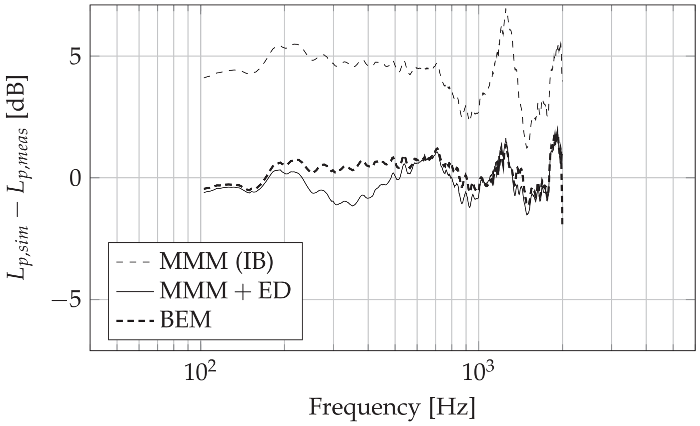

(c) Case 3F: $p(-0.6, 0.0, 0.1) / p(0.0, 0.0, 0.0)$.

Figure 109: Relative error in radiated pressure for the test horn with a small flange. Please note the different vertical scales.

9.4 CORNER PLACEMENT (FRACTIONAL SPACE)

The horn was also measured mounted in a large baffle and close to one or two extra walls. The large baffle was the same as used for the measurements in Section 9.2. The results for these two cases are presented below.

9.4.1 *Quarter Space (1π)*

Quarter space (1π steradians solid angle) was emulated by placing a second large surface in the form of a sheet of plywood (1450 mm wide by 1400 mm high) on the baffle in which the horn was mounted, and perpendicular to it. This surface was also parallel to one edge of the horn mouth, and was fixed to the horn baffle by an arrangement of clamps. The distance from the center of the horn mouth to the second surface was varied from almost touching the edge of the horn mouth, to 0.4 m. A few examples of the measured and simulated throat impedance are given in Figure 110. The simulated throat impedance for 2π solid angle is also shown for comparison. d indicates the distance from the horn mouth center to the second surface. All examples show reasonable to good agreement with measurements, and indicate the importance of including the mutual radiation impedance in the calculations.

In Figure 111, the sound pressure levels at two positions, relative to the horn mouth center, are shown. The closest position shows very little deviation from the measurements, while there is increasing deviation at low frequencies at the more distant position.

9.4.2 *Eighth Space (0.5π)*

Eighth space (0.5π steradians solid angle) is emulated by placing two large surfaces on the baffle in which the horn is mounted, perpendicular to it and to each other. One of the surfaces is the one used in Section 9.4.1, the other is a slightly smaller sheet of plywood 990 mm wide by 1070 mm high. The surfaces are parallel to the edges of the horn mouth, and again fixed in place by an arrangement of clamps. No sealing agent was used, but the plywood sheets were held as close together as practicable to minimize leakage. The distances from the center of the horn mouth to the surfaces were varied in various ways. A few examples of the measured throat impedance are given in Figure 112. The simulated throat impedance for 2π solid angle is also shown for comparison, as above. d_x and d_y indicate the distances from the horn mouth center to the surfaces in the two directions.

Figure 113 shows the sound pressure levels at two positions, relative to the horn mouth center. Again, there is good agreement with an increasing deviation at low frequencies.

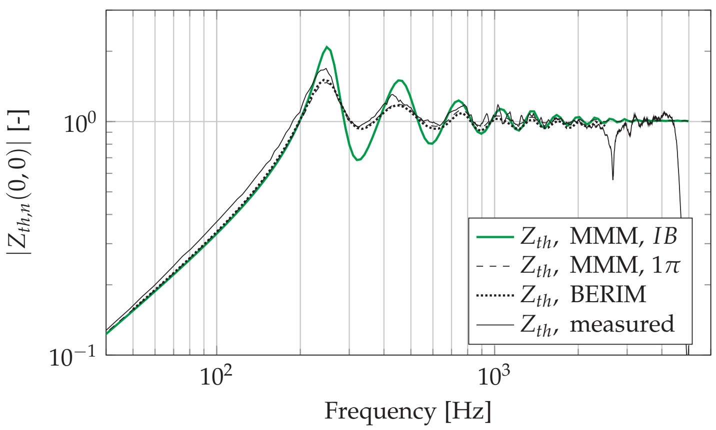

(a) Case 1: $d = 175\,\text{mm} = 0.51a_m$.

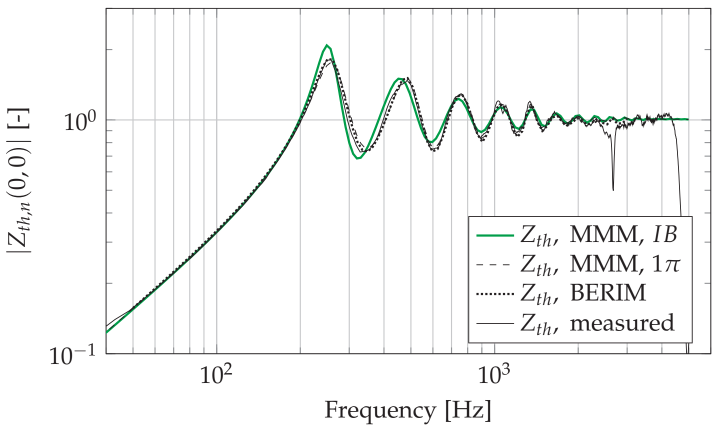

(b) Case 2: $d = 250\,\text{mm} = 0.73a_m$.

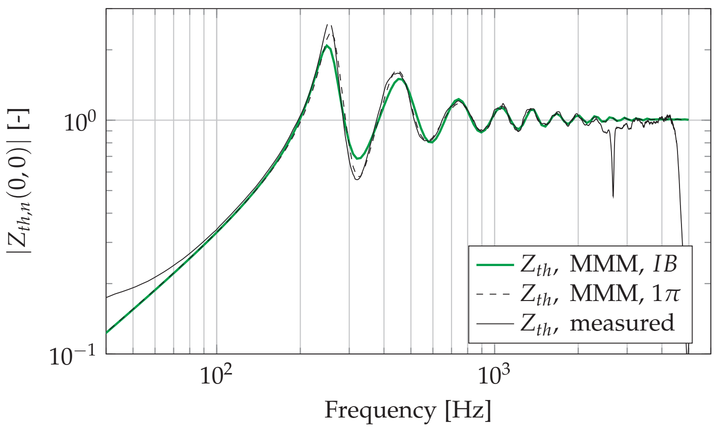

(c) Case 3: $d = 400\,\text{mm} = 1.2a_m$.

Figure 110: Throat impedance, quarter space.

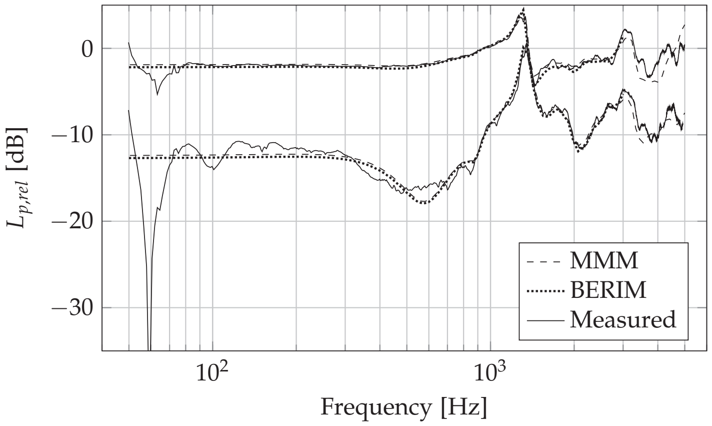

Figure 111: Relative sound pressure level, quarter space, $d = 250\,\mathrm{mm} = 0.73a_m$ (case 2). Upper curves correspond to position 0.0, 0.0, 0.05, the lower curve to position 0.0, 0.175, 0.5.

Case	$\max\epsilon_{\mathcal{M}}$	$\overline{\epsilon_{\mathcal{M}}}$	$\max\epsilon_{2\pi}$	$\overline{\epsilon_{2\pi}}$
1	0.14	0.034	0.30	0.069
2	0.17	0.025	0.18	0.043
3	0.21	0.026	0.23	0.036
4	0.22	0.053	0.80	0.14
5	0.18	0.040	0.40	0.072

Table 11: Normalized throat impedance relative error, 100 Hz-2 kHz. $\epsilon_{\mathcal{M}}$ and $\epsilon_{2\pi}$ are defined in the text. Horn near corner.

9.4.3 *Comments*

The maximum and mean deviations for the five cases presented in Section 9.4 are given in Tables 11 and 12. For the impedance, the relative error $\epsilon_{\mathcal{M}} = |Z - Z_{\mathcal{M}}| \,/\, |Z_{\mathcal{M}}|$ has been computed in the range between one octave below f_c, and 2 kHz, which is where the first mode in the impedance tube starts to influence the results. For the frequency response, the frequency range is limited to exclude the dip in the measured responses at 60 Hz.

In addition, the MMM simulated throat impedance for half-space is compared to corresponding measurements[1] for either quarter space or eighth space. The relative error is calculated as $\epsilon_{2\pi} = |Z_{2\pi} - Z_{\mathcal{M}}| \,/\, |Z_{\mathcal{M}}|$. As can be seen, the maximum error is significantly reduced for the shorter distances by including the mutual impedance. Additionally, the following points can be made:

---

[1] Note that in [51] the half-space simulations were compared to *simulations* for quarter space or eighth space.

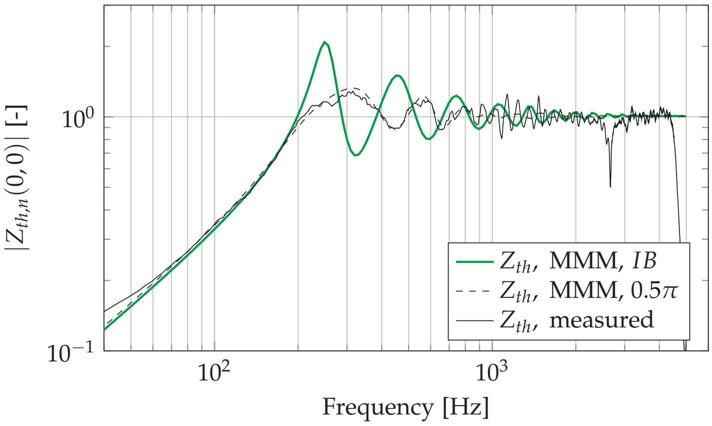

(a) Case 4: $d_x = 175\,\text{mm}$, $d_y = 175\,\text{mm}$.

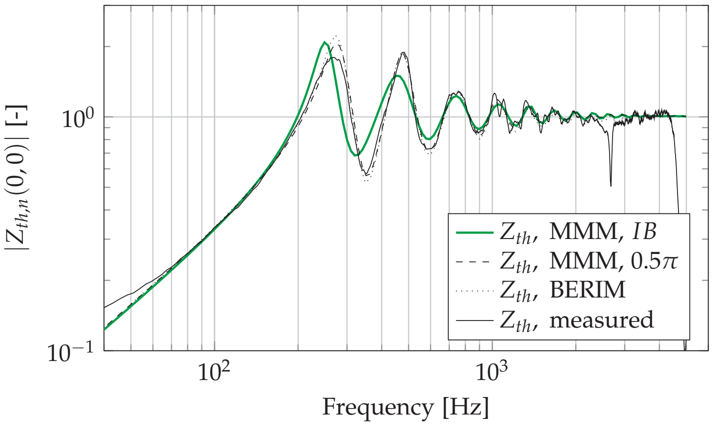

(b) Case 5: $d_x = 300\,\text{mm}$, $d_y = 250\,\text{mm}$.

Figure 112: Throat impedance, eighth space.

- The main cause of the impedance errors is a slight shift of the resonance peaks. In addition, the model is not always able to correctly predict the amplitude of the first resonance peak at larger distances, which may again be attributed to the finite size of the reflecting surfaces.

- The finite reflecting surfaces introduce edge diffraction effects that are not taken into account in the simulation. Including the effects in a Boundary Element model would increase the mesh size significantly, in particular because it is necessary to model thin structures. While it is possible to include edge diffraction in the MMM, as shown in Section 6.3, this was omitted since this contribution is rather small compared to the effect of the reflecting surfaces.

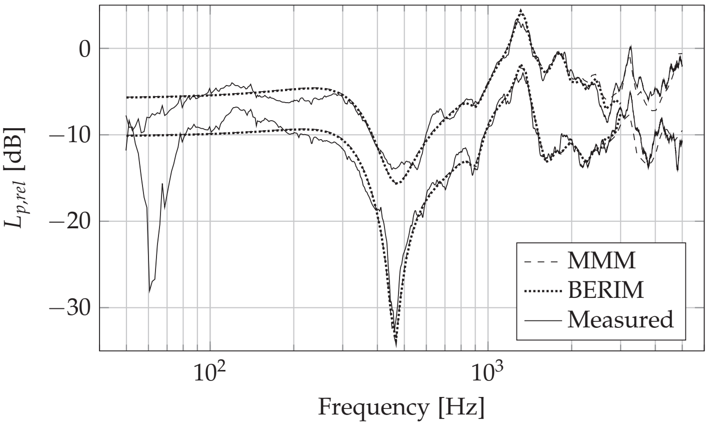

Figure 113: Relative sound pressure level, eighth space, $d_x = 300\,\mathrm{mm}$, $d_y = 250\,\mathrm{mm}$ (case 5). Upper curves correspond to position 0.0, 0.0, 0.25, the lower curves to position 0.175, 0.175, 0.5.

Case	$\max\lvert\Delta L_p\rvert$ [dB]	$\overline{\lvert\Delta L_p\rvert}$ [dB]
2	2.7	0.59
5	7.1	0.96

Table 12: Frequency response error, 80 Hz-4 kHz. Horn near corner

- The pressure diffracted from the edges of the reflecting surfaces is also most likely the cause of much of the unevenness of the measured frequency response at medium to high frequencies, but the high frequency break-up of the diaphragm may also contribute somewhat.

9.5 COMPUTATIONAL EFFICIENCY

A brief discussion of the computational efficiency will be given here. First it must be mentioned that in the comparisons above, different implementations have been used, as they were performed at various stages in the development of the tools used. All the computations have been performed on a computer that had an Intel i7-2600 CPU running at 3.4 GHz, and 8 GB RAM. Computation times are given for comparison purposes only.

Reference results have been computed using the Boundary Element Method (BEM) and Boundary Element Rayleigh Integral Method (BERIM). The computer codes for these methods are developed in FORTRAN by Stephen Kirkup [227, 191], but for the current application, the BEM code has been implemented in C++ with OpenMP parallelization [316]. The run time for the horn in Section 9.3, which had a quarter-symmetric mesh of 858 elements was about 20 minutes for 100 frequencies.

BERIM has previously been implemented in Pascal, and runs on only one core. The BERIM horn mesh for quarter space had 1659 elements, and the computation time was 1 h 47 min for 100 frequencies on a single core. The horn mesh for eighth space had 3324 elements, and the computation took 10 h 22 min, for 100 frequencies. The quarter space mesh is smaller due to the use of mirror elements for half the horn. The reflecting walls were also in both cases simulated by mirror elements. This not only reduces the memory requirement, but also shortens the solution time for the linear system of equations. The time required for building the matrices, however, still corresponds to the time required if the mirror elements were actual elements, in the current implementation. Previous experience with parallelizing boundary element code indicates that the speedup is almost linear. This indicates that a good estimate of computation time for BERIM on 4 cores would be one-fourth of the time reported above (27 min and 2 h 35 min respectively).

The efficiency of the edge diffraction computation used in this work is very low, due to the lack of parallelization of the code, and extensive use of nested for-loops, which is detrimental to speed in Matlab. The toolbox, as currently implemented, does not handle a large number of sources efficiently. Run time for the current problem was several hours. Significantly more efficient implementations are anticipated for compiled implementations tailored to the thin baffle case. An increase in efficiency could also be had by simulating the sources as a distributed source (one distributed source per radiation mode) instead of individual sources. This would enable more efficient computation of the edge source terms, as instead of handling 576 individual sources, for instance only 144 distributed sources (the maximum number of modes possible to extract with the used number of Gauss points) could be used.

Efficiency was not the main interest in this investigation, however, but rather to investigate the contribution of diffraction separately from the direct sound. This can hardly be done using conventional element-based methods like BEM.

For MMM, the computationally heaviest part is to compute the throat impedance and volume velocity transfer matrices, if Z_{IB} is precomputed and $Z^{(M)}$ is not needed at high frequencies. The Matlab implementation of MMM used for the work described in Section 9.3 took 10 minutes for 200 frequencies in the case where the horn had 256 modes and 100 duct elements. This figure does not include the computation of the radiation impedance, which is done in C++/OpenMP and takes another 10 minutes, or the interpolation of the tabulated values.

N_{modes}	$t_{50\,el}$ [s]	$t_{150\,el}$ [s]
16	5.2	10.8
36	8.7	20.6
64	16.0	42.6
144	52.8	156.3

Table 13: MMM run times for some combinations of modes and elements. Quarter space, 200 frequencies, 4 cores.

When fewer modes are needed, the computation is significantly faster. A C++ implementation of MMM was used for the results in Section 9.4 and uses about 15-20s (for 50 elements, 64 modes, 200 frequencies) when running on 4 cores. Other timing examples are given in Table 13. The infinite baffle radiation impedance had been precomputed and tabulated, the mutual impedance was computed on the fly. The computation time does not increase materially from going from the quarter space to the eighth space radiation condition. The time needed to compute the sound pressure from the Rayleigh integral, Eq. (156), is not included. This time is independent of the number of elements in the horn, but depends on the number of field points and on how the integration is performed.

From the above discussion, it is clear that a fair comparison of the efficiency of the various methods is not readily possible from the results in this chapter. A proper comparison would require that the same amount of care and optimization had been applied to all methods, so that each of them performed at its best. However, the objective of this chapter has been to experimentally and numerically verify the accuracy of the methods, although the timing results also indicate that the MMM has an advantage over BEM and BERIM efficiency-wise.

9.6 SUMMARY

In general, the agreement between simulation and measurement, and between the simulation methods used, is good. The errors are within limits acceptable for engineering use. The following observations can be made:

- For the infinite baffle case, the simulated throat impedance agrees very well with the measurements, even if the measured baffle is finite. The average error is in the order of 1%. If the baffle is "large enough", it behaves like an infinite baffle, see Figure 103.
- The simulated radiated pressure for the large/infinite baffle generally agrees well with the measurements with average er-

rors less than 1 dB, but there is some deviation at low frequencies when the observation point is close to the edge of the baffle.

- The effects of a small flange or baffle, cannot be ignored. Simulating the horn as if it was mounted in an infinite baffle gives average throat impedance errors on the order of 7%, and larger errors at low to medium frequencies.
- Part of this error comes from a frequency shift of the resonance peaks, but also from predicting the wrong amplitude of those peaks.
- When using MMM with edge diffraction, the error in throat impedance is reduced to below 5% for most of the frequency range, see Figure 107b. This is actually better than BEM over much of this range, although this could probably be improved by using a finer mesh, and by using a mesh closer to the actual geometry.
- Adding reflecting boundaries near the horn has the effect predicted by the simulations, even if the added walls are relatively small. The effect of this can be seen at low frequencies, and is most evident when the added walls are placed near the horn mouth.
- The agreement between MMM and BERIM for the infinite baffle case and for the case of extra reflecting boundaries is excellent, and the curves are virtually indistinguishable.

In conclusion, the experiments have shown that MMM with the extensions described in Chapter 6 and Chapter 7 can accurately simulate the throat impedance and radiated pressure for horns with small flanges, and mounted near reflecting boundaries. The ability of MMM to predict the throat impedance for horns mounted in an infinite baffle has already been demonstrated by Amir et al. [265] and Kemp [267], but as shown above, the method is also able to predict the radiated pressure with good accuracy.

Part III

EXTENSIONS

This part covers extensions and new applications of the Mode Matching Method beyond change of geometry and radiation impedance. This includes interfacing with the Boundary Element Method, simulating vibrating concave structures (like loudspeaker diaphragms) and simulating non-shoebox shaped rooms.

10

HYBRID METHODS

As discussed in Chapter 4, MMM can only be applied to cross-sectional geometries where the mode functions are known. But sometimes it is necessary to make a transition between two kinds of geometry, or to include a geometry that is not possible to describe in a separable coordinate system. In many cases, the main part of a horn may have a simple geometry, with special geometries only at certain points. For instance, a horn may be rectangular with a transition to circular at the throat, where it continues as a circular duct into the compression driver. In this case, most of the horn could be efficiently simulated by MMM, while the transition part could be simulated by either FEM or BEM. In addition, the exterior of the horn, like the enclosure, could be simulated using BEM. A combination of BEM and MMM is described by Shindo et al. [188], but the MMM part is implemented quite differently from the implementation used in this thesis, and the interface between the two methods is not clearly described. The motivation for using BEM for parts of the horn in [188] was to avoid numerical instability in the MMM part, a problem which is avoided in the method described in Chapter 4. Post and Hixon [206] describe a method where interior BEM is coupled to a hemisphere on which the sound field is described by spherical harmonics. The hemisphere is used as a “super-element”, and the coefficients of the spherical harmonics expansion are found as part of the solution of the BEM system of equations. This method is only applicable to the axisymmetric cases where the BEM part is closest to the mouth.

This chapter is based on the work described in [53]. The contributions in this chapter are to present simple methods to couple MMM and BEM, and to express these methods in a straightforward matrix form.

10.1 BEM AS LOAD

The BEM is described in more detail in Section 3.3.4, and the formulation and operators used in the current chapter are described there.

In order to turn a BEM surface into a load for an MMM horn, the impedance at the surface, as seen by the MMM horn, must be expressed in terms of a modal impedance matrix. For instance, the BEM horn shown in Figure 114 may be connected to an MMM horn at surfaces Θ and Π, and the pressure and velocity at the surface Θ must be converted into a modal impedance matrix.

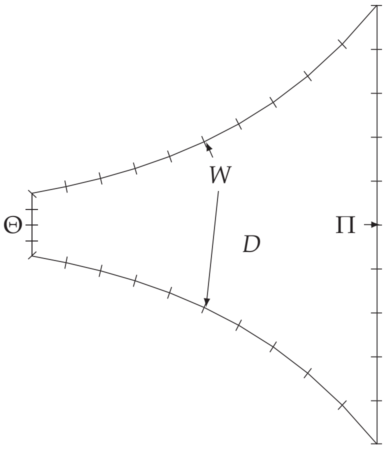

Figure 114: BEM Domain D bounded by surfaces Θ, W and Π.

From the definition of the modal impedance matrix, Eq. (76) on on page 74, and also from the derivation of modal radiation impedance (Eq. (179) and Eq. (180)), it can be seen that computing the impedance matrix is a two-step process that consists of first finding the pressure response across the surface for one excitation volume velocity mode of unit amplitude, and then decomposing this pressure into pressure modes. In summary,

$$Z_{mn} = \frac{j\omega\rho}{S^2} \int_{S_p} \left\{ \int_{S_q} G(\mathbf{p}|\mathbf{q}) \cdot \psi_m\left(\mathbf{q}\right) dS_q \right\} \psi_n\left(\mathbf{p}\right) dS_p \qquad (305)$$

where $G(\mathbf{p}|\mathbf{q})$ is a function that relates the velocity potential at $\mathbf{p}$ to a velocity at $\mathbf{q}$. For a surface in an infinite baffle, $G(\mathbf{p}|\mathbf{q}) = 2G_k(\mathbf{p}|\mathbf{q})$, where G_k is the free field Green's function as defined in Eq. (22), and the inner integral in curly brackets in Eq. (305) corresponds to the Rayleigh integral with the velocity distribution given by ψ_m. If the surface is part of a BEM mesh, G becomes the BEM solution process, giving the velocity potential at the elements for a given velocity distribution. By solving the BEM system of equations for the desired modal velocity distributions, and afterward applying Eq. (72), we will obtain the modal impedances on the surface. Due to collocation, the velocity potential is assumed constant over each element, and the discrete form of Eq. (72) becomes

$$P_n = -\frac{j\omega\rho}{S} \sum_{i=1}^{N_{e,t}} \varphi_i(\mathbf{p})\psi_n(\mathbf{p})S_i \qquad (306)$$

where $\varphi(\mathbf{p})$ is the velocity potential at the collocation point, and S_i is the area of the element. This can also be expressed as a matrix multiplication,

$$\vec{P} = -\frac{j\omega\rho}{S} \left(\Psi_{\Theta}^{w}\right)^{T} \varphi \tag{307}$$

where Ψ_{Θ}^{w} is an $N_{e,\Theta} \times N_{modes}$ matrix of mode functions for surface Θ, multiplied by integration weights, $N_{e,\Theta}$ being the number of elements in surface Θ.

Since the mode functions are orthonormal, $\vec{P}$ will contain the modal impedances of one column in the impedance matrix, for the corresponding velocity mode. Thus

$$\mathbb{Z} = -\frac{j\omega\rho}{S^2} \left(\Psi_{\Theta}^{w}\right)^{T} [\varphi_{\Theta}] \tag{308}$$

where $[\varphi_{\Theta}]$ is a $N_{e,\Theta} \times N_{modes}$ matrix of the solution of Eq. (31),

$$\begin{bmatrix} [M] & L_k \\ D_\alpha & D_\beta \end{bmatrix} \begin{bmatrix} \varphi \\ v \end{bmatrix} = \begin{bmatrix} 0 \\ F \end{bmatrix}, \tag{309}$$

for the surface Θ for N_{modes} velocity mode shapes. One should keep in mind that the discretization of Θ is also a discretization of the mode functions, so a sufficiently dense spatial sampling must be employed to avoid aliasing effects.

10.2 MMM AS LOAD

In this case, the boundary condition at the surface Π, see Figure 114, is available in the form of a modal impedance matrix $\mathbb{Z}$. In order to solve the BEM system of equations, we need to express the boundary conditions in a form similar to Eq. (30). Since there are no sources on this surface, $f(\mathbf{p}) = 0$, so on Π, Eq. (30) becomes

$$[\alpha]_{\Pi}\, \varphi_{\Pi} + [\beta]_{\Pi}\, v_{\Pi} = 0. \tag{310}$$

If the surface Π was mounted in an infinite baffle, we could use the Rayleigh integral, expressed in terms of the operator L_k so that

$$[I]\, \varphi_{\Pi} + [2L_k]_{\Pi}\, v_{\Pi} = 0 \tag{311}$$

where $[I]$ is the identity matrix. This would give us the Boundary Element Rayleigh Integral Method (BERIM) described in [191] and in Section 3.3.5 on page 56. From this it is clear that one way to proceed is to express the velocity potential at an element in Π as a function of the velocity at Π. From the relation in Eq. (76) we see that this is possible if we know the pressure, impedance and volume velocity in modal form. Thus the method becomes

1. Find the volume velocity amplitudes from a given velocity distribution from Eq. (74).

2. Find the pressure mode amplitudes from Eq. (76).
3. Find φ from Eq. (59) and the relation $p = -j\rho_0\omega\varphi$.

In order to allow for any possible velocity distribution, we must find $\vec{U}$ for each element when only that element has a velocity:

$$U_{n,i} = \int\limits_{\Gamma_i} v(\mathbf{q})\psi_n(\mathbf{q})d\Gamma_i. \tag{312}$$

It is only necessary to integrate over the actual element Γ_i, as the velocity of all other elements is zero. The mode functions ψ_n are defined by the shape of the surface Π. We use Eq. (312) to fill an $N_{modes} \times N_\Pi$ matrix $[U]$, where N_Π is the number of elements in Π. This also enables us, through superposition, to find $\vec{U}$ for any velocity distribution v_Π as $\vec{U} = [U]\vec{v}_\Pi$, where v_Π is a vector of the element velocities at Π.

From Eq. (76) we can now find an $N_{modes} \times N_\Pi$ matrix $[P]$ as

$$[P] = \mathbb{Z}[U] \tag{313}$$

which gives us the modal pressure amplitudes. From there, we can go back to φ at each element by multiplying $[P]$ by a $N_\Pi \times N_{modes}$ matrix Ψ_Π of mode functions. The result is that the boundary conditions at Π will be

$$[I]\,\varphi_\Pi - \frac{j}{\rho_0\omega}\left[\Psi_\Pi\mathbb{Z}[U]\right]_\Pi = 0 \tag{314}$$

where the change of sign comes from the definition of the direction of the surface normal.

The discretization does not limit the number of modes that can be used in $\mathbb{Z}$, contrary to what we found in the previous section. The reason for this is that, first, we know the exact velocity distribution when finding $[U]$, so the correct mode amplitudes can be found for an arbitrary number of modes. The integration over mode functions is not linked to the discretization of the surface Π in any other way than that the discretization defines the region of integration. Second, when we know the pressure mode amplitudes in $[P]$, the pressure can be found at as many spatial points as we wish. The discretization of the mode functions in this case does not influence the mode amplitudes.

10.3 THE MODE-MATCHING BOUNDARY ELEMENT METHOD (MMBEM)

The derivations given above can now be combined into a method where the BEM accepts a modal impedance matrix as boundary condition, and produces another impedance matrix at the other end. The linear system of equations become

$$\begin{bmatrix} [M] & [L] \\ [M_\alpha] & [M_\beta] \end{bmatrix} \begin{bmatrix} [\varphi] \\ [v] \end{bmatrix} = \begin{bmatrix} 0 \\ [F] \end{bmatrix} \tag{315}$$

where both the solution and the right hand side are matrices, with one column per mode. The sub-matrices are defined below.

The BEM matrices relate the three parts of the boundary to themselves and to each other:

$$[M] = -\begin{bmatrix} [M_k]_{\Pi\Pi} & [M_k]_{\Pi W} & [M_k]_{\Pi\Theta} \\ [M_k]_{W\Pi} & [M_k]_{WW} & [M_k]_{W\Theta} \\ [M_k]_{\Theta\Pi} & [M_k]_{\Theta W} & [M_k]_{\Theta\Theta} \end{bmatrix} - \frac{1}{2}I \tag{316}$$

$$[L] = \begin{bmatrix} [L_k]_{\Pi\Pi} & [M_k]_{\Pi W} & [M_k]_{\Pi\Theta} \\ [L_k]_{W\Pi} & [M_k]_{WW} & [M_k]_{W\Theta} \\ [L_k]_{\Theta\Pi} & [L_k]_{\Theta W} & [M_k]_{\Theta\Theta} \end{bmatrix} \tag{317}$$

The boundary condition matrices are divided between the three boundary parts in the same way, and for hard walls they will be:

$$[M_\alpha] = \begin{bmatrix} I & 0 & 0 \\ 0 & 0 & 0 \\ 0 & 0 & 0 \end{bmatrix} \tag{318}$$

$$[M_\beta] = \begin{bmatrix} -\frac{j}{\rho_0\omega}\left[\Psi_\Pi \mathbb{Z}[U]\right]_\Pi & 0 & 0 \\ 0 & I & 0 \\ 0 & 0 & I \end{bmatrix} \tag{319}$$

The solution matrices are

$$[\varphi] = \begin{bmatrix} \varphi_\Pi \\ \varphi_W \\ \varphi_\Theta \end{bmatrix}, \tag{320}$$

$$[v] = \begin{bmatrix} v_\Pi \\ v_W \\ v_\Theta \end{bmatrix}, \tag{321}$$

and finally, the right-hand side

$$F = \begin{bmatrix} 0 \\ 0 \\ [\Psi_\Theta] \end{bmatrix}, \tag{322}$$

where $[\Psi_\Theta]$ is a matrix of mode functions over Θ.

If a different boundary condition on W is needed, the center elements of $[M_\alpha]$ and $[M_\beta]$ can be set up according to Eq. (30). F for W would still be set to zero, to avoid sources in the horn.

The number of modes in the solution of v_Θ does not have to be the same as the number of modes in the modal impedance load matrix.

Part	S_{th}[cm²]	S_m[cm²]	L[cm]	N_e
A	10	100	20	401
B	100	1000	10	7/26/22
C	1000	2000	10	201

Table 14: Axisymmetric horn details. For part B, N_e indicates the number of elements in the Θ, W and Π surfaces, respectively.

Lastly, we need to find the modal velocity amplitudes over Π, given a certain modal velocity distribution over Θ. To do this, we use the already computed solution matrix giving the velocity at each element for each mode, Eq. (321), and by superposition we can find the velocity distribution on the surface by multiplying this matrix by the vector of volume velocity modes:

$$\vec{v}_S = \frac{1}{S_\Theta}[v]\vec{U}_\Theta \tag{323}$$

where $\vec{v}_S$ is a vector of the velocity at all elements in the surface. The mode amplitudes at Π are then found from $\vec{U}_\Pi = [U]\vec{v}_\Pi$, where v_Π is the vector of the element velocities at Π. $\vec{U}_\Pi$ can then be used as the input to the following MMM section.

10.4 RESULTS

In this section, a comparison between Mode Matching Boundary Element Method (MMBEM) and MMM or BERIM is presented. MMM is used as reference if possible, otherwise BERIM is used.

10.4.1 *Axisymmetric Example*

In this example, the horn illustrated in Figure 115, with dimensional details given in Table 14, is investigated. Here, an axisymmetric BEM segment (B, exponential) is added in between two axisymmetric MMM segments (A, conical, and C, exponential). The BEM section is made up of truncated cones as described in [227], with a mesh bandwidth of 7 kHz. 32 modes are used in section C, and 7 modes are used in section A, due to the limited spatial sampling of the A–B interface surface. This combination is compared to a full MMM simulation using 32 modes.

The mesh bandwidth *is understood as the frequency where the largest element of the mesh is not larger than* 1/6*th of a wavelength.*

The results for this combination are given in Figure 116, where throat impedance, throat impedance relative error, and mouth mode amplitudes are shown. The relative error is computed as $\epsilon_R = |(R_{MMBEM} - R_{MMM})/R_{MMM}|$ for the resistance, and similarly for the reactance. Figure 116b shows the relative errors to be mostly below 1% for resistance and 5% for reactance. It is also clear from comparing

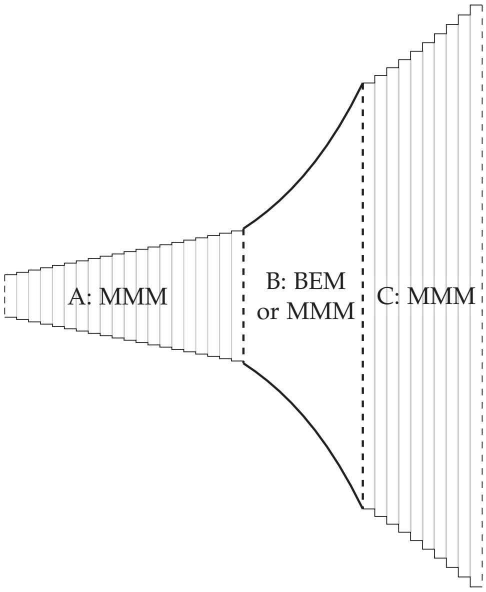

Figure 115: Axisymmetric horn example.

Figure 116a and Figure 116b that the error is below 1% for both in the ranges where the corresponding part of the impedance dominates.

In Figure 116c, the five first mouth volume velocity mode amplitudes are shown. The solid lines are for full MMM with 32 modes, and the dashed lines for MMBEM. As mentioned above, no more than 7 modes can be used to excite section B, due to the limited spatial sampling of the interface surface. As can be seen from Figure 116c, and with greater resolution in Figure 117, this has a clear effect on the mode amplitudes above about 2kHz. The amplitudes have errors in the order of 5 dB, and there is a dip around 3 kHz in the amplitudes of the higher order modes that should not be there. In order to check the reason for this behavior, an MMM simulation was run using 32 modes in sections B and C, but only 7 modes in section A. The results (dotted lines) show similar behavior to MMBEM, with very similar changes in the higher order mode amplitudes.

10.4.2 *Axisymmetric to Rectangular Example*

In this example, a horn with a transition from round to square cross section is simulated using BEM for the transition part, and MMM for the outer part. In addition, a reference simulation of the full horn is performed with BERIM. The average mesh bandwidth is 5 kHz, with a denser mesh close to the throat. The geometry and the full BERIM mesh is shown in Figure 118. Since the horn is quarter symmetric, only one quadrant is used in the simulation. For the hybrid simula-

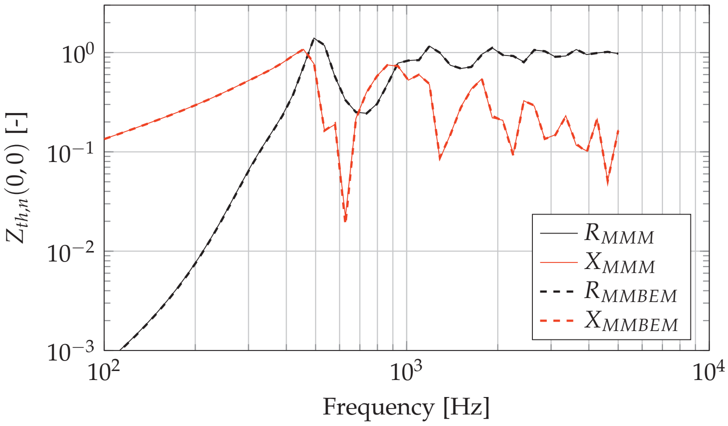

(a) Throat impedance.

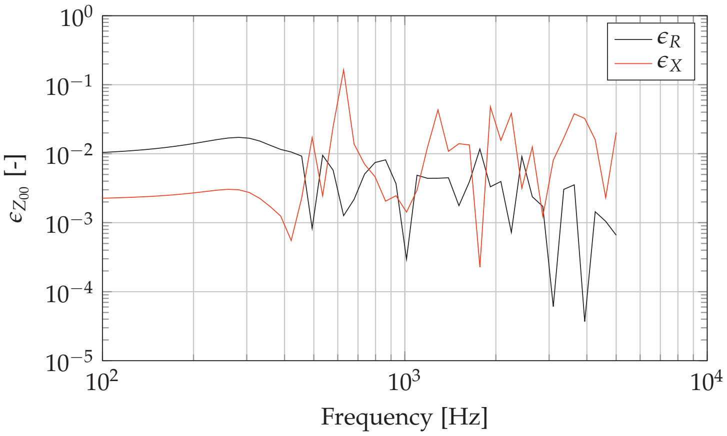

(b) Relative error in the throat impedance.

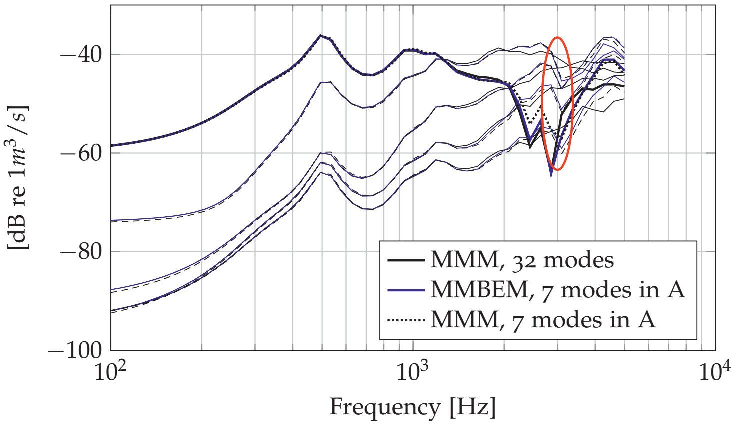

(c) Mouth mode amplitudes. The thickest curves correspond to the plane wave mode. The dip caused by using only 7 modes in part A is indicated by the red circle in the figure.

Figure 116: Simulation results for axisymmetric horn.

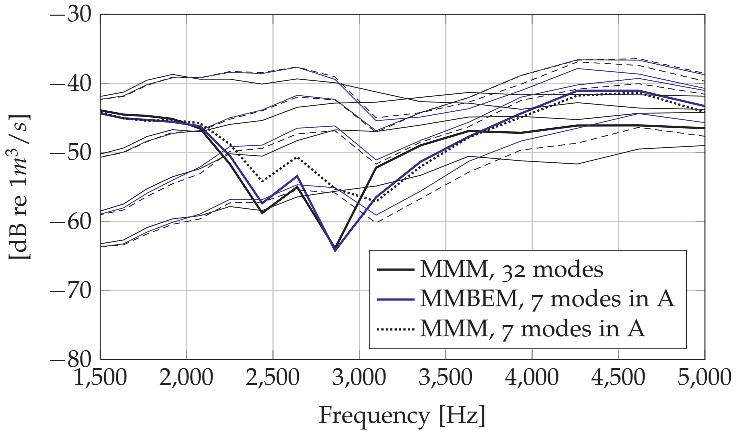

Figure 117: A close-up of the dip in Figure 116c.

Part	S_{th}[cm²]	S_m[cm²]	L[cm]	N_e
A	19.64	150	10	142 498 104
B	150	1000	10	201
BERIM	16.64	1000	20	1724

Table 15: Axisymmetric to rectangular horn details. For part A, N_e indicates the number of elements in the Θ, W and Π surfaces, respectively.

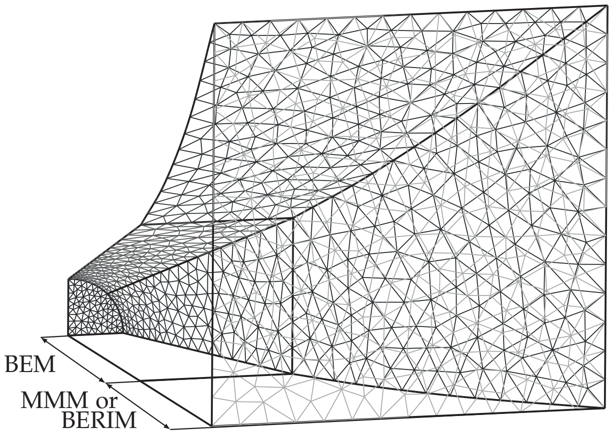

Figure 118: Axisymmetric to rectangular horn geometry and BERIM mesh. Only a quarter of the geometry is meshed, since the horn is quarter symmetric.

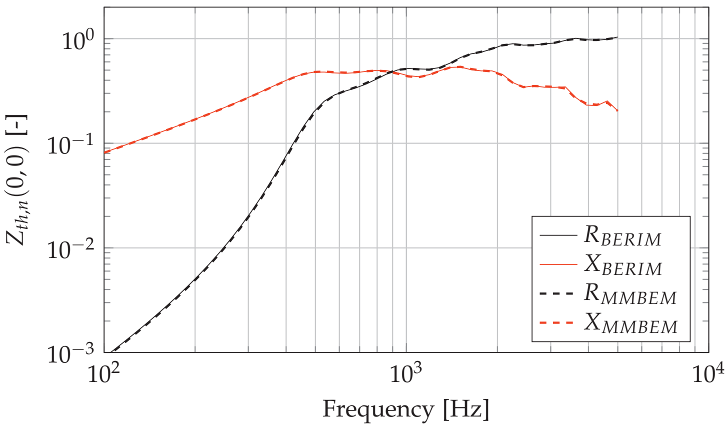

(a) Throat impedance.

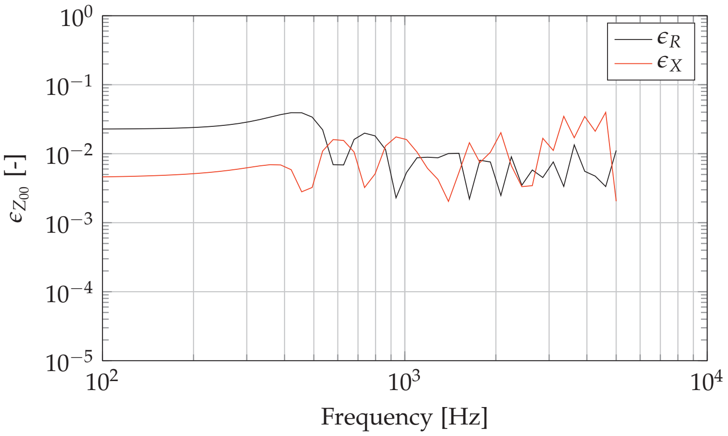

(b) Relative error in throat impedance.

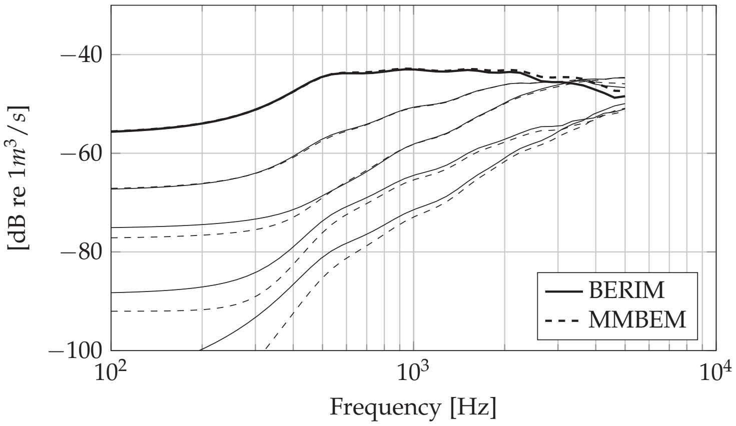

(c) Mouth volume velocity mode amplitudes. The thickest curves correspond to the plane wave mode.

Figure 119: Simulation results for axisymmetric-to-rectangular horn.

tion, the interface surface between the two parts is also meshed. The number of elements and other dimensions are indicated in Table 15. For the MMM part, 64 modes are used.

If the modal impedance matrix is desired at the throat surface, the circular mode functions must in this case include angular modes, since the axisymmetry is disturbed. For details, see [22] and [278, Ch. 9.2].

The results for the combination are given in Figure 119. The relative impedance errors oscillates around 1%, with similar variations as for the axisymmetric case.

The mode amplitudes are shown in Figure 119c, the first few mode amplitudes (modes (0,0), (0,1), (1,1), (0,2) and (1,2)) are shown. For the BERIM reference case, mouth velocity distribution has been decomposed into modes using Eq. (74). The circular throat is excited by a plane wave. The plane wave mode (thickest lines) and the lower order modes are reasonably similar in the two simulations, while the deviations are larger when the mode amplitudes are low, which they are for most of the higher order modes over most of the frequency range covered.

10.5 SUMMARY

Many horns fall into the category where a large part of the horn has a geometry with analytical mode functions, but where a small part does not. An example is the transition from round to rectangular geometry. In these cases, part of the horn must be simulated using other numerical methods, like BEM. In this chapter, a method has been developed to

- Let BEM be a load for for the MMM by converting the results from the BEM solution into a modal impedance matrix.
- Let BEM accept a modal impedance matrix as a boundary condition by defining a new type of Green's function.

It is therefore possible to couple MMM to both the throat and the mouth surfaces of the BEM section. The new method is termed the Mode Matching Boundary Element Method (MMBEM).

Simulation results, comparing MMBEM with either full MMM or full BERIM, show that

- There is good agreement between these methods.
- In the case where a BEM section is placed after an MMM section, it is important to excite the BEM section with enough modes to produce an accurate description of the sound field at the interface.

11

CONCAVE RADIATOR SIMULATION

This chapter is based on the work presented in [54], with some additional examples for annular geometries and reflectors.

The contribution in this chapter is the formulation of a method for the simulation of concave radiators derived from the MMM formulation used in this thesis, which is simple and straightforward to implement compared to the methods of Ando et al. [55] and Oie et al. [56].

11.1 BACKGROUND

The directivity of cone loudspeakers, as well as the radiation impedance, are topics that have been of interest to audio engineers for a long time. It is a common approach to use the approximation of a rigid plane piston for the study of these quantities, but it is also known that, in particular for the directivity, this is not a good approximation [288].

Quite early, Stenzel made extensive investigations of pistons and membranes during his time at AEG [317, 318, 319]. In 1941, Brown [320] gave expressions for the radiation from rigid and non-rigid cones, using a Kirchhoff approximation. The non-rigid cones were characterized by the sound speed in the cone material. Carlisle [321] provided a similar analysis, where the directivity was computed from the sum of the pressures radiated from annular rings. Another approximation was given by Geddes [33], who computed the velocity distribution at the mouth of the device, converted this velocity distribution into a modal representation, and used this to compute directivity. The radiation impedance was not computed.

Ando et al. [55] developed a method based on mode matching for calculating the radiation from a horn or loudspeaker cone mounted in the end of a semi-infinite circular tube. Ando's method appears to be extremely complex, and the paper requires a detailed study simply to figure out which equations to solve, and in what order. A similar method was presented by Oie et al [56] for a radiator in an infinite baffle. While the method for non-vibrating walls is described in detail, the transition from a horn structure to a structure with vibrating walls is not clear, and this method too appears rather complex.

Later analyses have usually depended on Finite Element or Boundary Element methods [322, 323, 324, 325, 326], but an interesting departure from this was demonstrated bu Murphy [327], who used a method similar to that of Carlisle. Murphy modeled the cone as a set of concentric rings and delay lines. The radiation impedances of the rings (considered separately) were used as radiation loads for a distributed mechanical model of the cone, where each ring was connected to the next by masses and springs to take sound propagation in the cone material into account. The total radiation impedance was not given explicitly, and it seems that trying to calculate it from the pressures and volume velocities in the circuit would also integrate the cone mass and flexural compliance into this impedance value.

The Mode Matching Method used in this thesis is well suited to simulate horns, however, it is not directly suited for simulating structures like a loudspeaker cone, since it is based on working one's way from the mouth of the horn back to the throat, given a radiation impedance specified at the mouth. If any surface inside the structure vibrates, its effect on other vibrating surfaces, like other parts of the wall, or the innermost (throat) surface, cannot easily be determined with this method [44]. While the velocity on each of these surfaces may be specified, the resulting pressure depends on the interaction of all the surfaces. Consequently, the same holds for the radiation impedance seen by the surfaces. Therefore, in order to find the pressures and velocities at all places inside the radiator, a large system of simultaneous equations must be solved.

It is clear that in order to completely simulate the radiation from a vibrating mechanical structure like a loudspeaker cone, the variation of velocity over the surface must be determined, and the acoustical loading of that surface must be taken into account. This is a complex problem, in particular when the description of the acoustic field is in terms of modes, and is considered beyond the scope of this thesis. The purpose of this chapter is therefore to develop the acoustic multimodal method described above to take vibrating walls into account, and compare its results to a reference method.

11.2 THEORY

The method will first be analyzed using a one-dimensional (plane wave) approximation, and the equations developed can then be extended to the multimodal case quite easily.

The geometry to be analyzed is shown in Figure 120. The cone is approximated by a stepped structure of cylindrical segments, and all horizontal surfaces are given an axial velocity. If the velocities are equal, this corresponds to a staircase approximation of a perfectly rigid cone. By refining this staircase approximation, it will converge to the smooth cone shape. Giving each surface a different velocity would correspond to a cone which is breaking up. If only u_0 is non-zero, the geometry corresponds to a staircase approximation to a horn, as in the standard MMM.

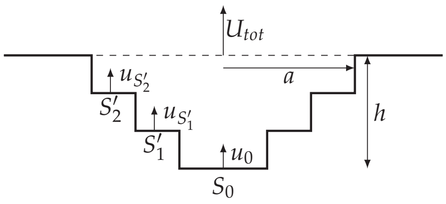

Figure 120: Geometry.

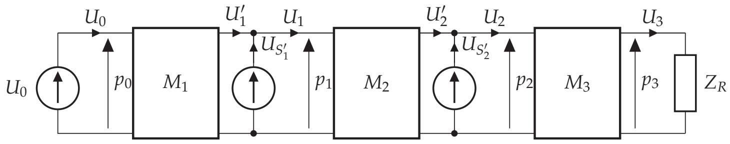

Figure 121: Principle of the one-dimensional model of Figure 120.

11.2.1 *One-Dimensional Approximation*

In the one-dimensional approximation, each segment is modeled as a straight duct, with each vibrating surface injecting a volume velocity into the system at the appropriate points, as shown in Figure 121. This method is based on the traditional Transmission Line Elements method for modeling horns described by Mapes-Riordan [240], but with sources of volume velocity added along the structure. Each duct segment, of length L_i, is described by a transfer matrix M_i such that

$$\begin{bmatrix} p_{i-1} \\ U_{i-1} \end{bmatrix} = M_i \begin{bmatrix} p_i \\ U'_i \end{bmatrix} = \begin{bmatrix} a_{11} & a_{12} \\ a_{21} & a_{22} \end{bmatrix} \begin{bmatrix} p_i \\ U'_i \end{bmatrix}. \tag{324}$$

For a straight duct, the matrix coefficients are defined as

$$\begin{aligned} a_{11} &= \cos kL_i, \\ a_{12} &= jZ_c \sin kL_i, \\ a_{21} &= jZ_c^{-1} \sin kL_i, \\ a_{22} &= \cos kL_i, \end{aligned} \tag{325}$$

where $Z_c = \rho c / S_i$. The conditions at the input end are specified as functions of the conditions at the output end as a reminder that the boundary condition (the radiation impedance) is given for the output end. It also corresponds to the way the multimodal version of Equation (324) has been defined in Chapter 4, as will be shown in the next Section.

Assuming we know U_0, $U_{S_{1'}}$ and $U_{S_{2'}}$, the appropriate relations between pressures and volume velocities can be set up. In this example we have seven unknowns, and the relations can be set up as a sparse linear system of equations:

$$\mathbb{M}\begin{bmatrix} p_0 \\ p_1 \\ U_1' \\ U_1 \\ p_2 \\ U_2 \\ U_2' \\ p_3 \\ U_3 \end{bmatrix} = \begin{bmatrix} 0 \\ U_0 \\ U_{S_1'} \\ 0 \\ 0 \\ U_{S_2'} \\ 0 \\ 0 \\ 0 \end{bmatrix} \tag{326}$$

where

$$\mathbb{M} = \begin{bmatrix} -1 & a_{11}^{(1)} & a_{12}^{(1)} & & & & & & \\ & a_{21}^{(1)} & a_{22}^{(1)} & & & & & & \\ & & -1 & 1 & & & & & \\ & -1 & & & a_{11}^{(2)} & a_{12}^{(2)} & & & \\ & & & -1 & a_{21}^{(2)} & a_{22}^{(2)} & & & \\ & & & & & -1 & 1 & & \\ & & & & -1 & & & a_{11}^{(3)} & a_{12}^{(3)} \\ & & & & & -1 & & a_{21}^{(3)} & a_{22}^{(3)} \\ & & & & & & & 1 & -Z_r \end{bmatrix}. \tag{327}$$

This system can then be solved for the unknown quantities. Z_r is the radiation impedance at the opening. As can be seen from the above equations, actually nine unknowns are solved for, although due to the relation $U_1' = U_1 + U_{s_1'}$, etc., two of the unknowns are redundant. This formulation, however, simplifies the right-hand side, and the general appearance of the equations are, as we will see, more similar to the multimodal version.

11.2.2 *Multimodal Formulation*

When higher order modes are included, the analysis is similar to that for plane waves, except that a formulation to couple the modes across the discontinuity will be needed. By using the expressions presented in Chapter 4, we have that pressure and volume velocity at a discontinuity are found as

$$\vec{P}^{(1)} = F\vec{P}^{(2)}, \tag{328}$$

$$\vec{U}^{(2)} = F^T\vec{U}^{(1)}, \tag{329}$$

and the pressure and volume velocity along a duct are given as

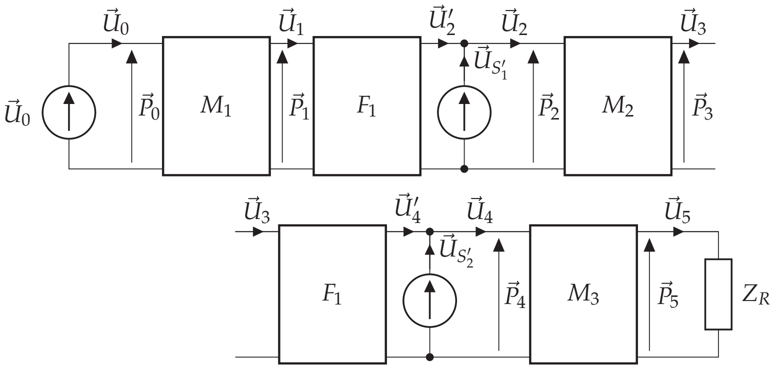

Figure 122: Principle of the multi-modal model of Figure 120.

$$\vec{P}_0 = D_1\vec{P}_1 + D_2 Z_c \vec{U}_1 \tag{330}$$

$$\vec{U}_0 = D_2 Z_c^{-1}\vec{P}_1 + D_1\vec{U}_1. \tag{331}$$

This can be seen to be the multimodal version of Equation (325), with $a_{11} = a_{22} = D_1$, $a_{12} = D_2 Z_c$ and $a_{21} = D_2 Z_c^{-1}$.

The step-by-step calculation of impedance and volume velocity presented in Chapter 4 cannot easily take into account the effects of vibrating walls, as this introduces an extra velocity component that will change the impedances seen by the other surfaces: there is mutual coupling between the vibrating rings. A new formulation is therefore required.

Figure 122 shows the multimodal equivalent of Figure 121, with the modal coupling at the discontinuities introduced in the form of F-matrices. Based on the method outlined in Section 11.2.1, it is possible to set up the following linear system of equations:

$$\mathbb{M} \begin{bmatrix} \vec{p}_0 \\ \vec{p}_1 \\ \vec{U}_1 \\ \vec{p}_2 \\ \vec{U}_2 \\ \vec{p}_3 \\ \vec{U}_3 \\ \vec{p}_4 \\ \vec{U}_4 \\ \vec{p}_5 \\ \vec{U}_5 \end{bmatrix} = \begin{bmatrix} 0 \\ \vec{U}_0 \\ 0 \\ \vec{U}_{S_1} \\ 0 \\ 0 \\ 0 \\ \vec{U}_{S_2} \\ 0 \\ 0 \\ 0 \end{bmatrix} \tag{332}$$

with

$$\mathbb{M} =$$
$$\begin{bmatrix}
-I & a_{11}^{(1)} & a_{12}^{(1)} & 0 & 0 & & & & & & \\
0 & a_{21}^{(1)} & a_{22}^{(1)} & 0 & 0 & & & & & & \\
0 & I & 0 & -F_1 & 0 & & & & & & \\
0 & 0 & -F_1^T & 0 & I & & & & & & \\
 & & & -I & 0 & a_{11}^{(2)} & a_{12}^{(2)} & 0 & 0 & & \\
 & & & 0 & -I & a_{21}^{(2)} & a_{22}^{(2)} & 0 & 0 & & \\
 & & & 0 & 0 & I & 0 & -F_2 & 0 & & \\
 & & & 0 & 0 & 0 & -F_2^T & 0 & I & & \\
 & & & & & & & -I & 0 & a_{11}^{(3)} & a_{12}^{(3)} \\
 & & & & & & & 0 & -I & a_{21}^{(3)} & a_{22}^{(3)} \\
 & & & & & & & 0 & 0 & I & -\mathbb{Z}_r
\end{bmatrix} \tag{333}$$

The difference from the previous system of equations is the inclusion of the F-matrices, and that each element of the matrix is an $N_m \times N_m$ sub-matrix. Apart from the F-matrices and the Z_r matrix, all matrices are diagonal, I is the identity matrix. The solution vector contains sub-vectors of pressure and volume velocity mode amplitudes.

The right hand side contains the volume velocity amplitudes of the exciting volume velocities. It is possible to specify a velocity distribution over each of the annular surfaces, but in practice one would use a constant value for each surface, as they are quite small. However, one must take into account that the surface is annular, and that the contributions of $\vec{U}_{S_1}$, $\vec{U}_{S_2}$, etc, are not that of plane waves. The annular excitation mode amplitudes can be found by multiplying the velocity distribution (here constant) with the mode function of the mode in question, and integrating over the surface as in Eq. (74):

$$U_{S_i,n} = 2\pi \int_{a_1}^{a_2} \psi_n(r) v_{S_i} r dr. \tag{334}$$

For a perfectly rigid diaphragm, all v_{S_i} will be identical. If the sound speed in the diaphragm is to be taken into account, a phase shift must be introduced between the individual ring velocities. Other effects, like diaphragm break-up, are also possible to simulate by adjusting the velocity distribution over the diaphragm. This is discussed further in Section 11.2.4.

Using the same approach as above, it is also possible to simulate a source inside a cavity. In the plane of the source, the mode amplitudes are found as in Eq. (334), only that integration is performed over the source. If the annulus is also vibrating, integration is also performed over this region. For a point source, no integration is required, and the mode functions are simply evaluated at the source position. In axisymmetric circular geometries, a point source is only possible if the source radial position, $r_s = 0$, otherwise the source will be a ring source. The mode amplitudes are in any case

$$U_{S_i,n} = 2\pi\psi_n(r_s)U_s r dr, \tag{335}$$

where U_s is the source volume velocity.

The main matrix can be seen to consist of three sub-matrix types; the upper left corner matrix of size $4N_m \times 5N_m$ that takes into account that $\vec{U}_0$ is known:

$$A_{start} = \begin{bmatrix} -I & a_{11}^{(1)} & a_{12}^{(1)} & & \\ & a_{21}^{(1)} & a_{22}^{(1)} & & \\ & I & & -F_1 & \\ & & -F_1^T & & I \end{bmatrix} \tag{336}$$

A general middle matrix of size $4N_m \times 6N_m$, placed with a $2N_m$ columns overlap to the previous one:

$$A_{middle} = \begin{bmatrix} -I & & a_{11}^{(2)} & a_{12}^{(2)} & & \\ & -I & a_{21}^{(2)} & a_{22}^{(2)} & & \\ & & I & & -F_2 & \\ & & & -F_2^T & & I \end{bmatrix} \tag{337}$$

An end matrix of size $3N_m \times 4N_m$, also placed with a $2N_m$ columns overlap to the previous one, and containing the end boundary condition expressed through the radiation impedance:

$$A_{end} = \begin{bmatrix} -I & & a_{11}^{(3)} & a_{12}^{(3)} \\ & -I & a_{21}^{(3)} & a_{22}^{(3)} \\ & & I & -\mathbb{Z}_r \end{bmatrix} \tag{338}$$

For more than three duct elements, matrices of the general middle matrix type are used for all elements except for the first and the last.

Expressions for the radiation impedance $\mathbb{Z}_r$ matrix are given in previous chapters.

11.2.3 *Sound Pressure and Radiation Impedance*

$\vec{U}_m$ gives the volume velocity at the output, or mouth, of the structure. Then the radiated pressure for a radiator in an infinite baffle, p_{IB}, can be calculated as described in Section 5.1.

The total radiation impedance seen by the vibrating structure is required to find the radiated power, and to include the model in a more complete loudspeaker model. In general, the mechanical radiation impedance is defined as the area integral of the specific radiation impedance $p/v_{\mathbf{n}}$, where $v_{\mathbf{n}}$ is the normal surface velocity [279]. The impedance will be the quotient of the total reaction force to the average axial velocity, so that

$$Z_{mr} = \frac{\sum_i p_i S_i}{S_{tot}^{-1} \sum_i v_{S_i} S_i}. \tag{339}$$

The velocities at the step surfaces are known, as they are part of the right hand side of Equation (332). The pressure is given in terms of mode amplitudes, so for each surface, the average pressure across the annular ring must be found by integration:

$$p_i = \frac{2\pi}{S_i} \int_{a_1}^{a_2} \sum_{n=0}^{N_m-1} \psi_n(r) p_{i,n} r dr \tag{340}$$

As a first approximation, the zeroth pressure mode amplitude can be used to avoid the integration, although the accuracy of this approach will depend on the ratio of rim velocity to the velocity through S_i due to other parts of the structure.

Only the pressure on vibrating surfaces must be taken into account in the computation of the radiation impedance, and the total area must also include only the active parts of the surface.

11.2.4 *Structural Coupling*

As mentioned in the introduction in Section 11.2, giving each vibrating surface in the structure a different velocity would correspond to a cone which is breaking up, and this must be taken into account in a complete loudspeaker model. If the acoustical loading on the mechanical structure is neglected (known as weak coupling), the vibration velocity distribution *in vacuo* can be found by methods like Finite Element Analysis (FEA). This velocity distribution can then be used as input for the model described above, for specifying the velocity at each element. Strong coupling would require that the acoustical loading is taken into account. Murphy [327] describes a lumped parameter version where the diaphragm is divided into rings, and each ring is modeled as a mass connected to the neighboring rings with springs. In addition, the radiation impedance of each ring in isolation is taken into account, but the acoustic coupling between the rings is neglected.

Introducing weak coupling into the model presented above would be possible by using a separate model of the mechanical structure to find the vibration velocity. This model could be either an FEA model, or a model similar to that presented by Murphy. Introducing strong coupling is rather more involved, and is considered future work beyond the scope of this thesis.

Rocking modes (side-to-side movement) can have a large influence on the output from loudspeakers at certain frequencies [328, 329]. In order to describe the effect of rocking modes on directivity and radiation impedance, non-axisymmetric modes would have to be introduced. This can, as previously stated, be done by introducing angular mode functions in the model, giving the new mode function (see Braden [22])

$$\psi_{mn\sigma}(r,\phi) = A_{mn} J_m\left(\gamma_{mn} r/a\right) \sin\left(m\phi + \frac{\sigma\pi}{2}\right) \tag{341}$$

where m is the index of the angular mode, and σ is a symmetry index with value either 0 or 1, and has the effect of rotating the angular mode pattern a through a right angle about the central axis. A_{mn} is a normalization factor. Please see [22] for details. It should be noted that the inclusion of angular modes would increase the size of the sub-matrices in Equation (333).

In [22], Braden also presented the F-matrix for the coupling between concentric circular ducts including angular modes. It is interesting to note that angular modes only couple to angular modes with the same number of nodal diameters. There is also no coupling between radial and angular modes. As the angular modes are periodic, their average value over a ring would be zero, and they would therefore not have any influence on the radiation impedance. Any change of radiation impedance would have to come from a change in the radial velocity distribution caused by structural coupling from the rocking modes.

As this thesis is mainly concerned with sound radiation, structural coupling will not be discussed any further.

11.3 IMPLEMENTATION AND VERIFICATION

The equations outlined above were implemented in Matlab, using the Gauss-Legendre rule for the numerical integration, and employing Matlab's sparse matrix functions to save memory and solution time. Using the sparse solver also had the advantage over the dense solver in that it was more numerically stable.

To verify the model, a simple two-step geometry was used, as shown in Figure 123, and compared with results from BERIM [191]. For the MMM model, each segment was divided into five elements lengthwise, for a total of 15 elements, and 10 modes were used in the simulation. This amounts to a linear system with 630 degrees of freedom, and the solution time for 100 frequencies was 0.4s. For this problem, Matlab appeared to be running on a single core. The computer had an Intel i7-2600 CPU running at 3.4 GHz, and 8 GB RAM.

The BERIM simulation (compiled code) used 64 axisymmetric elements, and used approximately 8 minutes 41 seconds on a single core for 100 frequencies.

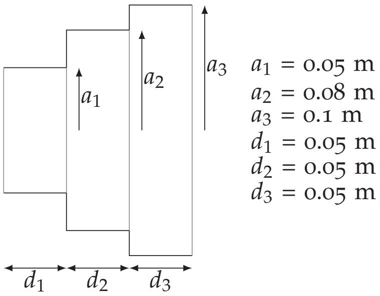

Figure 123: Geometry of the test case.

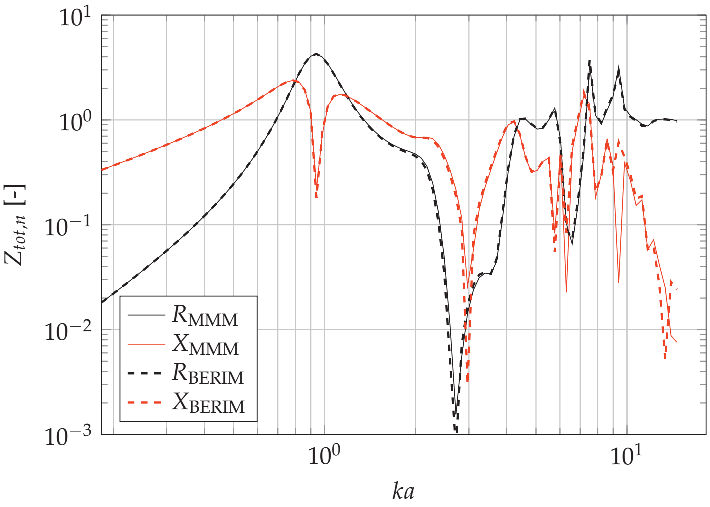

Figure 124: Radiation impedance for the test case in Figure 123.

Figure 124 compares the total radiation impedance, as defined in Equation (340), for the two methods. Differences are slight and appear mainly at high frequencies. Increasing the number of elements and modes in MMM does not materially change these results.

The SPL computed at a distance of 3 meters for several angles is shown in Figure 125. No detailed legend is given, since the intention is simply to show that the results are very similar for the two methods.

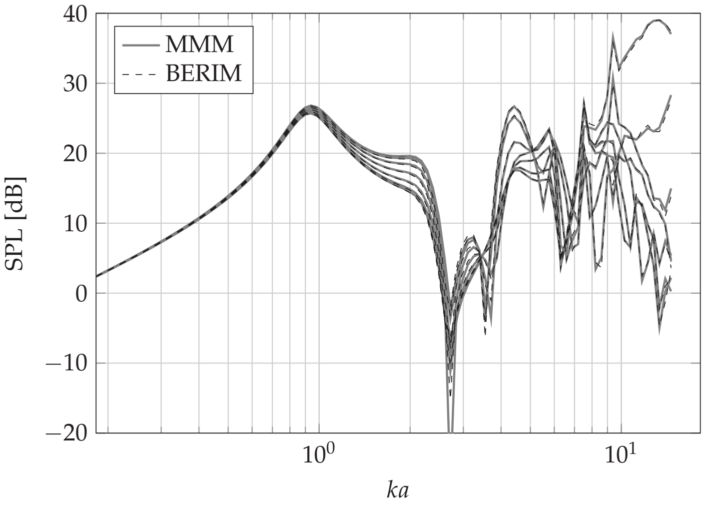

Figure 125: SPL response for the test case in Figure 123.

11.4 SIMPLE CIRCULAR EXAMPLES

The main purpose of the proposed method is to be able to simulate the radiation impedance and directivity of loudspeaker diaphragms. In this Section two geometries will be studied, see Figure 126. The outer radius a of both examples is 0.1 m, and the inner radius is 0.025 m. The depth h is $0.5a$. The diaphragm is divided into 20 segments, and 20 modes are used. All parts of the diaphragm are given the same axial acceleration, i.e. the diaphragm is assumed to be perfectly rigid.

The first example, Figure 126 a), is a straight-sided cone, which is a fairly typical geometry. The results are shown in Figure 127. The radiation impedance for a piston of the same size, mounted in an infinite baffle, is given for comparison. One notes a large peak in the

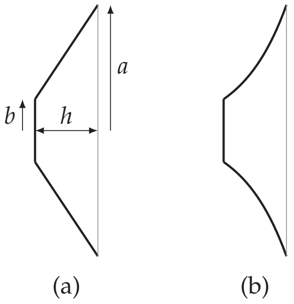

Figure 126: Example geometries.

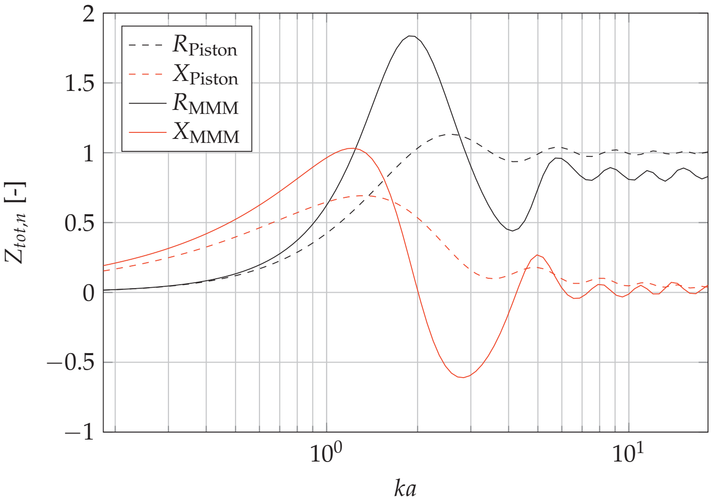

(a) Radiation impedance, conical diaphragm.

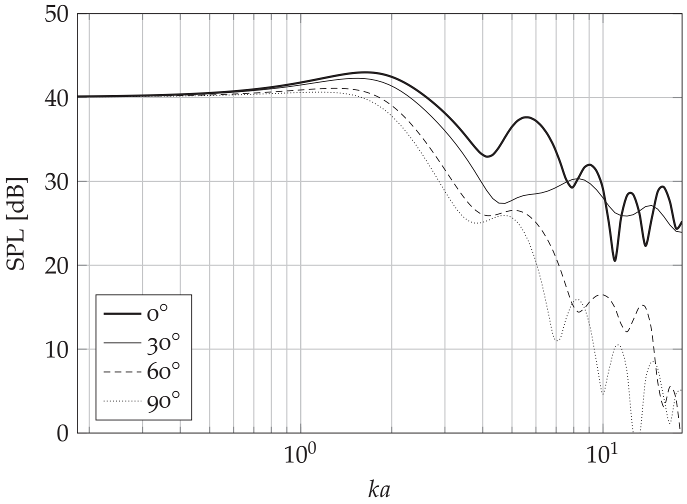

(b) Frequency response, conical diaphragm.

Figure 127: Results for the conical diaphragm.

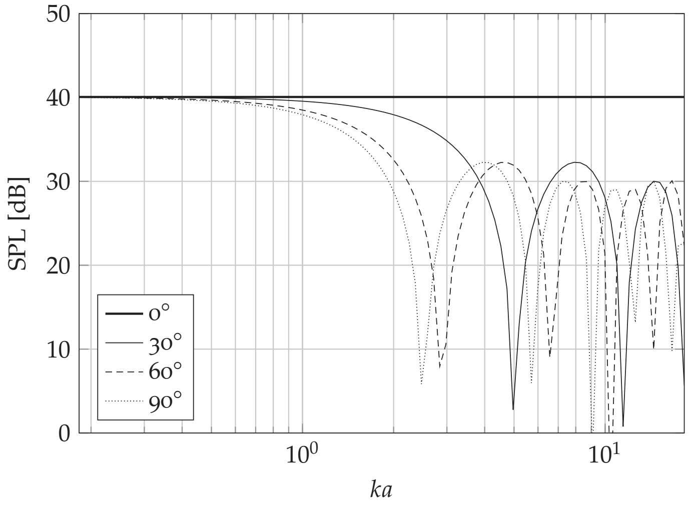

Figure 128: Directivity of a rigid piston, constant acceleration.

radiation resistance at around $ka = 1.9$ due to a cavity-like resonance, and a somewhat increased radiation mass below this frequency. In addition, the radiation resistance at high frequencies does not approach ρc, but a somewhat smaller value. This is due to the fact that it is the projected area that must be used in calculating the radiation impedance, not the actual surface area of the cone. The same can be found for other convex and concave, oscillating radiators, see for instance [330, 331].

The frequency response for the conical diaphragm when oscillating with a constant acceleration of $1\,\mathrm{m/s^2}$ is shown in Figure 127b for a few positions. Compared to a rigid piston operating under the same conditions, as shown in Figure 128, it is clear that the shape of the diaphragm has a significant influence on the directivity. Several differences can be noted. The piston has a flat on-axis frequency response for constant acceleration, while the directivity becomes narrow at high frequencies with significant side lobes. The on-axis response of the conical diaphragm is not flat at all, there is a low-pass filtering effect, and the response has a broad peak around $ka = 1.9$, due to the peak in the radiation resistance. The off-axis response is free of the deep notches or nulls, and the directivity is in general wider than for the piston. It should be mentioned that the low-pass filtering of the on-axis response does not correspond to a low-pass filtering of the radiated power, as the radiation resistance is nearly flat above $ka = 4$.

The general behavior of the exponentially shaped diaphragm, see Figure 129, is similar to that of the conical diaphragm. The radiation resistance peak is slightly higher in frequency, as can be expected

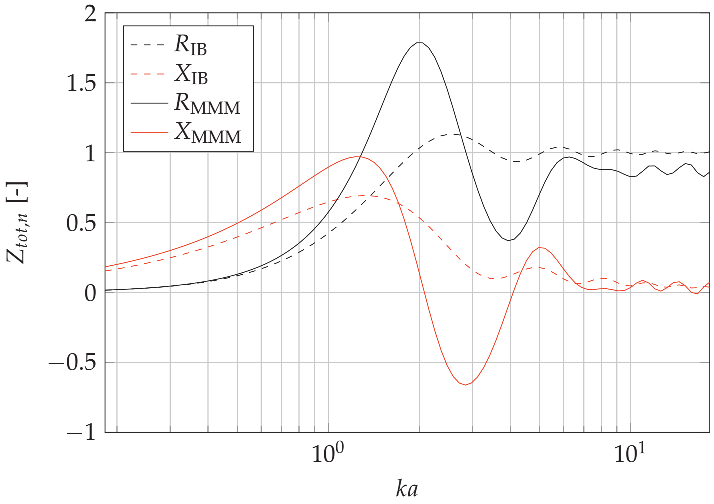

(a) Radiation impedance, exponential diaphragm.

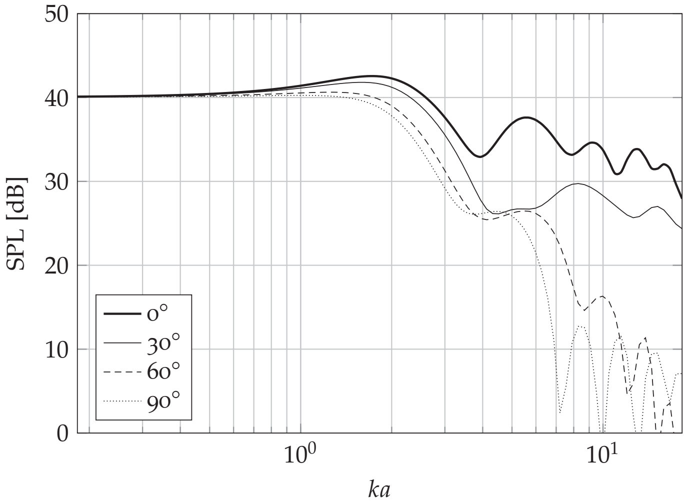

(b) Frequency response, exponential diaphragm.

Figure 129: Results for the exponentially shaped diaphragm.

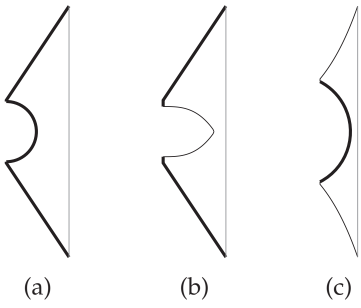
(a) (b) (c)

Figure 130: Example geometries.

from the slightly smaller air volume, but has roughly the same height. The on-axis response is smoother, and does not fall off as quickly.

It should also be noted that in the practical case of a non-rigid diaphragm, the difference between the two diaphragm shapes would also be strongly influenced by the different mechanical structures of the two geometries.

11.5 ANNULAR EXAMPLES

Three examples of annular geometries are shown in Figure 130. Thick lines in the figure indicates vibrating surfaces that have a vibration velocity in the z-direction. Now that the structure can have a central member, it is possible to simulate more realistic geometries. As examples, a cone with a hemispherical dust cap, (a), a cone with a non-moving phase plug, (b), and a convex dome in a short waveguide, (c), are studied. In the two first examples, the simulated results are compared to one of the examples above, the driver with a conical diaphragm and a flat dust cap, see Figure 126a.

11.5.1 *Convex Dust Cap*

This geometry corresponds to the geometry in Figure 130a. The outer radius is 0.1 m, the inner radius 0.025 m, the depth 0.05 m, and the radius (and height) of the hemispherical dust cap is 0.024 m. The geometry was simulated with 60 elements and 20 modes, and the computation time was 45 s for 150 frequencies. The difference in radiation impedance is rather small compared to a driver with a flat dust cap, Figure 131a, but there are clear differences in the frequency response, perhaps most noticeable is the dip around $ka = 15$. This probably comes from the contribution from the convex dome, as it is common for convex domes to exhibit this behavior, see for instance Beranek and Mellow [288].

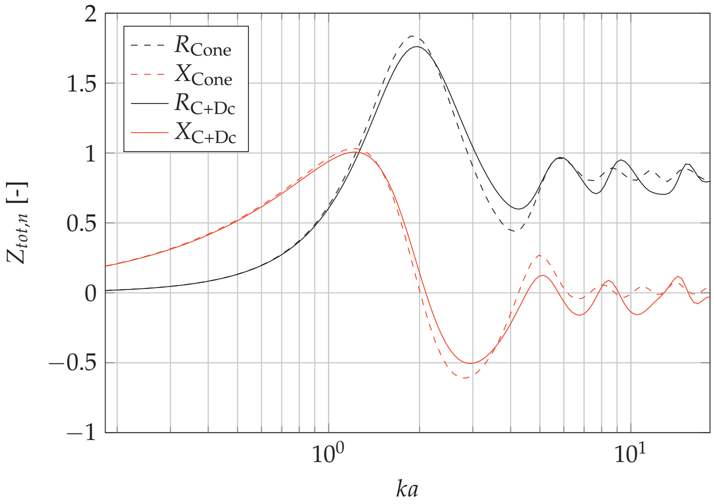

(a) Radiation impedance.

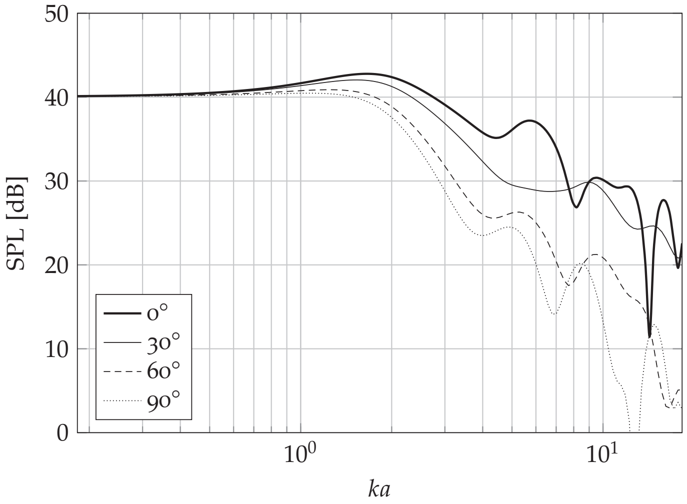

(b) Frequency response.

Figure 131: The results for the conical diaphragm with hemispherical dust cap.

11.5.2 *Phase Plug*

This geometry corresponds to the geometry in Figure 130b. The outer radius is 0.1 m, the inner radius 0.025 m, the depth 0.05 m, and the phase plug has a radius of 0.02 m and a length of 0.04 m. The shape is described as

$$r = R_p \left(1 - \left(\frac{z}{l_p}\right)^3\right)$$

where R_p and l_p are the maximum radius and length, respectively, of the phase plug, and z is the distance from the base. The geometry was simulated with 25 elements and 20 modes, and the computation time was 16 s for 150 frequencies. Comparing Figure 132a with Figure 127a, the difference in radiation impedance from that of a driver with a flat dust cap is again rather small. As for the frequency response, the sharp dip around $ka = 15$ in the on-axis response for the convex dustcap, Figure 131b is gone, see Figure 132b.

11.5.3 *Dome with Waveguide*

This case corresponds to the geometry in Figure 130c. The outer radius is 0.1 m, the inner radius 0.042 m, and the base radius and height of the dome are 0.04 m and 0.0285 m, respectively. The waveguide is 0.03 m deep, with an exponential profile. This geometry was simulated using 20 modes, and 25 elements. The computation time was 17 s for 150 frequencies. The radiation impedance, Figure 133a, is similar to that of a conical horn, but with slightly more low end gain.

The frequency response again shows on-axis dips, in this case as low as $ka = 3$, but the off-axis response is smoother than for the cases (a) and (b) shown above. The level is lower than for the conical diaphragms because the volume velocity is smaller due to the smaller vibrating surface.

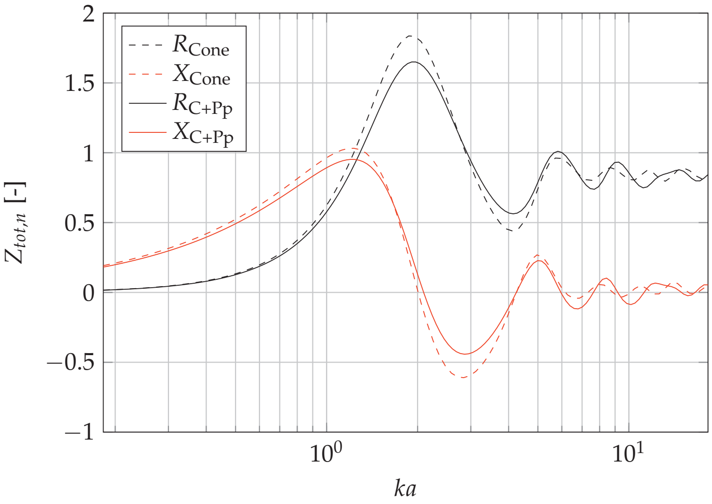

(a) Radiation impedance.

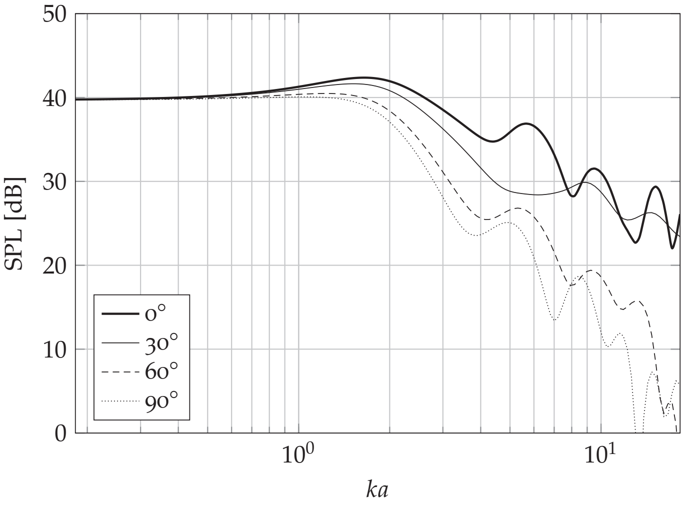

(b) Frequency response.

Figure 132: The results for the conical diaphragm with phase plug.

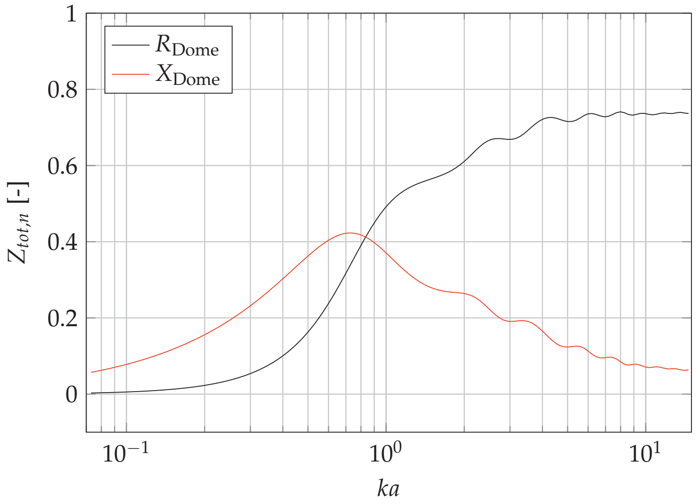

(a) Radiation impedance.

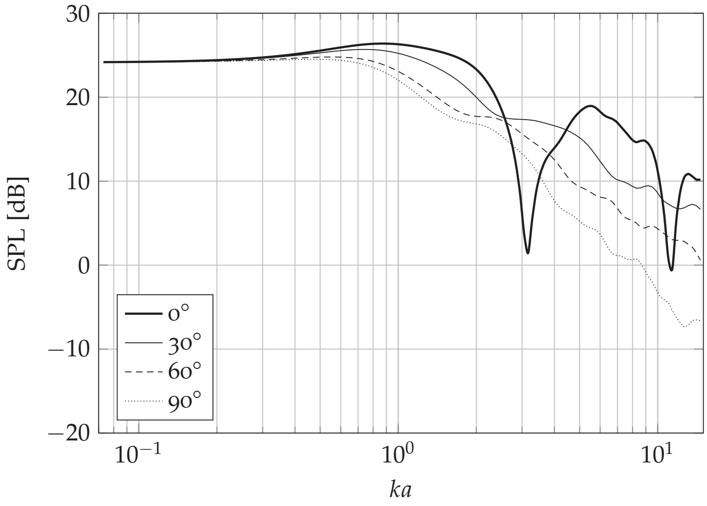

(b) Frequency response.

Figure 133: The results for the dome with waveguide.

11.6 REFLECTOR EXAMPLES

As a final example of applications of this extension of the MMM, we consider the problem of a reflector with a source within the cavity. This is possible by setting the wall velocity to zero, and introducing a source as per Eq. (335). Two geometries will be studied, Figure 134, where a source is placed at the focal point of a parabolic reflector, Figure 134a, or at the same position in a corresponding conical reflector, Figure 134b. A small portion of the bottom of the parabolic reflector is flat, in order to avoid very small elements, which would result in the $\mathbb{M}$-matrix being close to singular. Inner radii (flat bottom) and outer radii of the two geometries are 12.5 mm and 100 mm respectively, the depth is 51 mm. The source was placed 47 mm from the bottom.

Polar plots for a few wave numbers are shown in Figure 135. The curves for the parabolic reflector are on the left hand side, those for the cone are on the right hand side. a is the radius of the reflector. It is clear that the parabolic reflector has a narrower main lobe and better suppression of the side lobes than the conical reflector, as one would expect.

11.7 SUMMARY

The Mode Matching Method from Chapter 4 has been extended to be able to simulate concave structures where the entire wall vibrates. With the previous method it was possible to find impedance, pressure and volume velocity by working step by step from one end of the structure to the other. With the new method, pressure and volume velocity at all points in the structure must be found simultaneously, by solving a large but sparse linear system of equations. In this chapter, the method has been demonstrated for circular and annular geometries, but it can easily be applied to rectangular geometries by the appropriate choice of mode functions.

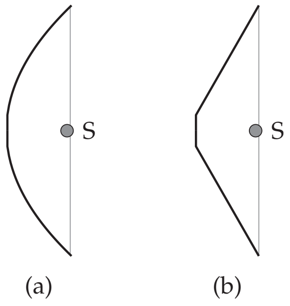

(a) (b)

Figure 134: Reflector geometries.

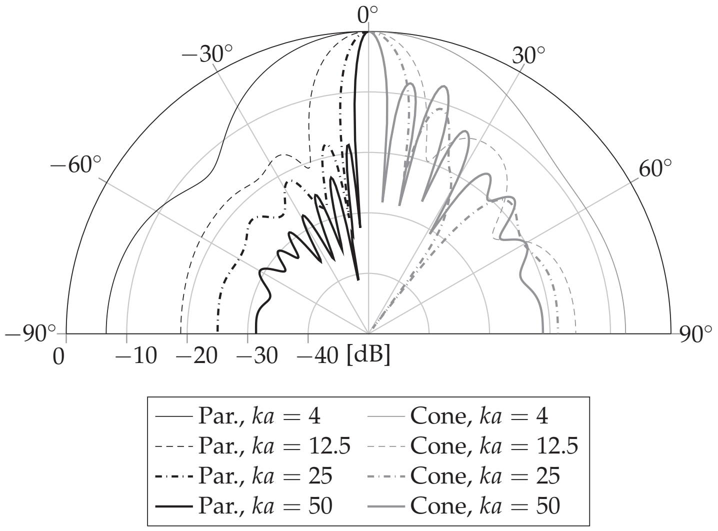

Figure 135: Polar response of the two reflectors in Figure 134. a is the radius of the reflector.

The method compares very well to BERIM, and gives results that are close even with a small number of modes. The method is also significantly faster, by several orders of magnitude, than BERIM. It can also be noted that by using different expressions for the radiation impedance, non-infinite baffle cases can be studied with the same numerical effort. This also includes horns and waveguides; the traditional Mode Matching Method can be used to give the horn modal throat impedance, which in turn can be used as the load impedance for the present method.

By introduction of annular mode functions, it is possible to analyze structures with a convex central member, like a dust cap or a phase plug, as long as it does not extend beyond the baffle plane. The equations for the mode functions and F-matrices for annular geometries are significantly more complex than for the purely circular geometry, but the complexity of the model framework does not change. In terms of programming, it is merely a question of calling different subroutines.

The radiation impedance and frequency response of five examples have been presented; a conical and a curved diaphragm, both with a planar dust cap, a conical diaphragm with a convex dust cap, a conical diaphragm with a phase plug, and a dome with a short waveguide. These examples illustrate some of the possible uses for this method. The computation time is in the order of seconds, making the method viable for use in optimization algorithms.

Two examples of loudspeaker diaphragm shapes have been given, demonstrating how the method could be used to optimize diaphragm shape.

In addition to radiators, it has been demonstrated that concave reflectors can be simulated as long as the source is inside the reflector. Two examples were given to illustrate this application.

12

APPLICATION OF THE MMM TO ROOM ACOUSTICS

A standard model for rooms in the low frequency region is the modal sum. The mode shapes and eigenfrequencies can easily be found analytically for a shoebox-shaped room with hard walls. For rooms of most other shapes, no analytical solutions exist, and we must resort to numerical methods.

One option is to employ general numerical methods like the Finite Element or Boundary Element Methods (BEM and FEM). In this chapter, MMM will be employed to solve the problem.

The Mode Matching Method used in this thesis has been developed to simulate horns, ducts and waveguides, and, as has been shown in the previous chapters, is able to predict the performance of these devices with good accuracy.

By considering a room to be a waveguide which is closed at the end, this method can be used to compute the room resonance frequencies, transfer functions and mode shapes for a large number of geometries. Amir and Starobinski [266] have considered this problem for two-dimensional cavities with two axes of symmetry.

The contribution of this chapter is the application of MMM to room acoustics as an alternative to FEM and BEM for finding the resonance frequencies and transfer function of a non-shoebox shaped room. It is an extension of the work by Amir and Starobinski to three-dimensional cavities, with alternative suggestions for finding the resonance frequencies. The chapter is based on the work described in [57].

12.1 PRACTICAL ISSUES

In MMM, the discretization process consists of dividing the room into short elements of constant cross section and uniform thickness, which have analytical mode functions. This leads to a few restrictions that will be described below.

12.1.1 *Allowable Geometries*

While the proposed method is not restricted to shoebox shaped rooms, there are still some restrictions on the geometry. In general, it must be possible to divide the room into slices (or elements) of constant thickness, each slice being rectangular. A few examples will make this more clear, see Figure 136.

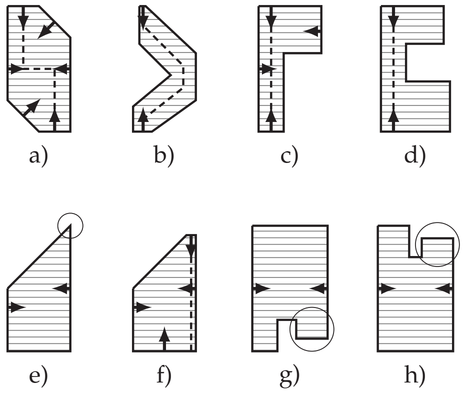

Figure 136: Examples of geometries. Arrows indicate possible propagation directions.

In all the examples, it is assumed that the room is discretized by dividing it into slices or elements, as indicated by the horizontal lines in the figures, and that the cross-section of each element is rectangular. That means that the height of the room can also vary, as long as the restriction on slice geometry is observed.

Room a) has a simple expansion and a contraction. It may be simulated lengthwise or sideways, or even perpendicular to the skewed walls.

Room b) has a skewed geometry, and it may be skewed in more than one direction. This room can only be simulated along the dashed line.

Rooms c) and d) are simple shapes that may easily be simulated, but care must be given to the large discontinuities to make sure the algorithm is numerically stable. It may be worthwhile to divide the F and V matrices into several matrices, each describing part of the discontinuity.

Room e) cannot be simulated the way it is discretized in the figure, since there is no wall at the far end that is parallel to the slices. This can be solved either by creating a very small flat portion at the far wall, as in f), or by changing the direction of simulation.

Room g) cannot be simulated due to the niche indicated by the circle. By changing the orientation of the room to that of d), this problem is solved.

Room h) has a similar problem, in that the end of the room splits into two niches. The problem may again be solved by changing the direction.

As indicated, many room shapes can be simulated by the proper choice of direction of simulation, but there are of course geometries that cannot be simulated by this method. An example would be if e) was the height profile of room g), in which case there is no direction

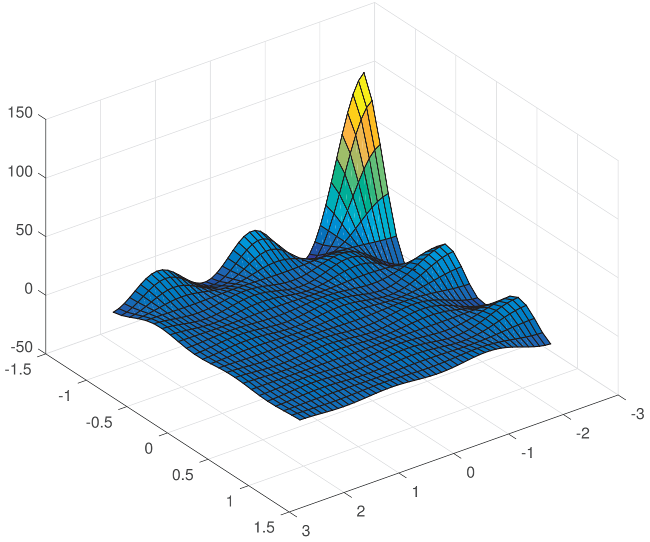

Figure 137: Example of velocity distribution for a point source in a corner, described by 36 (6 by 6) modes.

where all requirements are met. Also rooms with walls that are tilted in two directions are problematic.

12.1.2 *Sources and Receivers*

In room acoustics modeling, one usually wants to employ point sources, which can be positioned anywhere in the room. In the simplest implementation, the excitation of the room must be at the "starting wall", indicated by an arrow in Figure 136. Furthermore, an ideal point source is not possible to use, since all calculations are based on elements each having a 2D modal representation of a sound field. Therefore, a 2D modal representation of the point source must be found, i.e. the room must be excited with a number of modes, the relative amplitudes of which give the best possible approximation of a point source. The mode amplitudes are found as

$$U_m = \int_S v_\perp(x,y)\psi_m(x,y)dS. \tag{342}$$

To obtain a given volume velocity U_{tot}, one sets $v_\perp = U_{tot}/S$, and evaluates ψ_m at the source position, since for a point source, the velocity is zero everywhere else. It then turns out that the volume velocity mode amplitude vector is simply

$$U_m = \int_S \delta(x,y)v_\perp(x,y)\psi_m(x,y)dS = U_{tot}\psi_m(x,y). \tag{343}$$

An example of the velocity distribution representing a point source in a corner, described by a total of 36 modes, is shown in Figure 137.

As mentioned above, directly using the MMM as presented in Chapter 4, restricts the source location to the input surface of the structure. For this method to be useful for general room simulation, it must be possible to place sources at any location in the room. The method to do this was described in Chapter 11.

The problem to be solved, is that when a source is placed away from the “starting wall”, it is not possible to use an end-to-end calculation method as outlined in Chapter 4. Instead, a linear system of equations can be set up to solve for all pressures and volume velocities at the discontinuities simultaneously. The right hand side will include the additional source volume velocity in modal form. In the case of a room, the source is no longer a ring with constant velocity, but a point. The modal amplitudes are found as in Eq. (335). This solution method can of course be applied to the entire room, but it is also possible to use it for only the part between the “starting wall” and the source. From there and forward, the ordinary MMM can be used.

The receivers may be placed at any convenient location, but it is most convenient to place them at the interfaces between the elements. The desired receiver positions should therefore be taken into account in the discretization of the room. The impedance matrix at the receiver location must be saved, together with the volume velocity transfer matrix from the source to the receiver location. Given the source volume velocity vector and the transfer matrix, the volume velocity vector at the receiver point is found, and the sound pressure is computed using from Equations (76) and (70).

12.1.3 *Resonance Frequencies*

The resonance frequencies of the room will appear as peaks in the impedance curve at the input, or more specifically, as a phase reversal that can be seen as a jump in the imaginary part of the impedance. In the multimodal case, as is the case for MMM, the input impedance is a matrix, and it may be more convenient to find the peaks by looking at the pressure at the source point, which is found in the same way as the pressure at the receiver points as outlined above. Amir and Starobinski [266] suggest looking at peaks in the determinant of the impedance matrix, or minimum values in the determinant of the admittance matrix $\mathbb{Y} = \mathbb{Z}^{-1}$.

However, due to the presence of evanescent modes, some of the resonances may be extremely narrow and very difficult to spot in the impedance (or the pressure at the source point). It may therefore be easier to find the resonance frequencies by looking at the pressure response in one corner due to a source in a corner approximately diametrically opposite of the receiver corner. Looking at the imaginary part of the complex pressure, similar phase reversals as found in the impedance may be found, and these may be used to detect the resonance frequencies. The resonance frequencies may be found using root finding algorithms as found in [308]. Alternatively, it may be possible to reformulate the problem as a generalized eigenvalue problem, as done by Kirkup [332, 333], but this has not been tried.

12.1.4 *Mode Shapes*

The mode shapes can be illustrated by evaluating the sound pressure for a grid of receiver points when the room is excited with a frequency very close to the mode's resonance frequency. If the room has no losses, it is not possible to select the excitation frequency exactly at a mode resonance frequency, because of the infinite amplitude.

12.2 VERIFICATION: SHOEBOX SHAPED ROOM

The method described above can of course also be used for shoebox shaped rooms, and this case serves as a useful verification of the method.

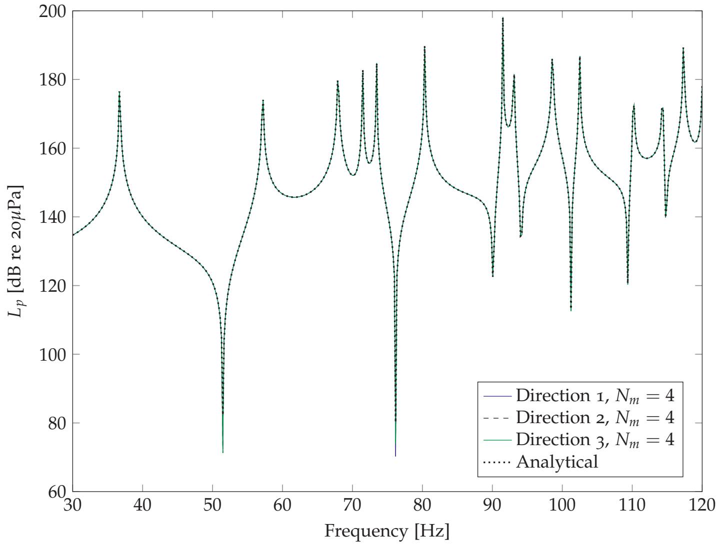

Figure 138: Frequency response for a shoebox shaped room, computed either with MMM or with the analytical method. 16 modes, two elements were used in the MMM simulation. Source and receiver in diagonally opposite corners.

The transfer function of a room, given in Eq. (255) on page 177, was used to compute the pressure at one corner due to a $1\text{m}^3/\text{s}$ volume velocity source in the diagonally opposite corner of a room $2.4 \times 3.0 \times 4.67$ meters, using a $\delta_N = 10^{-12}$. The result was compared to MMM using 16 modes (4 modes in each direction), Figure 138. All possible directions for the room were tried, all giving the same results, as can be seen from the figure.

It turned out that very few duct elements were needed for this case, and even with only two elements, the method still produced an accurate frequency response. With these parameters (two elements, 16 modes), the computation time for a Matlab implementation on a desktop computer was about 0.25 s for 500 frequencies. The analytical solution under identical conditions took only 7 ms.

12.3 NON-SHOEBOX EXAMPLE

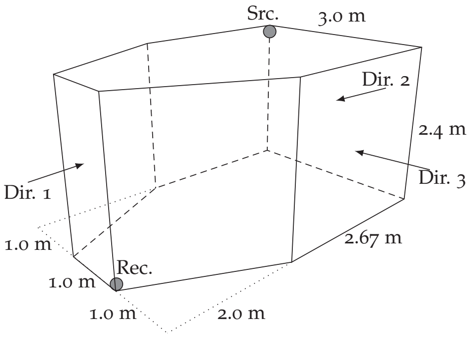

Figure 139: Non-shoebox shaped room used in the example. The gray circles indicate the positions of the source and receiver. The room is simulated using MMM along the three directions indicated.

Case	Elements	Modes
MMM, dir. 1	20	36
MMM, dir. 2	20	36
MMM, dir. 3	22	36

Table 16: Parameters for the MMM models.

Method	Freq. resp.	Mode fr.
FEM	76 s	4 s
MMM, dir. 1	5.0 s	-
MMM, dir. 2	6.0 s	-
MMM, dir. 3	5.7 s	-

Table 17: Computation times for 500 frequencies for the two methods. Note that the FEM simulation is run with compiled code, while MMM runs in Matlab.

40.56	59.83	71.50	74.07	82.20	82.28
93.24	102.96	109.01	110.43	114.10	116.58

Table 18: Resonance frequencies in Hz for the room in Figure 139, as found by FEM.

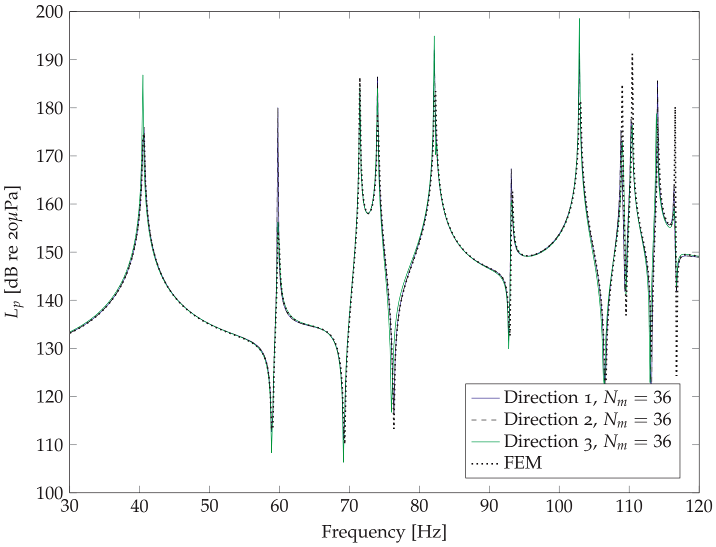

Figure 140: Frequency response for the room in Figure 139, computed either with MMM or FEM. Source and receiver in diagonally opposite corners.

A sketch of the test room, including dimensions and placement of the source and receiver, is shown in Figure 139. The room has a constant ceiling height of 2.4 m, a total length of 4.67 m, a maximum width of 3.0 m, and two skewed walls. Source and receiver positions are indicated in the sketch by gray circles. Also here, three directions are simulated, as a verification of the model. In addition, the mode frequencies (listed in Table 18) and the transfer function from the source to the receiver were computed using Comsol Multiphysics [334], using a model with a maximum mesh size of 0.45 m. The parameters for the MMM models are given in Table 16.

As can be seen from the frequency responses in Figure 140, the agreement between the results for the three directions of MMM simulation, and the FEM solution, is excellent. All resonance frequencies are found, although the two resonance frequencies around 82 Hz are so close that they cannot be discerned in the figure. Repeating the simulations with very high frequency resolution between 81.5 and 83 Hz shows that these two distinct resonance frequencies can also be

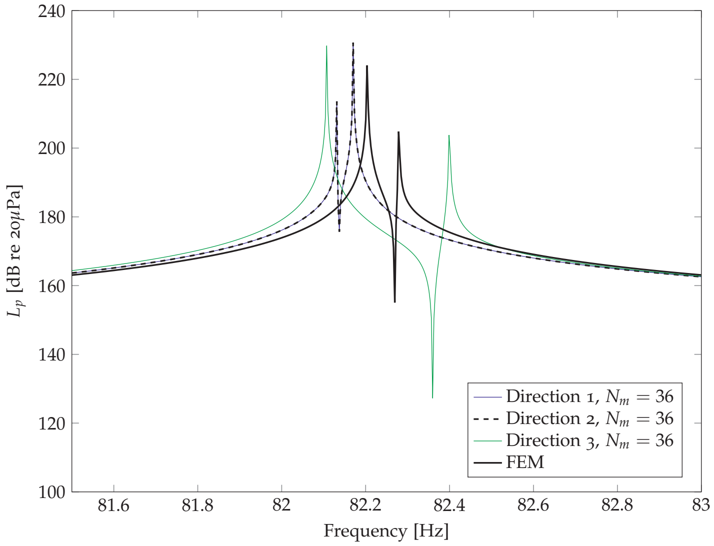

Figure 141: Close-up of the resonance frequencies near 82 Hz.

found with MMM, see Figure 141. It would, however, be hard (or expensive) to separate these frequencies using a root finding algorithm.

The resonance frequencies as found by MMM are 82.13 and 82.17 Hz when computed along the length of the room, and 82.11 and 82.40 Hz when simulated in direction 3, a slight difference from the FEM results given in Table 18. Changing the discretization in FEM and MMM did not materially improve the agreement, so the differences are attributed to slight differences in material parameters in FEM, perhaps due to a more detailed model of the fluid. With sharp peaks like this, minute changes in sound speed may have large effect. The differences in resonance frequencies also make for rather large differences in the sound pressure level close to the resonances. Since the sound pressure theoretically goes to infinity at these frequencies, a minute change of frequency around the resonance will result in a very large jump in sound pressure.

The horizontal mode shape at one of the two resonance frequencies near 82 Hz, as computed by MMM, is shown in Figure 142. This mode shape is calculated in a plane 1.2 m above the floor of the room. The horizontal mode shapes at the two resonance frequencies are almost identical, but the vertical mode shapes are slightly different, see Figure 143.

12.4 DISCUSSION

The results above show that the MMM gives results comparable to analytical and FEM solutions for shoebox shaped and non-shoebox

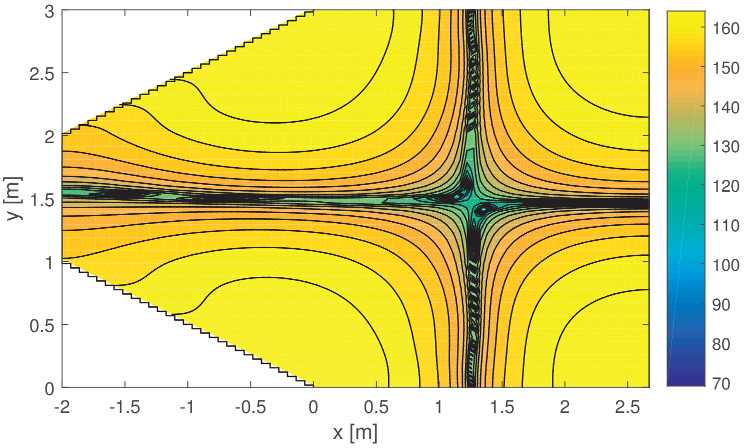

Figure 142: Horizontal mode shape near 82 Hz, simulated using MMM. The simulation used a finer discretization of the room than the frequency response simulation above, in order to show the details of the sound field. Dimensions in meters. Sound pressure level contours (arbitrary reference).

shaped rooms, respectively. For the shoebox shaped room, the analytical method is orders of magnitude faster, and is the method of choice. It also has the advantage that the resonance frequencies can be found analytically. For the other rooms, the MMM is significantly faster than FEM in computing the transfer function. It has not been attempted to find the resonance frequencies with high accuracy using the MMM, but it is not expected that a method using root finding algorithms will be competitive with FEM. FEM has the advantage that the resonance frequencies (eigenfrequencies) can be found by finding the eigenvalues of a frequency independent matrix, which is not the case for MMM.

The geometries that can be investigated with MMM are many, but there are restrictions. Many rooms can be simulated along several axes. The modes existing along the simulation axis will always be found, regardless of how many cross modes that are included in the computation time, although the accuracy may vary. Since the computation time depends on the number of cross modes used in the computation, and since a wide room necessitates more cross modes for an accurate description of the sound field, the simulation axis should be chosen to make the room, as seen along the axis, as long and narrow as possible. Otherwise, more modes may be needed if the room is short and wide.

As the method relies on the computation of modal impedances, with the impedance at the output end defined, it is straightforward to introduce damping into the room, in the form of an impedance at the end wall. It is also possible to let the impedance of this wall be made up from the impedance of a wall added to the input impedance of another room behind that wall, or, by using the radiation impedance

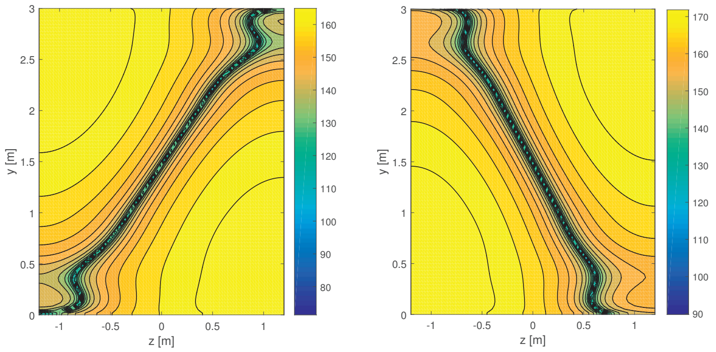

(a) Vertical mode shape, 82.11 Hz.

(b) Vertical mode shape, 82.40 Hz.

Figure 143: Vertical mode shapes near 82 Hz for the plane at $x = 0$ in Figure 142, simulated using MMM. Dimensions in meters. Sound pressure level contours (arbitrary reference).

for a duct opening in an infinite baffle, Section 5.5, even an open window may be simulated.

If a small part of the room is to be repeatedly changed, for instance if the objective is to optimize the room shape for some parameter, possibilities exist for reducing the total computation time. One would then compute the input impedance of the part of the room that is to be kept unchanged, and use this as the load impedance for the variable part, which has to be at the input end of the structure. The volume velocity transfer matrix may also be held fixed for the unchanging part, and then multiplied with the transfer matrix for the variable part to obtain the total transfer matrix for the room.

12.5 SUMMARY

The Mode Matching Method (MMM) has been applied to the problem of low frequency standing waves in rooms. While the method is slower than the analytical solution for a shoebox shaped room, the room shapes are not restricted to analytically solvable geometries. The room is discretized by dividing it into slices or elements, and the main restriction is that each element should be rectangular. In addition, the room must not fork into several separate paths, and a wave propagating through the series of slices should not have to turn back to fill the entire room. By careful choice of how the room is discretized, a large set of geometries can be simulated.

The MMM will efficiently compute the transfer function of a room, and for the example given in this paper, the algorithm is significantly faster than the Finite Element Method, and of comparable accuracy. The room resonance frequencies may be found using a root finding algorithm, but this is expected to be slower than using FEM modal analysis, due to the need to search through the frequency space for the resonances.

Part IV

CONCLUSION

13

DISCUSSION AND CONCLUSIONS

Each of the previous chapters in the thesis have concluded with a summary of the work covered in the respective chapter, and that will not be repeated here.

13.1 THE WORK IN THIS THESIS

The work in this thesis has concentrated on the Mode Matching Method (MMM). The method's usefulness for horn loudspeaker simulations for axisymmetric and rectangular geometries were investigated in my Master's project [285] and my Master's thesis [38], respectively, and were found to give good accuracy both for throat impedance and directivity, for the cases tested, all of which were restricted to an infinite baffle radiation condition. Restricting the studies to horns in an infinite baffle was chosen because expressions for the radiation impedance for this case were readily available.

This restriction, however, severely limits the applicability of the method to the few cases of horns mounted in walls or very large enclosures. Usually, horns may be free standing, mounted in an enclosure of a size comparable to the horn itself, or placed on a floor or in a corner (bass horns). The main motivation for this work has therefore been to extend the method to these more realistic cases.

As Section 6.2 shows, the infinite baffle case is still of high importance, as it describes the direct sound field from the horn, and is an important component of the total sound field radiated from the horn. Much work has therefore been expended on making these calculations efficient, especially the computation of the radiation impedance, which involves numerical integration of oscillatory integrals. This work is described in Chapter 5.

In addition, three distinct cases have been treated:

1. Free standing horns with no, or a small, flange. This work is described in Chapter 6.
2. Horns mounted in a wall near one or two hard boundaries extending to infinity. This work is described in Chapter 7.
3. Horns mounted in the wall of a room. This work is described in Chapter 8.

Due to the way the MMM works, there is no difference in how the horn itself is treated in each case. The differences come from the radiation impedance at the mouth of the horn, and from how the radiated pressure is calculated. The work in the three cases above has therefore been to develop the required expressions or methods to calculate these two quantities.

Experimental verifications, and comparisons with reference methods like BEM and BERIM, have also been performed, and have verified that the MMM, with the extensions developed in this thesis, is capable of good accuracy, as described in Chapter 9.

The computational efficiency of the MMM compared to other methods has not been extensively studied in this work, but some comparisons have been made, in addition to those in [38, 285]. What is clear from all these investigations, is that MMM can be very fast compared with other methods, and due to its simple scalability, it is easy to change the resolution to suit the problem.

In the course of this work, the MMM has also been expanded in other ways.

- By coupling MMM with BEM, as described in Chapter 10, the range of applicability is extended to horns where part of the horn has a geometry not compatible with the standard MMM geometries. BEM is used for the incompatible part, while MMM is used for the rest of the horn.

- By allowing the walls to also have a velocity, MMM can be used to simulate concave vibrating structures like loudspeaker cones, as described in Chapter 11. While the mode matching approach has been applied to this problem earlier [55, 56], Chapter 11 describes a much simpler and more straightforward approach. This method can also be used simulate concave reflectors.

- As rooms can be considered to be large horns that are closed at both ends, MMM can also be applied to room acoustics, as described in Chapter 12, as long as a few restrictions on geometry is observed. Direct use of the MMM requires the sound source to be at one wall of the room, but by employing the method used for reflectors, placing sources anywhere inside the room is possible.

Specifically, this work has made the following new contributions to the field:

- The low frequency multi-modal radiation resistance for a circular duct in an infinite baffle has been expressed in terms of polynomials to enable fast computation. Analytical expressions for the polynomial coefficients are given.

- High frequency approximations for the multi-modal radiation impedance matrix for baffled ducts, both circular (all modes) and rectangular (diagonal terms), have been found.

- The method of Snakowska for an unflanged circular duct has been applied to circular horns without baffle.
- The Edge Diffraction Method of Svensson has been applied to horns with a small flange. It has been demonstrated how the method can be used to find the radiation impedance and radiated pressure from such a horn.
- A method to compute the multi-modal mutual radiation impedance by means of matrix multiplications has been described.
- The sensitivity of horns to the distance from reflecting boundaries has been demonstrated.
- Analytical expressions for the multi-modal radiation impedance of a rectangular radiator in the wall of a room have been found.
- A simple method to couple BEM and MMM has been described.
- A straightforward method to simulate concave radiators using MMM has been developed. A method has been developed to place a source inside the radiator, making it possible to also simulate reflectors.
- It has been demonstrated how the MMM can be used to efficiently simulate non-shoebox-shaped rooms.

The extensions of the MMM described in this thesis have resulted in a set of tools that can be applied to a wide range of horn loudspeaker problems. But the tools and results are of course not restricted to horn loudspeakers; other duct-like systems, like musical instruments or ventilation systems can also be simulated using MMM, in addition to rooms, as has already been mentioned.

13.2 FUTURE WORK

When working in depth with a problem, it is natural that limitations are discovered, or that questions and ideas arise that are not directly related to the problem at hand, or that cannot be further investigated due to time restrictions, lack of resources, etc. However, these limitations, questions and ideas should not be forgotten. Here follows a list of ideas and questions that should be further investigated in order to make the MMM an even more useful tool to the horn designer.

- More work is needed for the case of horns in full space (free standing horns, Chapter 6). The analytical method explored for circular horns currently has some limitations making it unsuitable for horn simulation, and these limitations should either be removed, or a different method investigated. An approach that seems feasible, is to expand on the work on radiation from a plane piston in a sphere, presented in Beranek and Mellow [288]. By introducing a modal description of the sound field on the flat surface, the modal radiation impedance matrix, and the radiated pressure for each mode, may be found.

- More work is also needed to make the Edge Diffraction Method efficient and robust. This general method could then be used for all enclosure and flange geometries. The efficiency problem could probably be overcome by using compiled code with parallelization, like C++ with OpenMP. In addition, better handling of the singularities at receiver points coplanar with the edges is needed.

- Horns placed on a flat surface, but not mounted in a wall, cannot currently be simulated. This is a very common case for bass horns, which are almost always placed on a floor, but seldom built into the wall, and so it is an important problem. For this case, both edge diffraction and reflections must be taken into account.

- Horns, or in general, large, partially radiating structures, placed inside a room, cannot currently be efficiently simulated. The work done in connection with a horn mounted in the wall of a room, Chapter 8, was a step in this direction, and the analytical expressions found gave hope that similar expressions could be found for a hard, distributed source inside the room. However, it was not clear how to make the transition from a distributed monopole source to a distributed one-sided source, and work stopped. It does, however, appear possible to use the expression for the transfer function from a point source to a point receiver in a room as a Green's function in some sort of BEM implementation. This would make it possible to discretize only the object inside the room, without having to discretize the room itself.

- Dividing the sound path of a horn into several smaller paths, is a technique much used when folding bass horns. Also dividing a horn into cells that extend from a point near the throat to the mouth is a technique that was much used in the past. Making each path or cell of a horn so small that no, or very few, modes can propagate there, will simplify the description of the sound field significantly. In order to analyze such horns, the MMM should be adapted to structures employing two or more parallel paths.

- Folds in horns should be possible to simulate in MMM. In [288], Beranek and Mellow describes how the model developed for a bass reflex enclosure can be used to describe a 180° fold in a horn. Since this model is the basis for the model for multimodal radiation impedance of a duct exiting into the wall of a room, as presented in Section 8.2, a model for a 180° fold should be possible to develop along the same lines. It may also be possible to develop expressions for other types of folds, including junctions, using similar methods.

- At high frequencies, sound propagation approaches a line-of-sight propagation, and this is the basis for the ray-tracing methods used in room acoustics [335]. Direct use of ray-tracing alone for simulating horn directivity at high frequencies will probably not give good enough accuracy, and will clearly produce abrupt changes in the sound field at certain angles. It might, however, be possible to use ray-tracing as part as a more complete model, used for instance in combination with modal descriptions and edge diffraction. A similar idea is used by Sun et al. for the calculation of scattering from a rigid sphere [336].
- Use of the Edge Diffraction Method for horns consisting of a few flat panels. This may include horns of the Manta-Ray type [3], or folded bass horns, where flat panels are typically used to approximate the ideally curved surfaces. The EDM still has some challenges when the order of specular reflections becomes high, however, and work is needed to overcome these problems.
- The efficiency of the MMM, in combination with the simple description of geometry (simply a list of radius or height/width as function of distance from the throat), makes the method well suited for optimization, or as a forward model for inversion algorithms. This has not yet been tried, but is one of the obvious areas of application for the method. The far field sound pressure is determined by the mouth velocity mode amplitudes, Section 5.1.1, and these amplitudes can be found from a desired (or measured) far field response [33]. At low frequencies, many modes are evanescent in large parts of the horn, which can make it hard to fulfill certain directivity requirements. In addition, the contribution of the modes to the far field pressure varies with off-axis angle and frequency, and can be insignificant for certain combinations of these. The optimization algorithm may experience problems in such situations. If the required mode amplitudes for a given mouth size and directivity function are first found, one can produce a set of realistic mouth mode amplitude frequency responses that could be used in further optimization of the horn.
- In order to improve the accuracy of the MMM when an insufficient number of modes are used (for instance in order to reduce the computation time), Richardson extrapolation may be used [337].

Part V

APPENDIX

A

MMM VS. PLANE WAVE HORN THEORY

In [135, 140, 141], H. F. Olson gave the throat impedance curves for a series of exponential horn of different sizes, showing how the ripple is reduced as the horn approaches the infinite horn. These curves have been repeated by many authors, for instance Beranek [150], Merhaut [338] and Beranek and Mellow [288]. The curves do, however, not show any results for horns where the mouth circumference is larger than one cutoff wavelength, i.e. $k_c a_m > 1$. Although Flanders, in [73], showed that there is an optimum mouth size for an exponential horn, the general belief was for a long time that if the horn was increased in size, reflections and throat impedance ripple would decrease monotonically.

In 1973, D. B. Keele published a study [161], based on computer simulations, showing that this was not the case; there was an optimum mouth size beyond which the ripple would increase somewhat. Keele's study is, however, based on the plane wave horn theory, and plane waves cannot be assumed when the horn mouth is large.

It is the purpose of this Appendix to show that the throat impedance of a finite horn does indeed approach that of an infinite horn as size is increased, and at the same time show the difference between the plane wave horn theory and the more accurate MMM.

A.1 THE HORNS

All horns simulated here are mounted in an infinite baffle, and have a throat radius of $0.015\lambda_c$, where λ_c is the cutoff wavelength. The other dimensions are listed in Table 19.

Horn	r_m	L	$k_c a_m$
1	$0.05\lambda_c$	$0.192\lambda_c$	0.31
2	$0.10\lambda_c$	$0.302\lambda_c$	0.63
3	$0.15\lambda_c$	$0.367\lambda_c$	0.94
4	$0.19\lambda_c$	$0.405\lambda_c$	1.20
5	$0.23\lambda_c$	$0.429\lambda_c$	1.40
6	$0.32\lambda_c$	$0.486\lambda_c$	2.00
7	$0.64\lambda_c$	$0.597\lambda_c$	4.00

Table 19: Horn dimensions.

A.2 RESULTS

The plane wave results (designated PW in the figures) Figures 144 through 146 (note the change of scale) correspond to curves that can be found in available literature referenced above. Here the MMM results (using 16 modes) do not differ greatly from the plane wave results.

Figures 147 through 150 show the results for $k_c a_m > 1$. It is clear here that the ripple for the plane wave approximation increase for $k_c a_m > 1$, reaching a more or less asymptotic value, as reported by Keele [161]. However, the MMM results show a monotonously decreasing ripple magnitude, with a throat impedance curve that approaches the curve for an infinite horn, Figure 151, with some deviations around the cutoff frequency due to the presence of the radiation impedance.

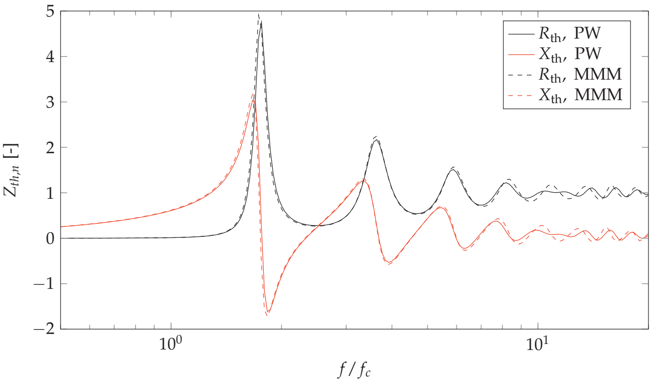

Figure 144: Horn 1: $k_c a_m = 0.31$.

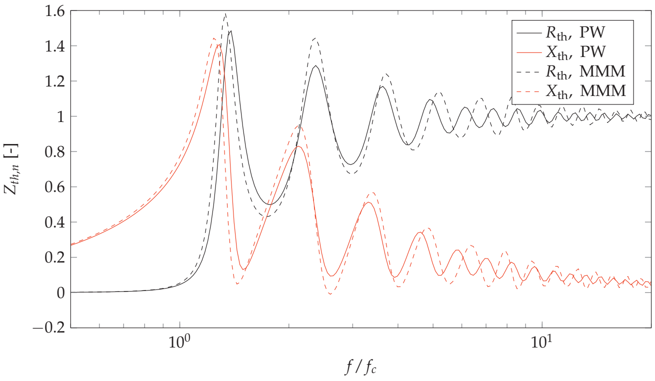

Figure 145: Horn 2: $k_c a_m = 0.63$.

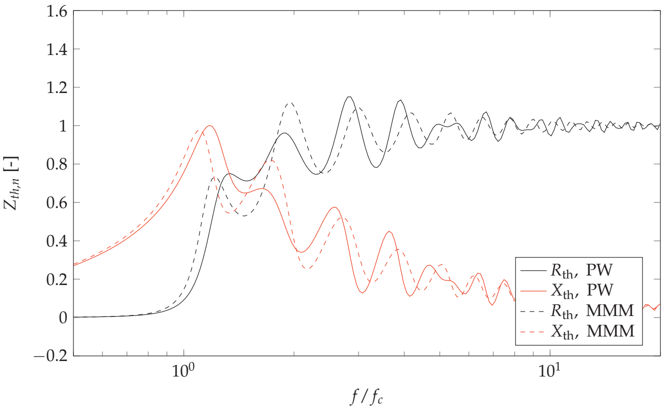

Figure 146: Horn 3: $k_c a_m = 0.94$.

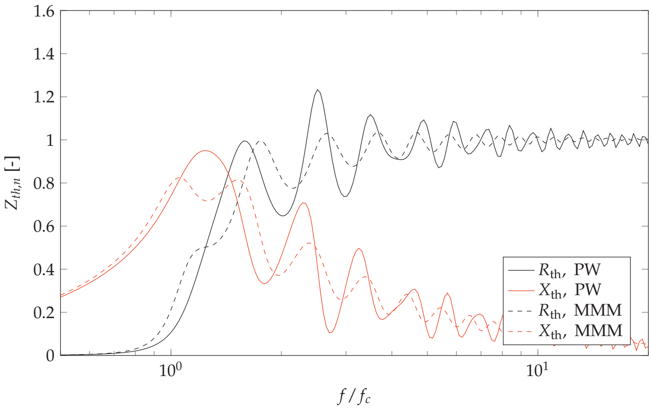

Figure 147: Horn 4: $k_c a_m = 1.2$.

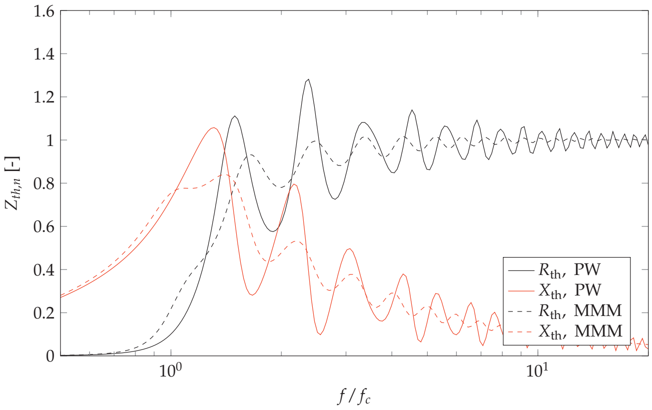

Figure 148: Horn 5: $k_c a_m = 1.4$.

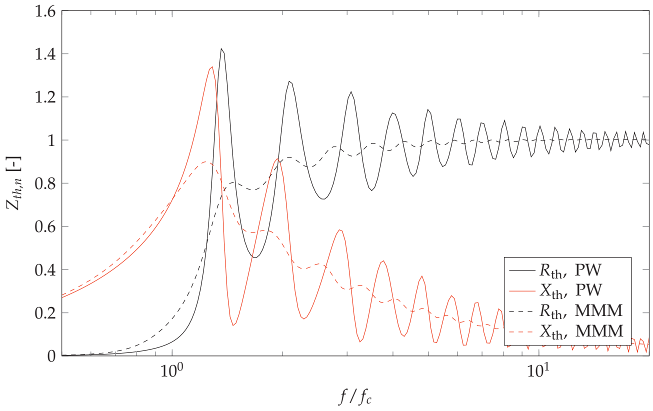

Figure 149: Horn 6: $k_c a_m = 2.0$.

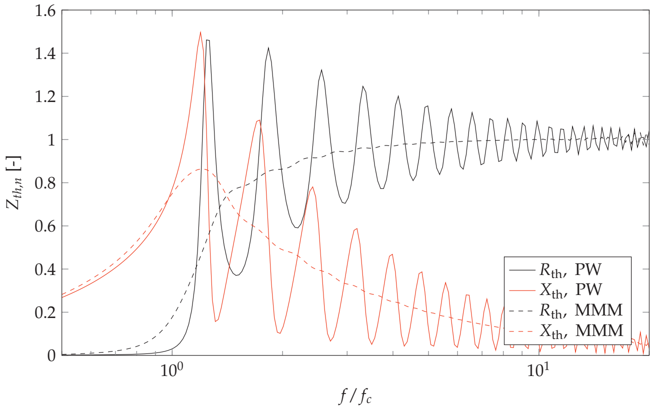

Figure 150: Horn 7: $k_c a_m = 4.0$.

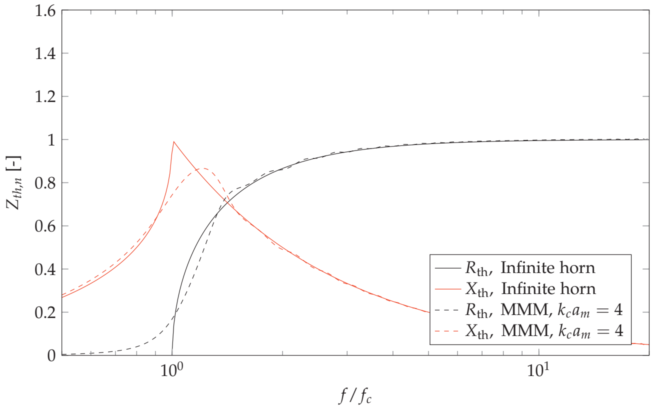

Figure 151: Horn 7 ($k_c a_m = 4.0$) compared to an infinite exponential horn.

B

POLYNOMIAL COEFFICIENTS FOR RADIATION RESISTANCE

The radiation resistance for a circular duct in an infinite baffle is

$$Z_{nm} = \frac{\rho c}{S} \int\limits_0^{\pi/2} \sin\phi D_n(\sin\phi) D_m(\sin\phi) d\phi \tag{344}$$

where

$$D_n(\tau) = \frac{-\sqrt{2}\tau J_1(\tau ka)}{\left(\frac{\mu_n}{ka}\right)^2 - \tau^2} \tag{345}$$

By expanding Eq. (345) around $ka = 0$, we get

$$\begin{aligned} D_n \approx -\frac{\tau^2 (ka)^3}{\sqrt{2}\mu_n^2} + \frac{(-8+\mu_n^2)\tau^4 (ka)^5}{8\sqrt{2}\mu_n^4} \\ - \frac{((192 - 24\mu_n^2 + \mu_n^4)\tau^6)(ka)^7}{192\sqrt{2}\mu_n^6} + \mathcal{O}(ka)^9 \end{aligned} \tag{346}$$

and

$$D_0 \approx \frac{ka}{\sqrt{2}} - \frac{\tau^2 (ka)^3}{8\sqrt{2}} + \frac{\tau^4 (ka)^5}{192\sqrt{2}} - \frac{\tau^6 (ka)^7}{192\sqrt{2}} + \mathcal{O}(ka)^9. \tag{347}$$

By integrating these expressions term by term, a polynomial expansion of the radiation resistance can be found. The polynomial coefficients are listed in the tables below.

$(ka)^n$	Coefficient
0	0
2	0
4	0
6	$\frac{4}{15\mu_m^2\mu_n^2}$
8	$\frac{8}{35\mu_m^4\mu_n^2}+\frac{8}{35\mu_m^2\mu_n^4}-\frac{2}{35\mu_m^2\mu_n^2}$
10	$\frac{64}{315\mu_m^2\mu_n^6}+\frac{64}{315\mu_m^4\mu_n^4}-\frac{16}{315\mu_m^2\mu_n^4}$ $+\frac{64}{315\mu_m^6\mu_n^2}-\frac{16}{315\mu_m^4\mu_n^2}+\frac{1}{189\mu\mu_n^2}$
12	$\frac{128}{693\mu_m^4\mu_n^6}-\frac{16}{693\mu_m^2\mu_n^6}+\frac{128}{693\mu_m^6\mu_n^4}-\frac{32}{693\mu_m^4\mu_n^4}$ $+\frac{8}{2079\mu_m^2\mu_n^4}-\frac{16}{693\mu_m^6\mu_n^2}+\frac{8}{2079\mu_m^4\mu_n^2}-\frac{1}{4158\mu_m^2\mu_n^2}$
14	$\frac{512}{3003\mu_m^6\mu_n^6}-\frac{64}{3003\mu_m^4\mu_n^6}+\frac{8}{9009\mu_m^2\mu_n^6}$ $-\frac{64}{3003\mu_m^6\mu_n^4}+\frac{8}{3003\mu_m^4\mu_n^4}-\frac{1}{9009\mu_m^2\mu_n^4}$ $-\frac{8}{9009\mu_m^6\mu_n^2}-\frac{1}{9009\mu_m^4\mu_n^2}+\frac{1}{216216\mu_m^2\mu_n^2}$

Table 20: Polynomial coefficients for R_{nm}.

$(ka)^n$	Coefficient, R_{0n}	Ckoefficient, R_{00}
0	0	0
2	0	$\frac{1}{2}$
4	$-\frac{1}{3\mu_n^2}$	$-\frac{1}{12}$
6	$-\frac{4}{15\mu_n^4}+\frac{1}{15\mu_n^2}$	$\frac{1}{144}$
8	$-\frac{8}{35\mu_n^6}+\frac{2}{35\mu_n^4}-\frac{1}{168\mu_n^2}$	$-\frac{1}{2880}$
10	$\frac{4}{315\mu_n^6}-\frac{4}{945\mu_n^4}+\frac{13}{45360\mu_n^2}$	$\frac{1}{90720}$
12	$-\frac{2}{2079\mu_n^6}+\frac{1}{1728\mu_n^4}-\frac{1}{133056\mu_n^2}$	$-\frac{1}{4790016}$
14	$\frac{1}{54054\mu_n^6}-\frac{1}{432432\mu_n^4}+\frac{1}{10378368\mu_n^2}$	$\frac{1}{498161664}$

Table 21: Polynomical coefficients for R_{0n} and R_{00}. Coefficients for R_{m0} are identical to those for R_{0n}, apart from using μ_m instead of μ_n.

C

UNFLANGED CIRCULAR DUCT

In this appendix, the equations governing the diffraction at the open end of a semi-infinite, unflanged circular duct, as used in 6.1, will be summed up. The summary is based on the work by Weinstein [295] and Snakowska [297, 46], and is included since references [297, 46] are in Polish and not easily accessible.

Note that to be more consistent with the notation in this thesis, k_n has been used for the axial wavenumber, instead of γ_n, which is used in the references. Also, in the summary, a sign convention of the imaginary unit opposite of that used in the rest of this thesis is employed. This is to avoid mistakes in the equations. In the final result, it is only necessary to take the complex conjugate to obtain the same sign convention as used in the rest of the thesis.

C.1 FUNDAMENTAL EQUATIONS

We must solve the wave equation

$$\frac{\partial^2\Phi}{\partial r^2} + \frac{1}{r}\frac{\partial\Phi}{\partial r} + \frac{\partial^2\Phi}{\partial z^2} + k^2\Phi = 0 \tag{348}$$

for the velocity potential Φ, with the boundary condition

$$\frac{\partial\Phi}{\partial r} = 0 \text{ for } r = a,\ z \leq 0. \tag{349}$$

This is similar to what was done in Section 4.2.1, and gives the mode function

$$\psi_n = \frac{J_0(\mu_n r/a)}{J_0(\mu_n)}. \tag{350}$$

For the case of an unflanged duct, we are interested in the geometry shown in Figure 152. We assume an incident wave to be propagating

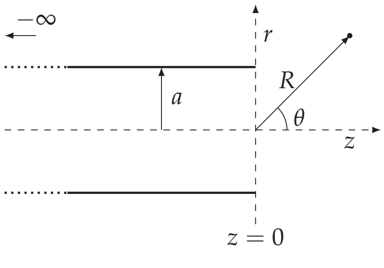

Figure 152: Geometry of the unflanged duct problem (after Snakowska [46]).

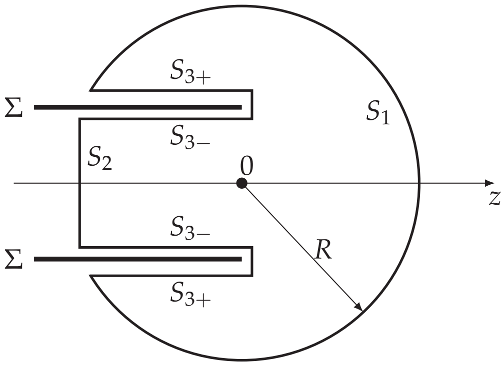

Figure 153: Integration contour (after Snakowska [46]). Σ indicates the duct wall.

from $z = -\infty$ towards the outlet. Due to the diffraction at the end of the duct, the sound field inside the duct will consist of the sum of the incident and the diffracted field, while outside the duct, we only have the diffracted field. Formally,

$$\Phi(r,z) = \begin{cases} \Phi_< = \Phi^{inc} + \Phi_<^{dif}, & r \leq a \\ \Phi_> = \Phi_>^{dif}, & r > a. \end{cases} \tag{351}$$

In order to solve the problem we make use of Green's second theorem,

$$\oint\limits_S (\Phi_1 \nabla \Phi_2 - \Phi_2 \nabla \Phi_1) \cdot \mathbf{n} ds = \int\limits_{V(S)} (\Phi_1 \Delta \Phi_2 - \Phi_2 \Delta \Phi_1)\, dV \tag{352}$$

where Φ_1 is a Green's function $G(\mathbf{r}, \mathbf{r}')$ and Φ_2 is the potential. This is also the basic idea in the Boundary Element Method. The result is that

$$\Phi(\mathbf{r}) = \oint\limits_S \left(G(\mathbf{r}, \mathbf{r}') \frac{\partial \Phi\left(\mathbf{r}'\right)}{\partial n'} - \Phi\left(\mathbf{r}'\right) \frac{\partial G(\mathbf{r}, \mathbf{r}')}{\partial n'} \right) ds' \tag{353}$$

where the prime indicates the source. The integration is over the composite surface (S_1, S_2, S_3) shown in Figure 153. Due to the Sommerfield radiation condition, the integral over surfaces S_1 and S_2 must be zero as R goes to infinity, and we are left with integration over the duct surfaces (inner and outer) only.

This leaves us with the following expression for the potential

$$\Phi(\mathbf{r}) = -a \int\limits_0^{2\pi} d\varphi' \int\limits_{-\infty}^{0} \Psi(a, \varphi', z') \frac{\partial}{\partial r} G(\mathbf{r}, \mathbf{r}') \Big|_{r'=a} dz' \tag{354}$$

where Ψ describes the jump of potential across the surface at $r = a$. Ψ can be expressed as

$$\Psi_l(z) = \Phi_l^{inc}(a, z) + f_l(z). \tag{355}$$

The Green's function for cylindrical coordinates is

$$G(r,r',\varphi,\varphi',z,z') = \frac{i}{8\pi}\sum_{n=-\infty}^{\infty} e^{in(\varphi-\varphi')}\times$$
$$\times\int\limits_{-\infty+i\eta}^{\infty+i\eta} dw e^{iw(z-z')}\left\{\begin{array}{c} H_n^{(1)}(vr)J_n(vr') \\ H_n^{(1)}(vr')J_n(vr)\end{array}\right\},\ \begin{array}{c} r>r' \\ r<r' \end{array} \tag{356}$$

which reduces to

$$G(r,r',z,z') = \frac{i}{8\pi}\int\limits_{-\infty+i\eta}^{\infty+i\eta} dw e^{iw(z-z')}\left\{\begin{array}{c} H_0^{(1)}(vr)J_0(vr') \\ H_0^{(1)}(vr')J_0(vr)\end{array}\right\},\ \begin{array}{c} r>r' \\ r<r' \end{array} \tag{357}$$

if the problem is axisymmetric. Note that it has a form of an inverse Fourier transform, and that the integration path is parallel to the real axis.

The potential then becomes

$$\Phi_l(r,z) = -\frac{ia}{4}\int\limits_{-\infty}^{\infty} dz'\Psi_l(z')\int\limits_{-\infty+i\eta}^{\infty+i\eta} dw e^{-iw(z-z')}v\times$$
$$\times\left\{\begin{array}{c} H_0^{(1)}(vr)'J_0(vr') \\ H_0^{(1)'}(vr')J_0(vr)\end{array}\right\},\ \begin{array}{c} r>r' \\ r<r' \end{array}, \tag{358}$$

with the boundary conditions given as

$$\left.\frac{\partial\Phi_l}{\partial r}\right|_{r=a} = 0 \Rightarrow \int\limits_{-\infty}^{\infty}\Psi_l(z')l(z-z')dz' = 0,\ z\leq 0. \tag{359}$$

and

$$l(z-z') = \frac{1}{2\pi}\int\limits_{-\infty}^{\infty} dw e^{-iw(z-z')}v^2 H_1^{(1)'}(va)J_1'(va). \tag{360}$$

Solution of the problem of the sound field inside and outside of a rigid, semi-infinite waveguide now boils down to determining the function Ψ_l in Eq. (359), which is a Wiener-Hopf equation with the offset kernel function $l(z-z')$. The function $l(z-z')$ must not be confused with the mode index subscript l.

$F_l(w)$ and $L(w)$ are the Fourier transforms of $f_l(z)$ and $l(z)$ respectively, $F_l(w) = \int_{-\infty}^{\infty} f_l(z)e^{-iwz}dz$ and $L(w) = \int_{-\infty}^{\infty} l(z)e^{-iwz}dz$.

By inspection, Eq. (360) has the form of an inverse Fourier transform of the function $v^2 H_1^{(1)'}(va)J_1'(va)$, therefore

$$L(w) = v^2 H_1^{(1)}(va)J_1(va). \tag{361}$$

By the application of the boundary conditions, it can be shown that

$$\Psi_l(z) = \frac{1}{2\pi} \int_{-\infty}^{\infty} F_l(w) e^{-iwz} dw + e^{-ik_l z} = 0,\ z > 0, \tag{362}$$

were the second term represents the incident wave, and

$$\left.\frac{\partial \Phi_l}{\partial r}\right|_{r=a} = 0 \Rightarrow \int_{-\infty}^{\infty} F_l(w) L(w) e^{-iwz} dw = 0,\ z \leq 0. \tag{363}$$

Eq. (362) says that in the continuation of (in front of) the duct, there is no jump of potential, while Eq. (363) says that there is a jump for $z \leq 0$, i.e. across the duct wall.

It is now possible by using the Wiener-Hopf technique [295] to find the expressions for $F_l(w)$ and $L(w)$ that satisfy Equations 362 and 363. First,

$$f_l(z) = -e^{-ik_l z}.$$

This is satisfied if $F_l(w)$ has a first order pole with the residue i^{-1} at the point $w = -k_l$, and uniformly tend to zero in the lower half plane for $|w| \to \infty$.

The equations to be solved for can be written in the form of contour integrals in the complex plane:

$$\int_C F_l(w) e^{iwz} dw \quad = 0, \quad z > 0, \tag{364}$$

$$\int_C F_l(w) L(w) e^{iwz} dw \quad = 0, \quad z \leq 0, \tag{365}$$

where C is the integration contour, consisting of a line parallel to the real axis and looping around the point $w = -k_l$.

The requirements for solving this set of equations are

1. Function $F_l(w)$ is analytic in the lower half-plane, $\text{Im}(w) < \text{Im}(k)$, excluding the point $w = -k_l$, which is a first-order pole with residue $1/i$, and tends to zero for $|w| \to \infty$.

2. The product $F_l(w)L(w)$ is analytical in the upper half-plane, $\text{Im}(w) > -\text{Im}(k)$, and tends to zero for $|w| \to \infty$.

If we assume that $L(w)$ can be factorized as

$$L(w) = L_+(w) L_-(w), \tag{366}$$

both conditions above can be satisfied if

$$F_l(w) = \frac{K}{(w + k_l)\, L_-(w)}. \tag{367}$$

It can be shown that

$$\text{Res}_{w=-k_l} F_l(w) = \lim_{w \to -k_l} F_l(w)(w + k_l) = \frac{K}{L_-(-k_l)}, \tag{368}$$

therefore $K = -iL_-(-k_l)$, and $F(w)$ can be expressed as

$$F_l(w) = \frac{L_-(-k_l)}{i(w+k_l)L_-(w)L_+} = \frac{L_+(k_l)L_+(w)}{i(w+k_l)L_-(w)L_+(w)}, \tag{369}$$

due to the property of L that $L_+(-w) = L_-(w)$, and Eq. (366).

It now remains to determine $L_+(w)$ and $L_-(w)$. This is a long and complex procedure, detailed in [297, page 233ff], and the results are

$$L_+(w) = (k+w)\left[J_0(vr)H_0'(va)\right]^{\frac{1}{2}} \mathrm{e}^{\mathcal{M}\frac{1}{2}(w)}, \tag{370}$$

$$L_+(w) = (k-w)\left[J_0(vr)H_0'(va)\right]^{\frac{1}{2}} \mathrm{e}^{-\frac{1}{2}\mathcal{M}(w)}. \tag{371}$$

The function $\mathcal{M}(w)$ is defined as

$$\mathcal{M}(w) = \frac{1}{\pi}\sum_{n=0}^{\infty}\int_{k_n}^{k_{n+1}} \left(\Omega(v'a) - \Omega(\mu_n)\right)\left(\frac{1}{w'+w} - \frac{1}{w'-w}\right) dw' \tag{372}$$

where

$$\Omega(va) = \arg H_1^{(1)}(va) - \frac{\pi}{2} = \arctan\frac{Y_1(va)}{J_1(va)} - \frac{\pi}{2} \tag{373}$$

and

$$\Omega(\mu_n) = n\pi,\ \Omega(0) = 0 \tag{374}$$

Therefore,

$$\mathcal{M}(w) = \frac{2w}{\pi}\sum_{n=0}^{\infty}\int_{k_n}^{k_{n+1}} \frac{\Omega(v'a) - n\pi}{w^2 - w'^2} dw' \tag{375}$$

or

$$\mathcal{M}(w) = \frac{2w}{\pi}\int_{k_0}^{i\infty} \frac{\Omega(v'a) - n\pi}{w^2 - w'^2} dw'. \tag{376}$$

By writing out the sum and collecting terms, it is possible to write $\mathcal{M}(w)$ as

$$\begin{aligned}\mathcal{M}(w) = \frac{1}{\pi}\sum_{n=0}^{\infty}\int_{k_n}^{k_{n+1}} \Omega(v'a)\left(\frac{1}{w'+w} - \frac{1}{w'-w}\right) dw' \\ + \lim_{M\to\infty}\left[\sum_{n=1}^{M}\ln\frac{k_n+w}{k_n-w} + M\ln\frac{k_n-w}{k_n+w}\right].\end{aligned} \tag{377}$$

In the sum $\lim_{M\to\infty}\sum_{n=1}^{M}\ln\frac{k_n+w}{k_n-w}$, the N_m first terms are logarithms of real numbers (the first N_m modes that are propagating), so by writing

$$\mathcal{M}(w) = \sum_{i=1}^{N_m}\ln\frac{k_n+w}{k_n-w} + S(w), \tag{378}$$

we get

$$e^{\mathcal{M}(w)} = \prod_{i=1}^{N_m} \frac{k_i + w}{k_i - w} e^{S(w)}, \tag{379}$$

and we can write

$$L_+(w) = (k+w)\left[J_0(vr)H_0'(va)\prod_{i=1}^{N_m}\frac{k_i + w}{k_i - w}\right]^{\frac{1}{2}} \mathrm{e}^{\frac{1}{2}S(w)} \tag{380}$$

$$L_-(w) = (k-w)\left[J_0(vr)H_0'(va)\prod_{i=1}^{N_m}\frac{k_i - w}{k_i + w}\right]^{\frac{1}{2}} \mathrm{e}^{-\frac{1}{2}S(w)}. \tag{381}$$

The function $S(w)$, which explicitly is written as

$$\begin{aligned} S(w) = \frac{1}{\pi}\sum_{n=0}^{\infty}\int_{k_n}^{k_{n+1}} \Omega(v'a)\left(\frac{1}{w'+w} - \frac{1}{w'-w}\right)dw' \\ + \lim_{M\to\infty}\sum_{n=N_m+1}^{M}\left(\ln\frac{k_n + w}{k_n - w} + M\ln\frac{k_n - w}{k_n + w}\right), \end{aligned} \tag{382}$$

can be split into real and imaginary parts [297, pages 251–254],

$$S(w) = X(w) + iY(w) \tag{383}$$

where

$$X(w) = \frac{1}{\pi}P\int_{-k}^{k}\frac{\Omega(v'a)}{w'-w}dw' \tag{384}$$

$$Y(w) = \frac{2wa}{\pi} - \Omega(va) - i\lim_{M\to\infty}\left[\sum_{n=N_m+1}^{M}\frac{k_n + w}{k_n - w} - \frac{1}{\pi}\int_{-k_N}^{k_N}\frac{\Omega(v'a)}{w'-w}dw'\right], \tag{385}$$

and the P in Eq. (384) indicates the principal value.

The velocity potential inside the duct, for a single incident mode, can now be described as

$$\Phi_l(r,z) = \frac{J_0(\mu_n r/a)}{J_0(\mu_n)}e^{ik_l z} - \frac{ai}{4}\int_{-\infty}^{\infty} dw e^{-iwz} v F_l(w) H_0^{(1)'}(va) J_0(vr). \tag{386}$$

The numerical implementation of these functions will be given in Section C.4.

C.2 REFLECTION FACTOR

With an incident mode of order l, the total sound field is given as

$$\Phi_l(r,z) = \frac{J_0\left(r\frac{\mu_l}{a}\right)}{J_0(\mu_l)}e^{ik_l z} + \sum_{n=0}^{N} R_{ln}\frac{J_0\left(r\frac{\mu_n}{a}\right)}{J_0(\mu_n)}e^{-ik_n z}, \tag{387}$$

where R_{ln} is the reflection factor from mode l into mode n. This reflection factor is then defined as

$$R_{ln} = \lim_{w \to k_l} L_+(w) \lim_{w \to k_n} \frac{w - k_n}{(w + k_l) L_-(w)}. \tag{388}$$

In order to be able to calculate R_{ln}, we will have to solve these limits for the L_+ and L_- functions. There are two cases: $l = 0$ and $l \neq 0$, that have to be handled separately. First for $l = 0$, we have that $w = k$ and $v = 0$, so the limit we have to solve is

$$\lim_{va \to 0} J_1(va) H_1^{(1)}(va) = i \lim_{va \to 0} J_1(va) Y_1(va). \tag{389}$$

Using the approximation to the Bessel functions for small arguments,

$$J_v(z) \cong \frac{1}{\Gamma(v+1)} \left(\frac{z}{2}\right)^2, \; v \geq 0, \; |z| \ll 1$$

$$Y_v(z) \cong -\frac{\Gamma(v)}{\pi} \left(\frac{2}{z}\right)^2, \; v > 0, \; |z| \ll 1$$

we find that

$$\lim_{va \to 0} J_1(va) H_1^{(1)}(va) = -\frac{i}{\pi}. \tag{390}$$

The other limit is for $l \neq 0$. In this case we have a case of $0/0$, and we have to use l'Hopital's rule. The limit can be split into two parts:

$$\lim_{w \to k_l} \frac{J_1(va) H_1^{(1)}(va)}{k_l - w} = \lim_{w \to k_l} \frac{J_1^2(va)}{k_l - w} - \lim_{w \to k_l} \frac{i J_1(va) Y_1(va)}{k_l - w}. \tag{391}$$

For the first part, and using the fact that $v^2 = k^2 - w^2$ giving $v = \mu_l / a$ when $w \to k_l$,

$$\lim_{w \to k_l} \frac{J_1^2(va)}{k_l - w} = 2 \underbrace{J_1(\mu_l)}_{=0} J_1'(\mu_l) \frac{k_l a^2}{\mu_l} = 0, \tag{392}$$

due to the fact that μ_l is the zero of J_1.

For the second part,

$$\lim_{w \to k_l} \frac{i J_1(va) Y_1(va)}{k_l - w} = i \left[J_1'(\mu_l) Y_1(\mu_l) - \underbrace{J_1(\mu_l) Y_1(\mu_l)}_{=0} \right] \frac{a k_l}{\frac{\mu_l}{a}} = \frac{i k_l a^2}{\mu_l} J_1'(\mu_l) Y_1(\mu_l). \tag{393}$$

Using the relations

$$J_1'(\mu_l) = J_0(\mu_l)$$

and

$$Y_1(\mu_l) = -\frac{2}{\pi \mu_l J_0(\mu_l)}$$

we arrive at

$$\lim_{w \to k_l} \frac{i J_1(va) Y_1(va)}{k_l - w} = -\frac{2 i k_l a^2}{\pi \mu_l^2}. \tag{394}$$

By now expanding L_+ and L_- in Eq. (388), the reflection factor can be expressed as

$$R_{ln} = -\frac{2k_l}{k_l + k_n}\left[\prod_{i=0,i\neq l}^{N_m} \frac{k_i + k_l}{k_i - k_l} \prod_{i=0,i\neq l}^{N_m} \frac{k_i + k_n}{k_i - k_n}\right]^{\frac{1}{2}} e^{\frac{1}{2}(S(k_l)+S(k_n))}. \quad (395)$$

It may be more convenient to express R_{ln} as modulus and phase,

$$R_{ln} = -\left|R_{ln}\right| e^{i\theta_{ln}},$$

in which case

$$\left|R_{ln}\right| = \frac{2k_l}{k_l + k_n}\left[\prod_{i=0,i\neq l}^{N_m} \left|\frac{k_i + k_l}{k_i - k_l}\right| \prod_{i=0,i\neq l}^{N_m} \left|\frac{k_i + k_n}{k_i - k_n}\right|\right]^{\frac{1}{2}} e^{\frac{1}{2}(X(k_l)+X(k_n))} \quad (396)$$

and

$$\theta_{ln} = \begin{cases} Y(k_l) + Y(k_n), & l+n \text{ even}, \\ Y(k_l) + Y(k_n) + \pi, & l+n \text{ odd}. \end{cases} \quad (397)$$

In calculating the matrix of reflection coefficients, much work can be saved by first calculating a vector of the values of the modal wave numbers k_n, and the four vectors of X and Y functions for the values of k_n employed. The remainder of the calculations consists then to a large degree of combining the tabulated values.

C.3 DIRECTIVITY

The sound field in outside of the waveguide can be expressed as [47]

$$\Phi_l(r,z) = \frac{ia}{4}k^2 \oint_{C_1} d\alpha e^{ikz\sin\alpha} \cos^2\alpha F(k\sin\alpha) \cdot \left\{ \begin{array}{c} J_0(kr\cos\alpha) H_0^{(1)'}(ka\cos\alpha) \\ J_0'(ka\cos\alpha) H_0^{(1)}(kr\cos\alpha) \end{array} \right\}, \quad \begin{array}{c} r > a \\ r < a \end{array} \quad (398)$$

using the complex variable α, defined as $w = k\sin\alpha$. C_1 is the contour of integration in the α complex plane. By using the asymptotic expansion of the Hankel function for large arguments,

$$H_0^{(1)}(z) = \sqrt{\frac{2}{\pi z}} e^{i\left(z-\frac{\pi}{4}\right)} \left\{1 + \frac{1}{8iz} + ...\right\},$$

and the saddle-point method, an expression for the potential in the far field can be found. The procedure is detailed in [47], and gives [48]

$$p_l(R,\theta) = -\frac{k}{2} P_l \sin\theta J_1(ka\sin\theta) F_l\left(-k\cos\theta\right) \frac{e^{ikR}}{R} = d_l(\theta)\frac{e^{ikR}}{R}, \quad (399)$$

where P_l is the pressure amplitude of mode l. The equation is valid for $kR\sin^2\theta \gg 1$ and holds for both $r > a$ and $r < a$, although it is arrived at in two slightly different ways for the two cases.

If the observation point is closer to the outlet, a higher order approximation is needed. This approximation is not used in this thesis, but the details are given in [47].

C.4 NUMERICAL CALCULATIONS

This section will give some details on the numerical implementation of the kernel functions given above. The details are taken from notes prepared by Dr. Jerzy Jurkiewicz.

C.4.1 *Function X*

Function $X(w)$ is defined as

$$X(w) = \frac{1}{\pi} P \int_{-k}^{k} \frac{\Omega(v'a)}{w' - w} dw' \tag{400}$$

with $v'^2 + w'^2 = k^2$. It is convenient to used normalized variables. We introduce $p = w/k$, $y = w'/k$, both in the range $[-1, 1]$, giving the scaled version

$$X(p) = \frac{1}{\pi} \int_{-1}^{1} \frac{\Omega\left(ka\sqrt{1-y^2}\right)}{y - p} dy. \tag{401}$$

With the following change of variables

$$\begin{aligned} y &= \cos t & dy &= -\sin t \\ p &= \cos r & r &= \arccos p \end{aligned}$$

we get

$$X(p) = -\frac{1}{\pi} \int_{\pi}^{0} \frac{\Omega\left(ka\sin t\right)\sin t}{\cos t - \cos r} dt = \frac{1}{2\pi} \int_{\pi}^{0} \frac{\Omega\left(ka\sin t\right)\sin t}{\sin\left(\frac{t+r}{2}\right)\sin\left(\frac{t-r}{2}\right)} dt \tag{402}$$

By now introducing the function

$$\Theta(x) = \frac{\Omega(x)}{x},\ \Theta(0) = 0,$$

we arrive at

$$X(p) = \frac{ka}{2\pi} \int_{\pi}^{0} \Theta\left(ka\sin t\right) \frac{\sin^2 t}{\sin\left(\frac{t+r}{2}\right)\sin\left(\frac{t-r}{2}\right)} dt \tag{403}$$

which can be integrated by standard methods except in the region $t \approx r$.

In this region we make use of the following transformation:

$$t \in (A, B) \; A = r - H, \; B = r + H$$

$$X(p) = \frac{ka}{2\pi} \int\limits_A^B f(t) \frac{1}{\sin\left(\frac{t-r}{2}\right)} dt \tag{404}$$

where

$$f(t) = \Theta(ka \sin(t)) \cdot \frac{\sin^2 t}{\sin\left(\frac{t+r}{2}\right)}. \tag{405}$$

We now introduce the new variable

$$x = \sin\left(\frac{t-r}{2}\right), \; t = r + 2\arcsin x$$

$$X(p) = \frac{ka}{2\pi} \int\limits_C^D \underbrace{2 \frac{f(r + 2\arcsin x)}{\sqrt{1-x^2}}}_{g(x)} \cdot \frac{1}{x} dx \tag{406}$$

where the new integration limits are

$$C = \sin\left(\frac{A-r}{2}\right), \; D = \sin\left(\frac{B-r}{2}\right)$$

The method used to integrate this expression is to make a polynomial approximation of $g(x)$, algorithmically perform a polynomial division by x, and integrate the resulting quotient and remainder. With

$$g(x) \approx ...c_3x^3 + c_2x^2 + c_1x + c_0 = W(x) \tag{407}$$

we perform the polynomial division $W(x)/x$ so that

$$W(x) = P(x) \cdot x + R.$$

We can now find the integral as

$$X(p) = \frac{ka}{\pi} \left[\int\limits_C^D P(x) dx + \int\limits_C^D \frac{R}{x} dx \right] \tag{408}$$

where the integral over $P(x)$ can be performed algorithmically, producing a new polynomial $Q(x) = \int P(x) dx$, and the second integral can be solved analytically:

$$X(p) = \frac{ka}{\pi} \left[Q(D) - Q(C) + R \{\ln D - \ln C\} \right] \tag{409}$$

For the endpoints, $p = \pm 1$, i.e. for $r = 0$ and $r = \pi$, we have first for $r = 0$:

$$X(p) = \frac{ka}{2\pi} \int\limits_\pi^0 \Theta(ka \sin t) \frac{\sin^2 t}{\sin^2 \frac{t}{2}} dt \tag{410}$$

where we can do the following rearrangement:

$$\left(\frac{\sin t}{\sin\frac{t}{2}}\right)^2 = \left(\frac{2\sin\frac{t}{2}\cos\frac{t}{2}}{\sin\frac{t}{2}}\right)^2 = 4\cos^2\frac{t}{2} = 2(1+\cos t),$$

and the resulting function

$$X(p) = \frac{ka}{2\pi}\int_{\pi}^{0} \Theta\left(ka\sin t\right)\left(1+\cos t\right)dt \tag{411}$$

can be integrated by standard methods. A similar procedure can be followed for $r = \pi$, giving a result that is identical, save for an opposite sign.

C.4.2 *Function Y*

Function $Y(w)$ is defined as

$$Y(w) = res + \frac{2w}{\pi}\int_{0}^{j\infty} \frac{\omega(v'a)}{w^2 - w'^2}dw' \tag{412}$$

with $v'^2 + w'^2 = k^2$, res is a residual, and[1]

$$\omega(x) = \Omega(x) + n\pi, \quad \mu_n < x < \mu_{n+1}. \tag{413}$$

By setting $y = jw'$ we get

$$Y(w) = res + \frac{2w}{\pi}\int_{0}^{\infty} \frac{\omega\left(a\sqrt{k^2+y^2}\right)}{w^2+y^2}dy \tag{414}$$

It is convenient to used normalized variables. We introduce $p = w/k$ and set $y = x \cdot k$, giving the scaled version

$$Y(p) = res + \frac{2p}{\pi}\int_{0}^{\infty} \frac{\omega\left(ka\sqrt{1+x^2}\right)}{p^2+x^2}dx. \tag{415}$$

We now split up the integral in a sum of sub-integrals over subranges limited by the zeros of J_1:

$$Y(p) = res + \frac{2p}{\pi}\sum_{n=0}^{M}\int_{\beta_n}^{\beta_{n+1}} \frac{\omega\left(ka\sqrt{1+x^2}\right)}{p^2+x^2}dx + \underbrace{\frac{2p}{\pi}\int_{\beta_{M+1}}^{\infty} \frac{\omega\left(ka\sqrt{1+x^2}\right)}{p^2+x^2}dx.}_{\text{tail}} \tag{416}$$

---

[1] Mind the difference between ω (omega) and w.

Here

$$\beta_n = \sqrt{\left(\frac{\mu_{N_m+n}}{ka}\right)^2 - 1} \tag{417}$$

where N_m is the index of the first mode in cutoff. The residual *res* is

$$res = -\left(\Omega\left(ka\sqrt{1-p^2}\right) - N\pi\right) \cdot \operatorname{sign}(p). \tag{418}$$

The tail of the integral is approximated as follows: for $n > M+1$, the integration sub-ranges are approximately of length π. The nominator changes almost linearly from 0 to π, and the most significant factor is $x^2 > \beta_{M+1}^2$. Therefore, the tail integral can be approximated as follows:

$$\begin{aligned} \text{tail} \approx \frac{2p}{\pi} \int\limits_{\beta_{M+1}}^{\infty} \frac{\pi/2}{p^2+x^2} dx = \int\limits_{\beta_{M+1}}^{\infty} \frac{p}{p^2+x^2} dx \\ = \left[\arctan \frac{x}{p}\right]_{\beta_{M+1}}^{\infty} = \arctan \frac{\beta_{M+|}}{p}. \end{aligned} \tag{419}$$

For the subranges, we proceed as for $X(w)$. Given

$$\int\limits_{\beta_n}^{\beta_{n+1}} \frac{\omega\left(ka\sqrt{1+x^2}\right)}{p^2+x^2} dx = \int\limits_{\beta_n}^{\beta_{n+1}} \frac{f(x)}{p^2+x^2} dx, \tag{420}$$

we make a polynomial approximation of $f(x)$, algorithmically perform a polynomial division by p^2+x^2, and integrate the resulting quotient and remainder. With

$$f(x) \approx ...w_3x^3 + w_2x^2 + w_1x + w_0 = W(x). \tag{421}$$

Now we perform the polynomial division to get

$$\frac{W(x)}{p^2+x^2} = P(x) + \frac{qx}{p^2+x^2} + \frac{r}{p^2+x^2} \tag{422}$$

where q and r are the remainders. This gives

$$\begin{aligned} \int\limits_{\beta_n}^{\beta_{n+1}} \frac{W(x)}{p^2+x^2} dx = \\ \int\limits_{\beta_n}^{\beta_{n+1}} P(x) dx + \int\limits_{\beta_n}^{\beta_{n+1}} \frac{qx}{p^2+x^2} dx + \int\limits_{\beta_n}^{\beta_{n+1}} \frac{r}{p^2+x^2} dx. \end{aligned} \tag{423}$$

The first part is integrated algorithmically, producing a new polynomial $Q(x) = \int P(x)dx$, and the to other parts are integrated analytically, giving

$$\int\limits_{\beta_n}^{\beta_{n+1}} \frac{W(x)}{p^2+x^2}dx = [Q(x)]_{\beta_n}^{\beta_{n+1}} + q\left[\frac{1}{2}\ln\left(1+\left(\frac{x}{p}\right)^2\right)\right]_{\beta_n}^{\beta_{n+1}} + \frac{p}{r}\left[\arctan\frac{x}{p}\right]_{\beta_n}^{\beta_{n+1}}. \qquad (424)$$

A suitable value for M is 30-100.

C.4.3 *Directivity Function*

The directivity function is given as

$$d_l(\theta) = -\frac{k}{2}\sin\theta J_1(ka\sin\theta)F_l\left(-k\cos\theta\right). \qquad (425)$$

In order to calculate the directivity function, a method to compute $L(w)$ and $F_l(w)$ is needed. We have that

$$L(w) = L_+(w)L_-(w) = v^2 J_1(va)H_1^{(1)}(va), \qquad (426)$$

and

$$F_l(w) = \frac{L_+(k_l)L_+(w)}{i(w+k_l)v^2 J_1(va)H_1^{(1)}(va)}. \qquad (427)$$

L_+ and L_- are defined in Eq. (380) and Eq. (381), respectively. With $w = k\cos\theta$ and $v = k\sin\theta$, $v^2 = k^2 - w^2$,

$$d_l(\theta) = -\frac{v}{2}J_1(av)F_l\left(-w\right). \qquad (428)$$

Let us now express L_+ as

$$\begin{aligned} L_+(w) &= (k_0+w)\left[J_1(va)H_1^{(1)}(va)\prod_{n=1}^{N_m}\frac{k_n+w}{k_n-w}\right]^{\frac{1}{2}} e^{\frac{1}{2}S(w)} \\ &= (k+w)\left[H_1^{(1)}(va)L1(w)\right]^{\frac{1}{2}} e^{\frac{1}{2}S(w)}, \end{aligned} \qquad (429)$$

where

$$L1(w) = J_1(va)\prod_{n=1}^{N_m}\frac{k_n+w}{k_n-w}. \qquad (430)$$

Le us also introduce normalized arguments, so that

$$\begin{aligned} w &= k\cdot p & p &= \cos\theta \\ q^2 &= 1-p^2 & & \\ v &= k\cdot q & q &= \sin\theta \\ k_n &= k\cdot g_n & g_n^2 &= 1-\left(\frac{\mu_n}{ka}\right)^2 \end{aligned}$$

which enables us to use normalized function calls, so we can use the normalized X and Y functions derived above. We now have

$$d_l(\theta) = -\frac{k \cdot q}{2} J_1(ka \cdot q) F_l\,(-p) \tag{431}$$

where

$$F_l(p) = \frac{1}{k} \cdot \frac{L_+(g_l) L_+(p)}{i(p+g_l)\,(ka \cdot q)^2\, J_1(ka \cdot q) H_1^{(1)}(ka \cdot q)}, \tag{432}$$

$$L_+(w) = (1+p)\left[H_1^{(1)}(ka \cdot q) L1(p)\right]^{\frac{1}{2}} e^{\frac{1}{2}S(p)}, \tag{433}$$

$$L1(p) = J_1(ka \cdot q) \prod_{n=1}^{N_m} \frac{g_n + p}{g_n - p}. \tag{434}$$

Now we can simplify $d(\theta)$:

$$\begin{aligned} d_l(\theta) = -\frac{k \cdot q}{2} J_1(ka \cdot q) &\frac{L_+(g_l) L_+(-p)}{ik(-p+g_l) k^2 q^2 J_1(ka \cdot q) H_1^{(1)}(ka \cdot q)} \\ &= -\frac{1}{2k^2 q} \cdot \frac{L_+(g_l) L_+(-p)}{i(-p+g_l) H_1^{(1)}(ka \cdot q)}. \end{aligned} \tag{435}$$

By introducing normalized function $L_+^k(p) = kL_+(p)$, we can further simplify to

$$d_l(\theta) = -\frac{1}{2q} \cdot \frac{L_+(g_l) L_+(-p)}{i(-p+g_l) H_1^{(1)}(ka \cdot q)}. \tag{436}$$

$J_1\,(ka \cdot q)$ has zeros when $p = g_n$, and we get an expression of the type $0/0$. In addition, as $p \to \pm 1$, $q \to 0$, and $Y_1\,(ka \cdot q) \to \infty$. We use the small argument approximation of J_1 and Y_1, so that

$$Y_1(z) \cong \frac{2}{\pi} \cdot \frac{1}{z}$$

$$J_1(z) \cong \frac{1}{2} z - \frac{z^2}{8\pi}$$

giving

$$J_1(z) Y_1(z) \cong \frac{1}{\pi} - \frac{z^2}{8\pi}.$$

We can now express the directivity function as

$$\begin{aligned} d_l(\theta) = -\frac{(1-p)}{2q} \cdot \frac{L_+(g_l)}{i(-p+g_l) H_1^{(1)}(ka \cdot q)} &\left[H_1^{(1)}(ka \cdot q) L1(-p) e^{S(-p)}\right]^{\frac{1}{2}} \\ = \frac{i \cdot L_+(g_l)}{2(p-g_l) H_1^{(1)}(ka \cdot q)} &\cdot \frac{(1-p)}{q} \\ \times &\left[H_1^{(1)}(ka \cdot q) J_1(ka \cdot q) \prod_{n=1}^{N_m} \frac{g_n - p}{g_n + p} . e^{S(-p)}\right]^{\frac{1}{2}}. \end{aligned} \tag{437}$$

D

MODEL HORN DESCRIPTION

The horn used in the many of the tests in this thesis has a cross-sectional area which follows the hyperbolic-exponential horn profile of Salmon-type horns [93]. The area expansion is given by

$$S(z) = S_{th} \left(\cosh k_c z + T \sinh k_c z\right)^2 \tag{438}$$

where k_c is the cutoff wavenumber, S_{th} is the throat area, and T is a parameter determining the shape of the horn. The horn is square with $S_{th} = 42.25\,\mathrm{cm}^2$, $S_m = 1188.80\,\mathrm{cm}^2$, $T = 0.7$ and a cutoff frequency of 200 Hz. The length of the horn is 0.5 m. It is manufactured using bent MDF sheets with an inner skin of 1 mm aluminium. Total wall thickness is 14 mm, and stiffening ribs are glued to the outside. The horn is fitted with a 0.5 by 0.5 m flange that fits into a large baffle.

A photo of the horn is shown in Figure 154.

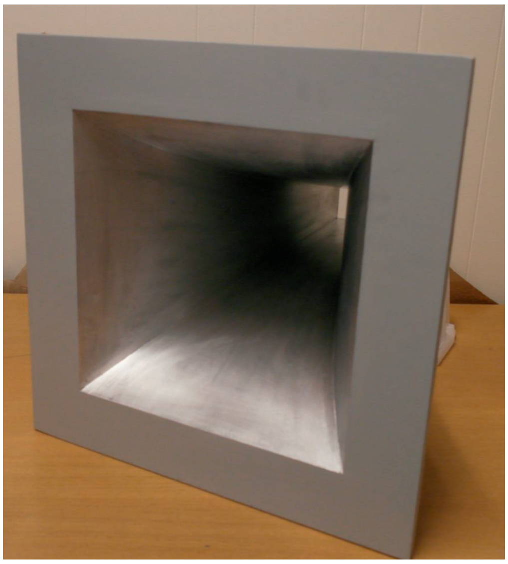

Figure 154: The horn used in the experiments.

E

DISTRIBUTED SOURCES IN ROOMS

During the work on horns in rooms or room walls, the approach of Method 1 outlined in Chapter 8 was investigated to see if it was possible to obtain the radiation impedance for a horn placed inside the room. A rectangular region of monopoles, as used in Section 8.1, clearly constitutes a radiator radiating in both directions. What is needed is a one-sided radiator. This could be achieved with a combination of a monopole and a dipole radiator, as described by Beranek and Mellow for the one-sided piston in a finite baffle [288]. It was tried using a dipole source consisting of two monopoles in antiphase, but it was soon realized that this would not be the appropriate source for this case, because it does not describe an open oscillating piston, but rather an open oscillating resilient disc.

While the investigations did not produce directly useful results for the radiation impedance and sound field of one-sided rectangular radiators in rooms, the equations derived in the process may be useful, and are therefore presented in this appendix.

A much-used function, that was also used in Chapter 8, is repeated here:

$$\begin{aligned}
Y_{m_x}^{m}(a, x_1, l_x) &= \int\limits_{x_1-a/2}^{x_1+a/2} N_{m_x} \cos\left(m_x\pi(x - x_1 + \frac{a}{2})/a\right) \cos\left(m\pi x/l_x\right) dx \\
&= \begin{cases}
a, & m = 0,\, m_x = 0 \\
\frac{2l_x}{m\pi} \cos\left(\frac{m\pi x_1}{l_x}\right) \sin\left(\frac{m\pi a}{2l_x}\right) & m > 0,\, m_x = 0 \\
0 & m = 0,\, m_x > 0 \\
\frac{\sqrt{2}a^2 l_x m\left(\sin\left(\frac{\pi m(a-2x_1)}{2l_x}\right) + (-1)^{m_x} \sin\left(\frac{\pi m(a+2x_1)}{2l_x}\right)\right)}{\pi(ma - m_x l_x)(ma + m_x l_x)} & m > 0,\, m_x > 0
\end{cases}
\end{aligned} \tag{439}$$

where m is the room mode index, and m_x is the mode index of the excitation.

The equations presented in this chapter, as well as those in Chapter 8, have all been computed using Mathematica symbolic software. Therefore the steps in the derivations cannot be shown.

E.1 DIPOLE SOURCE

Yousri and Fahy [339] give the mode function for a dipole source in a room as

$$\begin{aligned}\psi(x,y,z) = {}& \cos k_x \left(x - \frac{\Delta x}{2}\right) \cos k_y \left(y - \frac{\Delta y}{2}\right) \cos k_z \left(z - \frac{\Delta z}{2}\right) \\ & - \cos k_x \left(x + \frac{\Delta x}{2}\right) \cos k_y \left(y + \frac{\Delta y}{2}\right) \cos k_z \left(z + \frac{\Delta z}{2}\right) \\ & \backsimeq \Delta x k_x \sin\left(k_x x\right) \cos\left(k_y y\right) \cos\left(k_z z\right) \\ & + \Delta y k_y \cos\left(k_x x\right) \sin\left(k_y y\right) \cos\left(k_z z\right) \\ & + \Delta z k_z \cos\left(k_x x\right) \cos\left(k_y y\right) \sin\left(k_z z\right) \quad (440)\end{aligned}$$

where Δx etc. are the dipole moments in the coordinate directions. It is then possible to express the pressure in the room (assuming the dipole is aligned along the x axis) as

$$\begin{aligned}p(x,y,z) = {}& \frac{j\omega\rho c^2}{abV} U_{m_x,m_y} \sum_N \Omega_N \Delta z k_z \\ & \times \sin\left(\frac{q\pi z_0}{l_z}\right) Y^m_{m_x}(a,x_0,l_x) Y^n_{m_y}(b,y_0,l_y) \psi_N(x,y,z). \quad (441)\end{aligned}$$

The radiation impedance is then

$$\begin{aligned}Z_m = {}& -\frac{j\omega\rho c^2}{V} \sum_N \Omega_N \Delta z k_z \sin\left(\frac{q\pi z_0}{l_z}\right) \cos\left(\frac{q\pi z_0}{l_z}\right) \\ & \times Y^m_{m_x}(a,x_0,l_x) Y^n_{m_y}(b,y_0,l_y) Y^m_{n_x}(a,x_0,l_x) Y^n_{n_y}(b,y_0,l_y). \quad (442)\end{aligned}$$

E.2 ANGLED MONOPOLE SOURCE

Assuming a angled source in a room, with an angle θ to the z-axis. The source is parallel to the y-axis, but angled with respect to x and z. See Figure 155.

Let the line along the source in the $x - z$ plane be parametrized by $t = 0...1$, with corners in (x_1, z_1) and (x_2, z_2), and center in (x_c, z_c):

$$x = x_1 + t(x_2 - x_1) \quad (443)$$

$$z = z_1 + t(z_2 - z_1) \quad (444)$$

$$x_1 = x_c - \frac{a}{2}\cos\theta \quad (445)$$

$$x_2 = x_c + \frac{a}{2}\cos\theta \quad (446)$$

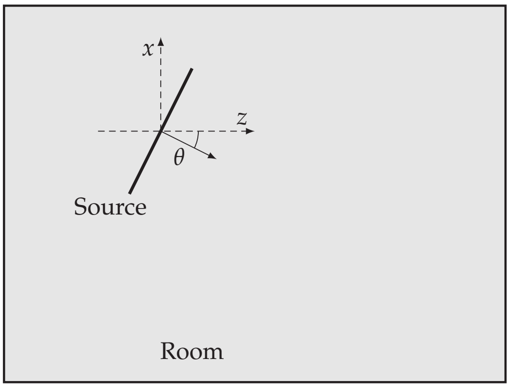

Figure 155: Angled source in a room.

$$z_1 = z_c + \frac{a}{2}\sin\theta \tag{447}$$

$$z_1 = z_c - \frac{a}{2}\sin\theta \tag{448}$$

$$x(t) = x_c - (\frac{1}{2} + t)a\cos\theta \tag{449}$$

$$z(t) = z_c + \left(\frac{1}{2} - t\right) a\cos\theta \tag{450}$$

For a piston, we solve the integrals

$$I_{zx}^{M} = \int\limits_0^1 \cos\left(\frac{m\pi x(t)}{l_x}\right)\cos\left(\frac{q\pi z(t)}{l_z}\right) dt \tag{451}$$

$$I_{zx}^{M} = \int\limits_0^1 \cos\left(\frac{m\pi\left(x_c - (\frac{1}{2}+t)a\cos\theta\right)}{l_x}\right)\cos\left(\frac{q\pi\left(z_c + \left(\frac{1}{2}-t\right)a\cos\theta\right)}{l_z}\right) adt \tag{452}$$

to give

$$\begin{aligned} I_{zx}^{M} = {} & \frac{2l_x l_z}{\pi\left(l_z m\cos\theta - l_x q\sin\theta\right)\left(l_z m\cos\theta + l_x q\sin\theta\right)}\times \\ & \left\{\cos\left(\frac{a\pi q\sin\theta}{2l_z}\right)\sin\left(\frac{a\pi m\cos\theta}{2l_x}\right)\left[l_z m\cos\theta\cos\left(\frac{m\pi x_c}{l_x}\right)\cos\left(\frac{q\pi z_c}{l_z}\right)\right.\right. \\ & \left. - l_x q\sin\theta\sin\left(\frac{m\pi x_c}{l_x}\right)\sin\left(\frac{q\pi z_c}{l_z}\right)\right] \\ & + \sin\left(\frac{a\pi q\sin\theta}{2l_z}\right)\cos\left(\frac{a\pi m\cos\theta}{2l_x}\right)\left[l_z m\cos\theta\sin\left(\frac{m\pi x_c}{l_x}\right)\sin\left(\frac{q\pi z_c}{l_z}\right)\right. \\ & \left.\left. - l_x q\sin\theta\cos\left(\frac{m\pi x_c}{l_x}\right)\cos\left(\frac{q\pi z_c}{l_z}\right)\right\}. \end{aligned} \tag{453}$$

For modes in the x-direction, the mode function will be

$$\psi_t = N_{n_x} \cos\left(m_x \pi t\right) \tag{454}$$

since it will go along the width of the horn, which is now parametrized as t. The resulting integral is

$$\begin{aligned} I_{zx}^{M} = \frac{a l_x l_z N_{m_x}}{4} \Bigg\{ (-1)^{m_x} \frac{1}{\pi} \Bigg(& \frac{1}{l_x l_z m_x + a l_z m \cos\theta - a l_x \sin\theta} \\ & - \frac{1}{l_x l_z m_x - a l_z m \cos\theta + a l_x \sin\theta} \Bigg) \sin\gamma_1 + \\ + \frac{2a}{\pi} \Bigg[& \frac{\left(l_z m \cos\theta - l_x q \sin\theta\right) \sin\gamma_2}{\left(l_x l_z m_x + a l_z m \cos\theta - a l_x \sin\theta\right)\left(l_x l_z m_x - a l_z m \cos\theta + a l_x \sin\theta\right)} + \\ & + \frac{\left(l_z m \cos\theta + l_x q \sin\theta\right)\left((-1)^{m_x} \sin\gamma_3 + \sin\gamma_4\right)}{\left(-l_x l_z m_x + a l_z m \cos\theta + a l_x \sin\theta\right)\left(l_x l_z m_x + a l_z m \cos\theta + a l_x \sin\theta\right)} \Bigg] \Bigg\} \end{aligned} \tag{455}$$

where

$$\gamma_1 = \frac{\pi\left(2 l_z m x_c + 2 l_x q z_c + a l_z m \cos\theta - a l_x q \sin\theta\right)}{2 l_x l_z} \tag{456}$$

$$\gamma_2 = \frac{\pi\left(2 l_z m x_c + 2 l_x q z_c - a l_z m \cos\theta + a l_x q \sin\theta\right)}{2 l_x l_z} \tag{457}$$

$$\gamma_3 = \frac{\pi\left(2 l_z m x_c - 2 l_x q z_c + a l_z m \cos\theta + a l_x q \sin\theta\right)}{2 l_x l_z} \tag{458}$$

$$\gamma_3 = \frac{\pi\left(-2 l_z m x_c + 2 l_x q z_c + a l_z m \cos\theta + a l_x q \sin\theta\right)}{2 l_x l_z}. \tag{459}$$

Some special cases:
$m = 0$, $q = 0$, $m_x = 0$:

$$I_{zx} = a_1 \tag{460}$$

$m = 0$, $q > 0$, $m_x = 0$:

$$I_{zx}^{M} = \frac{2 l_z \cos\left(\frac{q \pi z_c}{l_Z}\right) \sin\left(\frac{a \pi q \sin\theta}{2 l_z}\right)}{\pi q \sin\theta} \tag{461}$$

$m > 0$, $q = 0$, $m_x = 0$:

$$I_{zx}^{M} = \frac{2 l_x \cos\left(\frac{m \pi x_c}{l_x}\right) \sin\left(\frac{a \pi m \cos\theta}{2 l_x}\right)}{\pi m \cos\theta} \tag{462}$$

$m = 0$, $q = 0$, $m_x > 0$:

$$I_{zx} = 0 \tag{463}$$

$m = 0$, $q > 0$, $m_x > 0$:

$$I_{zx}^{M} = N_{m_x} a^2 l_z q \sin\theta \times \frac{\left(\sin\left(\frac{\pi q(2z_c + a\sin\theta)}{2l_z}\right) - (-1)^{m_x} \sin\left(\frac{\pi q(2z_c - a\sin\theta)}{2l_z}\right)\right)}{\pi\left(qa\sin\theta - m_x l_z\right)\left(qa\sin\theta + m_x l_z\right)} \tag{464}$$

$m > 0$, $q = 0$, $m_x > 0$:

$$I_{zx}^{M} = N_{m_x} a^2 l_x m \cos\theta \times \frac{\left(\sin\left(\frac{\pi m(2x_c - a\cos\theta)}{2l_x}\right) - (-1)^{m_x} \sin\left(\frac{\pi m(2x_c + a\cos\theta)}{2l_x}\right)\right)}{\pi\left(m_x l_x - am\cos\theta\right)\left(m_x l_x + am\cos\theta\right)} \tag{465}$$

E.3 angled dipole source

For an angled dipole source, there will be a dipole moment in two directions (denoting the dipole moment by D):

$$\Delta z = D\cos\theta \tag{466}$$

$$\Delta x = D\sin\theta \tag{467}$$

so that the mode function (disregarding a modal source distribution) is

$$\psi_N(x_0, y_0, z_0) = D\sin\theta\left(\frac{m\pi}{l_x}\right)\sin\left(\frac{m\pi x_c}{l_x}\right)\cos\left(\frac{n\pi y_c}{l_y}\right)\cos\left(\frac{q\pi z_c}{l_z}\right) + D\cos\theta\left(\frac{q\pi}{l_z}\right)\cos\left(\frac{m\pi x_c}{l_x}\right)\cos\left(\frac{n\pi y_c}{l_y}\right)\sin\left(\frac{q\pi z_c}{l_z}\right). \tag{468}$$

The integral to be solved is now

$$I_{zx}^{D} = \int_0^1 \left\{D\sin\theta\left(\frac{m\pi}{l_x}\right)\sin\left(\frac{m\pi x_c}{l_x}\right)\cos\left(\frac{n\pi y_c}{l_y}\right)\cos\left(\frac{q\pi z_c}{l_z}\right) + D\cos\theta\left(\frac{q\pi}{l_z}\right)\cos\left(\frac{m\pi x_c}{l_x}\right)\cos\left(\frac{n\pi y_c}{l_y}\right)\sin\left(\frac{q\pi z_c}{l_z}\right)\right\} a\,dt \tag{469}$$

which gives

$$I_{zx}^{D} = \frac{2D\left[\cos\left(\frac{a\pi q\sin\theta}{2l_z}\right)\sin\left(\frac{a\pi m\cos\theta}{2l_x}\right)F_1 - \sin\left(\frac{a\pi q\sin\theta}{2l_z}\right)\cos\left(\frac{a\pi m\cos\theta}{2l_x}\right)F_2\right]}{\left(l_z m\cos\theta - l_x q\sin\theta\right)\left(l_z m\cos\theta + l_x q\sin\theta\right)} \tag{470}$$

where

$$F_1 = \left(l_z^2 m^2 + l_x^2 q^2\right)\cos\theta\sin\theta\cos\left(\frac{q\pi z_c}{l_z}\right)\sin\left(\frac{m\pi x_c}{l_x}\right) + l_x l_z m q\cos\left(\frac{m\pi x_c}{l_x}\right)\sin\left(\frac{q\pi z_c}{l_z}\right) \tag{471}$$

$$
\begin{aligned}
F_2 = \left(l_z^2 m^2 + l_x^2 q^2\right) \cos\theta \sin\theta \cos\left(\frac{m\pi x_c}{l_x}\right) \sin\left(\frac{q\pi z_c}{l_z}\right) \\
+ l_x l_z m q \cos\left(\frac{q\pi z_c}{l_z}\right) \sin\left(\frac{m\pi x_c}{l_x}\right)
\end{aligned}
\tag{472}
$$

Special cases:
$m = 0$, $q = 0$, $m_x = 0$:

$$I_{zx} = 0 \tag{473}$$

$m = 0$, $q > 0$, $m_x = 0$:

$$I_{zx}^D = 2D \cot\theta \sin\left(\frac{q\pi z_c}{l_Z}\right) \sin\left(\frac{a\pi q \sin\theta}{2l_z}\right) \tag{474}$$

$m > 0$, $q = 0$, $m_x = 0$:

$$I_{zx}^D = 2D \tan\theta \sin\left(\frac{m\pi x_c}{l_x}\right) \sin\left(\frac{a\pi m \cos\theta}{2l_x}\right) \tag{475}$$

In the case of multimodal excitation,

$$
\begin{aligned}
I_{zx}^D = \\
N_{m_x} \int_0^1 \Bigg\{ D \sin\theta \left(\frac{m\pi}{l_x}\right) \sin\left(\frac{m\pi x_c}{l_x}\right) \cos\left(\frac{n\pi y_c}{l_y}\right) \cos\left(\frac{q\pi z_c}{l_z}\right) \\
+ D \cos\theta \left(\frac{q\pi}{l_z}\right) \cos\left(\frac{m\pi x_c}{l_x}\right) \cos\left(\frac{n\pi y_c}{l_y}\right) \sin\left(\frac{q\pi z_c}{l_z}\right) \Bigg\} \\
\times \cos\left(m_x \pi t\right) a dt
\end{aligned}
\tag{476}
$$

which gives

$$
\begin{aligned}
I_{zx}^D = \frac{a^2 D N_{m_x}}{2} \Big\{ \left((-1)^{m_x} \cos\gamma_1 - \cos\gamma_2 \right) \\
\times \frac{\left(l_z m \cot\theta - l_x q\right) \left(l_z m + l_x q \cot\theta\right)}{-a^2 \left(l_x q - l_z m \cot\theta\right)^2 + l_x^2 l_z^2 m_x^2 \csc^2\theta} + \\
+ \frac{1}{-a^2 \left(l_x q + l_z m \cot\theta\right)^2 + l_x^2 l_z^2 m_x^2 \csc^2\theta} \\
\times \Big[(-1)^{m_x} \cos\gamma_3 \left(l_x q + l_z m \cot\theta\right) \left(l_z m - l_x q \cot\theta\right) \\
+ \cos\gamma_4 \left(l_x q + l_z m \cot\theta\right) \left(l_x q \cot\theta - l_z m\right) \Big] \Big\}
\end{aligned}
\tag{477}
$$

where

$$\gamma_1 = \frac{\pi \left(2 l_z m x_c + 2 l_x q z_c + a l_z m \cos\theta - a l_x q \sin\theta\right)}{2 l_x l_z} \tag{478}$$

$$\gamma_2 = \frac{\pi \left(2 l_z m x_c + 2 l_x q z_c - a l_z m \cos\theta + a l_x q \sin\theta\right)}{2 l_x l_z} \tag{479}$$

$$\gamma_3 = \frac{\pi\left(2l_z m x_c - 2l_x q z_c + a l_z m\cos\theta + a l_x q\sin\theta\right)}{2l_x l_z} \tag{480}$$

$$\gamma_3 = \frac{\pi\left(-2l_z m x_c + 2l_x q z_c + a l_z m\cos\theta + a l_x q\sin\theta\right)}{2l_x l_z} \tag{481}$$

Special cases:
$m = 0$, $q = 0$, $m_x > 0$:

$$I_{zx} = 0 \tag{482}$$

$m = 0$, $q > 0$, $m_x > 0$:

$$\begin{aligned} I_{zx}^D &= N_{m_x} a^2 D q^2 \sin 2\theta \\ &\times \frac{\left(\cos\left(\frac{\pi q(2z_c + a\sin\theta)}{2l_z}\right) - (-1)^{m_x}\cos\left(\frac{\pi q(2z_c - a\sin\theta)}{2l_z}\right)\right)}{2\left(m_x l_z - qa\sin\theta\right)\left(m_x l_z - qa\sin\theta\right)} \end{aligned} \tag{483}$$

$m > 0$, $q = 0$, $m_x > 0$:

$$\begin{aligned} I_{zx}^D &= N_{m_x} a^2 D m^2 \sin 2\theta \\ &\frac{\left(\cos\left(\frac{\pi m(2x_c - a\cos\theta)}{2l_x}\right) - (-1)^{m_x}\sin\left(\frac{\pi m(2x_c + a\cos\theta)}{2l_x}\right)\right)}{2\left(am\cos\theta - m_x l_x\right)\left(am\cos\theta + m_x l_x\right)} \end{aligned} \tag{484}$$

E.4 RADIATION IMPEDANCE, ANGLED SOURCE

Again, we have that the radiation impedance is given as

$$\begin{aligned} Z_m = -\frac{j\omega\rho c^2}{V}\sum_N \Omega_N \int_{x_1}^{x_2}\int_{y_1}^{y_2} \psi_N(x_0, y_0, z_0)\,dx_0 dy_0 \\ \times \int_{x_1}^{x_2}\int_{y_1}^{y_2} \psi_N(x, y, z_0)\,dx dy \end{aligned} \tag{485}$$

which gives for a straight monopole source

$$\begin{aligned} Z_m = -\frac{j\omega\rho c^2}{V}\sum_N \Omega_N \cos^2\left(\frac{q\pi z_0}{l_z}\right) \\ \times \Upsilon_{m_x}^m(a, x_0, l_x)\Upsilon_{m_y}^n(b, y_0, l_y)\Upsilon_{n_x}^m(a, x_0, l_x)\Upsilon_{n_y}^n(b, y_0, l_y), \end{aligned} \tag{486}$$

and for a straight dipole source:

$$\begin{aligned} Z_m = -\frac{j\omega\rho c^2}{V}\sum_N \Omega_N \Delta z k_z \sin\left(\frac{q\pi z_0}{l_z}\right)\cos\left(\frac{q\pi z_0}{l_z}\right) \\ \times \Upsilon_{m_x}^m(a, x_0, l_x)\Upsilon_{m_y}^n(b, y_0, l_y)\Upsilon_{n_x}^m(a, x_0, l_x)\Upsilon_{n_y}^n(b, y_0, l_y). \end{aligned} \tag{487}$$

An angled monopole gives

$$Z_m = -\frac{j\omega\rho c^2}{V} \sum_N \Omega_N \left(I_{zx}^{M}(m, q, m_x, l_x, l_z, x_0, z_0) \right)^2 \times \Upsilon_{m_y}^{n}(b, y_0, l_y) \Upsilon_{n_y}^{n}(b, y_0, l_y), \quad (488)$$

and and angled dipole

$$Z_m = -\frac{j\omega\rho c^2}{V} \sum_N \Omega_N \left(I_{zx}^{D}(D, m, q, m_x, l_x, l_z, x_0, z_0) \right)^2 \times \Upsilon_{m_y}^{n}(b, y_0, l_y) \Upsilon_{n_y}^{n}(b, y_0, l_y). \quad (489)$$

BIBLIOGRAPHY

[1] Wente, E. C. and Thuras, A. L., "Symposium on wire transmission of symphonic music and its reproduction in auditory perspective: Loudspeakers and microphones," *Bell System Technical Journal*, vol. 13, pp. 259–277, Apr 1934, reprinted in J. Audio Eng. Soc., vol. 26, no. 7/8, Jul/Aug 1977 (Cited on pages 3 and 28.)

[2] Keele, D. B., "What's so sacred about exponential horns," *51st Convention of the Audio Engineering Society*, May 1975, preprint no. 1038 (Cited on pages 3 and 36.)

[3] Henricksen, C. A. and Ureda, M. S., "The Manta-Ray Horns," *J. Audio Eng. Soc.*, vol. 26, no. 9, pp. 629–634, Sep 1978 (Cited on pages 3, 4, 36, and 267.)

[4] Hudde, H. and Letens, U., "Scattering matrix of a discontinuity with a nonrigid wall in a lossless circular duct," *J. Acoust. Soc. Am.*, vol. 78, no. 5, pp. 1826–1837, Nov 1985 (Cited on pages 4 and 66.)

[5] Geddes, E. R., "Acoustic waveguide theory," *J. Audio Eng. Soc.*, vol. 37, no. 7/8, pp. 554–569, Jul/Aug 1989 (Cited on pages 4, 35, 40, 45, and 46.)

[6] Schmitt, R., "Causes of nonlinear compression driver distortions and their audibility," *99th Convention of the Audio Engineering Society*, Oct 1995, preprint no. 4131 (Cited on page 4.)

[7] Makarski, M., "Tools for the professional development of horn loudspeakers," Ph.D. dissertation, Rheinisch-Westfärlischen Technischen Hochschule Aachen, 2006 (Cited on pages 4, 8, and 37.)

[8] Morgans, R. C., "Optimisation techniques for horn loaded loudspeakers," Ph.D. dissertation, University of Adelaide, 2004 (Cited on pages 4, 37, 60, 61, and 67.)

[9] Rasetshwane, D. M., Neele, S. T., Allen, J. B., and Shera, C. A., "Reflectance of acoustic horns and solution of the inverse problem," *J. Acoust. Soc. Am.*, vol. 131, no. 3, pp. 1863–1873, Mar 2012 (Cited on page 5.)

[10] Ware, J. A. and Aki, K., "Continuous and discrete inverse-scattering problems in a stratified elastic medium i plane waves at normal incidence," *J. Acoust. Soc. Am.*, vol. 45, no. 4, pp. 911–921, 1969 (Cited on page 5.)

[11] Kemp, J. A., Campbell, D. M., and Amir, N., "Multimodal radiation impedance of a rectangular duct terminated in an infinite baffle," *Acta Acustica united with Acustica*, vol. 87, no. 1, pp. 11–15, Jan/Feb 2001 (Cited on pages 5, 116, and 117.)

[12] Kausel, W., "Bore reconstruction of tubular ducts from its acoustic input impedance curve," *Instrumentation and Measurement, IEEE Transactions on*, vol. 53, no. 4, pp. 1097–1105, 2004 (Cited on page 5.)

[13] Kausel, W., "Computer optimization of brass wind instruments," *Diderot Forum on Mathematics and Music*, 1999, ISBN 3-85403-133-5 (Cited on page 5.)

[14] Kausel, W., "Optimization of brass wind instruments and its application in bore reconstruction," *Journal of New Music Research*, vol. 30, no. 1, pp. 69–82, 2001 (Cited on page 5.)

[15] Scavone, G. P., "Modeling wind instrument sound radiation using digital waveguides," in *Proc. of the ICMC (1999)*. Citeseer, 1999, pp. 355–358 (Cited on pages 5 and 49.)

[16] Nederveen, C. J., *Acoustical aspects of woodwind instruments*. Fritz Knuf, Amsterdam, 1969 (Cited on page 5.)

[17] Keefe, D. H. and Benade, A. H., "Wave propagation in strongly curved ducts," *J. Acoust. Soc. Am.*, vol. 74, no. 1, pp. 320–332, Jul 1983 (Cited on page 5.)

[18] Ting, L. and Miksis, M. J., "Wave propagation through a slender curved tube," *J. Acoust. Soc. Am.*, vol. 74, no. 2, pp. 631–639, Aug 1983 (Cited on page 5.)

[19] Félix, S. and Pagneux, V., "Sound propagation in rigid bends: A multimodal approach," *J. Acoust. Soc. Am.*, vol. 110, no. 3, pp. 1329–1337, Sep 2001 (Cited on pages 5 and 65.)

[20] Félix, S. and Pagneux, V., "Multimodal analysis of acoustic propagation in three-dimensional bends," *Wave Motion*, vol. 36, pp. 157–168, 2002 (Cited on pages 5 and 65.)

[21] Félix, S., Dalmont, J.-P., and Nederveen, C. J., "Effects of bending portions of the air column on the acoustical resonances of a wind instrument," *J. Acoust. Soc. Am.*, vol. 131, pp. 4164–4172, 2012 (Cited on pages 5 and 65.)

[22] Braden, A. C. P., "Bore optimisation and impedance modelling of brass musical instruments," Ph.D. dissertation, University of Edinburgh, 2006 (Cited on pages 5, 65, 73, 75, 225, and 235.)

[23] Stewart, G. W., "Acoustic wave filters," *Phys. Rev.*, vol. 20, no. 6, pp. 528–551, 1922 (Cited on page 5.)

[24] Stewart, G. W., "A variable single band acoustic wave filter," *Phys. Rev.*, vol. 22, pp. 502–505, 1923 (Cited on page 5.)

[25] Stewart, G. W., "Acoustic wave filters," *Phys. Rev.*, vol. 23, pp. 520–524, 1924 (Cited on page 5.)

[26] Stewart, G. W., "Influence of a branch line upon acoustic transmission of a conduit," *Phys. Rev.*, vol. 26, pp. 668–690, 1925 (Cited on page 5.)

[27] Stewart, G. W., "Acoustic wave filters," *Phys. Rev.*, vol. 25, pp. 90–98, 1925 (Cited on page 5.)

[28] Mason, W. P., "Approximate networks of acoustic filters," *J. Acoust. Soc. Am.*, vol. 2, pp. 263–272, Jan 1930 (Cited on page 5.)

[29] Mason, W. P., *Electromechanical Transducers and Wave Filters*. D. Van Nostrand Co., New York, 1942 (Cited on page 5.)

[30] Yeow, K. W., "Webster's wave equation in two dimensions," *J. Acoust. Soc. Am.*, vol. 56, no. 1, pp. 19–21, Jul 1974 (Cited on pages 6 and 35.)

[31] Demir, A. and Rienstra, S., "Sound radiation from an annular duct with jet flow and a lined centerbody," *AIAA paper*, vol. 2718, 2006 (Cited on page 6.)

[32] Rienstra, S., "Sound transmission in slowly varying circular and annular lined ducts with flow," *Journal of Fluid Mechanics*, vol. 380, pp. 279–296, 1999 (Cited on page 6.)

[33] Geddes, E. and Lee, L., *Audio Transducers*. GedLee LLC, Novi, MI, 2002, ISBN 0-9722085-0-X (Cited on pages 6, 45, 46, 66, 98, 99, 102, 178, 227, and 267.)

[34] Rayleigh, J. W. S., "On the propagation of sound in narrow tubes of variable section," *Phil. Mag.*, vol. 31, pp. 89–96, 1916 (Cited on pages 6 and 19.)

[35] Webster, A. G., "Acoustical impedance and the theory of horns and of the phonograph," *Proc. Nat. Ac. Sci.*, vol. 5, no. 7, pp. 275–282, Jul 1919 (Cited on pages 6 and 19.)

[36] Alfredson, R. J., "The propagation of sound in a circular duct of continuously varying cross-sectional area," *J. Sound Vibr.*, vol. 23, no. 4, pp. 433–442, 1972 (Cited on pages 7 and 64.)

[37] Roure, A., "Propagation guidée, étude des discontinuités," Ph.D. dissertation, Universit'e Aix-Marseille, 1976 (Cited on pages 7, 65, and 71.)

[38] Kolbrek, B., "Modal sound propagation in curved horns of rectangular cross-section," Master's thesis, Norges Teknisk-Naturvitenskapelige Universitet (NTNU), Institutt for elektronikk og telekommunikasjon, Trondheim, Norway, 2013. [Online]. Available: http://ntnu.diva-portal.org/smash/record.jsf?pid=diva2:649777 (Cited on pages 7, 9, 130, 263, and 264.)

[39] Klipsch, P. W., "A low-frequency horn of small dimensions," *J. Acoust. Soc. Am.*, vol. 13, pp. 137–144, Oct 1941 (Cited on pages 7 and 36.)

[40] Waterhouse, R. V., "Output of a sound source in a reverberation chamber and other reflecting environments," *The Journal of the Acoustical Society of America*, vol. 30, no. 1, pp. 4–13, Jan 1958 (Cited on pages 7 and 164.)

[41] Behler, G. K. and Makarski, M., "Two-port representation of the connection between horn driver and horn," *J. Audio Eng. Soc.*, vol. 51, no. 10, pp. 883–897, Oct 2003 (Cited on page 8.)

[42] Klippel, W., "Nonlinear system models for horn loudspeakers," *99th Convention of the Audio Engineering Society*, Oct 1995, preprint no. 4083 (Cited on pages 8 and 37.)

[43] Keith Robert Holland, r., "A study of the physical properties of mid-range loudspeaker horns and their relationship to perceived sound quality," Ph.D. dissertation, University of Southampton, 1992 (Cited on page 8.)

[44] Evensen, K. B., "Høyttalersimulering med mode-basert metode (in Norwegian)," Master's thesis, Norges Teknisk-Naturvitenskapelige Universitet (NTNU), Institutt for fysikk, Trondheim, Norway, 2014 (Cited on pages 9, 71, 84, and 228.)

[45] Kolbrek, B. and Svensson, U. P., "Using mode matching methods and edge diffraction in horn loudspeaker simulation," *Acta Acustica united with Acustica*, vol. 101, no. 4, pp. 760–774, Jul/Aug 2015 (Cited on pages 9, 10, 71, 106, 131, and 191.)

[46] Snakowska, A., *Analiza pola akustycznego falowodu cylindrycznego z uwzględnieniem zjawisk dyfrakcyjnych na wylocie (Analysis of the acoustic field of a cylindrical duct considering diffraction at the open end, in Polish)*. Rzeszów, 2007 (Cited on pages 9, 132, 141, 277, and 278.)

[47] Snakowska, A., "The acoustic far field of an arbitrary Bessel mode radiating from a semi-infinite unflanged cylindrical waveguide," *Acoustica*, vol. 77, pp. 53–62, 1992 (Cited on pages 9, 139, 284, and 285.)

[48] Snakowska, A., Jurkiewicz, J., and Gorazd, L., "Single mode directivity characteristics of the multimode sound wave radiated from unflanged cylindrical duct – theory and experiment," *62nd Polish Open Seminar on Acoustics,*, 2015 (Cited on pages 9, 134, and 284.)

[49] Svensson, U. P., Fred, R. I., and Vanderkooy, J., "An analytic secondary source model of edge diffraction impulse responses," *J. Acoust. Soc. Am.*, vol. 106, no. 5, pp. 2331–2344, Nov 1999 (Cited on pages 9, 80, 131, 143, and 144.)

[50] Svensson, U. P., Calamia, P., and Nakanishi, S., "Frequency-domain edge diffraction for finite and infinite edges," *Acta Acustica united with Acustica*, vol. 95, pp. 568–572, 2009 (Cited on pages 9 and 143.)

[51] Kolbrek, B., "Horns near reflecting boundaries," *139th Convention of the Audio Engineering Society*, Oct/Nov 2015, preprint no. 9412 (Cited on pages 10, 161, 191, and 207.)

[52] Sjösten, P., Svensson, U. P., Evensen, K. B., and Kolbrek, B., "The effect of Helmholtz resonators on the acoustic room response," *Baltic-Nordic Acoustic Meeting*, Jun 2016 (Cited on pages 10 and 177.)

[53] Kolbrek, B., "Modal impedances and the boundary element method: An application to horns and ducts," *139th Convention of the Audio Engineering Society*, Oct 2015, preprint no. 9369 (Cited on pages 10 and 215.)

[54] Kolbrek, B., Evensen, K. B., and Svensson, U. P., "Simulating axisymmetric concave radiators using mode matching methods," *J. Audio Eng. Soc.*, vol. 64, no. 5, pp. 311–319, May 2016 (Cited on pages 11 and 227.)

[55] Ando, Y. and Koizumi, T., "Sound radiation from a semi-infinite circular pipe having an arbitrary profile of orifice," *J. Acoust. Soc. Am.*, vol. 59, no. 5, pp. 1033–1039, May 1976 (Cited on pages 11, 66, 227, and 264.)

[56] Oie, S., Takeuchi, R., and Shindo, T., "Sound radiation from concave radiator in an infinite baffle," *Acustica*, vol. 46, no. 3, pp. 268–275, Nov 1980 (Cited on pages 11, 66, 227, and 264.)

[57] Kolbrek, B. and Svensson, U. P., "Modeling non-shoebox shaped rooms with the mode matching method," *140th Convention of the Audio Engineering Society*, Jun 2016, preprint no. 9506 (Cited on pages 11 and 249.)

[58] Miller, D. C., *Anectotal History of the Science of Sound*. The Macmillan Company, New York, 1935 (Cited on pages 13 and 14.)

[59] Hunt, F. V., *Origins in Acoustics*. Yale University Press, 1978 (Cited on page 13.)

[60] Eisner, E., "Complete solutions of the Webster horn equation," *J. Acoust. Soc. Am.*, vol. 41, no. 4 (2), pp. 1126–1146, 1966 (Cited on pages 16 and 42.)

[61] Barton, E. H., "On spherical radiation and vibrations in conical pipes," *Phil. Mag., series 5*, vol. 15, no. 85, pp. 69–81, 1908 (Cited on page 16.)

[62] Hunt, F. V., *Electroacoustics*. Harvard University Press,, 1954 (Cited on pages 17 and 27.)

[63] Fagen, M. D., Ed., *A History of Engineering and Science in the Bell System — The Early Years (1875–1925)*. Bell Telephone Laboratories, Inc., 1975 (Cited on page 17.)

[64] Pursell, C. W., Ed., *Technology in America - A History of Individuals and Ideas*. The MIT Press, 1990 (Cited on page 17.)

[65] Siemens, E. W., "Magneto-electric apparatus," US Patent 149 797, filed Jan. 20, 1874, issued Apr. 14, 1874 (Cited on page 17.)

[66] Keller, A. C., "Sound recording and reproducing," AT&T Archives, Box 84 10 03 (Cited on page 19.)

[67] Hochheiser, S., "What makes the picture talk: AT&T and the development of sound motion picture technology," *IEEE Transactions on Education*, vol. 35, no. 4, pp. 278–285, Nov 1992 (Cited on page 19.)

[68] Kennelly, A. and Pierce, G., "The impedance of telephone receivers as affected by the motion of their diaphragms," *Proc. Am. Ac. Arts Sci.*, vol. 48, pp. 113–151, Sep 1912 (Cited on page 20.)

[69] Franklin, W. S., "Some mechanical analogies in electricity and magnetism," *General Electric Review*, vol. 19, no. 4, pp. 264–269, April 1916 (Cited on page 20.)

[70] Stewart, G. W., "The performance of conical horns," *Phil. Mag.*, vol. 16, no. 4, pp. 313–326, 1920 (Cited on pages 20 and 22.)

[71] Hanna, C. R. and Slepian, J., "The function and design of horns for loud speakers (and discussion)," *Trans. Am. Inst. Elec. Eng.*, vol. 43, pp. 393–411, Feb 1924 (Cited on page 20.)

[72] Harrison, H. C., "Improvements in acoustic horns," GB Patent 213 528, filed Oct. 32, 1923, issued Feb. 2, 1925 (Cited on page 21.)

[73] Flanders, P. B., "Improvements in acoustic horns," GB Patent 245 415, filed Sept. 24, 1925, issued Dec. 24, 1926 (Cited on pages 21, 35, and 271.)

[74] "Contributors to this issue: H. C. Harrison," *Bell Laboratories Record*, vol. 10, no. 11, p. 403, Jul 1932 (Cited on page 21.)

[75] Flanders, P. B. and Quarles, D. A., "MM-913 Horn theory - case 32184," Memorandum, March 13 1924 (Cited on page 21.)

[76] Flanders, P. B. and Quarles, D. A., "MM-949 Horn theory - case 32184," Memorandum, April 23 1924 (Cited on page 21.)

[77] Crandall, I. B., *Theory of Vibrating Systems and Sound*. D. Van Nostrand Co., New York, 1926 (Cited on page 21.)

[78] Goldsmith, A. N. and Minton, J. P., "The performance and theory of loudspeaker horns," *Proc. Inst. Rad. Eng.*, vol. 12, pp. 423–478, Aug 1924 (Cited on page 22.)

[79] Hoersch, V. A., "Non-radial vibrations within a conical horn," *Phys. Rev.*, vol. 25, pp. 218–224, 1925 (Cited on pages 22, 44, and 64.)

[80] Hoersch, V. A., "Theory of the optimum angle in a receiving conical horn," *Phys. Rev.*, vol. 25, pp. 225–229, 1925 (Cited on page 22.)

[81] Stewart, G. W., "Comments on Hoersh's theory of the optimum angle of a receiving conical horn," *Phys. Rev.*, vol. 25, pp. 230–231, 1925 (Cited on page 22.)

[82] Williams, S., "Recent developments in the recording and reproduction of sound," *Journal of the Franklin Institute*, vol. 202, no. 4, pp. 413 – 448, 1926. [Online]. Available: http://www.sciencedirect.com/science/article/pii/S0016003226906534 (Cited on page 22.)

[83] Wilson, P. and Wilson, G. L., "Horn theory and the phonograph," *J. Audio Eng. Soc.*, vol. 23, no. 3, pp. 194–199, Apr 1975 (Cited on page 23.)

[84] Wilson, P., *The Gramophone Jubilee Book*, 1975, ch. Reproducing the Record, pp. 24–36 (Cited on page 23.)

[85] Wilson, P. and Webb, G. W., *Modern Gramophones and Electrical Reproducers*. Cassell and Co., London, 1929 (Cited on page 23.)

[86] Voigt, P. G. A. H., "Improvements in or relating to sound reproducers," GB Patent 238 310A, filed May 20, 1924, issued Aug 20, 1925 (Cited on page 23.)

[87] Edgar, B. C., "An interview with Paul Voigt, part 1," *Speaker Builder*, no. 3, pp. 12–16, 1981 (Cited on page 23.)

[88] Rice, C. W., , and Kellogg, E. W., "Notes on the development of a new type of hornless loudspeaker," *J. Am. Inst. Elec. Eng.*, vol. 44, pp. 982–991, 1925 (Cited on pages 23 and 29.)

[89] Voigt, P. G. A. H., "Improvements in horns for acoustic instruments," GB Patent 278 098, filed Oct. 5, 1926, issued Jul. 5, 1927 (Cited on pages 23 and 138.)

[90] Ballantine, S., "On the propagation of sound in the general Bessel horn of infinte length," *J. Frankl. Inst.*, vol. 203, pp. 85–103, Jan 1927 (Cited on pages 23 and 42.)

[91] Hanna, C. R., "On the propagation of sound in the general Bessel horn of infinte length," *J. Frankl. Inst.*, vol. 203, pp. 849–853, Jun 1927 (Cited on page 24.)

[92] Norton, E. L., "Sound reproducer," US Patent 1 792 655, filed May 31, 1929, issued Feb. 17, 1931 (Cited on page 24.)

[93] Salmon, V., "A new family of horns," *J. Acoust. Soc. Am.*, vol. 17, no. 3, pp. 212–218, Jan 1946 (Cited on pages 24, 33, 42, and 291.)

[94] Stewart, G. W. and Lindsay, R. B., *Acoustics*. D. Van Nostrand Co., New York, 1930 (Cited on page 24.)

[95] Stenzel, H., "Über die Theorie und Anwendung des Hornlautsprechers," *Zeitschr. f. techn. Physik*, no. 12, pp. 621–627, 1931 (Cited on page 25.)

[96] Fischer, F. and Lichte, H., Eds., *Tonfilm: Aufnahme und Wiedergabe nach dem Klangfilm-Verfahren (System Klangfilm -Tobis)*. Hirzel, 1931 (Cited on page 25.)

[97] Hall, W. M., "An investigation of sound fields in regions restricted by finite boundaries," Master's thesis, Mass. Inst. Tech., 1928 (Cited on page 25.)

[98] Hall, W. M., "Comments on the theory of horns," *J. Acoust. Soc. Am.*, vol. 3, pp. 552–561, 1932 (Cited on pages 25 and 41.)

[99] Olson, H. F., "Horn loud speakers part II," *RCA Review*, pp. 263–277, 1937 (Cited on pages 25 and 31.)

[100] Goldman, S., "Supersonic measurements of the directional characteristics of horns," *J. Acoust. Soc. Am.*, vol. 5, no. 1, pp. 181–195, Jan 1934 (Cited on page 25.)

[101] Sato, K., "On the sound field due to a conical horn with a source at the vertex," *Japanese Journal of Physics*, vol. 5, no. 3, pp. 103–109, 1929 (Cited on pages 25 and 44.)

[102] Sato, K., "On the acoustical properties of conical horns (pt 2): On the sound field due to a conical horn with a source at its vertex (in japanese)," *Report of the Aeronautical Research Institute, Tokyo Imperial University*, vol. 5, no. 64, pp. 261–285, Nov 1930 (Cited on pages 25 and 44.)

[103] Wolff, I. and Malter, L., "Directional radiation of sound," *J. Acoust. Soc. Am.*, vol. 2, no. 2, pp. 201–233, Oct 1930 (Cited on page 25.)

[104] McLachlan, N. W., *Loud Speakers*. Oxford, 1934 (Cited on pages 25 and 41.)

[105] Thuras, A. L., Jenkins, R. T., and O'Neil, H. T., "Extraneous frequencies generated in air carrying intense sound waves," *Bell System Technical Journal*, vol. 14, pp. 159–172, Jan 1935, also published in JASA, vol. 6, pp. 173-180. (Cited on pages 25 and 37.)

[106] Goldstein, S. and McLachlan, N. W., "Sound waves of finite amplitude in an exponential horn," *J. Acoust. Soc. Am.*, vol. 6, pp. 275–278, Apr 1935 (Cited on pages 25 and 37.)

[107] McLachlan, N. W., *Bessel Functions for Engineers*. Oxford, 1935 (Cited on page 25.)

[108] McLachlan, N. W. and McKay, A. T., "Transient oscillations in a loudspeaker horn," *Proceedings of the Cambridge Philosophical Society, Mathematical and Physical Sciences*, vol. 32, pp. 265–275, 1936 (Cited on page 25.)

[109] Freehafer, J. E., "The velocity potential of an hyperbolic horn," Ph.D. dissertation, Mass. Inst. Tech., 1937 (Cited on pages 26, 42, and 46.)

[110] Freehafer, J. E., "The acoustical impedance of an infinite hyperbolic horn," *J. Acoust. Soc. Am.*, vol. 11, pp. 467–476, Apr 1940 (Cited on pages 26, 42, and 46.)

[111] Finehout, R., "Pioneering the talkies," *American Cinematographer*, pp. 36–40, Jan 1998 (Cited on page 26.)

[112] Maxfield, J. P. and Harrison, H. C., "Methods of high quality recoding and reproduction of music and speech based on telephone research," *Bell System Technical Journal*, vol. 5, pp. 493–523, Jul 1926 (Cited on page 26.)

[113] Hochheiser, S., "AT&T and the developement of sound motion-picture technology," pp. 23–33, 1989 (Cited on page 27.)

[114] Watkins, S., "Madam, will you talk," *Bell Laboratories Record*, vol. 24, no. 8, pp. 289–295, Aug 1946 (Cited on page 27.)

[115] Wilcox, H., "Development and use of the sound motion picture, part i," *International Projectionist*, vol. 3, no. 3, pp. 16, 30–33, Sept 1932 (Cited on page 28.)

[116] Kolbrek, B., "Development of horn loudspeakers before 1940," in *Proceedings of Forum Acusticum 2014*, 2014 (Cited on page 28.)

[117] McGinn, R. E., "Stokowski and Bell Telephone Laboratories," *Technology and Culture*, vol. 24, pp. 38–75, Jan 1983 (Cited on page 28.)

[118] Hilliard, J. K., "A study of theatre loud speakers and the resultant development of the shearer two-way horn system," *J. Soc. Mot. Pic. Eng.*, vol. 27, no. 1, pp. 45–60, Jul 1936 (Cited on page 29.)

[119] Wolff, I., May, P., and Ringel, A., "Auditorium loud speaker," US Patent 1 866 831, filed Aug. 3, 1928, issued Jul. 12, 1932 (Cited on page 29.)

[120] Kellogg, E. W., "History of sound motion pictures (part 1)," *J. Soc. Mot. Pic. Telev. Eng.*, vol. 64, pp. 291–302, Jun 1955 (Cited on page 29.)

[121] "Frank Massa – 1906–1990," *J. Acoust. Soc. Am.*, vol. 92, no. 4, p. 2265, Oct. 1992 (Cited on page 30.)

[122] Olson, H. F., "A new high-efficiency theatre loudspeaker of the directional baffle type," *J. Acoust. Soc. Am.*, vol. 2, pp. 485–498, Apr 1931 (Cited on pages 29 and 30.)

[123] Olson, H. F., "Recent developments in theater loudspeakers of the directional baffle type," *J. Soc. Mot. Pic. Eng.*, vol. 18, no. 5, pp. 571–583, May 1932 (Cited on page 29.)

[124] Olson, H. F. and Massa, F., *Applied Acoustics*. P. Blakiston's son & co., inc., Philadelphia, 1934. [Online]. Available: https://babel.hathitrust.org/cgi/pt?id=wu.89050884915;view=2up;seq=8 (Cited on page 30.)

[125] Olson, H. F. and Massa, F., "A high efficiency wide range horn loudspeaker mechanism," RCA Victor Co., Inc., Tech. Rep. TR223, Dec. 6 1933, in: Box 131, RCA Corporation records (Accession 2069), Hagley Museum and Library, Wilmington, DE 19807 (Cited on page 30.)

[126] Olson, H. F. and Massa, F., "Low frequency loud speaker," RCA Victor Co., Inc., Tech. Rep. TR-237, Jul. 18 1934, in: Box 132,

RCA Corporation records (Accession 2069), Hagley Museum and Library, Wilmington, DE 19807 (Cited on page 30.)

[127] Olson, H. F. and Massa, F., "Compound horn loud speaker," RCA Victor Co., Inc., Tech. Rep. TR-256, Mar. 20 1935, in: Box 132, RCA Corporation records (Accession 2069), Hagley Museum and Library, Wilmington, DE 19807 (Cited on page 30.)

[128] Olson, H. F. and Massa, F., "A compound horn loudspeaker," *J. Acoust. Soc. Am.*, vol. 8, pp. 48–52, Jul 1936 (Cited on page 30.)

[129] Olson, H. F. and Massa, F., "Theatre loud speaker of the compound horn type," RCA Victor Co., Inc., Tech. Rep. TR-277, May 13 1935, in: Box 132, RCA Corporation records (Accession 2069), Hagley Museum and Library, Wilmington, DE 19807 (Cited on page 30.)

[130] Olson, H. F., "Engineer's note book 2158," Aug. 19 1934, in: Box 1111, Folder 1, Harry F. Olson papers (Accession 2464.32), Hagley Museum and Library, Wilmington, DE 19807 (Cited on pages 30, 32, and 33.)

[131] Olson, H. F. and Massa, F., "Compound horn loud speaker (double horn radio type)," RCA Victor Co., Inc., Tech. Rep. TR-265, Apr. 19 1935, in: Box 132, RCA Corporation records (Accession 2069), Hagley Museum and Library, Wilmington, DE 19807 (Cited on page 31.)

[132] Olson, H. F. and Hackley, R., "Combination horn and direct radiator loudspeaker - a complete description of the 64-A unit," *Broadcast News*, no. 27, pp. 8–9, 14–15, Dec. 1937 (Cited on page 31.)

[133] Olson, H. F. and Massa, F., "Theory of the finite conical horn," RCA Victor Co., Inc., Tech. Rep. TR-269, May 13 1935, in: Box 132, RCA Corporation records (Accession 2069), Hagley Museum and Library, Wilmington, DE 19807 (Cited on page 31.)

[134] Olson, H. F., "Characteristics of exponential horns," RCA Victor Co., Inc., Tech. Rep. TR-334, Sep. 14 1936, in: Box 133, RCA Corporation records (Accession 2069), Hagley Museum and Library, Wilmington, DE 19807 (Cited on page 31.)

[135] Olson, H. F., "Horn loud speakers part i," *RCA Review*, pp. 68–83, 1937 (Cited on pages 31 and 271.)

[136] Olson, H. F., "Personal communication with G. W. Stewart," 1937, in: Box 1113, Folder 14, Harry F. Olson papers (Accession 2464.32), Hagley Museum and Library, Wilmington, DE 19807 (Cited on page 33.)

[137] Olson, H. F., "A horn consisting of manifold exponential sections," RCA Victor Co., Inc., Tech. Rep. TR-360, Jun. 8 1937, in: Box 133, RCA Corporation records (Accession 2069), Hagley Museum and Library, Wilmington, DE 19807 (Cited on page 33.)

[138] Olson, H. F., "A horn consisting of manifold exponential sections," *J. Soc. Mot. Pic. Eng.*, vol. 30, no. 5, pp. 511–518, May 1938 (Cited on pages 33 and 62.)

[139] Graham, M. L., "New high powered sound projectors," *Broadcast News*, no. 27, pp. 4–5,19, Dec. 1937 (Cited on page 33.)

[140] Olson, H. F., *Elements of Acoustical Engineering*, 2nd ed. D. Van Nostrand Co., New York, 1947 (Cited on pages 33, 62, and 271.)

[141] Olson, H. F., *Elements of Acoustical Engineering*, 2nd ed. D. Van Nostrand Co., New York, 1957 (Cited on pages 33 and 271.)

[142] Salmon, V., "The sound field and radiation impedance of a hyperbolic horn," Ph.D. dissertation, Mass. Inst. Tech., 1938 (Cited on pages 33 and 42.)

[143] Salmon, V., "Generalized plane wave horn theory," *J. Acoust. Soc. Am.*, vol. 17, no. 3, pp. 199–211, Jan 1946 (Cited on pages 33 and 42.)

[144] Salmon, V., "Acoustic horn," US Patent 2 338 262, filed Jul. 23, 1942, issued Jan. 4, 1944 (Cited on pages 33 and 42.)

[145] Plach, D. J. and Williams, P. B., "Horn-loaded loudspeakers," *Proceedings of the National Electronics Conference*, vol. 7, pp. 108–114, 1951 (Cited on page 33.)

[146] Plach, D. J., "Design factors in horn-type speakers," *J. Audio Eng. Soc.*, vol. 1, no. 4, pp. 276–281, Oct 1953 (Cited on page 33.)

[147] Thuras, A. L., "Electrodynamic device," US Patent 1 707 544, filed Aug. 4, 1926, issued Apr. 2, 1929 (Cited on page 33.)

[148] "The biennial award given to dr. Vincent Salmon," *J. Acoust. Soc. Am.*, vol. 18, no. 1, pp. 217–218, Jul. 1946 (Cited on page 34.)

[149] Morse, P. M., *Vibration and Sound*, 2nd ed. McGraw-Hill, 1948 (Cited on pages 33, 35, 43, 98, and 99.)

[150] Beranek, L. L., *Acoustics*. McGraw-Hill, 1954 (Cited on pages 33 and 271.)

[151] Locanthi, B., "Application of electrical circuit analogies to loudspeaker design problems (reprint)," *J. Audio Eng. Soc.*, vol. 19, no. 9, pp. 778–785, Sep 1971, (Originally published 1952) (Cited on pages 34 and 48.)

[152] Leach, W. M., "On the specification of moving coil drivers for low-frequency horn-loaded loudspeakers," *J. Audio Eng. Soc.*, vol. 27, no. 12, pp. 950–959, Dec 1979 (Cited on pages 34 and 35.)

[153] Mawardi, O. K., "Generalized solutions of Webster's horn theory," *J. Acoust. Soc. Am.*, vol. 21, no. 4, pp. 323–330, Jul 1949 (Cited on pages 34 and 42.)

[154] Molloy, C. T., "Response peaks in finite horns," *J. Acoust. Soc. Am.*, vol. 22, no. 5, pp. 551–557, Sep 1950 (Cited on page 34.)

[155] Molloy, C. T., "Calculation of the directivity index for various types of radiators," *J. Acoust. Soc. Am.*, vol. 20, no. 4, pp. 387–405, Jul 1948 (Cited on page 34.)

[156] Lambert, R. F., "Acoustical study of the tractrix horn, part i," *J. Acoust. Soc. Am.*, vol. 26, pp. 1024–1028, Nov 1954 (Cited on pages 34 and 138.)

[157] Lambert, R. F., "Acoustical study of the tractrix horn, part II," *J. Acoust. Soc. Am.*, vol. 26, pp. 1029–1033, Nov 1954 (Cited on page 34.)

[158] Stevenson, A. F., "Exact and approximate wave equations for wave propagation in acoustic horns," *J. App. Phys.*, vol. 22, no. 12, pp. 1461–1463, Dec 1951 (Cited on pages 35, 44, and 64.)

[159] Holtsmark, J., Lothe, J., Tjøtta, S., and Romberg, W., "Theoretical investigation of sound transmission through horns of small flare, with special emphasis on the exponential horn," *Arch. Math. Naturvidenskap*, vol. 53, no. 8, pp. 139–181, 1955 (Cited on pages 35, 45, and 64.)

[160] Maezawa, S., "On the three-dimensional corrections for one-dimensional theory of acoustic horn," *Reports of the Faculty of Engineering, Yamanashi University*, pp. 69–79, 1957 (Cited on pages 35 and 45.)

[161] Keele, D. B., "Optimum horn mouth size," *46th Convention of the Audio Engineering Society*, Sep 1973, preprint no. 933 (Cited on pages 35, 271, and 272.)

[162] Kolbrek, B., "Horn theory: An introduction, part 1," *audioXpress*, March 2008 (Cited on page 35.)

[163] Keele, D. B., "Low-frequency horn design using Thiele-Small driver parameters," *57th Convention of the Audio Engineering Society*, May 1977, preprint no. 1250 (Cited on page 35.)

[164] Small, R. H., “Suitability of low-frequency divers for horn-loaded loudspeaker systems,” *57th Convention of the Audio Engineering Society*, May 1977, preprint no. 1251 (Cited on page 35.)

[165] Benade, A. H. and Jansson, E. V., “On plane and spherical waves in horns with non-uniform flare part 1,” *Acoustica*, vol. 31, pp. 79–98, 1974 (Cited on pages 35 and 41.)

[166] Jansson, E. V. and Benade, A. H., “On plane and spherical waves in horns with non-uniform flare part 2,” *Acoustica*, vol. 31, no. 4, pp. 185–202, 1974 (Cited on page 35.)

[167] Geddes, E. R., “Acoustic waveguide theory,” *83rd Convention of the Audio Engineering Society*, Oct 1987, preprint no. 2547 (Cited on pages 35, 36, and 45.)

[168] Putland, G. R., “Comments on "Acoustic waveguide theory" and author’s reply,” *J. Audio Eng. Soc.*, vol. 39, no. 6, pp. 469–472, Jun 1991 (Cited on pages 35 and 44.)

[169] Geddes, E. R., “Acoustic waveguide theory revisited,” *J. Audio Eng. Soc.*, vol. 41, no. 6, pp. 452–461, Jun 1993 (Cited on pages 35, 45, and 46.)

[170] Putland, G. R., “Every one-parameter acoustic field obeys Webster’s horn equation,” *J. Audio Eng. Soc.*, vol. 41, no. 6, pp. 435–451, Jun 1993 (Cited on pages 35 and 44.)

[171] Klipsch, P. W., “Horn for loudspeaker,” US Patent 2 310 243, filed Feb. 5, 1940, issued Feb. 9, 1943 (Cited on page 36.)

[172] Sinclair, R., “Optimization of two-segment exponential horns,” *63rd Convention of the Audio Engineering Society*, May 1979, preprint no. 1509 (Cited on page 36.)

[173] Geddes, E. R., “Source radiation characteristics,” *J. Audio Eng. Soc.*, vol. 34, no. 6, pp. 464–478, Jun 1986 (Cited on page 36.)

[174] Geddes, E. R., “Sound radiation from acoustic apertures,” *J. Audio Eng. Soc.*, vol. 41, no. 4, pp. 214–230, Apr 1993 (Cited on pages 36 and 98.)

[175] Gloukhov, A., “A method of loudspeaker directivity prediction based on Huygens-Fresnel principle,” *115th Convention of the Audio Engineering Society*, Oct 2003 (Cited on page 36.)

[176] Di Cola, M. and Doldi, D., “Horn’s directivity related to the pressure distribution at their mouth,” *109th Convention of the Audio Engineering Society*, Sep 2000, preprint no. 5214 (Cited on page 36.)

[177] Di Cola, M., “Analysis of directivity anomalies in mid and high freqyency horn loudspeakers,” *111th Convention of the Audio Engineering Society*, Sep 2001, convention Paper no. 5432 (Cited on page 36.)

[178] Di Cola, M., Doldi, D., and Saronni, D., “Horns directivity related to the pressure distribution at their mouth: part 2,” *110th Convention of the Audio Engineering Society*, May 2001, convention Paper no. 5319 (Cited on page 36.)

[179] Kagawa, Y., Yamabuchi, T., and Yoshikawa, T., “Finite element approach to acoustic transmission-radiation systems and application to horn and silencer design,” *J. Sound Vibr.*, vol. 69, no. 2, pp. 207–228, 1980 (Cited on page 36.)

[180] Morita, S., Kyono, N., Sakai, S., Yamabuchi, T., and Kagawa, Y., “Acoustic radiation of a horn loudspeaker by the finite element method – a consideration of the acoustic characteristic of horns,” *J. Audio Eng. Soc.*, vol. 28, no. 7/8, pp. 482–489, Jul/Aug 1980 (Cited on page 36.)

[181] Kyouno, N., Sakai, S., Morita, S., Yamabuchi, T., and Kagawa, Y., “Acoustic radiation of a horn loudspeaker by the finite element method – acoustic characteristics of a horn loudspeaker with an elastic diaphragm,” *69th Convention of the Audio Engineering Society*, May 1981, preprint no. 1756. [Online]. Available: http://www.aes.org/e-lib/browse.cfm?elib=5141 (Cited on page 36.)

[182] Kristiansen, U. R., “Sound radiation from axisymmetric sources of complex shape,” *J. Sound Vibr.*, vol. 113, no. 1, pp. 204–207, 1987 (Cited on pages 36 and 50.)

[183] Kristiansen, U. R. and Johansen, T. F., “The horn loudspeaker as a screen-diffraction problem,” *J. Sound Vibr.*, vol. 133, no. 3, pp. 449–456, 1989 (Cited on pages 36 and 55.)

[184] Johansen, T. F., “Implementation and use of a numerical technique for studies of directional properties of the sound radiation from horn loudspeakers,” Ph.D. dissertation, Norges Tekniske Høgskole, 1991 (Cited on pages 37, 44, and 55.)

[185] Johansen, T. F., “On the directivity of horn loudspeakers,” *J. Audio Eng. Soc.*, vol. 42, no. 12, pp. 1008–1019, Dec 1994 (Cited on page 37.)

[186] Henwood, D. J., “The boundary-element method and horn design,” *J. Audio Eng. Soc*, vol. 41, no. 6, pp. 485–496, June 1993. [Online]. Available: http://www.aes.org/e-lib/browse.cfm?elib=6995 (Cited on page 37.)

[187] Geaves, G. P. and Henwood, D. J., "Horn optimisation using numerical methods," *100th Convention of the Audio Engineering Society*, May 1996, preprint no. 4208 (Cited on page 37.)

[188] Shindo, T., Yoshioka, T., and Fukuyama, K., "Calculation of sound radiation from an unbaffled, rectangular-cross-section horn loudspeaker using combined analytical and boundary-element methods," *J. Audio Eng. Soc.*, vol. 38, no. 5, pp. 340–349, May 1990 (Cited on pages 37, 65, and 215.)

[189] Hodgson, T. H. and Underwood, R. L., "BEM computations of a finite-length acoustic horn and comparison with experiment," in *Computational Acoustics and its Environmental Applications*, 1997 (Cited on page 37.)

[190] Bright, A., Holland, K., and Fahy, F. J., "Analysis of a folded acoustic horn," *J. Audio Eng. Soc.*, vol. 52, no. 10, pp. 1029–1042, 2004. [Online]. Available: http://www.aes.org/e-lib/browse.cfm?elib=13023 (Cited on page 37.)

[191] Kirkup, S. M., Thompson, A., Kolbrek, B., and Yazdani, J., "Simulation of the acoustic field of a horn loudspeaker by the Boundary Element-Rayleigh Integral Method," *Journal of Computational Acoustics*, vol. 21, no. 1, pp. 1–17, 2013 (Cited on pages 37, 56, 209, 217, and 235.)

[192] Holm, J., "Applying the Finite Element Method for modelling loudspeaker waveguide directivity," Master's thesis, Aalto University, May 2010 (Cited on page 37.)

[193] Wadbro, E. and Berggren, M., "Topology optimization of an acoustic horn," *Computer Methods in Applied Mechanics and Engineering*, vol. 196, no. 1–3, pp. 420 – 436, 2006. [Online]. Available: http://www.sciencedirect.com/science/article/pii/S0045782506001745 (Cited on page 37.)

[194] Wadbro, E., Udawalpola, R., and Berggren, M., "Shape and topology optimization of an acoustic horn-lens combination," *Journal of Computational and Applied Mathematics*, vol. 234, pp. 1781–1787, 2009 (Cited on page 37.)

[195] Udawalpola, R. and Berggren, M., "Optimization of an acoustic horn with respect to efficiency and directivity," *International Journal for Numerical Methods in Engineering*, vol. 73, no. 11, pp. 1571–1606, 2008. [Online]. Available: http://dx.doi.org/10.1002/nme.2132 (Cited on page 37.)

[196] Bequin, P. and Morfey, C. L., "Weak nonlinear propagation of sound in a finite exponential horn," *J. Acoust. Soc. Am.*, vol. 109, no. 6, pp. 2649–2659, Jun 2001 (Cited on page 37.)

[197] Zamorski, T., “Waves with finite amplitude in bessel horns,” *Archives of Acoustics*, vol. 15, no. 3-4, pp. 531–542, 1990 (Cited on page 37.)

[198] Klippel, W., “Parameter measurement and identification of the nonlinear system structure on horn loudspeakers,” *99th Convention of the Audio Engineering Society*, Oct 1995, preprint no. 4084 (Cited on page 37.)

[199] Klippel, W., “Nonlinear wave propagation in horns and ducts,” *J. Acoust. Soc. Am.*, vol. 98, no. 1, pp. 431–436, Jul 1995 (Cited on page 37.)

[200] Klippel, W., “Modeling the nonlinearities in horn loudspeakers,” *J. Audio Eng. Soc.*, vol. 44, no. 6, pp. 470–480, Jun 1996 (Cited on page 37.)

[201] Holland, K. R. and Morfey, C. L., “A model of nonlinear propagation in horns,” *J. Audio Eng. Soc.*, vol. 44, no. 7/8, pp. 569–580, Jul/Aug 1996 (Cited on page 37.)

[202] Voishvillo, A. G., “Comparative analysis of nonlinear distortion in compression drivers and horns,” *117th Convention of the Audio Engineering Society*, Oct 2004, no. 6192 (Cited on page 37.)

[203] Kikkawa, T., Yukiyoshi, A., and Sakamoto, N., “A new horn loudspeaker design yields low distortion and wide dispersion,” *55th Convention of the Audio Engineering Society*, Oct 1976, preprint no. 1151 (Cited on page 37.)

[204] Tsuchiya, T., Kagawa, Y., Doi, M., and Tsuji, T., “Finite element simulation of non-linear acoustic generation in a horn loudspeaker,” *J. Sound Vibr.*, vol. 266, pp. 993–1008, 2002 (Cited on page 37.)

[205] Makarski, M., “Simulation of harmonic distortion in horns using an extended BEM postprocessing,” *119th Convention of the Audio Engineering Society*, Oct 2005, convention Paper no. 6591 (Cited on page 38.)

[206] Post, J. T. and Hixon, Elmer T., r., “A modeling and measurement study of acoustic horns,” Ph.D. dissertation, University of Texas, May 1994 (Cited on pages 41, 57, 193, and 215.)

[207] Nagarkar, B. N. and Finch, R. D., “Sinusoidal horns,” *J. Acoust. Soc. Am.*, vol. 50, no. 1 (1), pp. 23–31, 1971 (Cited on page 42.)

[208] Leach, W. M., “A two-port analogous circuit and SPICE model for Salmon’s family of acoustic horns,” *J. Acoust. Soc. Am.*, vol. 99, no. 3, pp. 1459–1464, Mar 1996 (Cited on page 42.)

[209] Forbes, B. J. and Pike, E. R., "Acoustical Klein-Gordon equation: A time-independent perturbation analysis," *Phys. Rev. Lett.*, vol. 93, no. 5, p. 054301, Jul 2004 (Cited on page 42.)

[210] Martin, P. A., "On Websters horn equation and some generalizations," *J. Acoust. Soc. Am.*, vol. 116, no. 3, pp. 1381–1388, Sep 2004 (Cited on page 42.)

[211] Mercier, J.-F. and Maurel, A., "Acoustic propagation in non-uniform waveguides: revisiting Webster equation using evanescent boundary modes," in *Proc. R. Soc. A*, vol. 469, no. 2156. The Royal Society, 2013, p. 20130186 (Cited on page 42.)

[212] Lukkari, T. and Malinen, J., "A posteriori error estimates for Webster's equation in wave propagation," *Journal of Mathematical Analysis and Applications*, vol. 427, no. 2, pp. 941–961, 2015 (Cited on page 42.)

[213] Sato, K., "On the acoustical properties of conical horns (in Japanese)," *Report of the Aeronautical Research Institute, Tokyo Imperial University*, vol. 4, no. 42, pp. 1–19, Jun 1928 (Cited on page 44.)

[214] Pagneux, V., Amir, N., and Kergomard, J., "A study of wave propagation in varying cross-section waveguides by modal decomposition. Part I. Theory and validation," *J. Acoust. Soc. Am.*, vol. 100, no. 4, pp. 2034–2048, Oct 1996 (Cited on pages 44, 65, 68, 83, and 90.)

[215] Geddes, E. R., Bauman, P. D., and Adamson, A. B., "Acoustic waveguides – in practice," *J. Audio Eng. Soc.*, vol. 41, no. 6, pp. 462–470, Jun 1993 (Cited on pages 45 and 46.)

[216] Barjau, A. and Gibiat, V., "Delay lines, Finite Differences and Cellular Automata: Three close but different schemes for simulating acoustical propagation in 1D systems," *Acta Acustica united with Acustica*, vol. 88, pp. 554–566, 2002 (Cited on page 49.)

[217] Kagawa, Y., Tsuchiya, T., Fujii, B., and Fujioka, K., "Discrete Huygens' model approach to sound wave propagation," *Journal of sound and vibration*, vol. 218, no. 3, pp. 419–444, 1998 (Cited on page 49.)

[218] Kagawa, Y., Tsuchiya, T., Fujioka, K., and Takeuchi, M., "Discrete Huygens' model approach to sound wave propagation–reverberation in a room, sound source identification and tomography in time reversal," *Journal of Sound and Vibration*, vol. 225, no. 1, pp. 61–78, 1999 (Cited on page 49.)

[219] Christopoulos, C., Ed., *The Transmission Line Modeling Method: TLM*. IEEE Press, 1995 (Cited on page 49.)

[220] Smith III, J. O., "A basic introduction to digital waveguide synthesis (for the technically inclined)," *Center for Computer Research in Music and Acoustics (CCRMA), Stanford University.*, 2006. [Online]. Available: http://ccrma.stanford.edu/~{}jos/swgt (Cited on page 49.)

[221] Southern, A., Murphy, D., Campos, G., and Dias, P., "Finite difference room acoustic modelling on a general purpose graphics processing unit," *128th Convention of the Audio Engineering Society*, 2010, convention Paper no. 8028 (Cited on page 49.)

[222] Noreland, D., "A numerical method for acoustic waves in horns," *Acta Acustica united with Acustica*, vol. 88, pp. 576–586, 2002 (Cited on page 50.)

[223] Zienkiewicz, O. C., *The Finite Element Method*. McGraw-Hill Book Company, London, 1977 (Cited on page 50.)

[224] Petyt, M., *Theoretical Acoustic and Numerical Techniques*. Springer Verlag Wien–New York, 1983, ch. Finite Element Techniques for Acoustics, pp. 51–103 (Cited on page 50.)

[225] Kristiansen, U. R. and Viggen, E. M., *Computational Methods in Acoustics*. Department of Electronics and Telecommunications, NTNU, 2010 (Cited on pages 50 and 52.)

[226] Bettess, P., "Infinite elements," *J. Numerical Methods in Engineering*, vol. 11, no. 1, pp. 53–64, 1977 (Cited on page 50.)

[227] Kirkup, S., *The Boundary Element Method in Acoustics*, 2nd ed. Integrated Sound Software, 2007, no. ISBN: 0953403106 (Cited on pages 52, 53, 54, 55, 198, 209, and 220.)

[228] Schenck, H. A., "Improved integral formulation for acoustic radiation problems," *J. Acoust. Soc. Am.*, vol. 44, no. 1, pp. 41–58, 1968 (Cited on page 54.)

[229] Burton, A. J. and Miller, G. F., "The application of integral equation methods to the numerical solution of some exterior boundary vaoue problems," *Proc. R. Soc. A*, vol. A323, pp. 201–210, 1971 (Cited on page 55.)

[230] Mohsen, A., Piscoya, R., and Ochmann, M., "The application of the dual surface method to treat the nonuniqueness in solving acoustic exterior problems," *Acta Acustica United with Acustica*, vol. 97, no. 4, pp. 699–707, 2011 (Cited on page 55.)

[231] Cheng, A. H.-D. and Cheng, D. T., "Heritage and early history of the boundary element method," *Engineering Analysis with Boundary Elements*, vol. 29, no. 3, pp. 268–302, 2005 (Cited on page 55.)

[232] Kirkup, S. and Thompson, A., "Computing the acoustic field of a radiating cavity by the Boundary Element - Rayleigh Integral Method (BERIM)," *Proceedings of the World Congress on Engineering*, vol. 2, 2007. [Online]. Available: http://www.kirkup.info/papers/SKAT07.pdf (Cited on page 56.)

[233] Saad, Y. and Schultz, M. H., "GMRES: a generalized minimal residual algorithm for solving nonsymmetric linear systems," *Siam J. Sci. Stat. Comput.*, vol. 7, no. 3, pp. 856–869, Jul 1986 (Cited on page 57.)

[234] Sifuentes, J., "Preconditioning the integral formulation of the Helmholtz equation via deflation," Master's thesis, Rice University, Houston, Texas, 2006 (Cited on page 57.)

[235] Liu, Y., *Fast multipole boundary element method: theory and applications in engineering*. Cambridge university press, 2009 (Cited on page 57.)

[236] Koopmann, G. and Fahnline, J., *Designing Quiet Structures*. Academic Press, 1997 (Cited on page 57.)

[237] Murphy, D. J. and Morgans, R., "Modelling acoustic horns with FEA," *128th Convention of the Audio Engineering Society*, May 2010, convention Paper no. 8076 (Cited on page 57.)

[238] Godinho, L., Mendes, P. A., Ramis, J., Cardenas, W., and Carbajo, J., "A numerical MFS model for computational analysis of acoustic horns," *Acta Acustica united with Acustica*, vol. 98, no. 6, pp. 916–927, 2012 (Cited on pages 59 and 61.)

[239] Candy, J., "Accurate calculation of radiation and diffraction from loudspeaker enclosures at low frequency," *J. Audio Eng. Soc*, vol. 61, no. 6, pp. 356–365, 2013. [Online]. Available: http://www.aes.org/e-lib/browse.cfm?elib=16828 (Cited on pages 59 and 60.)

[240] Mapes-Riordan, D., "Horn modeling with conical and cylindrical transmission-line elements," *J. Audio Eng. Soc.*, vol. 41, no. 6, pp. 471–484, Jun 1993 (Cited on pages 62, 63, and 229.)

[241] Holland, K. R., Fahy, F. J., and Morfey, C. L., "Prediction and measurement of the one-parameter behavior of horns," *J. Audio Eng. Soc.*, vol. 37, no. 5, pp. 315–337, May 1991 (Cited on pages 62 and 63.)

[242] Young, F. J., “The natural frequencies of musical horns,” *Acta Acustica united with Acustica*, vol. 10, no. 2, pp. 91–97, 1960 (Cited on page 62.)

[243] Plitnik, G. R. and Strong, W. J., “Numerical method for calculating input impedances of the oboe,” *The Journal of the Acoustical Society of America*, vol. 65, no. 3, pp. 816–825, 1979 (Cited on page 62.)

[244] Molloy, C. T., “Use of four-pole parameters in vibration calculations,” *J. Acoust. Soc. Am.*, vol. 29, no. 7, pp. 842–853, Jul 1957 (Cited on page 63.)

[245] Lampton, M., “Transmission matrices in electroacoustics,” *Acoustica*, vol. 39, pp. 239–251, 1978 (Cited on page 63.)

[246] Caussé, R. and Kergomard, J., “Input impedance of brass musical instruments – comparison between experiment and numerical models,” *J. Acoust. Soc. Am.*, vol. 75, no. 1, pp. 241–254, Jan 1984 (Cited on page 63.)

[247] Keefe, D. H., “Acoustical wave propagation in cylindrical ducts,” *J. Acoust. Soc. Am.*, vol. 75, no. 1, pp. 58–62, Jan 1984 (Cited on page 63.)

[248] McLean, J. S., Post, J. T., and Hixon, E. T., “A theoretical and experimental investigation of the throat impedance characteristics of constant directivity horns,” *J. Acoust. Soc. Am.*, vol. 92, no. 5, pp. 2509–2550, Nov 1992 (Cited on page 63.)

[249] Fletcher, N. H. and Rossing, T., *The physics of musical instruments*. Springer Science & Business Media, 2012 (Cited on page 63.)

[250] Berners, D. P., “Acoustics and signal processing techniques for physical modeling of brass instruments,” Ph.D. dissertation, Stanford University, 1999 (Cited on page 64.)

[251] Berners, D. P. and Smith III, J. O., “Super-spherical wave simulation in flaring horns,” *Proceedings of the International Computer Music Conference*, 1995 (Cited on page 64.)

[252] Hélie, T., “Unidimensional models of acoustic propagation in axisymmetric waveguides,” *J. Acoust. Soc. Am.*, vol. 114, no. 5, pp. 2633–2647, Nov 2003 (Cited on page 64.)

[253] Agullo, J., Barjau, A., and Keefe, D. H., “Acoustic propagation in flaring, axisymmetric horns: I. A New family of unidimensional solutions,” *Acta Acustica united with Acustica*, vol. 85, no. 2, pp. 278–284, 1999. [Online]. Available: http://www.ingentaconnect.com/content/dav/aaua/1999/00000085/00000002/art00015 (Cited on page 64.)

[254] Eveno, P., Dalmont, J.-P., Caussé, R., and Gilbert, J., "Wave propagation and radiation in a horn: Comparisons between models and measurements," *Acta Acustica united with Acustica*, vol. 98, pp. 158–165, 2012 (Cited on pages 64 and 67.)

[255] Hélie, T., Hézard, T., Mignot, R., and Matignon, D., "One-dimensional acoustic models of horns and comparison with measurements," *Acta Acustica united with Acustica*, vol. 99, no. 6, pp. 960–974, 2013 (Cited on page 64.)

[256] Rayleigh, J. W. S., *The Theory of Sound*, 2nd ed. Dover Publications, 1894, vol. 2 (Cited on pages 64 and 111.)

[257] Miles, J., "The reflection of sound due to a change in cross section of a circular tube," *J. Acoust. Soc. Am.*, vol. 16, no. 1, pp. 14–19, Jul 1944 (Cited on page 64.)

[258] Miles, J. W., "The analysis of plane discontinuities in cylindrical tubes. Part I," *J. Acoust. Soc. Am.*, vol. 17, no. 3, pp. 259–271, 1946. [Online]. Available: http://scitation.aip.org/content/asa/journal/jasa/17/3/10.1121/1.1916327 (Cited on page 64.)

[259] Miles, J. W., "The analysis of plane discontinuities in cylindrical tubes. Part II," *J. Acoust. Soc. Am.*, vol. 17, no. 3, pp. 272–284, 1946. [Online]. Available: http://scitation.aip.org/content/asa/journal/jasa/17/3/10.1121/1.1916328 (Cited on page 64.)

[260] Miles, J. W., "The diffraction of sound due to right-angled joints in rectangular tubes," *J. Acoust. Soc. Am.*, vol. 19, no. 4, pp. 572–579, Jul 1947. [Online]. Available: http://scitation.aip.org/content/asa/journal/jasa/19/4/10.1121/1.1916523 (Cited on page 64.)

[261] Miles, J. W., "The equivalent circuit for a bifurcated cylindrical tube," *The Journal of the Acoustical Society of America*, vol. 19, no. 4, pp. 579–584, Jul 1947. [Online]. Available: http://scitation.aip.org/content/asa/journal/jasa/19/4/10.1121/1.1916524 (Cited on page 64.)

[262] Mittra, R. and Lee, S. W., *Analytical Techniques in the Theory of Guided Waves*. The MacMillan Company, 1971 (Cited on pages 64 and 66.)

[263] Eleftheriades, G. V., Omar, A. S., Katehi, L. P., and Rebeiz, G. M., "Some important properties of waveguide junction generalized scattering matrices in the context of the mode matching technique," *Microwave Theory and Techniques, IEEE Transactions on*, vol. 42, no. 10, pp. 1896–1903, 1994 (Cited on page 64.)

[264] Kergomard, J., Garcia, A., Tagui, G., and Dalmont, J., "Analysis of higher order mode effects in an expansion chamber using

modal theory and equivalent electrical circuits," *J. Sound Vibr.*, vol. 129, no. 3, pp. 457–475, Mar 1989 (Cited on page 65.)

[265] Amir, N., Pagneux, V., and Kergomard, J., "A study of wave propagation in varying cross-section waveguides by modal decomposition. Part II. results," *J. Acoust. Soc. Am.*, vol. 101, no. 5, pp. 2504–2517, May 1997 (Cited on pages 65, 195, and 212.)

[266] Amir, N. and Starobinski, R., "Finding the eigenmodes of two-dimensional cavities with two axes of symmetry," *Acustica united with Acta Acustica*, vol. 82, no. 6, pp. 811–822, Des 1996 (Cited on pages 65, 73, 83, 249, and 252.)

[267] Kemp, J. A., "Theoretical and experimental study of wave propagation in brass musical instruments," Ph.D. dissertation, University of Edinburgh, 2002. [Online]. Available: http://www.kempacoustics.com/thesis2/ (Cited on pages 65, 71, 77, 83, 90, 105, 106, 107, 110, 116, and 212.)

[268] Félix, S. and Pagneux, V., "Sound attenuation in lined bends," *J. Acoust. Soc. Am.*, vol. 116, pp. 1921–1931, 2004 (Cited on page 65.)

[269] Félix, S. and Pagneux, V., "Ray-wave correspondence in bent waveguides," *Wave Motion*, vol. 41, pp. 339–355, 2005 (Cited on page 65.)

[270] Schuhmacher, A. and Rasmussen, K. B., "Modelling of horn-type loudspeakers for outdoor sound reinforcement systems," *Applied Acoustics*, vol. 56, pp. 25–37, 1999 (Cited on pages 65 and 195.)

[271] Hudde, H., "The propagation constant in lossy circular tubes near the cutoff frequencies of higher-order modes," *J. Acoust. Soc. Am.*, vol. 83, no. 4, pp. 1311–1318, Apr 1988 (Cited on page 66.)

[272] Hudde, H., "Acoustical higher-order mode scattering matrix of circular nonuniform lossy tubes without flow," *J. Acoust. Soc. Am.*, vol. 85, pp. 2316–2330, 1989 (Cited on page 66.)

[273] Furnell, G. D. and Bies, D. A., "Matrix analysis of acoustic wave propagation within curved ducting systems," *Journal of Sound and Vibration*, vol. 132, pp. 245–263, 1986 (Cited on page 66.)

[274] Furnell, G. D. and Bies, D. A., "Characteristics of modal wave propagation within longitudinally curved acoustic waveguides," *Journal of Sound and Vibration*, vol. 130, pp. 405–423, 1989 (Cited on page 66.)

[275] Muehleisen, R. T., "Reflection, radiation, and coupling of higher order modes at discontinuities in finite length rigid walled rectangular ducts," Ph.D. dissertation, The Pennsylvania State University, 1996 (Cited on page 66.)

[276] Frey, P. and George, P.-L., *Mesh generation*. John Wiley & Sons, 2013 (Cited on page 67.)

[277] Evensen, K. B. and Kolbrek, B., "Mode matching method for concentric horns," *62nd Polish Open Seminar on Acoustics,*, 2015 (Cited on page 71.)

[278] Morse, P. M. and Ingard, U., *Theoretical Acoustics*. McGraw-Hill, 1986 (Cited on pages 71 and 225.)

[279] Pierce, A. D., *Acoustics*. Acoustical Society of America, New York, 1994 (Cited on pages 71, 77, 104, and 234.)

[280] Zorumski, W. E., "Generalized radiation impedances and reflection coefficients of circular and annular ducts," *J. Acoust. Soc. Am.*, vol. 54, no. 6, pp. 1667–1673, 1973 (Cited on pages 75, 108, and 110.)

[281] Cummings, A., "Sound transmission in a folded annular duct," *J. Sound Vibr.*, vol. 41, no. 3, pp. 375–379, 1975 (Cited on page 75.)

[282] Abramowitz, M. and Stegun, I. A., Eds., *Handbook of Mathematical Functions*, 1970 (Cited on page 76.)

[283] Roure, A., "Propagation du son dans des conduits a section continuement variable - application a la determination des frequences propres de certains volumes complexes," in *Proceedings Euromech 94*, Sept 1977 (Cited on page 83.)

[284] Kergomard, J. and Garcia, A., "Simple discontinuities in acoustic waveguides at low frequencies: Critical analysis and formulae," *J. Sound Vibr.*, vol. 114, no. 3, pp. 465–479, May 1987 (Cited on page 92.)

[285] Kolbrek, B., "Modal propagation in acoustic horns," Norwegian University of Science and Technology, (Unpublished), 2012. [Online]. Available: kolbrek.hoyttalerdesign.no/images/misc/evaluation_mpm_2012_bk.pdf (Cited on pages 92, 263, and 264.)

[286] Kinsler, L. E., Frey, A. R., Coppens, A. B., and Sanders, J. V., *Fundamentals of Acoustics*, 4th ed. John Wiley & Sons, Inc., 2004 (Cited on page 98.)

[287] Jurkiewicz, J., Snakowska, A., and Smolik, D., "Acoustic impedance of outlet of a hard-walled unbaffled cylindrical duct for multimode incident wave," *Acta Physica Polonica A*, vol. 119, pp. 1061–1067, 2011 (Cited on pages 105 and 131.)

[288] Beranek, L. L. and Mellow, T. J., *Acoustics - Sound Fields and Transducers*. Academic Press, 2012 (Cited on pages 106, 177, 181, 182, 184, 186, 227, 241, 266, 271, and 293.)

[289] Li, W. L., "An analytical solution for the self-and mutual radiation resistances of a rectangular plate," *Journal of sound and vibration*, vol. 245, no. 1, pp. 1–16, 2001 (Cited on page 120.)

[290] Stenzel, H., "Die Akustische Strahlung der Rechteckigen Kolbenmembran," *Acustica*, vol. 2, no. 6, pp. 263–281, 1952 (Cited on page 121.)

[291] Burnett, D. S. and Soroka, W. W., "Tables of rectangular piston radiation impedance functions, with application to sound transmission loss through deep apertures," *J. Acoust. Soc. Am.*, vol. 51, no. 5 (2), pp. 1618–1623, 1969 (Cited on page 121.)

[292] Lindemann, O. A., "Transient fluid reaction on a baffled plane piston of arbitrary shape," *The Journal of the Acoustical Society of America*, vol. 55, no. 4, pp. 708–717, Apr 1974 (Cited on page 122.)

[293] Stepanishen, P. R., "The impulse response and time dependent force on a baffled circular piston and a sphere," *J. Sound Vibr.*, vol. 26, no. 3, pp. 287–298, 1973 (Cited on page 122.)

[294] Levine, H. and Schwinger, J., "On the radiation of sound from an unflanged circular pipe," *Phys. Rev.*, vol. 73, no. 4, pp. 383–406, Feb 1948 (Cited on page 131.)

[295] Weinstein, L. A., *The Theory of Diffraction and the Factorization Method*. The Golem Press, 1969 (Cited on pages 131, 277, and 280.)

[296] Snakowska, A., "Impedancja wylotu rury cylindrycznej bez odgrody dla fali płaskiej padającej na wylot," *Archivum Akustyki (Archives of Acoustics, Polish Edition)*, vol. 13, no. 3, pp. 223–234, 1978 (Cited on page 132.)

[297] Snakowska, A. and Wyrzykowski, R., *Wybrane zagadnienia teorii dyfrakcji (Selected topics of the theory of diffraction, in Polish)*. Wydawnictwo Wyższej Skoły Pedagogicznej w Rzesowie, 1984 (Cited on pages 132, 277, 281, and 282.)

[298] Snakowska, A. and Wyrzykowski, R., "Calculation of the acoustical field of a semi-infinite cylindrical wave-guide by means

of the green function expressed in cylindrical coordinates," *Archives of Acoustics*, vol. 11, no. 3, pp. 261–285, 1986 (Cited on page 132.)

[299] Brick, H., "Application of the Boundary Element Method to combustion noise and half-space problems," Ph.D. dissertation, Chalmers University of Technology, 2009 (Cited on page 142.)

[300] Asheim, A. and Svensson, U. P., "An integral equation formulation for the diffraction from convex plates and polyhedra," *J. Acoust. Soc. Am.*, vol. 133, no. 6, pp. 3681–3691, Jun 2013 (Cited on pages 144 and 145.)

[301] Biot, M. A. and Tolstoy, I., "Formulation of wave propagation in infinite media by normal coordinates with an application to diffraction," *J. Acoust. Soc. Am.*, vol. 29, pp. 381–391, 1957 (Cited on page 143.)

[302] Asheim, A. and Svensson, U. P., "Efficient evaluation of edge diffraction integrals using the numerical method of steepest descent," *J. Acoust. Soc. Am.*, vol. 128, no. 4, pp. 1590–1597, Oct 2010 (Cited on page 143.)

[303] Svensson, U. P. (2013) Edge diffraction toolbox for matlab. [Online]. Available: http://www.iet.ntnu.no/~{}svensson/software/index.html (Cited on page 145.)

[304] Martín Román, S. R., Svensson, U. P., Šlechta, J., and Smith, J. O., "A hybrid method combining the edge source integral equation and the boundary element method for scattering problems," *J. Acoust. Soc. Am.*, vol. 139, no. 4, p. 2202, 2016, abstract. [Online]. Available: http://scitation.aip.org/content/asa/journal/jasa/139/4/10.1121/1.4950568 (Cited on page 151.)

[305] Klapman, S., "Interaction impedance of a system of circular pistons," *J. Acoust. Soc. Am.*, vol. 11, pp. 289–295, Jan 1940 (Cited on page 161.)

[306] Arase, E. M., "Mutual radiation impedance of square and rectangular pistons in a rigid infinite baffle," *The Journal of the Acoustical Society of America*, vol. 36, no. 8, pp. 1521–1525, 1964. [Online]. Available: http://scitation.aip.org/content/asa/journal/jasa/36/8/10.1121/1.1919236 (Cited on page 161.)

[307] Sha, K., Yang, J., and Gan, W.-S., "A simple calculation method for the self- and mutual-radiation impedance of flexible rectangular patches in a rigid infinite baffle," *Journal of Sound and Vibration*, vol. 282, no. 1–2, pp. 179–195, 2005. [Online].

Available: http://www.sciencedirect.com/science/article/pii/S002246oX04001488 (Cited on page 161.)

[308] Press, W. H., Teukolsky, S. A., Vetterling, W. T., and Flannery, B. P., *Numerical Recipes in C*, 2nd ed. Cambridge University Press, 1992 (Cited on pages 163 and 253.)

[309] Blackford, L. S., Demmel, J., Dongarra, J., Duff, I., Hammarling, S., Henry, G., Heroux, M., Kaufman, L., Lumsdaine, A., Petitet, A., Pozo, R., Remington, K., and Whaley, R. C., "An updated set of Basic Linear Algebra Subprograms (BLAS)," *ACM Trans. Math. Soft.*, vol. 28-2, pp. 135–151, 2002 (Cited on page 164.)

[310] Pritchard, R., "Mutual acoustic impedance between radiators in an infinite rigid plane," *J. Acoust. Soc. Am.*, vol. 32, no. 6, pp. 730–737, Jun 1960 (Cited on page 164.)

[311] Holland, K. R. and Newell, P. R., "Loudspeakers, mutual coupling and phantom images in rooms," *103rd Convention of the Audio Engineering Society*, Sep 1997, preprint no. 4581 (Cited on page 166.)

[312] Kuttruff, H., *Room Acoustics*, 5th ed. Spon Press, London and New York, 2009, ISBN 0-203-87637-7 (Cited on page 177.)

[313] Backman, J., "Subwoofers in rooms: Effect of absorptive and resonant room structures," *127th Convention of the Audio Engineering Society*, Oct 2009 (Cited on page 177.)

[314] *ISO-10534-2:1998(E) Acoustics – Determination of sound absorption coefficient and impedance in impedance tubes – Part 2: Transfer-function method*, ISO Std. ISO-10 534-2:1998(E), Nov 1998 (Cited on page 193.)

[315] Bängtson, E., Noreland, D., and Berggren, M., "Shape optimization of an acoustic horn," *Computer Methods in Applied Mechanics and Engineering*, vol. 192, no. 11–12, pp. 1533 – 1571, 2003. [Online]. Available: http://www.sciencedirect.com/science/article/pii/S0045782502006564 (Cited on page 194.)

[316] Chapman, B., Jost, G., and Van Der Pas, R., *Using OpenMP: portable shared memory parallel programming*. MIT Press, 2008 (Cited on page 209.)

[317] *Jahrbuch des Forschungs-Instituts der Allgemeinen Elektricitäts-Gesellschaft 1928–1929*. Julius Springer, Berlin, 1930, vol. I (Cited on page 227.)

[318] *Jahrbuch des Forschungs-Instituts der Allgemeinen Elektricitäts-Gesellschaft 1930*. Julius Springer, Berlin, 1931, vol. II (Cited on page 227.)

[319] Stenzel, H., *Leitfaden zur Berechnung von Schallvorgängen*. Verlag von Julius Springer, 1939 (Cited on page 227.)

[320] Brown Jr., W., "Theory of conical sound radiators," *J. Acoust. Soc. Am.*, vol. 13, no. 1, pp. 20–22, Jul 1941 (Cited on page 227.)

[321] Carlisle, R. W., "Conditions for wide angle radiation from conical sound radiators," *J. Acoust. Soc. Am.*, vol. 15, no. 1, pp. 44–49, Jul 1943 (Cited on page 227.)

[322] Geddes, E., Porter, J., and Tang, Y., "A boundary-element approach to finite-element radiation problems," *J. Audio Eng. Soc.*, vol. 35, no. 4, pp. 211–229, Apr 1987. [Online]. Available: http://www.aes.org/e-lib/browse.cfm?elib=5215 (Cited on page 227.)

[323] Kyouno, N., Yamabuchi, T., and Kagawa, Y., "Acoustic radiation of a cone-type loudspeaker by the finite element method – acoustic characteristics and sound field," *85th Convention of the Audio Engineering Society*, Nov 1988, preprint no. 2700 (Cited on page 227.)

[324] Vollesen, H., "Control of loudspeaker directivity by mechanical optimization of the diaphragm," *94th Convention of the Audio Engineering Society*, Mar 1993, preprint no. 3528 (Cited on page 227.)

[325] Macey, P., "Cone shape optimization based on FE/BE simulation to improve the radiated sound field," *127th Convention of the Audio Engineering Society*, Oct 2009, preprint no. 7836. [Online]. Available: http://www.aes.org/e-lib/browse.cfm?elib=15031&fmt=bibtex (Cited on page 227.)

[326] Kyouno, N., Usagawa, T., Yamabuchi, T., and Kagawa, Y., "Acoustic response simulation of a cone-type loudspeaker by the finite element method," *117th Convention of the Audio Engineering Society*, Oct 2004, preprint no. 6242. [Online]. Available: http://www.aes.org/e-lib/browse.cfm?elib=12899 (Cited on page 227.)

[327] Murphy, D. J., "Axisymmetric model of a moving-coil loudspeaker," *J. Audio Eng. Soc.*, vol. 41, no. 9, pp. 679–690, Sep 1993. [Online]. Available: http://www.aes.org/e-lib/browse.cfm?elib=6987 (Cited on pages 227 and 234.)

[328] Bright, A., "Vibration behaviour of single-suspension electrodynamic loudspeakers," *109th Convention of the Audio Engineering Society*, Sep 2000, preprint no. 5213 (Cited on page 235.)

[329] Cardenas, W. and Klippel, W., "Loudspeaker rocking modes (part 1: Modeling)," *139th Convention of the Audio Engineering Society*, Oct 2015, preprint no. 9410 (Cited on page 235.)

[330] Suzuki, H. and Tichy, J., "Sound radiation from convex and concave domes in an infinite baffle," *J. Acoust. Soc. Am.*, vol. 69, no. 1, pp. 41–49, Jan 1981 (Cited on page 239.)

[331] Panzer, J., "Radiation impedance of cones at high frequencies," *112th Convention of the Audio Engineering Society*, May 2002, convention Paper no. 5520. [Online]. Available: http://www.aes.org/e-lib/browse.cfm?elib=11422 (Cited on page 239.)

[332] Kirkup, S. M. and Amini, S., "Solution of the Helmholtz eigenvalue problem via the boundary element method." *International Journal of Numerical Methods in Engineering*, vol. 36, no. 2, pp. 321–330, 1993 (Cited on page 253.)

[333] Kirkup, S. M. and Jones, M., "Computational methods for the acoustic modal analysis of an enclosed fluid with application to a loudspeaker cabinet," *Applied Acoustics*, vol. 48, no. 4, pp. 275–299, 1996 (Cited on page 253.)

[334] *Introduction to Comsol Multiphysics 5.1*, 2015. [Online]. Available: http://www.comsol.com (Cited on page 255.)

[335] Krokstad, A., Strøm, S., and Sørsdal, S., "Calculating the acoustical room response by the use of a ray tracing technique," *Journal of Sound and Vibration*, vol. 8, no. 1, pp. 118–125, 1968 (Cited on page 267.)

[336] Sun, Z., Gimenez, G., Vray, D., and Denis, F., "Calculation of the impulse response of a rigid sphere using the physical optic method and modal method jointly," *J. Acoust. Soc. Am.*, vol. 89, no. 1, pp. 10–18, 1991 (Cited on page 267.)

[337] Cheney, W. and Kincaid, D., *Numerical Mathematics and Computing*, 3rd ed. Brooks/Cole Publishing Co., 1994 (Cited on page 267.)

[338] Merhaut, J., *Theory of Electroacoustics*. McGraw-Hill, 1981, ISBN 0-07-041478-5 (Cited on page 271.)

[339] Yousri, S. and Fahy, F. J., "An analysis of the acoustic power radiated by a point dipole source into a rectangular reverberation chamber," *Journal of Sound and Vibration*, vol. 25, no. 1, pp. 39–50, 1972 (Cited on page 294.)